2016-03-01

Simple Models for Estimating the Rotational Stiffness of Steel Column-to-Footing Connections

Joshua Edwin Tryon
Brigham Young University - Provo

Simple Models for Estimating the Rotational Stiffness of Steel Column-to-Footing Connections

Joshua Edwin Tryon

A thesis submitted to the faculty of
Brigham Young University
in partial fulfillment of the requirements for the degree of

Master of Science

Paul W. Richards, Chair
Fernando S. Fonseca
Kyle M. Rollins

Department of Civil and Environmental Engineering

Brigham Young University

March 2016

ABSTRACT

Simple Models for Estimating the Rotational Stiffness of
Steel Column-to-Footing Connections

Joshua Edwin Tryon
Department of Civil and Environmental Engineering, BYU
Master of Science

Despite the crucial role they play in transferring loads from the superstructure to the foundation, steel column-to-footing connections have received little attention in research. Though shallow embedded connections are typically characterized as pinned, studies have shown that they exhibit significant rotational stiffness. The objective of this thesis is to quantify the rotational stiffness of such connections. A method named the continuum model is developed by which the rotational stiffness of embedded connections may be calculated. Outputs from this model are compared with experimental data on steel connections embedded in concrete. The continuum model is shown to be capable of reasonably predicting the rotational stiffness of such connections. Results from the model were consistent with those of previous experimental studies that showed that embedment lengths greater than twice the column depth fail to significantly increase stiffness. Plots of rotational stiffness vs. embedment length developed from the continuum model are provided such that rotational stiffness may be calculated for any wide flange shape at any embedment length. Simplified equations provide a simpler way for engineers to estimate the same information.

Keywords: steel column-to-footing connections, stiffness, embedment, beam on elastic foundation, modeling, foundations, modulus of subgrade reaction

ACKNOWLEDGMENTS

This thesis is the product of the support, collaboration, and encouragement of many individuals. First, I would like to acknowledge the constant guidance and tutelage of Dr. Paul Richards. He has been patient with me through the ups and downs of this research, and his insight and counseling have been indispensable. I am very grateful to him, especially for identifying a research topic that matched my skill set so perfectly. In addition, I would like to thank my wife, Ginger, for her unfailing support and patience throughout the ordeal of this research and for her example of hard work and dedication. She has walked this same path before me, and her encouragement has been indispensable. I would also like to recognize the support of Trevor Jones, Joseph Eixenberger, and John Niedfeldt. Their friendship, collaboration, and expertise have catalyzed this research and improved its presentation in this thesis. Finally, these acknowledgments would be incomplete without recognition of Tom Schlafly, director of research at the American Institute of Steel Construction (AISC), whose funding made this entire project possible.

TABLE OF CONTENTS

LIST OF TABLES

LIST OF FIGURES

CHAPTER 1. INTRODUCTION

1.1 Overview of Steel Column-to-Footing Connections

In the design of steel buildings, most columns are selected based on their ability to withstand vertical loads and transmit them to the foundation of the structure. Three types of steel column-to-footing connections are commonly used: exposed, embedded, and shallow embedded connections. Exposed connections, such as the one illustrated in Figure 1.1(a), are typically used in buildings such as industrial facilities where aesthetics are unimportant and the exposed base plate and anchor bolts do not interfere with facility functions. Embedded connections, as shown in Figure 1.1(b), are used in moment frame design due to their superior moment and shear capacity. Such connections can be expensive and complicated because of the major concrete work that must be done after the structural steel is placed. These may be referred to as deeply embedded connections throughout this work. Shallow embedded connections like the one depicted in Figure 1.1(c) are the most common steel column-to-footing connection, being more economical than embedded connections and more aesthetically appealing than exposed connections.

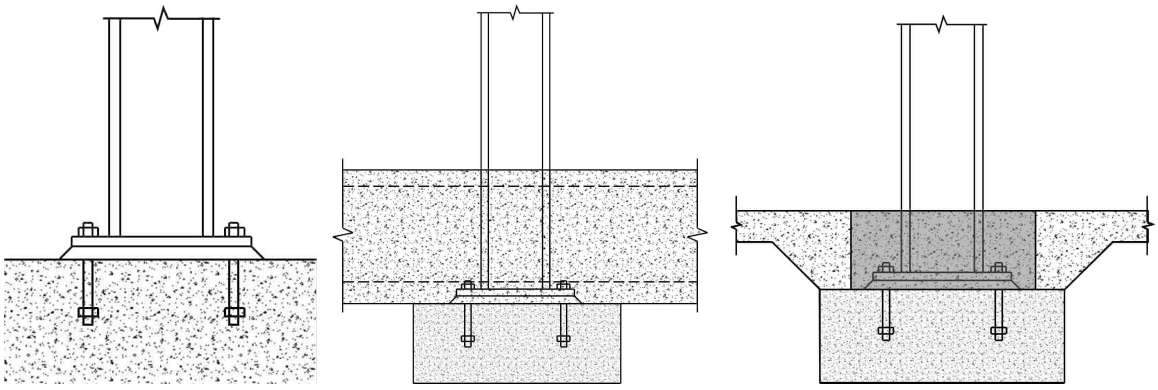

(a) Exposed (b) Embedded (c) Shallow Embedded

Figure 1.1: Steel Column-to-Footing Connections

When constructing shallow embedded connections, a part of the concrete slab is left unfilled, as shown in Figure 1.2. After the steel column is installed, the unfilled region, or block-out, is filled with unreinforced concrete. This additional concrete may provide significant moment resistance which is neglected in current design models. In current design practice, shallow embedded connections are assumed to be pinned for structural analysis purposes, transmitting only vertical gravity loads into the foundation and providing no lateral stiffness. While shallow embedded connections do not provide as much fixity as deeply embedded connections, their rotational stiffness may be quantifiable and usable in design. As such, these connections may be more accurately termed partially fixed. In other words, they transmit both vertical and lateral loads into the foundation, but both the column and the concrete slab contribute to deflections and rotations. To clarify, a fixed connection is assumed to be one where only the column contributes to deflections and rotations; the concrete slab is assumed to remain elastic.

Figure 1.2: Typical Block-out

1.2 Scope of Research

Recent research suggests that shallow embedded connections with no reinforcement may provide moment resistance closer to that of fixed connections than previously believed. Several experimental tests on pipe pile-to-pile cap specimens identify mechanisms pertinent to shallow embedded connections that may contribute to their moment resistance. One source of additional stiffness reported by Eastman is the bearing resistance of the column against the embedment material [1]. Another study by Richards, et al, suggests that friction between the column and the embedment material may provide additional moment resistance [2]. This suggests that the block-out concrete provides additional lateral strength and stiffness that is currently unaccounted for in design. Most recently, a series of tests performed by Barnwell on shallow embedded connections showed that such connections have significant lateral strength and stiffness [3].

It is the goal of structural engineers to economically design structures that are safe for human use. If the concrete block-out in shallow embedded connections can be relied upon to provide lateral strength and stiffness, quantified values for such strength and stiffness may assist structural engineers in designing safe steel column-to-footing connections more economically. For example, the inclusion of shallow embedded connections may reduce the need for deeply embedded connections, and embedment lengths required for such connections may be reduced. This represents significant reduction in material and labor costs, as well as in time required for construction.

This work develops models to quantify the rotational stiffness provided by shallow embedded connections. Two methods are developed, which are called the continuum model and the stiffness method model. To develop the continuum model, the theory of beams on elastic foundation derived by Hetenyi is applied [4]. The stiffness method of structural analysis is the basis for the appropriately named method. Both models use these methods to account for the stiffness of the embedment material. Using these approaches, both the properties of the column and the embedment material can be used to calculate the rotational stiffness of the connection. As the stiffness method model is essentially a complex, discretized version of the continuum model, most attention is paid to the continuum model in this work.

To validate the accuracy of the continuum model, its outputs were compared with those from Barnwell [3], whose work was mentioned previously, and Grilli, et al [5], who performed similar testing on deeply embedded column connections. Upon finding reasonable agreement,

normalization methods were used to produce rotational stiffness vs. embedment length curves. These plots will enable engineers to calculate the rotational stiffness of any embedded wide flange shape. Simplified piecewise equations were also developed to obtain the same information more quickly at the cost of some accuracy.

1.3 Outline

This chapter has served as a brief introduction to the need of additional research on the lateral stiffness provided by steel column-to-footing connections. It also introduced the methods by which this work seeks to model shallow embedded connections and quantify their rotational stiffness. Chapter 2 reviews the work of previous researchers, outlining contributions relevant to this work. The methods used to develop the continuum model and validate it using experimental data are discussed in Chapter 3. Results generated using the continuum model are presented and discussed in Chapter 4. Conclusions to this thesis and propositions for further research are outlined in Chapter 5. The previously mentioned stiffness method model is secondary to the continuum model and is detailed in Appendix A.

CHAPTER 2. LITERATURE REVIEW

Previous research concerning steel column-to-footing connections has been fairly limited. Nevertheless, several studies offering noteworthy contributions were identified and reviewed to provide background on these connections. To expand the library of pertinent research, it is noted that steel column-to-footing connections bear some similarity to steel pile-to-cap connections. As such, several articles discussing such connections were also reviewed. Articles pertaining to similar connection types, such as corbel, composite, and concrete filled steel tube connections, were also reviewed. This chapter serves to summarize these and other relevant articles, highlighting their pertinent experimental procedures, analytical models, and conclusions. Section 2.1 discusses studies on exposed, embedded, and shallow embedded connections. Articles on pile-to-cap and other similar connections are summarized in Section 2.2.

2.1 Studies on Steel-Column-to-Footing Connections

2.1.1 Exposed Connections

Recognizing the need to understand the behavior of exposed column connections under moment loads, DeWolf and Sarisley identified two possible methods of characterizing the strength of column base plates under eccentric axial loading [6]. The first of these methods, the working stress method, assumes that moments are resisted by two elastic mechanisms in the base plate. Tensile uplift is resisted by anchor rod engagement, and compression is resisted by bearing of the plate against the concrete surface. In this model, it is assumed that the compression occurs in the form of a triangular stress block, as shown in Figure 2.1(a). Given the base plate geometry and by assuming the maximum compressive stress f_p is the allowable concrete compressive stress f'_c, the tension T in the anchor bolts and the length a of the compression stress block can be calculated using statics. Then for a given eccentricity e, the maximum allowable load P can be found.

Alternatively, the ultimate strength method assumes that the anchor bolt is at yield stress. Following conventions in reinforced concrete design, the maximum compressive stress f_s is $0.85f'_c$. It is assumed in this method that the bearing of the plate on the concrete produces a uniformly distributed stress block. Given plate dimensions, anchor bolt cross-sectional area, and material properties, as well as either the eccentricity or the applied load P, all other information may be calculated through statics. The ultimate strength method is depicted in Figure 2.1(b).

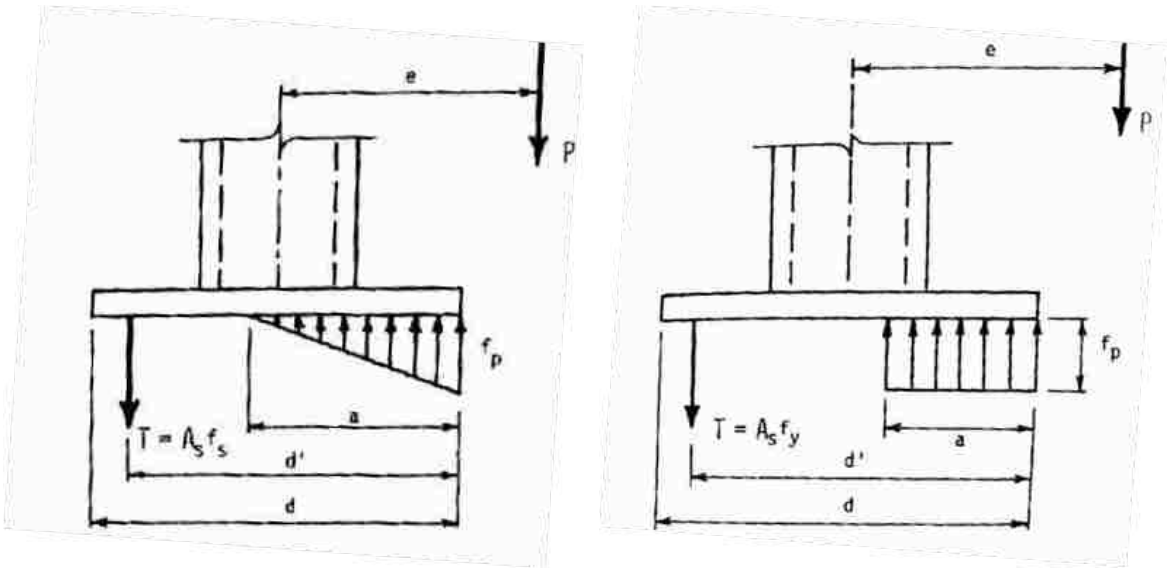

(a) Working Stress Method (b) Ultimate Strength Method

Figure 2.1: Base Plate Strength Methods (DeWolf and Sarisley)

In an effort to test their accuracy, the researchers predicted the ultimate strength of sixteen exposed connection specimens using both the working stress and ultimate strength methods. These specimens were then tested under axial loads of varying eccentricities until failure. From the experimental data, the researchers calculated factors of safety for each method. The working stress method had an average factor of safety of 2.16, whereas the ultimate strength method yielded a factor of safety of 1.11. Despite not incorporating all of the mechanisms involved in base plate resistance, the authors concluded that both methods were reasonable for predicting the strength of exposed column connections. Of the two methods, the researchers preferred the ultimate strength method since it more accurately predicted the true behavior of the connection.

Experimental testing by Thambiratnam and Paramasivam investigated the effect of load eccentricity and base plate thickness on the strength of exposed column connections [7]. Twelve test specimens were designed with three different plate thicknesses and four varying load eccentricities. Each specimen was loaded axially, with loading occurring gradually until one of three failure modes occurred. These modes included cracking of the concrete block, yielding of the base plate, and yielding of the anchor bolts. A representation of these specimens is provided in Figure 2.2.

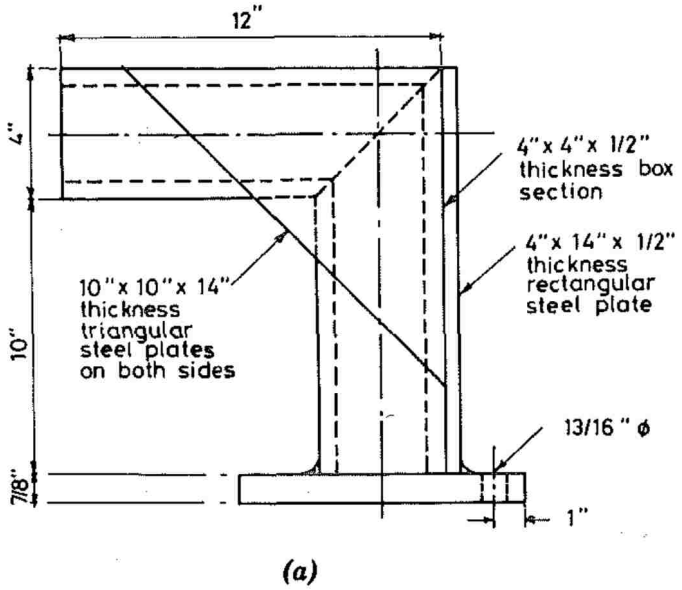

Figure 2.2: Exposed Connection Specimen Schematic (Thambiratnam and Paramasivam)

The recorded strengths from these experiments were compared with predicted strength values determined by using the working stress method described previously. It was found that the specimens exhibited significantly larger flexural capacity than was expected. Factors of safety ranged from 1.09 to 1.89, with a mean value of 1.35. Furthermore, it was found that base plates of the greatest thickness did not always exhibit the largest moment capacity. Since thicker base plates behave more rigidly, larger bending moments tend to cause such plates to overturn more uniformly. Due to the lower bearing area this causes, the resultant bearing stresses increase, contributing to premature failure. As such, the use of thinner base plates in design may serve to increase the flexural capacity of such connections.

The researchers found that compressive bearing stresses developed in the concrete were non-uniform along the length of the base plate. In particular, the greatest strain was observed to occur directly underneath the column, and smallest strains occurred at the edge of the base plate. It can be inferred that the bearing stresses were small under the edges of the base plate, and were largest under the column. The researchers explain this behavior by assuming the base plate to be flexible under plate bending. Though this behavior was observed under axial loading, it is likely that the same behavior is observed when plate bending is caused by large bending moments. If such is the case, then the contribution of the edges of the base plate may be negligible in determining the rotational stiffness contribution of the base plate in shallowly embedded connections. Furthermore, this suggests that the assumption of a triangular stress block with the highest stress at the edge of the base plate, as is assumed in the working stress method, is incorrect. For this and other reasons, the researchers suggest that the working stress method does not apply to the specimens tested in this study.

Recent testing performed by Kanvinde and Deierlein yielded a wealth of experimental data that provides insight on the behavior of exposed column base connections under several different loading conditions [8]. Greater detail on the results of this experimentation is reported by Gomez [9]. Their results were compared with recommendations made in the AISC *Steel Design Guide No. 1, Base Plate and Anchor Rod Design* [10]. Twenty large-scale specimens were tested among three experimental regimens. Of particular value to this work is the first series of experiments, which investigated the moment capacity of the first of seven specimens. To do so, each connection underwent cyclic lateral loading until failure occurred. It was found that each specimen remained elastic up to 7% drift, with some remaining elastic up to 10% drift. The *AISC Seismic Provisions* specify that connections remain elastic up to column drifts of up to 4% [11]. Furthermore, the experimentally observed flexural strength of each specimen was found to be an average of 80% higher than their estimated strength. Considering these results, the researchers suggest that a high degree of conservatism exists in current design methods. An image of one of these specimens post-failure is provided in Figure 2.3.

Figure 2.3: Specimen from First Round of Experiments (Kanvinde and Deierlein)

To supplement the data provided through these experiments, Kanvinde, et al, developed a method to approximate the rotational stiffness of exposed base connections [12]. In current design provisions, such connections are assumed to be pinned and therefore to have zero rotational stiffness, similar to shallow embedded connections. However, as suggested by the experiments just discussed, a more accurate description of such connections is that they are partially fixed; that is, they are neither pinned nor fixed. Due to the various components of the system, characterization of the rotational stiffness of exposed column connections is quite complicated. As such, Kanvinde, et al, break down the method of determining the rotational stiffness into three steps. Though not explained in detail here, these steps include first, the characterization of the design strength M_y, second, the calculation of the associated deformations of individual connection components, and third, compatibility enforcement to find the connection rotation due to an applied base moment. The rotational stiffness can then be calculated to be the base moment divided by the connection rotation, as described by Equation 2.1. The method of computing design stress follows the provisions specified in AISC *Steel Design Guide No. 1, Base Plate and Anchor Rod Design* [10]. On the tension side, a point load represents the tensile resistance of the anchor bolt, and a rectangular stress block represents the compressive bearing resistance of the base plate against the concrete or grout surface, as depicted in Figure 2.4. A representation of a deformed base plate connection under lateral load is shown in Figure 2.5.

$$\beta_y^{method} = \frac{M_y}{\theta_y} \tag{2.1}$$

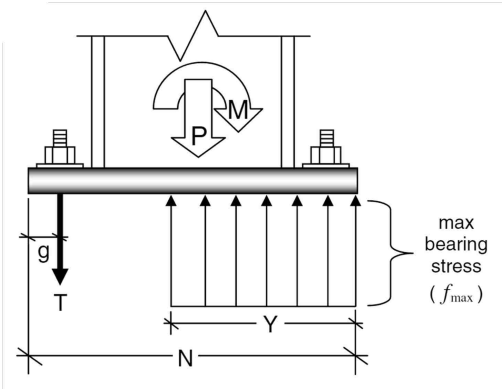

Figure 2.4: Exposed Connection Loading Under High Eccentricity (Kanvinde, et al)

The researchers validated the accuracy of the method against two sets of experimental data, one of which are the experiments by Gomez discussed above [9], and the other from an older study by Picard and Beaulieu [13]. In doing so, it was found that the method had excellent ability to predict the rotational stiffness of exposed column connections with high eccentricity, with $\beta_y^{test}/\beta_y^{method} = 1.08$ and a coefficient of variation of 0.12. However, the method was found to be less accurate for applications with lower eccentricity. Furthermore, due to the simplicity of the method, several details were necessarily excluded from consideration. As such, the researchers suggest that the method be used only to predict the rotational stiffness of connections with similar geometries to the specimens tested and that are expected to undergo high eccentricity loading.

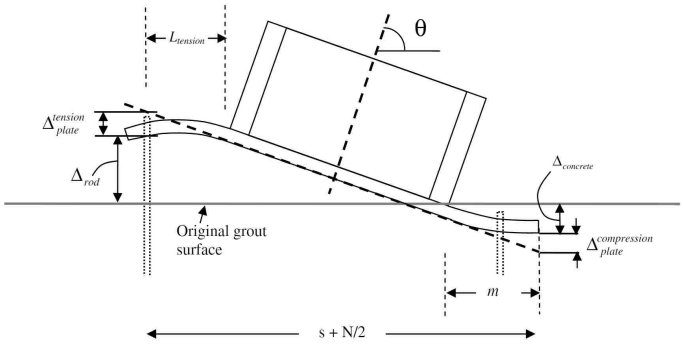

Figure 2.5: Deformed Exposed Connection Under Lateral Load (Kanvinde, et al)

It may be observed that all of the methods discussed thus far make several simplifying assumptions when determining the strength or stiffness of exposed column connections, some of which may not even be correct. The behavior of base plates under lateral loading conditions is very complex, making accurate yet simple models for determining their strength and stiffness difficult to design. In realization of this fact, Kanvinde, Jordan, et al, performed a finite element (FE) simulation on exposed column connections [14]. Such a study has the potential to provide significant benefits since FE software is capable of considering far more complex interactions than can feasibly be considered by hand. In particular, FE simulations have the capability of analyzing stress distributions. Much of the lack of understanding with regard to the behavior of exposed connections under lateral load can be attributed to the unknown stress distribution underlying the base plate. This is manifested in the form of varying compressive stress block configurations in current models, with some assuming it to be triangular, and others rectangular. As such, insight provided by FE analysis may serve to improve the accuracy of such simplified models in the future.

A representative FE model constructed by the researchers is shown in Figure 2.6. All FE models were constructed using the ABAQUS simulation platform. As can be observed in the figure, FE software allowed for behavioral analysis of all components of the column connection, including the column, base plate, anchor rods, grout pad, and concrete footing.

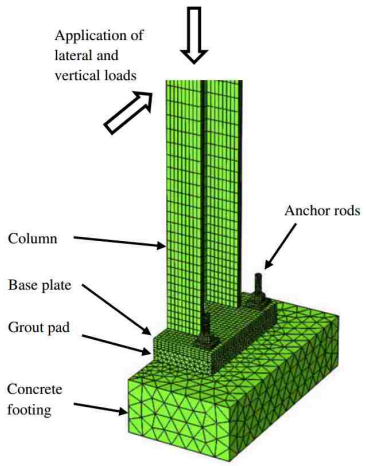

Figure 2.6: Representative Finite Element Exposed Connection (Kanvinde, et al)

Each FE model was constructed to mirror the specimens tested in Gomez's work and then simulated under the same loading conditions [9]. Upon completion of the simulations, their results were compared with those from Gomez's experiments. It was found that the FE analysis predicted similar results to those yielded in the experiments. A plot comparing the anchor rod force felt in each case is shown in Figure 2.7. It was found that design methods accurately characterize the force in the anchor rods.

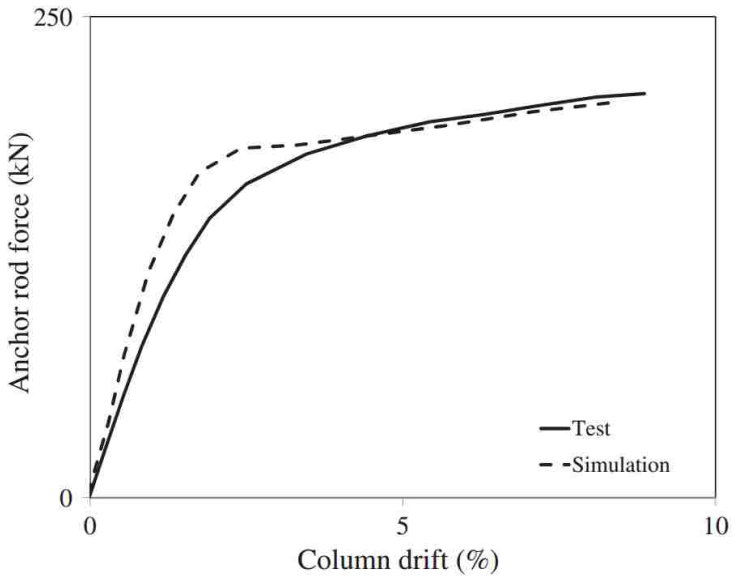

Figure 2.7: Anchor Rod Force Comparison from Tests and FE Analysis (Kanvinde, et al)

An important finding of the study was that the stress block underlying the base plate is rarely rectangular. This contradicts current design provisions, such as those suggested in the AISC *Steel Design Guide No. 1, Base Plate and Anchor Rod Design* [10]. For thicker base plates, the distribution is more accurately approximated as triangular. As for thinner base plates, stresses are highest beneath the compression flange of the column. This suggests that local flexure is likely to occur at the corner connecting the column flange and the base plate. The researchers suggest that current design provisions may be non-conservative for thicker base plate designs. They also note that though the insights provided by the analysis are useful, they are limited in scope and

further investigation may be necessary to obtain more comprehensive understanding of exposed connection behavior under lateral loads.

2.1.2 Embedded Connections

Numerical simulation and experimental tests run by Pertold, et al, provide notable insight on the properties of embedded column bases [15]. Though this study specifically isolated limit states associated with the vertical loading capacity of embedded steel column bases, it still provides valuable background on factors that may account for the unexpectedly high moment capacity of such connections. Prior to beginning their experimentation, the researchers identified crushing strength and bond strength as the two major components affecting the transfer of axial force from the column to the foundation. Two different experiments were designed to isolate each failure mode, with three specimens tested in each. To remove the contribution of crushing strength, the first specimens were designed without concrete at the base, as shown in Figure 2.8(a). Conversely, the effects of bond strength were removed in the second set of specimens by greasing the column prior to embedment, as depicted in Figure 2.8(b). Both sets of specimens were loaded axially to 15 kN to determine the initial stiffness of the column base and then reloaded to failure.

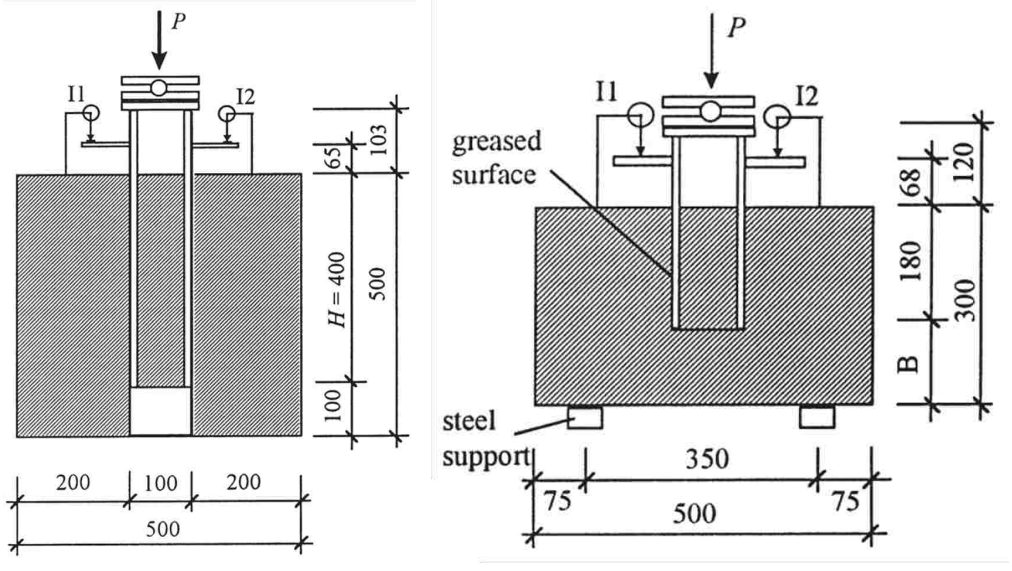

(a) First Set (b) Second Set

Figure 2.8: Test Specimen Drawings, Side View (Pertold, et al; units in mm)

Numerical analyses were performed using the finite element software SBETA. A number of different cases were simulated to isolate the strength contributions of various features of embedded connections. These features include the horizontal stress transfer mechanism between the column flanges and concrete, the embedded base plate behavior, and the stress distribution in concrete along the column flanges. Similar to the experimental regimens, alterations were made to the finite element model to isolate the effects of each individual mechanism.

Of the two components, it was found that bond strength played a greater role in vertical load resistance than did crushing strength for the specimens tested. Bond strength can be increased by deepening the embedment of the column, and crushing strength can be increased by deepening the foundation. It is likely that bond strength also plays a role in moment resistance, providing a frictional couple moment along the concrete-steel interface. This mechanism may explain some of the unexpectedly high flexural strength exhibited in experimental tests on shallow embedded connections. Since the bond strength of concrete-steel connections is higher than anticipated in current design methods, shallower embedment lengths may be used to achieve the desired moment capacity. Results from the simulations indicated that the axial resistance of an embedded column base connection is about 15% higher than that of an exposed connection.

Accompanying their experimental tests, Pertold, et al, proposed a design model by which the moment, shear, and vertical resistance of an embedded connection may be calculated [16]. Of particular value to this work is the design of embedded connections to resist moments; as such, design for shear and vertical loads will not be discussed here. In typical design of embedded connections, an embedment length ranging between one and two times the effective width of the column width is used. This effective width may be computed using Equation 2.2.

$$b_{eff} = \min \left\{ \begin{array}{c} b_c + 0.5h_c \\ 2b_c - t_{wc} \end{array} \right\} \tag{2.2}$$

In Equation 2.2, b_c is the column flange width, h_c is the column depth, and t_{wc} is the thickness of the column web. After taking a few additional steps and assuming a stress distribution within the embedded region of the column, the researchers present an equation that specifies the embedment length required to resist a given shear and bending moment load. This equation is

given in Equation 2.3. A depiction of the stress distribution assumed by the researchers is shown in Figure 2.9.

$$H = \frac{1.56V_{sd} + \sqrt{4.74V_{sd}^2 + 6.22M_{sd}f_{ck}b_{eff}}}{b_{eff}f_{cd}} \tag{2.3}$$

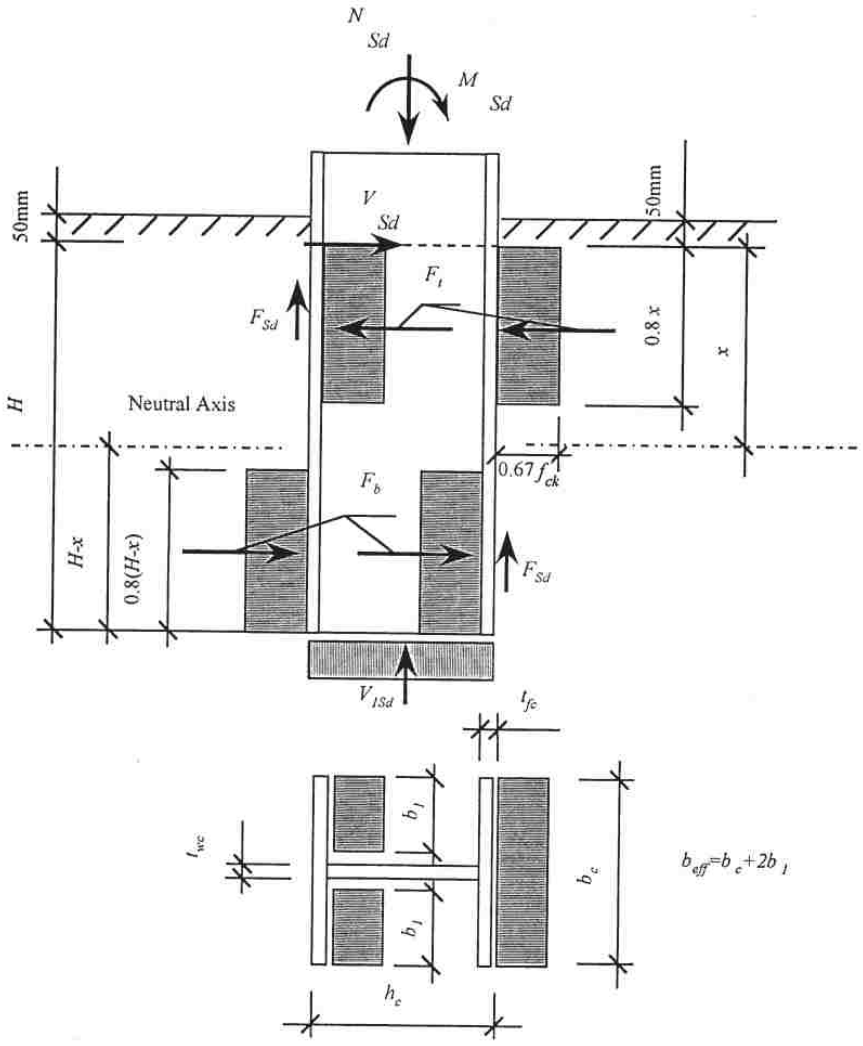

Figure 2.9: Assumed Stress Distribution (Pertold, et al)

In Equation 2.3, V_{sd} is the design shear load, M_{sd} is the design moment, f_{ck} is the tested 28-day concrete strength, b_{eff} is the effective column width, and f_{cd} is the design concrete strength.

When compared with the embedment lengths used in their experimental specimens, the researchers found that Equation 2.3 accurately yet conservatively predicted adequate embedment lengths for the failure loading applied to them. A graphical comparison of their results for moment and shear loading is provided in Figure 2.10.

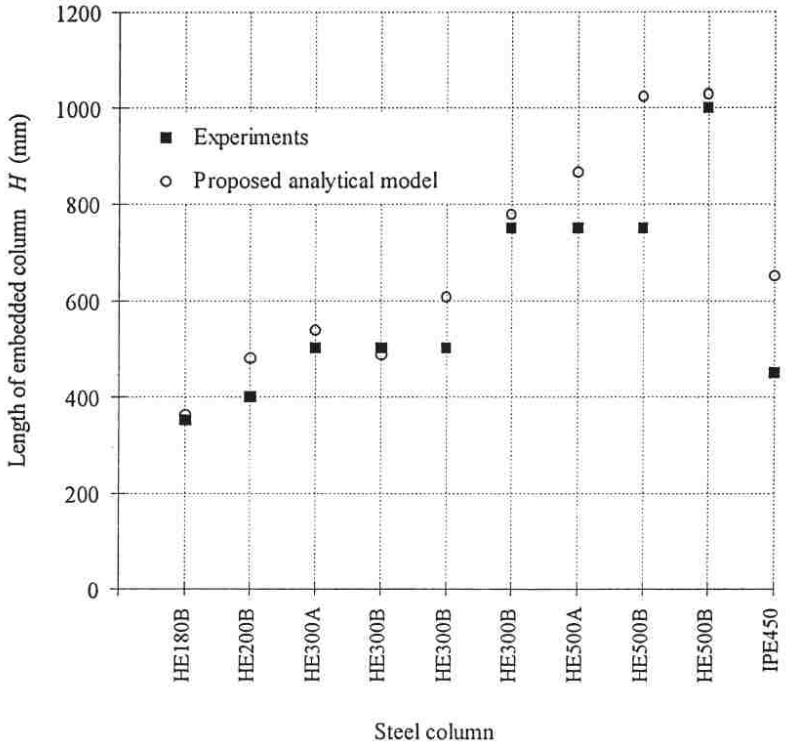

Figure 2.10: Comparison of Analytical and Experimental Embedment Lengths

Recent experimental testing by Grilli and Kanvinde sought to examine the seismic response of embedded column base (ECB) connections to seismic loading [5]. Their work reports the results of five full scale tests on ECB connection specimens subjected to cyclic lateral loads under tensile or compressive axial loading. In particular, the effects of embedment length, column size, and axial load were investigated. This research was motivated by the sparseness of available studies on the subject and the lack of design guidelines for ECB connections, with the goal of eventually establishing design guidelines for them. In addition to the experiments, a strength characterization

model was developed to predict the lateral strength of ECB connections. The model predicts the lateral strength of the specimens used in the experiments with very good accuracy. Since the present work is focused on stiffness instead of on strength, however, attention will merely be paid to the experiments and their results.

The specimens tested were W14X370 and W18X311 wide flange columns with varying amounts of embedment and axial load. An image of one of the specimens along with the test setup is shown in Figure 2.11. Each specimen underwent quasi-static, displacement-controlled cyclic lateral loading. Four of the specimens also underwent axial loading, with three of them loaded in compression and the fourth loaded in tension. Axial loads were applied prior to the application of lateral loads and were held constant throughout each test. Tests #1 and #2 were loaded to failure, Tests #3 and #4 were loaded incrementally until deformations were excessive, and Test #5 was terminated before completion of the loading protocol to due to unrecoverable slippage. To facilitate comparison of the effect of the parameters of interest (embedment length, column shape, and axial load), an experimental matrix was arranged. For example, the effect of embedment length can be directly investigated by comparing Tests #1 and #4, the effect of column shape can be observed by comparing Tests #1 and #2, and the effect of axial load can be studied by comparing Tests #3, #4, and #5. This matrix is presented tabularly in Table 2.1.

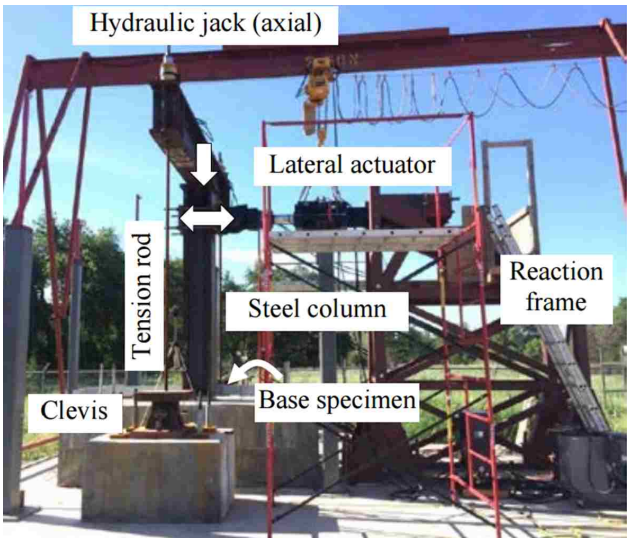

Figure 2.11: Test Setup for ECB Connection Specimen (Grilli & Kanvinde)

Table 2.1: Test Matrix and Results

Test #	Column Size (b_f [mm])	P [kN]	d [mm]	Base Plate, $t_p \times N \times B$ [mm]	z [m]	M_{base}^{max} [kN-m]	$\beta_{base}^{test\ *}$ [10^5 kN-m/rad]	$\frac{\Delta_{test}}{\Delta_{fixed}}$	$\frac{M_{base}^{y}}{M_{base}^{max}}$	Δ_{max} [%]
1	W14X370 (419)	445 (C)	508	51 x 762 x 762	2.84	2579(+)	3.23	1.21	0.87	3.85
						2613(-)			0.69	3.82
2	W18X311 (305)			51 x 864 x 711		2324(+)	3.84	1.16	0.71	3.01
						2168(-)			0.66	2.89
3	W14X370 (419)	0	762	51 x 762 x 762	3.10	3741(+)	3.07	1.30	0.72	6.97
						3444(-)			0.67	7.77
4		445 (C)				4124(+)	3.38	1.30	0.66	6.48
						3612(-)			0.81	5.09
5		667 (T)				3800(+)	3.25	1.29	0.73	2.72†
						3464(-)			0.72	2.65†
							Mean	1.25	0.72	4.98
							CoV	0.05	0.07	0.38

*Average stiffness of both directions

†Test terminated due to slip prior to failure; not included in mean or coefficient of variance

It may be observed from Table 2.1 that increased embedment length served to significantly increase the lateral strength of the specimens. Though damage progression was similar in all experiments, lateral stiffness was observed to decrease more gradually in specimens with greater embedment length. Damage began in the form of diagonal cracks progressing radially from the corners of each column with slight bulging of the concrete between the cracks. This damage was followed by flexural cracks on the sides and top of the pedestal. Failure in the shallower embedded specimens was caused by the formation of a cone, causing concrete rupture due to uplift. Those specimens with deeper embedment lengths failed from gradual strength deterioration from concrete spalling and crushing.

Further observation of Table 2.1 suggests that specimens with wider flanges exhibit greater lateral strength: M_{base}^{max} was larger in Test #1 than in Test #2. It is suggested that a greater flange width increases bearing area. Since lateral strength is directly proportional to bearing area, the experiments indicate that the use of a wider flange should increase lateral strength. The presence

of tensile axial load only moderately decreased the flexural strength of the corresponding specimen. However, the presence of compressive axial load served to increase flexural capacity by more than tensile load would decrease it.

Grauvilardell, et al, compiled a comprehensive document on base plate design and the various research discoveries made concerning them [17]. Also included in this document are a commentary on the behavior of embedded column base connections and a prioritized list of various aspects of base plate design that require additional research. The effect of the following items on base plate connection behavior were deemed to have a high priority for further research: concrete strength, column size, embedment length, presence of grade beam, presence of diagonal brace, moment/shear ratios, axial loads, welding details, tensile steel reinforcement and shear ties, composite action of shear studs, and interior and exterior column placement.

In the commentary, Grauvilardell, et al, cite numerous sources that suggest that full fixity can be approximated when embedment length is no less than $2D$, where D is the lateral dimension of the column cross section in the plane of bending. For I-shaped columns, it was found that both flanges contribute to moment resistance. Also discussed was the primary means by which moments, axial forces, and shear forces are resisted in such connections. Such loads are resisted primarily by the bearing of the column and base plate against the concrete. In the experiments cited, this bearing stress occurred in two regions of the column embedment. Bearing stresses in the upper region were oriented in the same direction as the applied lateral load, whereas the lower region felt bearing stresses oriented opposite to the applied load. Through finite element modeling, it was found that as the embedment length increased, the bearing stresses felt in the lower region approached zero, suggesting that the base plate offered little to no lateral resistance under such embedment conditions. However, the presence of a base plate significantly affected the ductility of shallow embedded columns, as did the embedment length. Furthermore, the inclusion of a base plate significantly affected the performance of the column under axial load. As discussed by Pertold, et al, crushing strength is one of the primary failure modes of columns undergoing axial load [15]. By including a base plate at the base of the column, the bearing area is increased significantly, improving the ability of the foundation to receive axial load from the column. As such, even if a base plate is unnecessary for lateral stability, it should often be included for axial resistance.

2.1.3 Shallow Embedded Connections

Though little research has been performed exclusively on shallow embedded connections, several studies have investigated structures that behave similarly. One such study by Cui, et al, investigated the effect on moment resistance caused by embedding an exposed connection a shallow depth into a floor slab [18]. This slab allows the exposed column base to function similarly to a shallow embedded connection, such as the one shown in Figure 1.1(c).

To examine the floor slab effect on the column base connection, Cui, et al, designed and fabricated eight specimens with varying amounts of reinforcement [18]. Design sketches of one of these specimens is shown in Figure 2.12. Some specimens were embedded 100 mm (3.94 in) into the slab, while others were embedded 200 mm (7.87 in). The specimens were placed in a loading frame and subjected to displacement-controlled cyclic loading. Each specimen was deformed to incremental drift angles until reaching a drift angle of 0.1 radians or until ten of the twelve anchor bolts fractured. After analyzing the results of the experiments, the researchers proposed a model to calculate the maximum resisting moment of a shallow embedded column base. Contributions to the maximum resisting moment are provided by the exposed column base, the concrete slab covering, and the reinforcing bars.

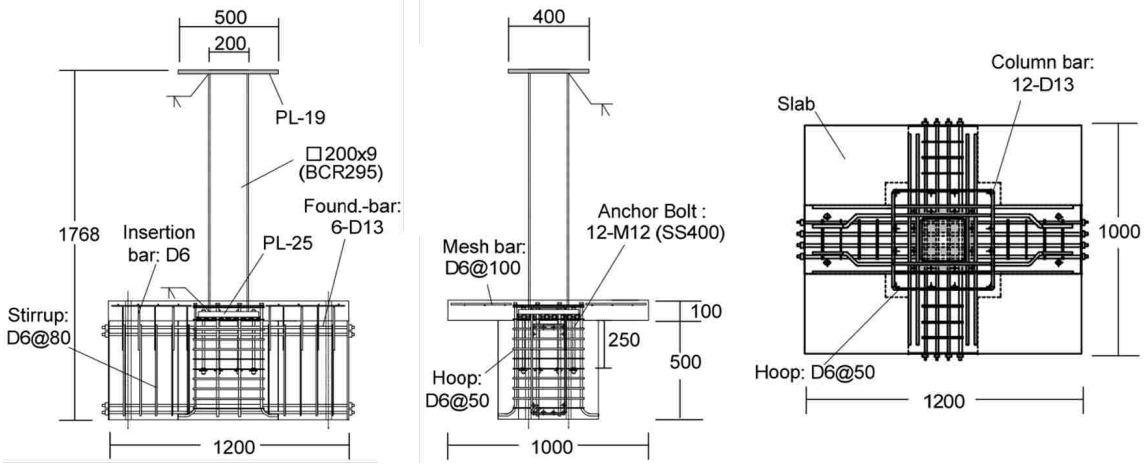

(a) Front Elevation (b) Side Elevation (c) Plane View

Figure 2.12: Sample Test Specimen, (Cui, et al; units in mm)

Results from the tests showed that the 100 mm and 200 mm embedded specimens exhibited 1.1 and 1.5 times the predicted elastic stiffness of the exposed column connections, respectively. It is suggested that the additional stiffness that is not accounted for in current models is provided by slab covering the exposed column base. This implies that the connection provides stiffness and moment capacity that is currently ignored in shallow embedded connection design.

Recent testing conducted by Barnwell provides valuable experimental data on shallow embedded column connections under lateral loads [3]. In Barnwell's experiments, twelve shallow embedded connection specimens were designed and fabricated to a two-thirds scale of typical connections in practice. Each specimen was created by pouring a concrete slab, leaving a portion of floor blocked out. A base plate was included on each specimen, designed in accordance with AISC *Steel Design Guide No. 1, Base Plate and Anchor Rod Design* [10]. The columns were later bolted in, and unreinforced concrete was poured into the block-out. A picture of one of these specimens immediately after the block-out was filled is shown in Figure 2.13. These specimens varied in orientation, embedment length, and column size. Particular emphasis was placed on embedment length, with some specimens designed with 8 inches of embedment, and others with 16 inches. Table 2.2 provides data for these specimens, including their embedment length, axis orientation, and column shape.

Figure 2.13: Shallow Embedded Column Specimen After Block-Out Pour (Barnwell)

Table 2.2: Specimen Data for Barnwell's Experiments

Specimen	Embedment [in]	Orientation	Shape
A1	8	Strong	W8X35
A2	8	Strong	W8X48
A3	8	Weak	W8X35
A4	8	Weak	W8X48
B1	16	Strong	W8X35
B2	16	Strong	W8X48
B3	16	Weak	W8X35
B4	16	Weak	W8X48
CA2	8	Strong	W8X48
DA2	8	Strong	W8X48
CB2	16	Strong	W8X48
DB2	16	Strong	W8X48

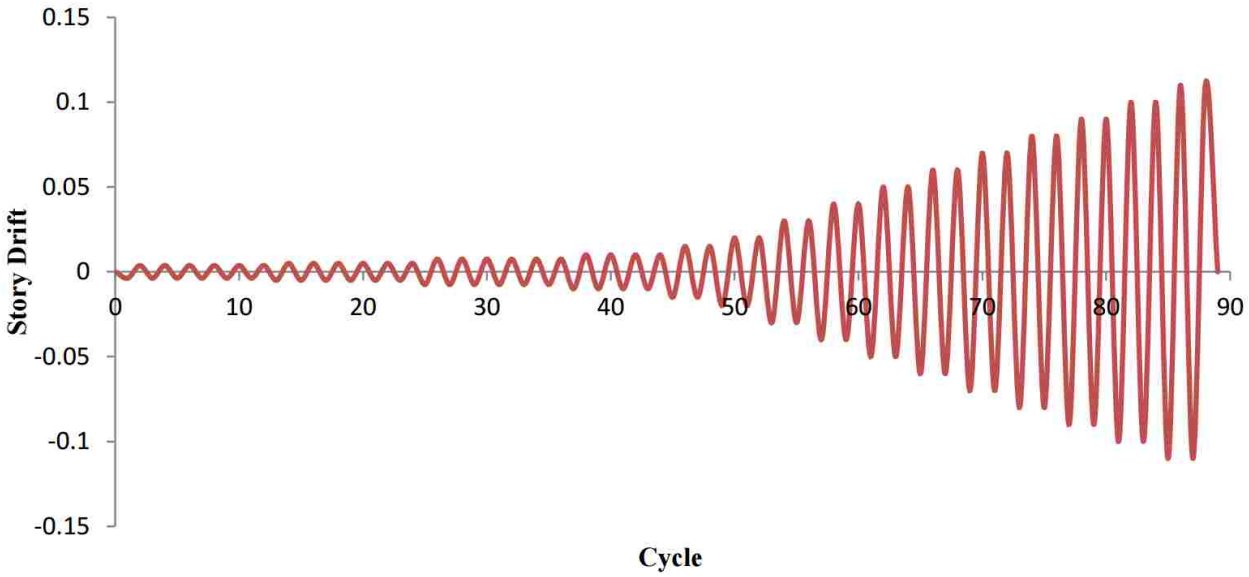

Figure 2.14: Loading Protocol Used in Barnwell's Experiments

All specimens underwent identical loading protocol, shown in Figure 2.14, consisting of drift-based cyclic lateral loading with no axial load. As discussed by Gomez, the presence of compressive axial load typically serves to stiffen column connections [9]. With no compressive axial load applied to these specimens, the results can be expected to be more conservative. Each specimen was loaded until failure or significant loss in strength occurred. Throughout the course of the loading, the load applied to the structure at each displacement was recorded. A picture of one specimen post-failure is shown in Figure 2.15.

Figure 2.15: Specimen B2 Post-Failure (Barnwell)

Barnwell proposed a model for computing the connection stiffness of the specimens [3]. When a lateral load is applied to a column embedded in concrete, some amount of deflection is introduced into the column structure. Two sources contribute to this deflection: the response of the steel column, and that of the embedding concrete connection. The sum of these two deflections yield the total deflection of the column structure, which was measured in Barnwell's experiments. This is depicted in Figure 2.16. The total stiffness of the column structure, k_t, can then be computed by dividing the lateral load by the total displacement, as given in Equation 2.4.

$$k_t = \frac{V}{\Delta_t} \tag{2.4}$$

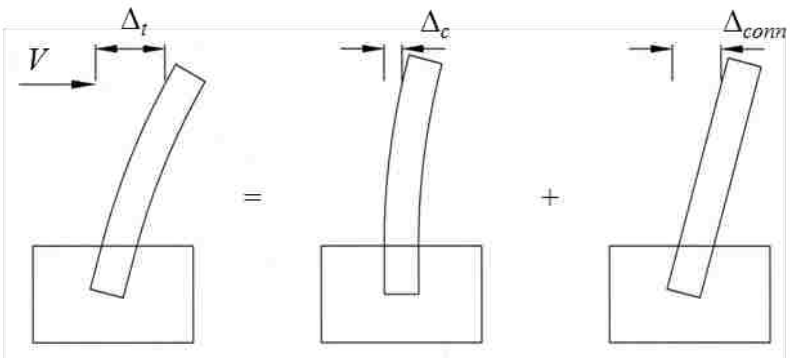

Figure 2.16: Lateral Displacement Contributions (Barnwell)

Both V, the lateral load, and Δ_t, the total displacement, were obtained experimentally. The stiffness of the steel column, k_c, can be obtained from the equation for the theoretical stiffness of an embedded column, as expressed in Equation 2.5.

$$k_c = \frac{3EI}{L^3} \tag{2.5}$$

In Equation 2.5, E is the modulus of elasticity of the column material, I is the area moment of inertia of the column shape, and L is the protruding length of the column. The equation for springs in series can then be used to find the connection stiffness, k_{conn}, as given by Equation 2.6.

$$\frac{1}{k_t} = \frac{1}{k_c} + \frac{1}{k_{conn}} \tag{2.6}$$

Data obtained through Barnwell's experiments were analyzed to compute the initial total stiffness, k_t of each specimen. These data are represented graphically in Figure 2.17. Three linear elastic portions were analyzed, which are highlighted in Figure 2.17. Values for total stiffness for each portion are equal to the slope of the curve at that portion. The first stiffness, k_1, is the slope of the line connecting the first and second data points of the first loading cycle. Similarly, the second stiffness, k_2, is the slope of the line connecting the last two data points prior to achieving a drift of 0.1 inches. Finally, the third stiffness, k_3, is the slope of the line connecting the first data point and the last data point prior to achieving the same 0.1 inch drift.

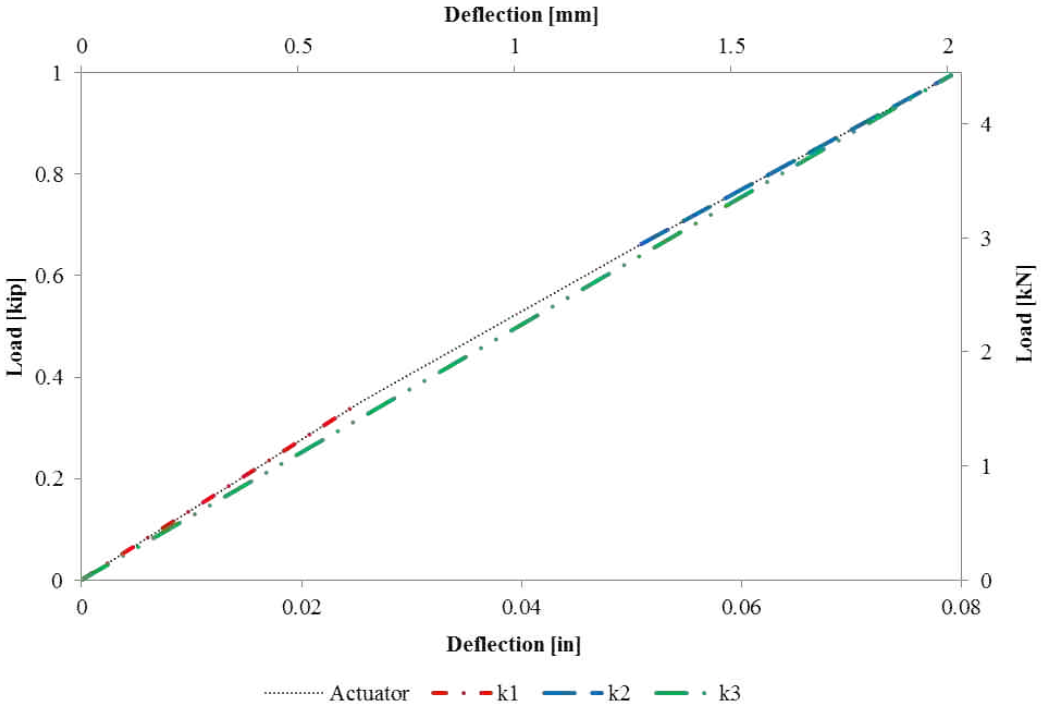

Figure 2.17: Data from First Loading Cycle (Barnwell)

Resulting total stiffness values were then input into Equation 2.6 and solved for k_{conn}. A comparison of the k_{conn} values for each specimen showed that the third stiffness, k_3, was the most consistent of the three. The resulting stiffness values for eight of these specimens are included in Table 2.3.

Table 2.3: Stiffness Data from Barnwell's Experiments

Specimen	Shape	Orientation	Embedment Length [in]	Exposed Length [in]	Structure Stiffness [kip/in]
A1	W8X35	Strong	8	80.25	30.49
A2	W8X48	Strong	8	80.25	36.02
CA2	W8X48	Strong	8	80.25	32.04
B1	W8X35	Strong	16	83.25	62.52
B2	W8X48	Strong	16	83.25	91.82
B3	W8X35	Weak	16	83.25	26.60
CB2	W8X48	Strong	16	83.25	92.42

Methods outlined in the *Baseplate Design Guide* were used to calculate the expected yield and ultimate strength of the specimens. It was found that the shallower embedded specimens exhibited 86% greater yield strength and 32% greater ultimate strength than was expected. Similarly, the deeper embedded specimens were shown to have 144% greater yield strength and 64% greater ultimate strength than calculated using AISC *Steel Design Guide No. 1, Base Plate and Anchor Rod Design* [10]. In addition, the specimens were shown to have approximately 50% to 75% of the expected stiffness of a fully embedded column. Barnwell's results suggest that current practices for designing shallow embedded connections are too conservative. To approximate a shallow embedded connection as a pinned support is a severe understatement of the moment resistance provided by such a connection.

2.2 Studies on Similar Connection Types

2.2.1 Corbel Connections

A study performed by Marcakis and Mitchell reports on the results of a series of experimental tests on corbel connections, which bear some similarity to shallow embedded connections [19]. These tests were conducted in an effort to produce an improved model for predicting the capacity of embedded steel members. Specifically, they studied the effects of column axial load, effective connection width, welded reinforcement, member shape, and loading eccentricity on this capacity. Three series of tests were performed on a total of 25 specimens. The specimens were loaded with varying amounts of axial and shear load until failure. A schematic of the specimen detailing is provided in Figure 2.18.

The researchers studied the potential load-bearing mechanisms in the specimens they tested in an effort to develop a model that would adequately predict their shear capacity. This study resulted in Equation 2.7, which calculates the nominal shear capacity of a steel column-to-concrete connection without additional reinforcement. This equation is included in the 2004 edition of the PCI handbook, and is known as the Marcakis and Mitchell equation [20].

$$V_r = \frac{0.85 f'_c b l_e}{1 + 3.6e/l_e} \tag{2.7}$$

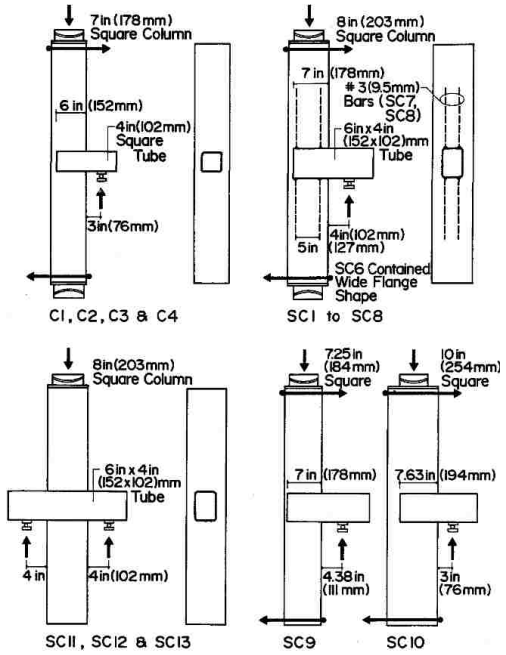

Figure 2.18: Detailing of Specimens Tested (Marcakis and Mitchell)

In Equation 2.7, f'_c is the concrete compressive strength, b is the effective width of the compression stress block, l_e is the embedment length of the corbel, and $e = a + \frac{l_e}{2}$, where a is the exposed length of the column. When comparing the results of the experiments with the predictions made using the Marcakis and Mitchell equation, they observed that the equation "conservatively predicts the capacity of connections incorporating embedded steel members" [19]. Further discussion on this equation is provided later in this section.

2.2.2 Pile-to-Cap Connections

Though different in many respects, pile-to-cap connections behave similarly to and share many behavioral characteristics with shallow embedded connections. In addition, such connections are typically approximated as pinned, neglecting any rotational strength or stiffness they may provide. Furthermore, pile-to-cap connections have received significant attention in research, providing useful background on shallow embedded connections. As such, a number of studies on pile-to-cap connections will be discussed in this section.

Due to the expense of detailing pile-to-cap connections, Harries and Petrou sought to investigate the viability of relying solely on embedment to provide full fixity of such connections [21].

As such, the objective of their research was to demonstrate that full fixity of a pile-to-pile cap connection can be obtained through embedment alone, and that no special detailing of the connection is required provided sufficient embedment length. To prove that this is the case, Harries and Petrou designed two pile-to-pile cap specimens with no detailing or reinforcement. These two specimens were loaded with both constant axial load and reversed cyclic lateral load, relying solely on embedment length to provide fixity. The specimens were designed such that these conditions would be fulfilled. Figure 2.19 provides detail of the embedded region of one of these specimens prior to concrete casting.

Figure 2.19: Embedment Detail (Harries & Petrou)

Two conditions were selected to demonstrate that, if fulfilled, the connection was fully fixed in nature. First, rotation occurring in the embedment must be so small that its contribution to the drift of the connection assembly be negligible. Second, any deterioration of the connection, such as spalling of the concrete cover, must not cause plastic hinging to occur in the embedded region. This condition was selected based on previous research performed by Harries on the subject of ductile coupled flexural walls where spalling of the concrete cover significantly affected the fixity of the connection [22].

Both of the pile specimens performed as the researchers expected. There was no observed damage to the embedment region in either specimen, and pile curvature data indicated that rotation of the pile cap had no measurable effect on pile deflections. This holds true to the conditions set

by the researchers for a fully fixed pile-to-cap connection. As such, the researchers concluded that full fixity could be achieved solely through sufficient embedment of the pile. The researchers recommend that embedment length of no less than 12 inches or the width of the pile be used for pile-to-cap connections when fixity is to be achieved through embedment alone.

Further investigation by Richards, et al, also studied the behavior of pile-to-cap specimens with minimal flexural reinforcement [2]. To experimentally determine the moment capacity of such connections, four pile-to-cap specimens with little to no reinforcement were prepared and tested with cyclic lateral load in the field. The lack of reinforcement allowed the researchers to observe solely the fixity of the embedment mechanism. A picture of the test setup is provided in Figure 2.20.

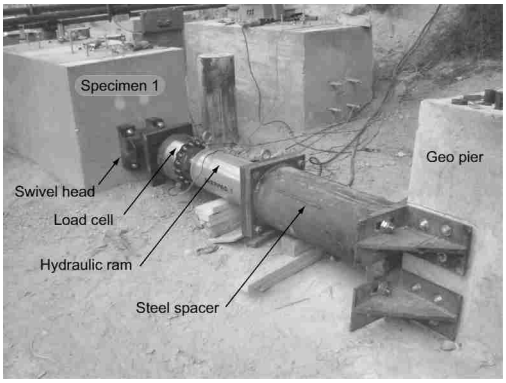

Figure 2.20: Test Setup (Richards, et al)

Previous to the experiments, the moment capacity of each component of the specimens was predicted using current design conventions. The total moment capacity was then computed by summing the individual capacities of each component. After completion of the testing, each pile specimen was found to exhibit at least 1.4 times the most generous calculated moment capacity. Two factors that are currently unaccounted for in present models that could provide unanticipated moment resistance capability were identified. These two factors are dowel action in the pile and the friction-resistance mechanism between the steel pipe and the concrete pile. The researchers suggest that the friction-resistance mechanism is the main contributor to this unexpected moment capacity.

These findings suggest that significant fixity may be attainable in connections with embedment lengths shallower than those prescribed by Harries and Petrou.

In order to determine the contribution of a friction mechanism for pile-to-cap or steel-column-to-concrete-footing connections, it is important to know the coefficient of static friction between steel and concrete. Baltay and Gjelsvik ran a series of experiments seeking to determine this coefficient of friction and perhaps explain in part the bond between reinforcing bars and concrete [23]. In these experiments, two short 5-inch diameter pipe sections were filled with standard concrete. Acting as friction pads, these pipes were placed on either side of a steel sample. A normal force was applied to both concrete pads such that they pressed against the steel as it was pushed or pulled. Figure 2.21 provides a schematic of the test setup.

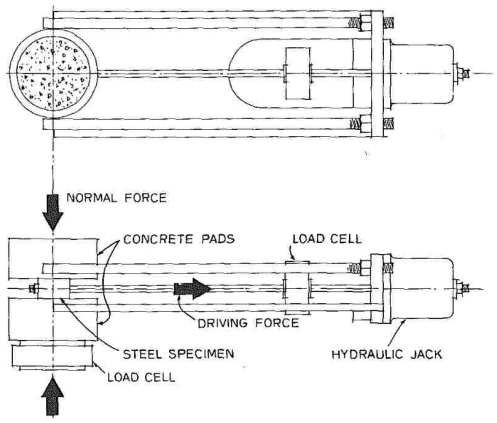

Figure 2.21: Test Setup (Baltay & Gjelsvik)

It was found in their tests that the average coefficient of friction between steel and concrete was 0.47 for stresses between 1 and 68000 psi [2]. This value was used by Richards, et al, in their proposed model for improving the flexural capacity calculation of embedded pipe piles.

As discussed earlier, Marcakis and Mitchell developed an equation for approximating the shear capacity of steel members embedded in concrete [19]. The Marcakis and Mitchell equation considers an embedment mechanism that resists rotation at the connection. To test their equation, Eastman conducted an experimental study testing the moment capacity of pile-to-cap connections

for pipe piles lacking reinforcement [1]. In his experiments, three pile-to-cap specimens with embedment lengths ranging from 4.56 to 17.9 inches were loaded laterally to failure. A force-controlled cyclic loading protocol was used for the first specimen, while a displacement-controlled cyclic loading protocol was used for the others. A depiction of Eastman's test setup is shown in Figure 2.22.

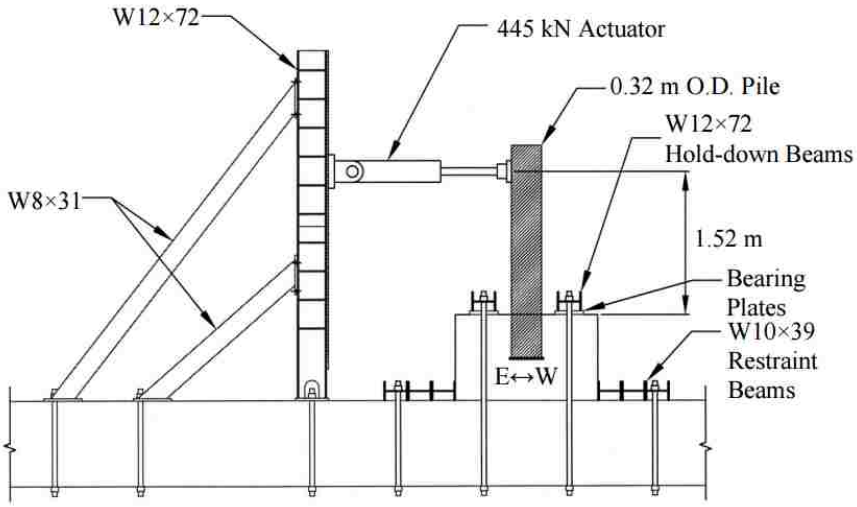

Figure 2.22: Test Setup (Eastman)

The pile-to-cap specimens exhibited a significant amount of lateral strength. This strength is notably greater than what was predicted using the Marcakis and Mitchell equation. As such, Eastman proposed an improved model based off of the work of Marcakis and Mitchell, but including a bearing mechanism and a friction mechanism at the end of the pile. This updated model more accurately predicts the moment capacity demonstrated by the pile-to-cap specimens tested in Eastman's experiments.

An experimental study conducted by Xiao, et al, provides further background on the unexpected moment capacity of pile-to-cap connections [24]. In this study, five H-shaped piles representative of a bridge support in California were tested in cyclic vertical and lateral loads to assess their seismic performance. Each specimen was an HP14X89 shape embedded five inches into the

footing. The behavior of the pile-to-cap connections was observed with respect to several variables, including axis orientation and loading protocol. Figure 2.23 shows the test setup for specimens that underwent cyclic vertical load only and cyclic lateral load with constant vertical load.

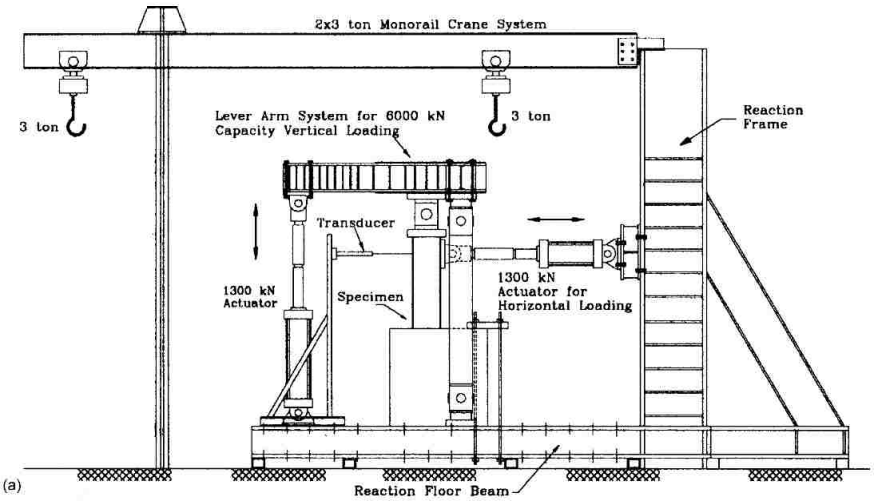

Figure 2.23: Test Setup (Xiao, et al)

Similar to other testing already discussed, the specimens displayed significant moment resistance, despite being approximated as a pinned connection by current design methods. The researchers note that this may be undesirable, as such connections may fail in unexpected failure modes in the event of a seismic hazard.

Castilla, et al, conducted a study on the fixity of steel piles embedded in concrete [25]. Previous to their work, a rule of thumb was used in the military for pile fixity based on embedment length. A pile was considered to be pinned if it was embedded 1 foot or less, partially fixed if it was embedded between 1 and 2 feet, and fully fixed if it was embedded 4 feet or more. However, this rule of thumb had no experimental or theoretical backing. As such, the researchers sought to determine what embedment length would be sufficient to provide full fixity for an embedded pile.

Computer models were used to examine the fixity of embedded piles through different models. One of these models idealized the pile-to-cap connection as a linearly elastic steel section supported by a series of independent springs. The other model used a program called ANSYS

to perform finite element analysis on the connection. Both of these models were used to analyze HP14X117 and HP14X73 steel pile shapes at embedment lengths of 2 ft and 4 ft. A parameter sketch of the first model is provided in Figure 2.24.

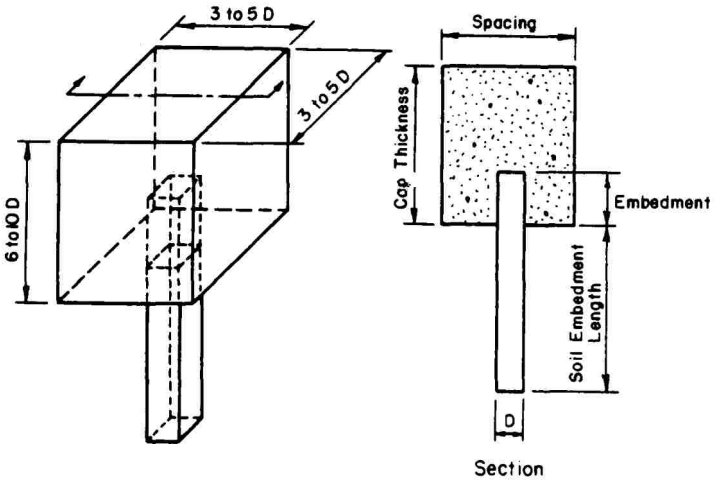

Figure 2.24: Cap-Member-Soil Model (Castilla, et al)

This study resulted in two important conclusions. First, an embedment length of at least twice the pile depth is sufficient to approximate full fixity. Second, the computed response of members with embedment lengths less than or equal to 1 foot indicated that they would develop 61 to 83 percent of the moment developed for members embedded 4 feet. This suggests that piles with 1 foot or less of embedment length are not pinned, but in fact partially fixed. As such, the rule of thumb used previous to this study is conservative.

2.2.3 Composite Connections

Another connection type that bears similarity to shallow embedded connections is a composite connection. Composite structural systems consist of elements comprised of differing materials. For example, one type of composite connection is a steel beam embedded into a concrete column. Such connections offer significant economical benefits for high-rise structures since steel

is far less expensive for beams and horizontal load-bearing members due to construction costs. Conversely, reinforced concrete is far more economical in the construction of columns in similar structures. Thus, composite moment frames are a popular design choice in structures ranging 40-70 stories in height.

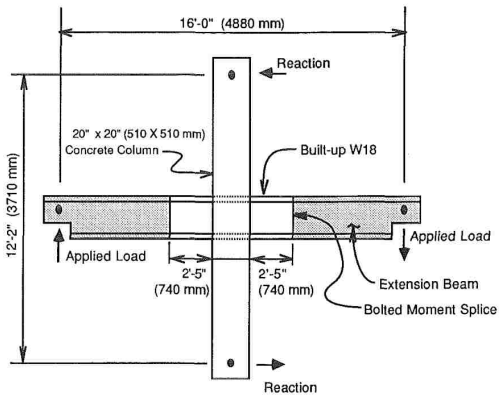

Figure 2.25: Typical Test Specimen (Sheikh, et al)

Several studies have been conducted on the behavior of composite connections under a variety of loading conditions. Sheikh, et al, performed one such study in which experiments were run on 15 two-thirds scale composite connection specimens with varying details [26]. The study focused on the assessment of strength and stiffness of such connections. Seven of the specimens were tested under monotonic loading, and the other eight underwent reversed cyclic loading. Each column used was a 20-inch by 20-inch square, and each beam was a built-up W8X18 section. The steel section was selected such that its flexural capacity would exceed that of the connection. Various reinforcement configurations were tested among the specimens. A typical test specimen is depicted in Figure 2.25. The researchers report that the specimens tested exhibited sufficient stiffness at service loads, and that failure of the specimens was ductile. It was also observed that simple detailing of the specimens served to increase the joint strength by up to 180%.

Accompanying this study, Deierlein, et al, provide recommendations for composite beam-column design calibrated to the results of the experimentation discussed by Sheikh, et al [27]. In their work, Deierlein, et al, identify two primary failure modes that govern the strength of such

connections. These modes include joint shear failure and vertical bearing failure. The researchers indicate that when design of composite connections is executed such that the beam and column function as a single unit, the connections are strengthened against these failure modes. In other words, the greater the fixity of the connection, the more protected it is against failure.

Governing the strength of the connections is the panel shear strength, which is carried by three mechanisms of the connection. These mechanisms, which are shown in order in Figure 2.26, include the steel web panel, concrete compression strut, and concrete compression field. Equations for calculating the capacity of each component are included in Equations 2.8 through 2.10.

$$V_s = 0.6F_{yw}t_w jh \tag{2.8}$$

$$V_n = 0.63\sqrt{f_c'}b_p h \tag{2.9}$$

$$V_n' = 0.63\sqrt{f_c'}b_o h <= V_c' + V_s' \tag{2.10}$$

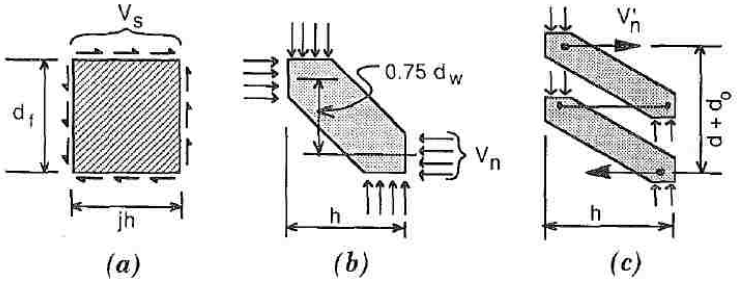

Figure 2.26: Panel Shear Strength Mechanisms (Deierlein, et al)

In Equations 2.8 through 2.10, V_s is the panel shear strength, $0.6F_{yw}$ is the shear yield stress of the web steel, t_w is the web thickness, jh is the panel length, f_c' is the concrete compressive strength after 28 days, b_p is the bearing plate width limited to 1.5 times the beam flange width, h is the column width, V_n' is the horizontal shear force resisted by the concrete compression field, b_o is the effective compression field width, and $V_c' + V_s'$ are the individual concrete and reinforcement

components required to carry V_n'. When strengths calculated using this model were compared with those obtained experimentally, it was found that the model calculated strengths ranging from 4% to 35% lower than were observed in the experiments. Thus, the proposed model conservatively estimated the strengths of the experimental composite connection specimens.

Further research on the subject of composite connections was performed by Shahrooz, et al [28]. In their work, the cyclic response of three half-scale composite connection specimens was evaluated. Rather than embed the steel beams into concrete columns, as was done in the previous discussion, Shahrooz, et al, embedded the column into the in-plane direction of a concrete shear wall. Using various reinforcement detailing and loading conditions, the researchers sought to determine the strength and stiffness of the connections. Each specimen consisted of a 10-inch thick and 79.5-inch tall concrete shear wall with a built-up W-shaped steel beam 4 inches wide and 9 inches tall embedded therein. Each specimen underwent displacement-controlled cyclic loading normal to the steel beam and in plane with the concrete shear wall until failure occurred. A picture of general test dimensions is provided in Figure 2.27.

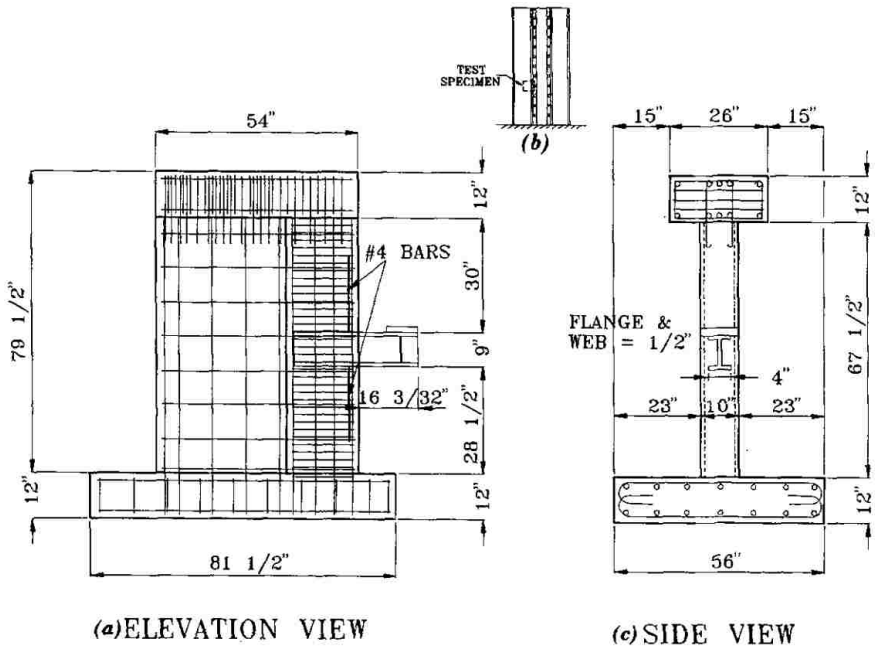

Figure 2.27: Test Specimen Dimensions (Shahrooz, et al)

According to the researchers, a coupling beam such as those tested should exhibit high stiffness, hysteretic stability, and energy dissipation. The specimens demonstrated satisfactory hysteretic stability and energy dissipation; however, their fixity was observed to be less than was expected. As such, the researchers proposed a model by which the initial stiffness of such connections might be reasonably predicted. In calculations performed prior to experimentation, the connections were assumed to be fully fixed, and that the fixity began at the concrete interface. However, significant deformations caused by bearing of the flanges proved to reduce this initial stiffness. To counteract this, the researchers calibrated a length *e* into the embedment at which the connection could reasonably be assumed to be fixed, depicted in Figure 2.28. This reduces the embedment length, thereby increasing the expected deflections, shear forces, and bending moments.

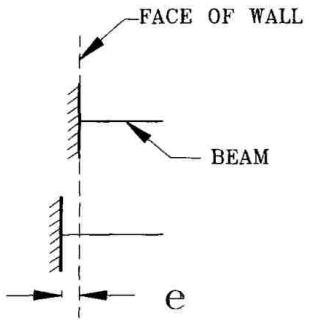

Figure 2.28: Effective Fixity with *e* (Shahrooz, et al)

Additional experimental analysis on composite connections was performed by Motter, et al [29]. In their research, four large-scale specimens consisting of steel cantilever coupling beams embedded into concrete shear walls were tested under reversed cyclic loading on both the beam and the shear wall. Couple beams used were W12X96 shapes trimmed to a flange width of 5.5 inches, representing a one-half scale W24X250. Shear walls were 12 inches in width, 96 inches wide, and 156 inches tall. The study sought to investigate the effects of embedment length, beam span length, reinforcement configuration, and applied wall loading on the behavior of the connection. An image of the test setup is provided in Figure 2.29.

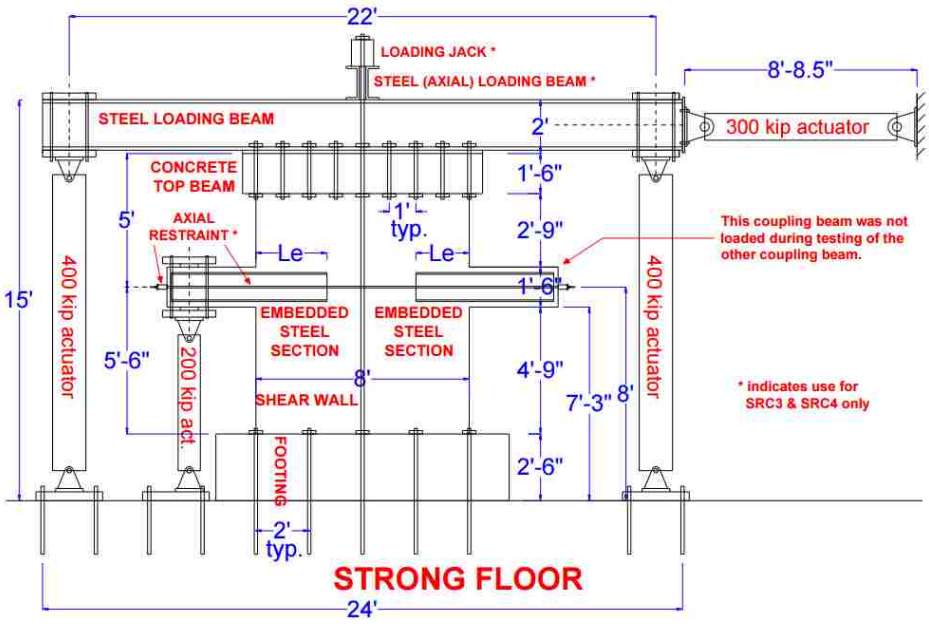

Figure 2.29: Test Setup (Motter, et al)

Similar to the results of previous experimentation previously discussed, the specimens at large performed adequately under the prescribed loading. Among them, the first specimen, which had deeper embedment length and more favorable loading conditions, exhibited excellent performance, with rotational capacity exceeding 12%. The other specimens suffered greater strength degradation, embedment damage, and load-displacement response due to shallower embedment length and reduced wall boundary reinforcement. As a result, the researchers specify the use of Equation H4-2 of the 2010 AISC *Seismic Provisions* to calculate the required embedment length of coupling beams, given below in Equation 2.11 [11]. They also note that the use of face bearing plates or auxiliary transfer bars is not required to attain favorable performance of composite connections, given that sufficient embedment length is provided.

$$V_n = 1.54\sqrt{f'_c}\left(\frac{t}{b}\right)\beta_1 b(L_e - c)\left(\frac{0.58 - 0.22\beta_1}{0.88 + (L+2c)/2(L_e - c)}\right) \tag{2.11}$$

In Equation 2.11, V_n is the shear strength of the connection, f'_c is the specified concrete compressive strength, t is the wall thickness, b is the bearing width, L_e is the embedment length, c is the depth of spalling, and β_1 is the ACI stress block factor.

2.2.4 Concrete Filled Steel Tubes

Concrete filled steel tubes (CFT) are an alternative and economical option for embedded connections. To investigate the viability of circular CFT in connection design, Roeder and Lehman performed a series of experiments on CFT specimens of varying embedment length [30]. Though CFT differs fundamentally from the I-shaped columns typically used for steel column-to-footing connections, some relevant information was gleaned from Roeder's tests. The researchers performed large-scale tests on 12 CFT connections intended to simulate either a full-size building column or a half-scale bridge pier. Each specimen connection had an embedment length of either 0.5, 1.0, or 1.5 times the column diameter D and was tested under axial compression and cyclic lateral load in several variations. The test setup is provided in Figure 2.30.

A significant increase in stability was observed when increasing the embedment length of the CFT connection from $0.6D$ to $0.75D$ or $0.9D$, where D is the column diameter. Furthermore, it was observed that current design recommendations for CFT embedment lengths were conservative. Currently, it is recommended that an embedment length of $1.5D$ to $2D$ be used to achieve high drift capacities required by high seismic zones. However, the specimens tested in Roeder's study achieved such capacities with an embedment length of $0.75D$ to $0.9D$.

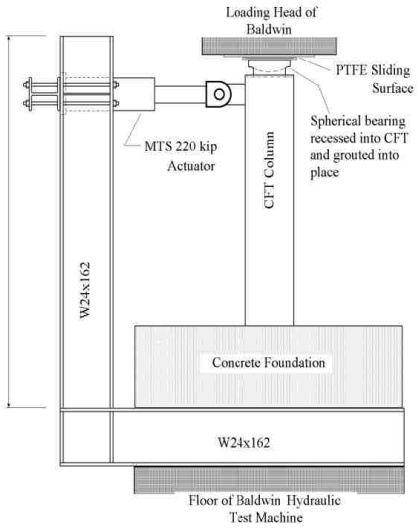

Figure 2.30: Test Setup (Roeder & Lehman)

CHAPTER 3. METHODOLOGY

In seeking out a model to estimate the rotational stiffness of steel column-to-footing connections, several methods were employed. The primary model extends derivations performed by Hetenyi to model the embedded column as a continuous beam to calculate the deflections and rotations at the endpoints of the column and is called the continuum model [4]. A secondary model uses the stiffness method of structural analysis to determine the same information, which is discussed in Appendix A. Results from the models were compared with the resulting stiffness values and hysteretic plots from experiments run by Barnwell at Brigham Young University [3] and by Grilli, et al, at the University of California at Davis [5]. This chapter details the primary method used to both model steel column-to-footing connections and compare results with experimental data.

3.1 Continuum Model

3.1.1 Approach

The approach made to model a steel column-to-footing connection is depicted in Figure 3.1. Three main components of the structure can be identified. The first is the exposed column, which can be analyzed using classic Bernoulli beam theory. Second is the embedded column. In this work, it is analyzed using beam on elastic foundation theory derived by Hetenyi [4]. This is an untraditional and innovative use of Hetenyi's work, which is typically used to model beams resting on an elastic continuum. The third component is the base plate. A rotational spring is used to model its stiffness contribution. Equations are derived later in this section for calculating its rotational stiffness. It is noted that additional resistance may also be provided by the side shear or friction mechanism of the steel against the concrete. However, this resistance mechanism is not considered in this work.

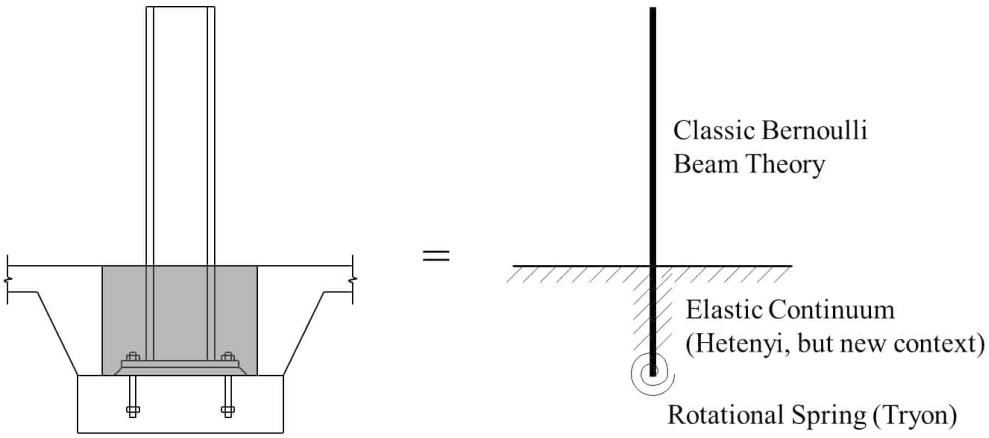

Figure 3.1: Beam on Elastic Foundation Under Point Load

Of particular importance to this work are the deflections and rotations resulting in the embedded connection, which is comprised of the embedded column, the base plate, and the elastic continuum. The combined stiffness of these mediums comprise the rotational stiffness of the connection. Deformation in the exposed column is neglected in order to encapsulate the stiffness of the connection only. Once the rotations and deflections at the concrete interface can be calculated, the rotational stiffness may also be calculated.

3.1.2 Beams of Infinite Length (Hetenyi)

Previous work performed by Hetenyi derives closed-form solutions for the deflection, rotation, shear, and bending moment at any point on a beam supported on an elastic foundation [4]. After solving for these values in the general case, a number of specific cases are addressed, several of which are useful for modeling the embedded column and determining its rotational stiffness. In this section, a brief overview of Hetenyi's general derivation will be discussed, followed by the specific cases and closed form solutions used in this work.

Figure 3.2 depicts a beam of infinite length l continuously supported by an elastic foundation under a point load P located a distance a from one end. The point load causes the beam to deflect continuously into the foundation. This deflection at any point is denoted by y.

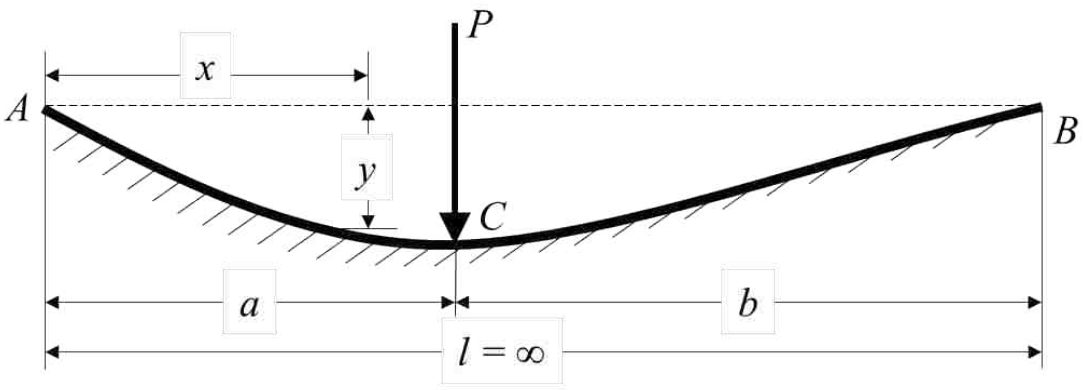

Figure 3.2: Beam on Elastic Foundation Under Point Load

By cutting out a small section of length dx from the beam, the shear at that point may be analyzed. A depiction of such a section is shown in Figure 3.3. Internal shear forces V and bending moments M are located at either cut, and a uniformly distributed load representing the reaction of the foundation is located at the bottom. To account for the variation in shear and bending moment from one side of the section to another, dV and dM are added on the right side. In response to the applied load, the elastic medium supporting the beam produces a continuously varying distributed reaction with intensity equal to the stiffness of the medium times the deflection of the beam. For the increment dx, this value is expressed as $ky\,dx$. The stiffness k is equal to the modulus of subgrade reaction of the material, k_0, times the width of the beam.

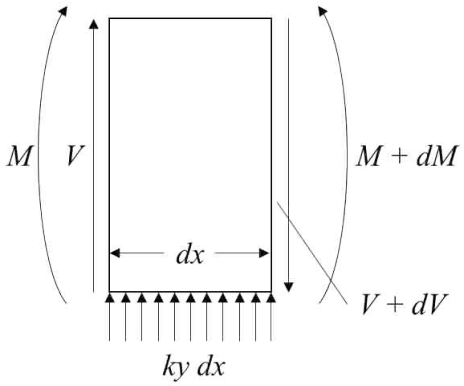

Figure 3.3: Continuous Beam Element

From the free body diagram, the equation of equilibrium can be written as follows:

$$V - (V + dV) + ky\,dx = 0 \tag{3.1}$$

This equation is simplified in Equation 3.2.

$$\frac{dV}{dx} = ky \tag{3.2}$$

By applying various relationships from Bernoulli beam theory, the differential equation eventually becomes

$$EI\frac{d^4y}{dx^4} = -ky \tag{3.3}$$

Substituting e^{mx} into Equation 3.3 yields the characteristic equation below.

$$m^4 = -\frac{k}{EI} \tag{3.4}$$

The roots of this equation are

$$m_1 = -m_3 = \sqrt[4]{\frac{k}{4EI}}(1+i) = \lambda(1+i) \tag{3.5}$$

$$m_2 = -m_4 = \sqrt[4]{\frac{k}{4EI}}(-1+i) = \lambda(-1+i) \tag{3.6}$$

where

$$\lambda = \sqrt[4]{\frac{k}{4EI}} \tag{3.7}$$

The term λ is a constant that incorporates the material properties of both the elastic medium and the beam, and it is referred to as the characteristic of the system. The general solution to this problem is presented in Equation 3.8. Each constant of integration may be found by applying boundary conditions depending on the specific problem. Once those constants are found, the equation may be used to calculate the deflection of the beam at any point x on the beam. Similarly, the derivatives of Equation 3.8 may be used to compute the rotation, bending moment, and shear at any

point. Given that the purpose of this section is to apply Hetenyi's work to steel column-to-footing connections, this derivation will not be explored further except as necessary.

$$y = e^{\lambda x}(C_1 \cos \lambda x + C_2 \sin \lambda x) + e^{-\lambda x}(C_3 \cos \lambda x + C_4 \sin \lambda x) \tag{3.8}$$

3.1.3 Beams of Finite Length (Hetenyi)

As previously noted, the general solution presented in Equation 3.8 represents the case of a beam of infinite length. However, in many practical applications, a beam of finite length is more useful. Equations for the deflection, rotation, bending moment, and shear of a finite beam can be obtained by superimposing another infinite beam upon the general case. The second infinite beam is superimposed in such a way that the loading and deformation values at the end points of the finite beam and the corresponding points on the infinite beam superposition are equal.

Due to the inherent complexity of this superposition, Hetenyi presents a number of closed form solutions for many particular beam cases [4]. Two of these cases are especially helpful in the case of the continuum model. These cases are a finite beam with a concentrated force on one end and a finite beam with a concentrated moment at one end. Hetenyi provides equations for the deflection, rotation, bending moment, and shear at any point, as well as specific equations for the deflection and rotation at the end points. These equations defining the deflection and rotation at the end points are of particular interest in this model. Figures 3.4 and 3.5 below depict each load case, and Equations 3.9 through 3.16 provide the closed form solutions for the deflections and rotations for each case at the end points.

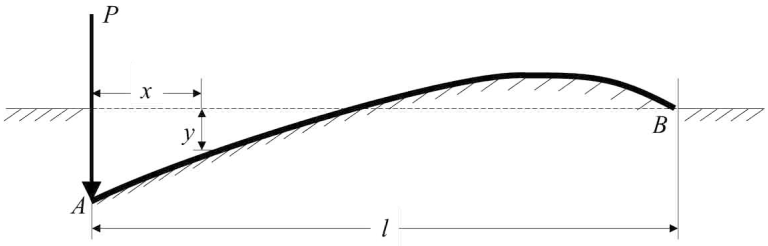

Figure 3.4: Beam on Elastic Foundation with a Concentrated Load at One End

Deflections at the end points under point load P:

$$y_A = \frac{2P\lambda}{k}\frac{\sinh\lambda l\cosh\lambda l - \sin\lambda l\cos\lambda l}{\sinh^2\lambda l - \sin^2\lambda l} \tag{3.9}$$

$$y_B = \frac{2P\lambda}{k}\frac{\sinh\lambda l\cos\lambda l - \sin\lambda l\cosh\lambda l}{\sinh^2\lambda l - \sin^2\lambda l} \tag{3.10}$$

Slopes at the end points under point load P:

$$\theta_A = -\frac{2P\lambda^2}{k}\frac{\sinh^2\lambda l + \sin^2\lambda l}{\sinh^2\lambda l - \sin^2\lambda l} \tag{3.11}$$

$$\theta_B = -\frac{4P\lambda^2}{k}\frac{\sinh\lambda l\sin\lambda l}{\sinh^2\lambda l - \sin^2\lambda l} \tag{3.12}$$

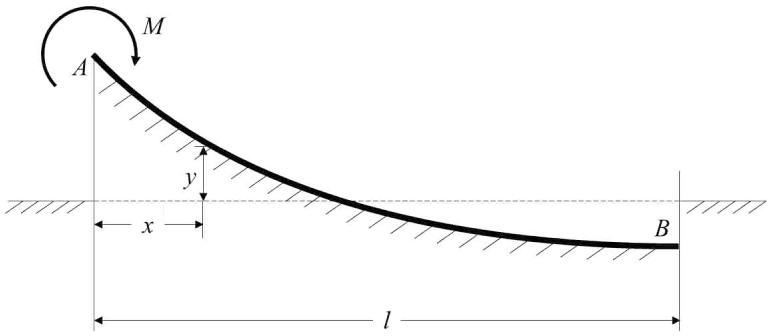

Figure 3.5: Beam on Elastic Foundation with a Concentrated Moment at One End

Deflections at the end points under point moment M:

$$y_A = -\frac{2M\lambda^2}{k}\frac{\sinh^2\lambda l + \sin^2\lambda l}{\sinh^2\lambda l - \sin^2\lambda l} \tag{3.13}$$

$$y_B = -\frac{4M\lambda^2}{k}\frac{\sinh\lambda l\sin\lambda l}{\sinh^2\lambda l - \sin^2\lambda l} \tag{3.14}$$

Slopes at the end points under point moment M:

$$\theta_A = \frac{4M\lambda^3}{k}\frac{\sinh\lambda l\cosh\lambda l+\sin\lambda l\cos\lambda l}{\sinh^2\lambda l-\sin^2\lambda l} \tag{3.15}$$

$$\theta_B = \frac{4M\lambda^3}{k}\frac{\sinh\lambda l\cos\lambda l+\sin\lambda l\cosh\lambda l}{\sinh^2\lambda l-\sin^2\lambda l} \tag{3.16}$$

3.1.4 Application to Steel Column-to-Footing Connections

Hetenyi's work can be extended to the case of steel columns embedded in concrete. The length of steel beam embedded in the concrete may be treated as a beam, and the surrounding concrete may represent the elastic medium. A shear force V and moment M are applied at the concrete interface to represent the loads transferred to the connection by the exposed column. The applied moment has magnitude VS, where S is the exposed length of the column. A rotational spring with stiffness k_s represents the stiffness contribution of the base plate at the bottom. This model is depicted in Figure 3.6. The resistance of the concrete continuum is represented by a continuously varying distributed load of intensity ky, where k is the stiffness of the concrete medium and y is the deflection at any point.

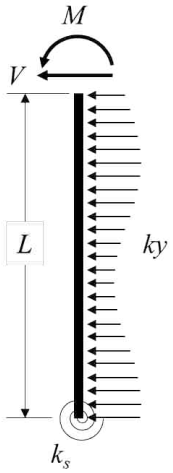

Figure 3.6: Continuum Model

The objective of this model is to calculate the deflection and rotation at the concrete interface and thereby determine the rotational stiffness of the structure. To do so, the model may be seen as the superposition of three specific finite beams. These are one beam with a concentrated point load at one end and two beams with a concentrated moment at either end. Using the method of superposition, the cases presented in Section 3.1.3 may be used to calculate the total displacement and rotation of the embedded steel beam at the concrete interface. This superposition is depicted in Figure 3.7.

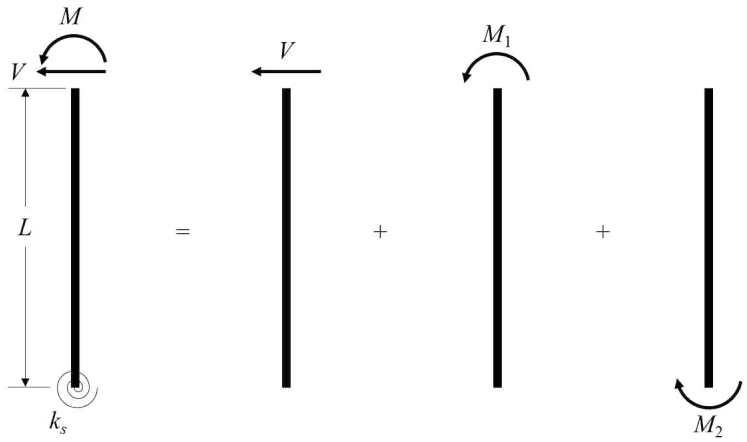

Figure 3.7: Continuous Model Superposition

Prior to applying the method of superposition to this model, several accommodations must be made to account for the specific case of a wide flange column embedded into a concrete medium. The first of these accommodations refers to the duality of the flanges in strong-axis orientation. Another is used to obtain the rotational stiffness of the base plate, which is critical for calculating the moment developed and rotation prevented by the base plate.

3.1.5 Accounting for Flange Duality

It may be recalled that in Equations 3.9 through 3.16, the value k is equal to the modulus of subgrade reaction of the concrete times the width of the column. When oriented along its strong

axis, as shown in Figure 3.8, both flanges assist in resisting the applied lateral load. For a similar shape oriented about its weak axis, such as the column slice shown in Figure 3.9, only the depth of the shape provides resistance. The width used in calculating the stiffness k should be equal to the effective width of components resisting lateral load. In the case of a strong-axis oriented column, this width is twice the flange width minus the web thickness, or $2b_f - t_w$; for weak-axis, it is simply the depth d. Equations for calculating the stiffness for each orientation are provided in Equations 3.17 and 3.18.

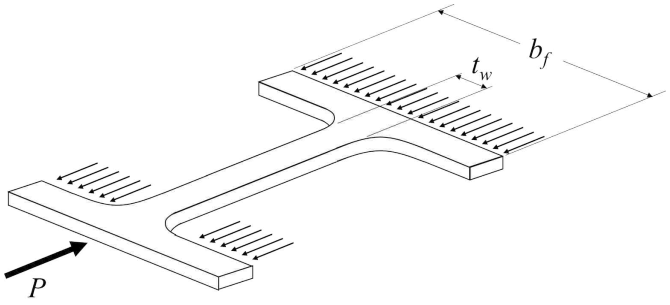

Figure 3.8: Strong Axis Resisting Surfaces

$$k = k_0(2b_f - t_w) \tag{3.17}$$

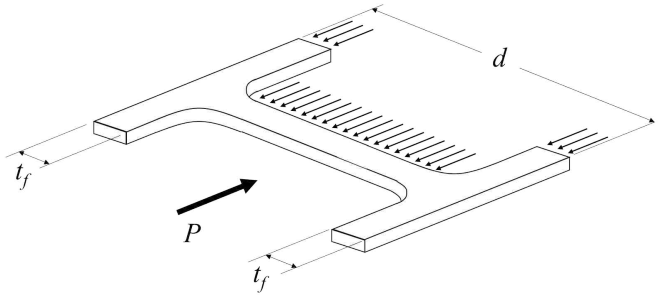

Figure 3.9: Weak Axis Resisting Surfaces

$$k = k_0 d \tag{3.18}$$

3.1.6 Calculating Base Plate Rotational Stiffness

Under lateral loading conditions, the base plate may be represented by a rigid beam of length w supported continuously by an elastic medium of stiffness k and loaded by a moment M. This loading causes the beam to rotate an angle γ, pushing half of it into the elastic medium and pulling the other half away. In turn, the elastic medium responds to this deformation in the form of a triangularly distributed load along the length of the beam. The amount of vertical displacement and the intensity of the distributed load at any point are proportional to the distance from that point to the centerline. The stiffness k of the elastic medium is the same as what was calculated in Section 3.1.5. A depiction of this representation is shown in Figure 3.10, with the undisturbed beam on the left and the loaded beam on the right. Using small angle approximations, the deflection as a function of x can be calculated using Equation 3.19. Since force is the product of deflection and stiffness, the force per unit length of plate as a function of x can be expressed as shown in Equation 3.20.

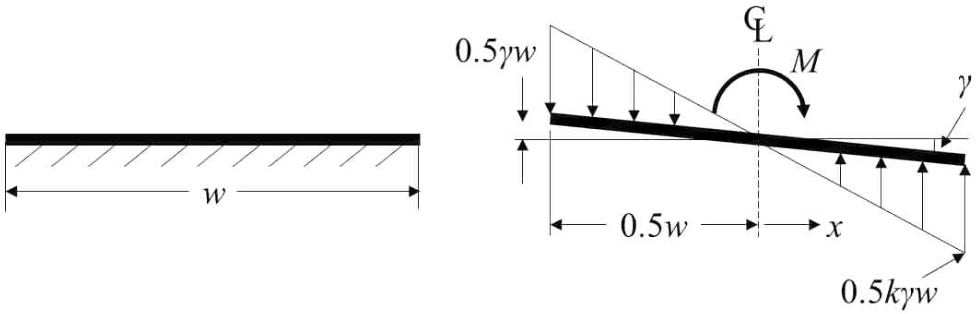

Figure 3.10: Continuous Base Plate Model

$$\delta = \gamma x \tag{3.19}$$

$$F(x) = k\gamma x \tag{3.20}$$

The triangular distributed may be more easily visualized as a series of infinitesimally thin line loads emanating from the centerline with intensity proportional to their distance from the

centerline. This is depicted in Figure 3.11. The moment produced by one of these line loads is equal to $F(x)$ times $x\ dx$, where dx is the width of one of the infinitesimally thin line loads. Accounting for symmetry, the total moment produced by the base plate is equal to twice the integral of all of the moments on one side. This moment can be calculated using Equation 3.21.

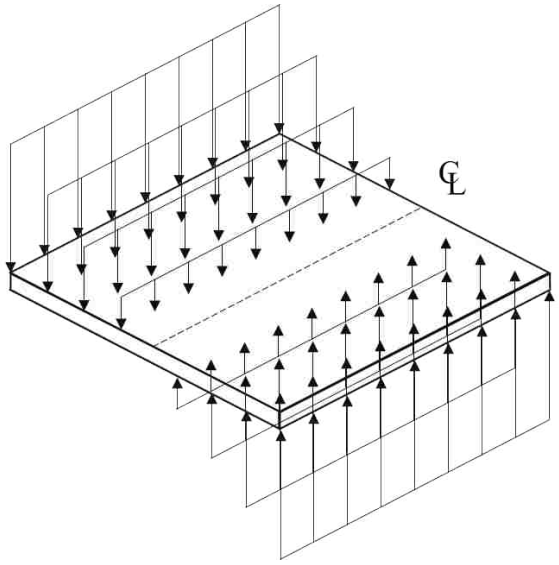

Figure 3.11: Continuous Base Plate Model

$$M(x) = 2\int_0^{\frac{w}{2}} k\gamma x^2 dx = \frac{k\gamma w^3}{12} \tag{3.21}$$

Rotational stiffness is simply the moment divided by the rotation. Thus, the rotational stiffness k_s is provided in Equation 3.22.

$$k_s = \frac{kw^3}{12} \tag{3.22}$$

In the case of a rectangular column and a perfectly rigid base plate, Equation 3.22 would be sufficient. However, since the base plate is not assumed to be perfectly rigid everywhere, the block-out concrete may differ in stiffness from the slab concrete, and the column is frequently not rectangular, several adjustments must be made.

It may be recalled that Thambiratnam and Paramasivam observed that most of the bearing stress felt by eccentrically loaded exposed connections occurred immediately underneath the foot of the column, with little stress propagating to the ends of the base plate [7]. This bearing mechanism can be visualized as shown in Figure 3.12. Though their study was on exposed connections under eccentric axial load and the present work is focused on shallow embedded connections, their observations may be extended to the stiffness of embedded base plates. From this information, it may be conservatively assumed that the base plate outside the rectangle projected by the column is flexible. As such, the dimension w used in Equations 3.21 and 3.22 is equal to the column depth d for strong axis columns and the flange width b_f for weak axis columns, as shown in Figures 3.12(a) and 3.12(b), respectively.

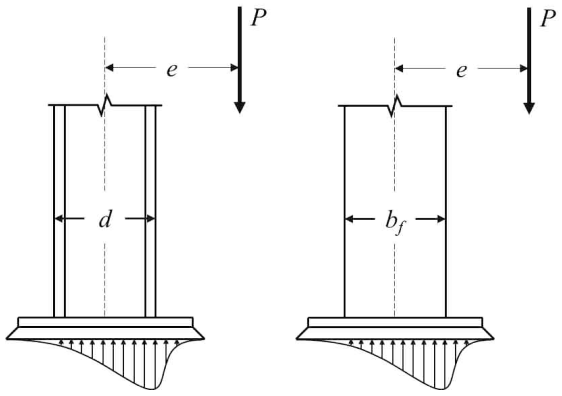

(a) Strong Axis (b) Weak Axis

Figure 3.12: Bearing Mechanism of Eccentrically Loaded Exposed Connections

Next, a factor must be included to account for variance in concrete stiffness from the block-out to the slab. Upon rotation, half of the base plate pushes up into the block-out concrete while the other half pushes down into the slab. As such, a modulus of elasticity equal to the average of the modulus of the block-out and the slab should be adopted. It should be noted that the modulus of elasticity of concrete is empirically derived from its strength. Equation 3.23 is the standard formula for computing the modulus of elasticity of concrete [32].

$$E = 57000\sqrt{f'_c} \tag{3.23}$$

Since the stiffness k is adopted from the block-out, the appropriate factor should be the ratio of this average modulus to the modulus of elasticity of the block-out. This ratio is expressed and simplified in Equation 3.24. It should be noted that if the block-out and slab are comprised of equal strength concrete, Equation 3.24 reduces to 1.

$$\frac{\left(\frac{E_{blockout}+E_{footing}}{2}\right)}{E_{blockout}} = \frac{1}{2}\left(\frac{E_{footing}}{E_{blockout}}+1\right) \tag{3.24}$$

The last adjustment to be made simply undoes any shape modifications made to k based on flange duality. For strong-axis columns, k is calculated assuming two flanges engaging in resisting the lateral load. Since the base plate clearly does not have two flanges, the base plate rotational stiffness should be multiplied by the ratio of the flange width to the width used to calculate k originally for strong-axis columns. Since flange duality is not a factor for weak-axis columns, no such adjustment is necessary for them. Equations 3.25 and 3.26 are simplified adaptations of Equation 3.22 accounting for each of the factors discussed for both strong- and weak-axis columns, respectively.

$$k_s = \frac{kd^3}{24}\left(\frac{b_f}{2b_f - t_w}\right)\left(\frac{E_{footing}}{E_{blockout}}+1\right) \tag{3.25}$$

$$k_s = \frac{kb_f^3}{24}\left(\frac{E_{footing}}{E_{blockout}}+1\right) \tag{3.26}$$

3.1.7 Method of Superposition

With the adjustments made in the previous sections, sufficient information is known to continue with the calculation of the deflection and rotation of the column at the concrete interface. The continuum model can be seen as a superposition of the three systems shown previously in Figure 3.7. Of the three loads, the concentrated load V and the concentrated moment M_1 are known, but the concentrated moment M_2 is not. The value of M_2 is the moment produced by the base plate in resistance to the applied loading V and M_1. To calculate this moment, it must be first put in terms of the total rotation at the base plate. The total rotation is equal to the sum of the rotation at the base plate caused by all three systems. It is also equal to the moment M_2 divided by the rotational spring stiffness k_s. The rotations are given in Equations 3.27 through 3.31.

$$\theta_{1,bottom} = \frac{4V\lambda^2}{k}\frac{\sinh\lambda l\sin\lambda l}{\sinh^2\lambda l-\sin^2\lambda l} \tag{3.27}$$

$$\theta_{2,bottom} = \frac{4M_1\lambda^3}{k}\frac{\sinh\lambda l\cos\lambda l+\sin\lambda l\cosh\lambda l}{\sinh^2\lambda l-\sin^2\lambda l} \tag{3.28}$$

$$\theta_{3,bottom} = -\frac{4M_2\lambda^3}{k}\frac{\sinh\lambda l\cosh\lambda l+\sin\lambda l\cos\lambda l}{\sinh^2\lambda l-\sin^2\lambda l} \tag{3.29}$$

$$\theta_{total,bottom} = \theta_{1,bottom}+\theta_{2,bottom}+\theta_{3,bottom} \tag{3.30}$$

$$\theta_{total} = \frac{M_2}{k_s} \tag{3.31}$$

Substituting Equations 3.27 through 3.29 and 3.31 into Equation 3.30 and solving for M_2 yields

$$M_2 = \frac{4\lambda^2k_s(V\sinh\lambda l\sin\lambda l+M_1\lambda(\sinh\lambda l\cos\lambda l+\sin\lambda l\cosh\lambda l))}{k(\sinh^2\lambda l-\sin^2\lambda l)+4\lambda^3k_s(\sinh\lambda l\cosh\lambda l+\sin\lambda l\cos\lambda l)} \tag{3.32}$$

It may be noted that for the case where there is no base plate (i.e. k_s = 0), there is no moment at the base (i.e. M_2 = 0). Knowing the value of M_2, the total rotation at the concrete interface may be computed by summing Equations 3.11, 3.15, and 3.16. Furthermore, the total rotation at the point of application of the applied load may be calculated by summing Equations 3.9, 3.13, and 3.14, dividing by the exposed column length S, and adding the total rotation at the concrete interface. These calculations are given in Equations 3.33 through 3.39 and are shown visually in Figure 3.13.

$$\theta_{total} = \frac{\delta_1+\delta_2+\delta_3}{S}+\theta_1+\theta_2+\theta_3 \tag{3.33}$$

$$\delta_1 = \frac{2V\lambda}{k}\frac{\sinh\lambda l\cosh\lambda l-\sin\lambda l\cos\lambda l}{\sinh^2\lambda l-\sin^2\lambda l} \tag{3.34}$$

$$\delta_2 = \frac{2M_1\lambda^2}{k}\frac{\sinh^2\lambda l + \sin^2\lambda l}{\sinh^2\lambda l - \sin^2\lambda l} \tag{3.35}$$

$$\delta_3 = -\frac{4M_2\lambda^2}{k}\frac{\sinh\lambda l\sin\lambda l}{\sinh^2\lambda l - \sin^2\lambda l} \tag{3.36}$$

$$\theta_1 = \frac{2V\lambda^2}{k}\frac{\sinh^2\lambda l + \sin^2\lambda l}{\sinh^2\lambda l - \sin^2\lambda l} \tag{3.37}$$

$$\theta_2 = \frac{4M_1\lambda^3}{k}\frac{\sinh\lambda l\cosh\lambda l + \sin\lambda l\cos\lambda l}{\sinh^2\lambda l - \sin^2\lambda l} \tag{3.38}$$

$$\theta_3 = -\frac{4M_2\lambda^3}{k}\frac{\sinh\lambda l\cos\lambda l + \sin\lambda l\cosh\lambda l}{\sinh^2\lambda l - \sin^2\lambda l} \tag{3.39}$$

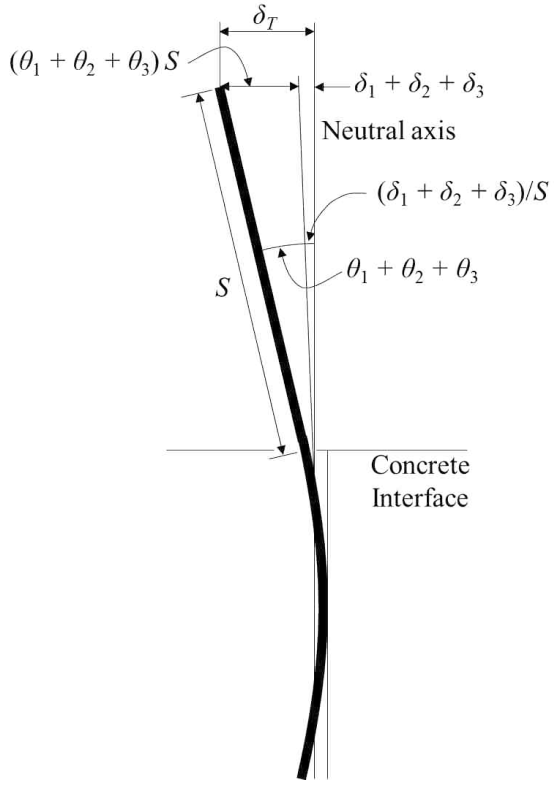

Figure 3.13: Strong Axis Resisting Surfaces

Finally, the rotational stiffness of the column connection may be calculated by dividing the applied moment by the total rotation, as expressed in Equation 3.40.

$$\beta = \frac{M}{\theta_{total}} \tag{3.40}$$

3.2 Comparing Results with Barnwell

Data from Barnwell's experiments were used to verify the ability of both the continuum and the stiffness method models to calculate the rotational stiffness of an embedded connection. To do this, first a tool was developed in Microsoft Excel using VBA code to input experimental data and plot results. A number of different parameters are required by the tool. In order to provide results comparable to those from Barnwell's experiments, specimen data must be input into the tools. The parameters required are member shape and orientation, modulus of elasticity of both the block-out and footing concrete, the connection stiffness, the embedment length, and the exposed column length. As mentioned previously, the modulus of elasticity of concrete is found empirically from its compressive strength (See Equation 3.23). Table 3.1 shows these specimen data from Barnwell's experiments.

Table 3.1: Specimen Data from Barnwell's Experiments

Specimen	Shape	Orientation	Embedment Length [in]	Exposed Length [in]	Connection Stiffness [kip/in]
A1	W8X35	Strong	8	80.25	30.49
A2	W8X48	Strong	8	80.25	36.02
CA2	W8X48	Strong	8	80.25	32.04
B1	W8X35	Strong	16	83.25	62.52
B2	W8X48	Strong	16	83.25	91.82
B3	W8X35	Weak	16	83.25	26.60
CB2	W8X48	Strong	16	83.25	92.42

For all of these specimens, the concrete compressive strength was 1600 psi for the block-out and 4000 psi for the footing. Using Equation 3.23, the modulus of elasticity of concrete is 2280

ksi for the block-out and 3600 ksi for the footing. From this information, the tools are capable of performing all calculations using the derivation from Section 3.1 as well as section data from the AISC Steel Construction Manual [31].

It should be noted that though Barnwell reports embedment lengths of 8 and 16 inches for shallow and deep embedded columns, respectively, these values are not fully accurate for the purpose of this analysis [3]. This is due to the presence of grout underneath each of the specimens. The grout effectively reduces the embedment length of each specimen by about 2 inches. As such, embedment lengths of 6 and 14 inches were used for analyzing shallowly and deeply embedded columns, respectively.

The results of Barnwell's experiments did not provide any information regarding the modulus of subgrade reaction of concrete, which is a necessary parameter in the continuum model. As such, it became important to obtain a method by which the modulus of subgrade reaction might be calibrated such that the model could replicate Barnwell's results. The stiffness of the connection k_{conn} is equal to the shear force V applied to it divided by the displacement Δ_{conn} caused by the application of that force, as expressed in Equation 3.41.

$$k_{conn} = \frac{V}{\Delta_{conn}} \tag{3.41}$$

By assuming a shear force of 1 kip and inputting the stiffness values presented in Table 3.1, the corresponding connection displacement of each specimen was obtained. Code was written for the tool that could incrementally change the modulus of subgrade reaction until the output connection displacement was within a user-specified tolerance of the values obtained using Equation 3.41. All of these calibrated moduli of subgrade reaction fell within the range of 300 to 600 kips/in^3.

Analytical means were also attempted to estimate the modulus of subgrade reaction of concrete. Sall, et al, compiled a number of models which have been used to calculate the modulus of subgrade reaction of soil [33]. All of the equations compiled follow a similar form. The general equation form is given in Equation 3.42.

$$k_0 = a\frac{E_s}{1-\nu^2}\left(\frac{E_s B^4}{EI}\right)^{\gamma} \tag{3.42}$$

In Equation 3.42, E_s is Young's modulus of the subgrade material, B is the foundation width, ν is Poisson's ratio, E is Young's modulus of the bearing material, I is the moment of inertia of the bearing material, and a and γ are calibrated constants according to the author of each model. Each of the different models was applied to Barnwell's specimens to estimate the modulus of subgrade reaction. To do so, the modulus of elasticity of the block-out concrete was used for E_s, the resisting width of concrete was used for B, a typical value of 0.2 was used for Poisson's ratio, a standard 29000 ksi was used for E, and the moment of inertia of the steel column was used for I. The resulting values ranged from 128 to 348 kips/in^3.

Several concerns exist with this method. First, the output modulus of subgrade reaction is very dependent on the input moment of inertia. It is unintuitive and incorrect to assume that a property of the embedded material would change the stiffness of the embedment medium. Furthermore, the models compiled by Sall are calibrated for use with soils and are not necessarily intended for use with concrete. Despite these concerns, the output moduli are encouraging in that they overlap some of the values calibrated from the continuum and stiffness method models. As such, 300 kips/in^3 was selected as a conservative estimate of modulus of subgrade reaction for comparison with experimental data from Barnwell and Grilli, et al.

The k_0 value of 300 kips/in^3 provides reasonable yet conservative results for Barnwell's experiments. However, it may be recalled that this modulus of subgrade reaction describes the stiffness of lower strength concrete. In compliance with assumptions made in Section 3.1.6, values providing reasonable results in Barnwell's experiments should be multiplied by the ratio of the moduli of elasticity for 1600 psi and 4000 psi concrete to appropriately adjust for normal strength concrete. The lowest calibrated k_0 value was 325 kips/in^3. Multiplying this value by the ratio of 3600 to 2280 results in a value of 513 kips/in^3. As such, for normalization purposes, a conservative value for k_0 of 500 kips/in^3 is used.

Two forms of comparison were developed to evaluate the ability of the continuum and stiffness method models to predict the rotational stiffness of the specimens tested by Barnwell. The first is a set of hysteretic plots provided by Barnwell. Superimposed on these plots are three lines representing the predicted elastic stiffness using the continuum model. These lines were generated using values of 300, 600, and 10×10^{10} kips/in^3 for the modulus of subgrade reaction. Values of 300 and 600 kips/in^3 provide an envelope for the calibrated modulus, whereas 10×10^{10}

kips/in^3 approximates the stiffness of a fixed connection. The second form of comparison is a set of graphs on which the rotational stiffness of an embedded connection is plotted as a function of its embedment length using the continuum model. Also plotted on these graphs are the specimen data from Barnwell's experiments using the calibrated moduli of subgrade reaction. The curves of rotational stiffness against embedment length were plotted using values for the modulus of subgrade reaction equal to 100, 300, 600, and 2000 kips/in^3 to provide an envelope of potential rotational stiffness curves.

3.3 Comparison with Data from University of California at Davis

A study on embedded steel column-to-footing connections performed by Grilli and Kanvinde was discussed in Section 2.1.2 [5]. Data from Grilli's experiments were input into the continuum model to verify its accuracy. Table 3.2 contains specimen data pertinent to this verification, including embedment length, exposed column length, and column shape. Each specimen in this study was tested in strong axis orientation. Since the specimens tested by Grilli, et al, were embedded in normal strength concrete, values of 500, 1000, and 10×10^{10} kips/in^3 were tested for the modulus of subgrade reaction. Values of 500 and 1000 kips/in^3 provide a similar envelope to the one used for Barnwell's hysteretic plots, and 10×10^{10} kips/in^3 approximates a perfectly fixed connection.

Table 3.2: UC Davis Specimen Data for Continuous Model Verification

Test #	Column Size	d [mm]	z [m]
1	W14X370 (419)	508	2.84
2	W18X311 (305)		
3	W14X370 (419)	762	3.10
4			
5			

Inputting these data into the continuum model under a unit load results in horizontal displacements at the point of application of the lateral load for each specimen. These horizontal displacements may be used to back calculate corresponding drift percentages for assumed values of bending moment. For this comparison, drifts were calculated based on an arbitrarily selected value of 3000 kNm. These drifts were plotted on hysteretic plots provided by Grilli and Kanvinde. The continuum model can be assumed to reasonably approximate the results of the study if the slope from the origin to the plotted points is close to the slope of the elastic region of the hysteretic plots.

3.4 Normalization of Rotational Stiffness vs. Embedment Length Curves

The continuum model presented is relatively complex and may be difficult to replicate. As such, efforts were made by which rotational stiffness might more easily be computed for specific cases. Using the conservative estimate for modulus of subgrade reaction of 500 kips/in^3 for normal strength concrete, the plotted embedment length was divided by the depth of each column shape. Rotational stiffness was also normalized, but instead by multiplying by $\lambda^{2.85}$ and dividing by the flange width or the depth of the column shape for strong and weak axis oriented columns, respectively. The exponent of 2.85 is calibrated such that the rotational stiffness roughly converges to a single value at deeper embedment lengths. Though varying exposed length values change the output values, the variation was very little. As such, a typical value of 90 inches was used for the exposed column length. This value was selected on the basis that rotational stiffness is typically calculated for half of a story height. Equations are also provided that may be used to conservatively calculate the rotational stiffness of any embedded connection for embedment lengths of twice the column depth or greater.

CHAPTER 4. RESULTS

This chapter provides several forms of data demonstrating a number of aspects of the continuum and stiffness method models presented in Chapter 3. These include hysteretic plots provided by Barnwell [3], and by Grilli, et al [5], with elastic stiffness data calculated from the continuum model superimposed thereon; a table comparing the elastic stiffness data from Barnwell's tests with output rotational stiffness values from the continuum model for k_0 values of 300 and 600 kips/in^3; plots of rotational stiffness as a function of embedment length as an envelope of Barnwell's stiffness data using the continuum model; and normalized plots of rotational stiffness as a function of embedment length for W8 shapes using the continuum model. Also included are observations based on the data presented and simplified piecewise equations that are proposed for rough estimation of the rotational stiffness of steel column-to-footing connections.

4.1 Superimposed Elastic Stiffness Slopes on Hysteretic Plots (Barnwell)

By superimposing elastic stiffness slopes on hysteretic plots for varying assumed values of k_0, the ability of the continuum model to predict the elastic stiffness of an embedded column connection can be evaluated. Figures 4.1 through 4.7 below show the hysteretic plots of the specimens prepared and tested by Barnwell with such elastic stiffness slopes superimposed. From left to right, the different slopes were prepared for concrete base stiffness values of 300, 600, and 10×10^{10} kips/in^3, respectively. A range of 300 to 600 kips/in^3 serves as an envelope for the true modulus of subgrade reaction of the concrete. The value of 10×10^{10} kips/in^3 was used to simulate a perfectly fixed connection (i.e. $k_0 = \infty$), and therefore is labeled as fixed on the plots. Similar information, as well as percent error values for 300 and 600 kips/in^3 are tabulated in Table 4.1. The fixed data was not included in the table because as the modulus of subgrade reaction approaches infinity, so does the rotational stiffness of the connection.

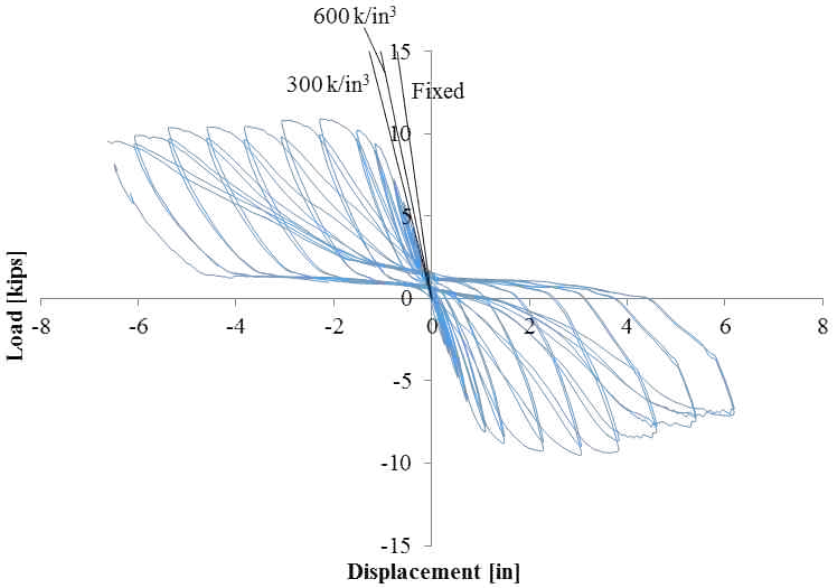

Figure 4.1: Specimen A1 Hysteretic Plot (Barnwell)

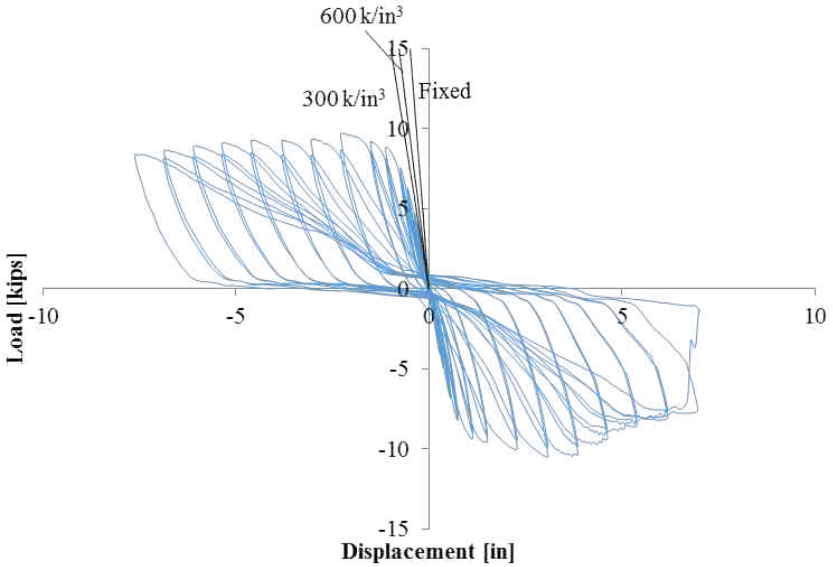

Figure 4.2: Specimen A2 Hysteretic Plot (Barnwell)

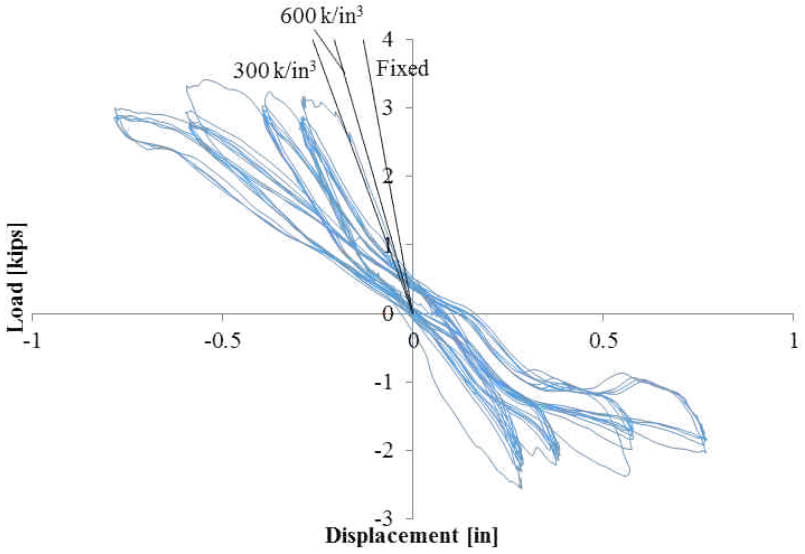

Figure 4.3: Specimen CA2 Hysteretic Plot (Barnwell)

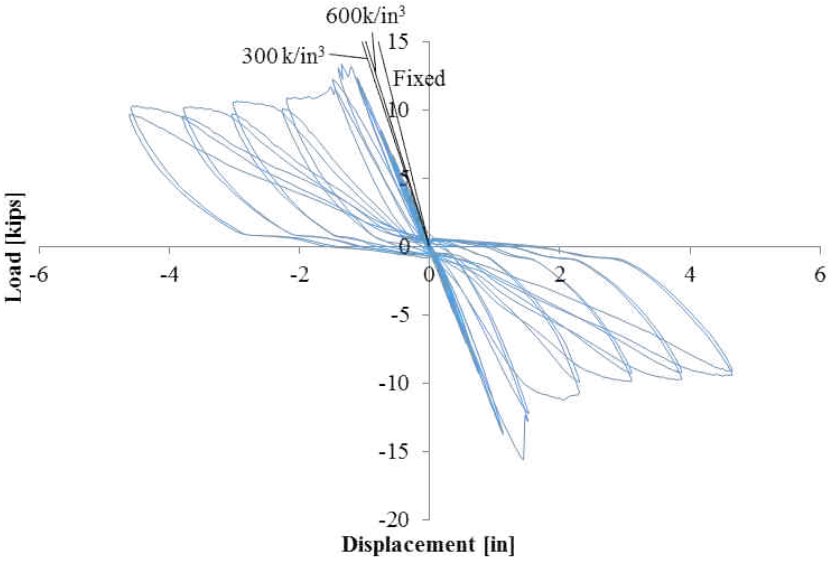

Figure 4.4: Specimen B1 Hysteretic Plot (Barnwell)

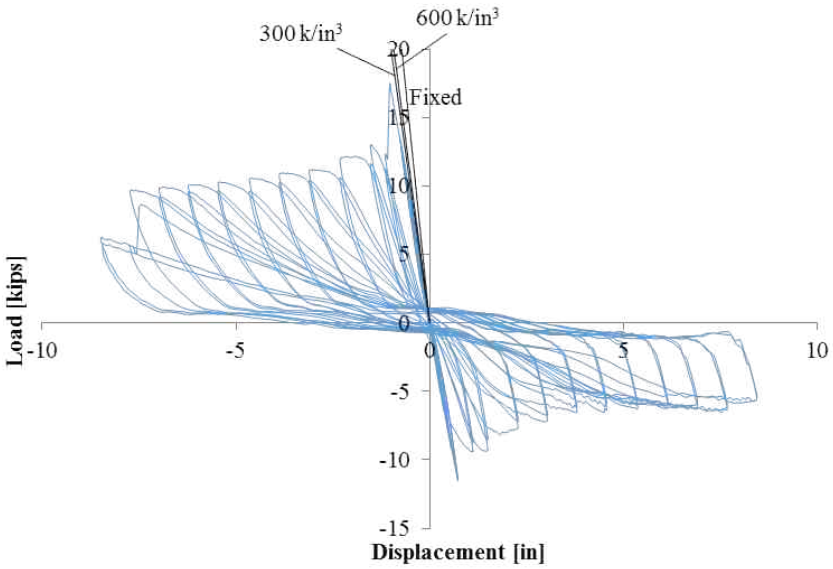

Figure 4.5: Specimen B2 Hysteretic Plot (Barnwell)

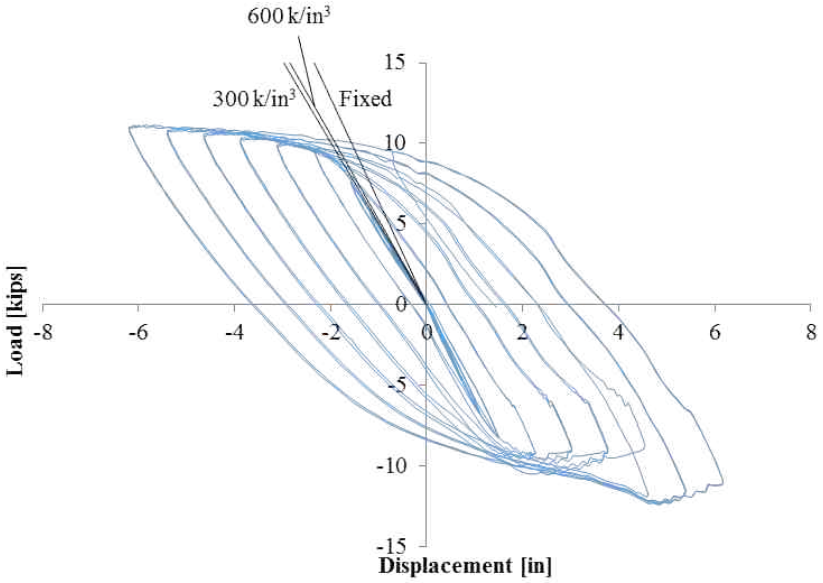

Figure 4.6: Specimen B3 Hysteretic Plot (Barnwell)

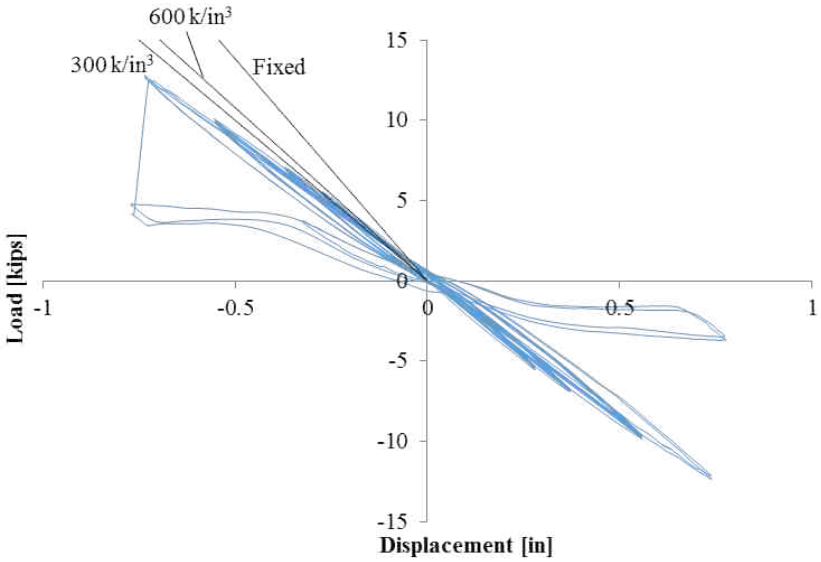

Figure 4.7: Specimen CB2 Hysteretic Plot (Barnwell)

Table 4.1: Experimental vs. Theoretical Rotational Stiffness of Barnwell's Specimens

Specimen	Rotational Stiffness [1000 kip-in/rad]		
	Experimental	k_0 = 300 kip/in^3	k_0 = 600 kip/in^3
A1	196	168	285
A2	232	193	335
CA2	206	193	335
B1	433	405	526
B2	636	496	670
B3	184	161	202
CB2	640	496	670
Error [%]		19.6	16.4

It can be observed that the elastic stiffness lines align very closely with the elastic stiffness region on the hysteretic plots. Closer observation shows that the 300 kips/in^3 line is slightly shallower than the elastic region, the 600 kips/in^3 line is slightly steeper than the elastic region, and the fixed line is significantly steeper than the elastic region. According to these plots, the specimens

tested by Barnwell cannot be described as fixed; however, they clearly are not flexible. These shallow embedded connection specimens can be more accurately described as partially fixed.

4.2 Rotational Stiffness vs. Embedment Length Plots (Barnwell)

The curves plotted in Figures 4.8 through 4.10 show how the rotational stiffness of wide flange shape varies with embedment length for the column shapes and orientations represented in Barnwell's experiments. These curves correspond to k_0 values of 100, 300, 600, and 2000 kips/in^3. The stiffness data from Barnwell's experiments are also plotted. Similar plots were not produced for the UC Davis specimens since no numerical data regarding their elastic stiffness values were given. A dashed line indicates a k_0 value that was not conservative with the data. Bold lines indicate k_0 values that closely predicted the rotational stiffness of the specimens.

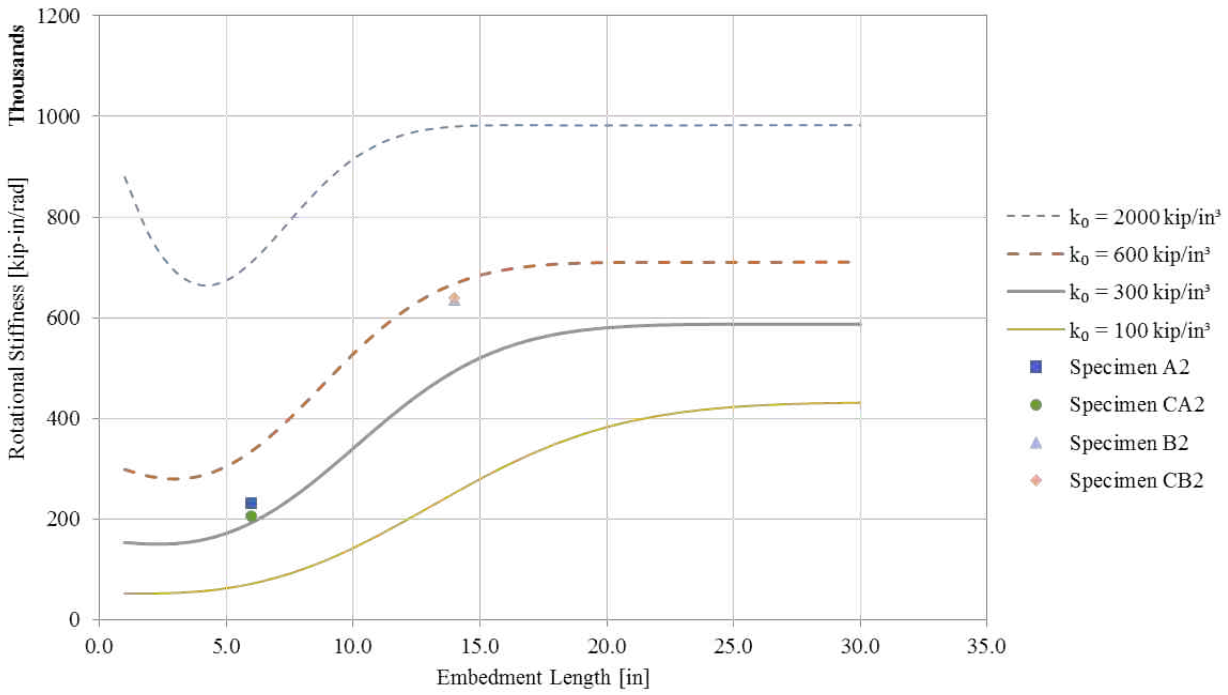

Figure 4.8: Rotational Stiffness vs. Embedment Length for W8X48 Strong Axis Shapes

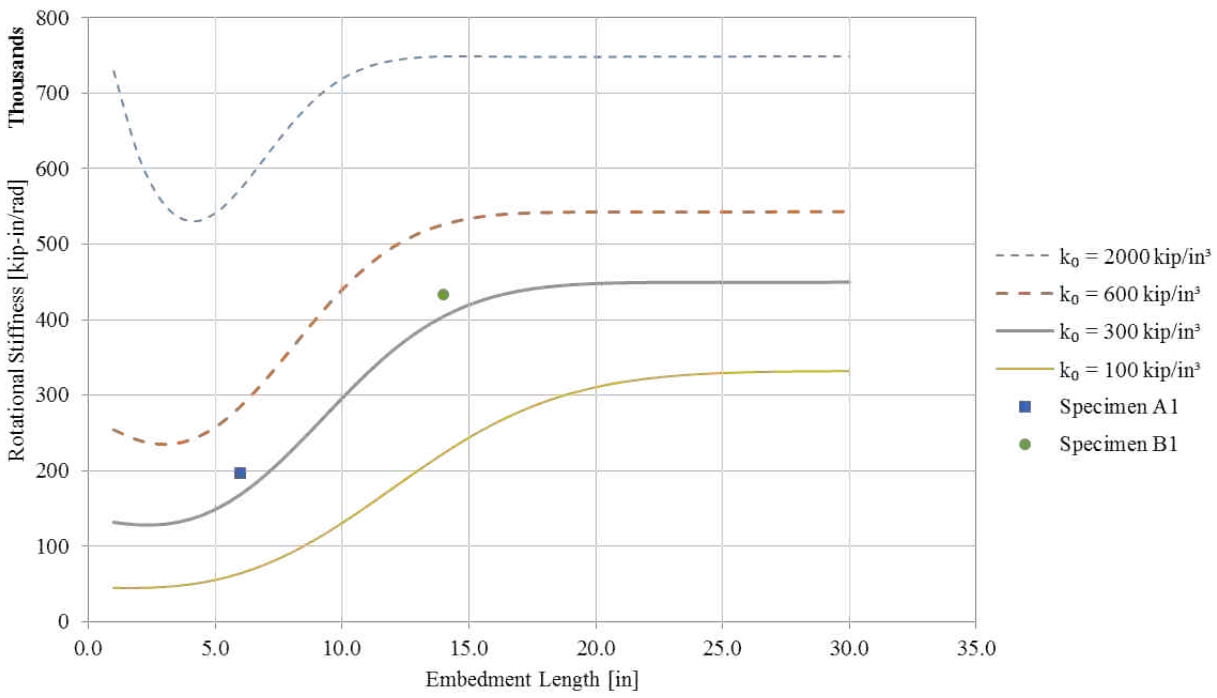

Figure 4.9: Rotational Stiffness vs. Embedment Length for W8X35 Strong Axis Shapes

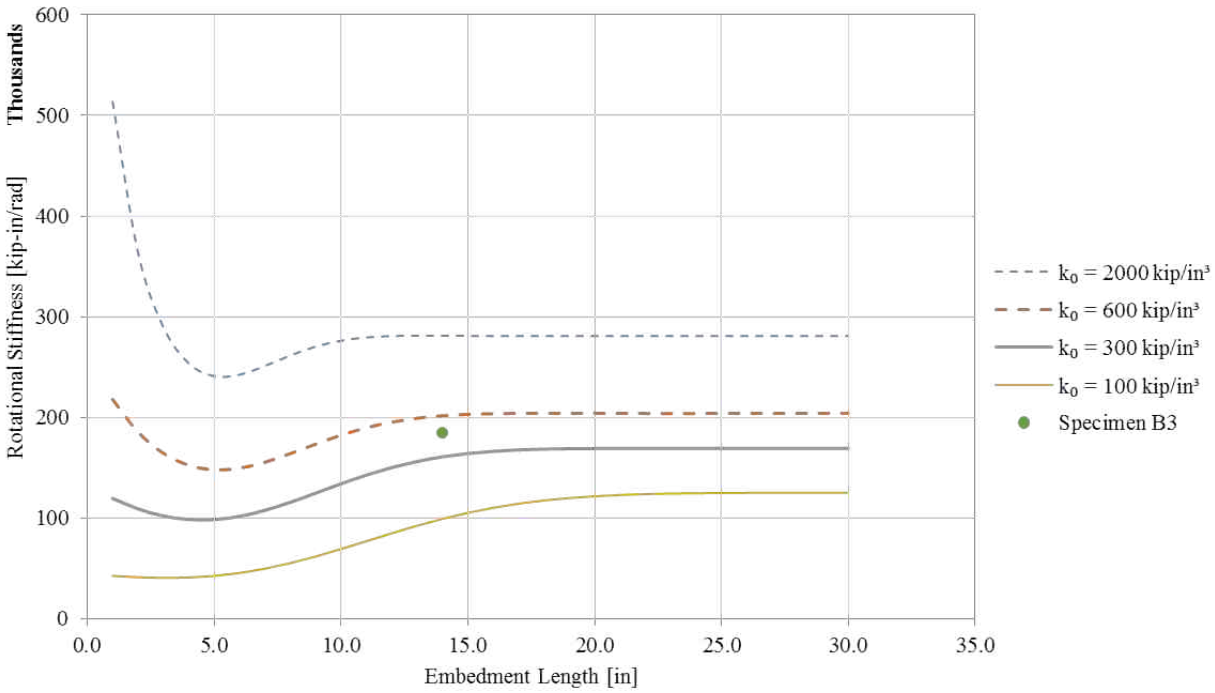

Figure 4.10: Rotational Stiffness vs. Embedment Length for W8X35 Weak Axis Shapes

Several observations can be made from these plots. Of particular note is the dip at the beginning of some curves, particularly for higher k_0 values on the strong axis oriented plots and on all of the weak axis oriented curves. The stiffness of a cantilever beam is equal to $3EI/L^3$; thus, its stiffness is inversely proportional to the cube of its length. As such, doubling the length of a cantilever beam serves to make it 8 times more flexible. Even a small increase in length can serve to significantly reduce the fixity of a cantilever beam. By extension, a very shallowly embedded column has very little embedment material to prevent displacement from occurring under lateral loads. Thus, such shallow embedment lengths may not produce sufficient stiffness to counteract the stiffness loss due to a slightly increased column length. As the embedment length approaches zero, the rotational stiffness of the column approaches the rotational spring stiffness k_s explained in Chapter 3.

It may also be observed that after some amount of embedment, increasing embedment length fails to produce additional stiffness. The amount of embedment at which this occurs varies

depending on the modulus of subgrade reaction. It may be recalled that in Section 2.2.2, findings by Castilla, et al, were discussed [25]. In their work, it was found that a pile may be approximated as fixed at an embedment length equal to twice the depth of the pile. Similarly, it is at about twice the column depth that additional embedment length fails to produce additional stiffness in Figures 4.8 through 4.10. These plots agree with the research performed by Castilla, et al. It may also be observed that the stiffer the embedment material is, the less embedment length is required to obtain maximum rotational stiffness.

4.3 Superimposed Elastic Stiffness Slopes on Hysteretic Plots (Grilli, et al)

Figures 4.11 through 4.15 below show data predicting the elastic rotational stiffness of embedded connection specimens tested by Grilli, et al [5]. Data presented in Table 3.1 were used to calculate the displacement caused by a unit load for each specimen using various values of k_0. From left to right, the three lines represent the elastic rotational stiffness of the specified column for k_0 values of 10×10^{10}, 1000, and 500 kip/in^3. The leftmost line approximates a perfectly fixed connection, while the other two lines provide an envelope similar to those used previously.

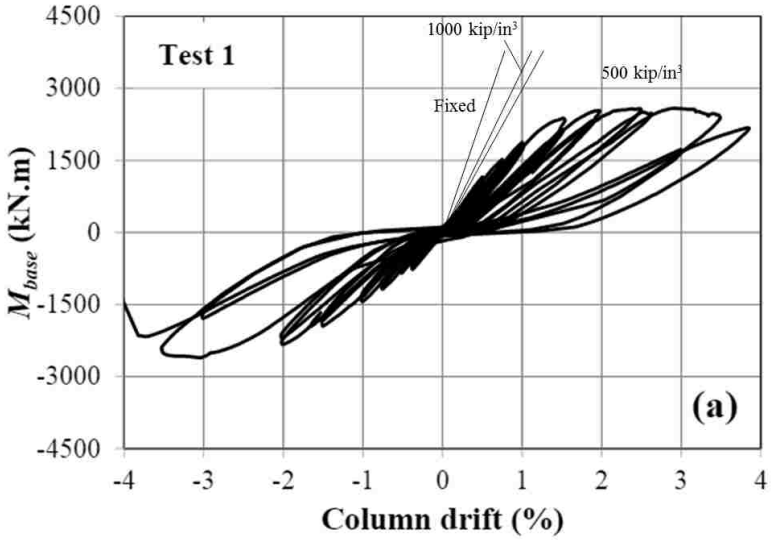

Figure 4.11: Test 1 Hysteretic Plot (Grilli, et al)

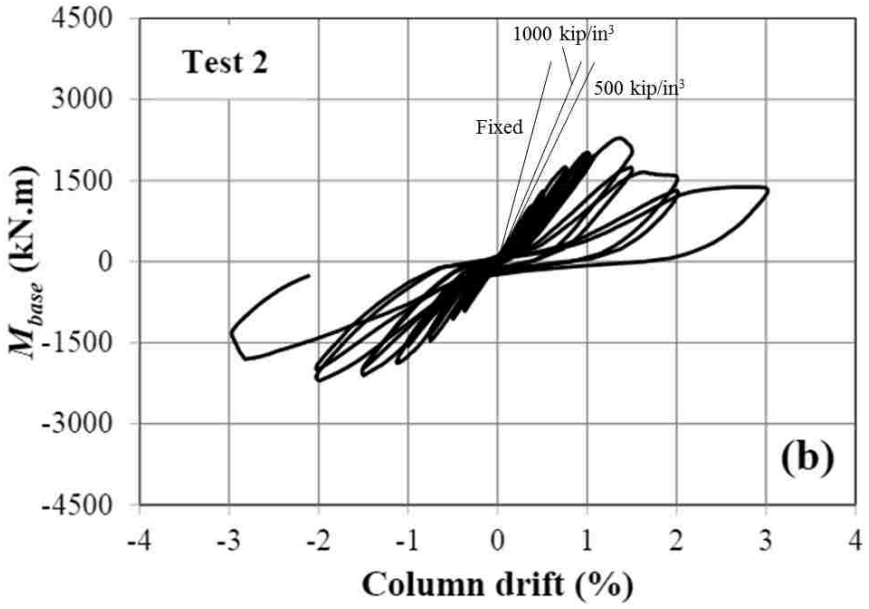

Figure 4.12: Test 2 Hysteretic Plot (Grilli, et al)

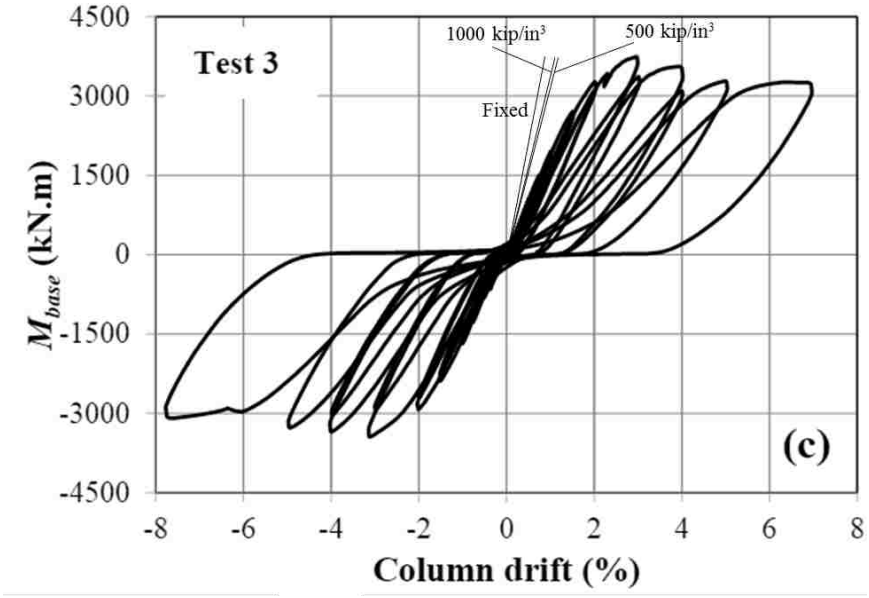

Figure 4.13: Test 3 Hysteretic Plot (Grilli, et al)

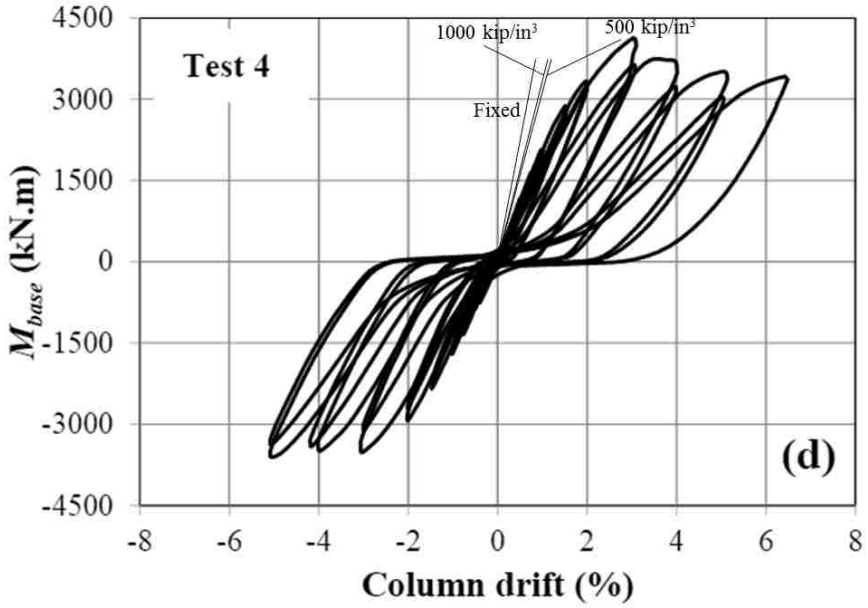

Figure 4.14: Test 4 Hysteretic Plot (Grilli, et al)

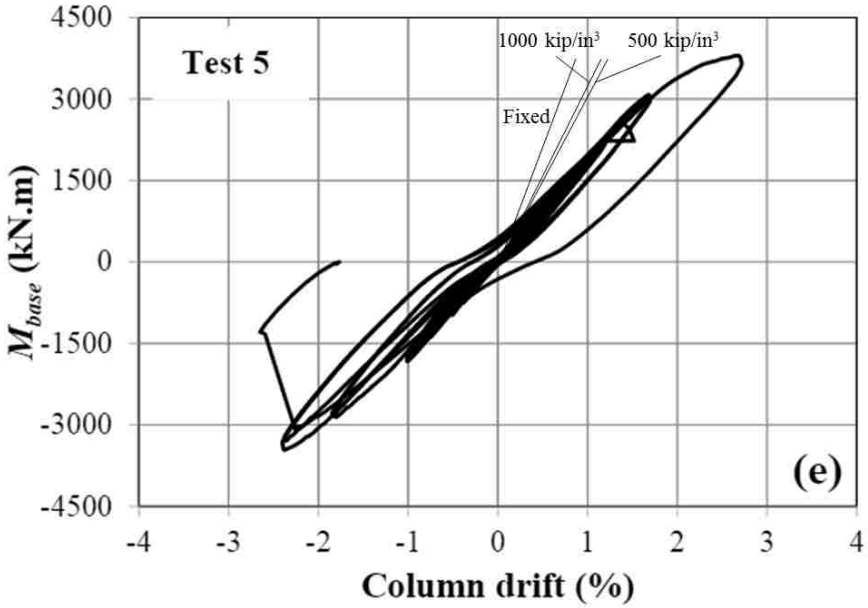

Figure 4.15: Test 5 Hysteretic Plot (Grilli, et al)

These hysteretic plots bear many similarities to those provided by Barnwell. It may be observed that the elastic stiffness lines for 500 and 1000 kips/in^3 closely approximate the elastic region of each of the specimens, albeit with less accuracy than for Barnwell's experiments. One factor that may have reduced the accuracy is the presence of axial load. Grilli's experiments were loaded axially as well as laterally; Barnwell's specimens were loaded only laterally. The continuum model does not consider the presence of axial load on the column, which may reduce the accuracy of the results. Despite this inaccuracy, the envelope provided by k_0 values ranging from 500 to 1000 kip/in^3 reasonably estimates the elastic stiffness of the specimens. It may also be observed that the line representing a perfectly fixed connection fails to adequately align to the elastic region of any of the specimens. As such, these embedded connections should not be approximated as perfectly fixed, but as partially fixed with high rotational stiffness. These results agree with the conclusions made by Grilli, et al [5].

4.4 Normalized Rotational Stiffness vs. Embedment Length Curves

Due to the inherent complexity in implementing the continuum model, efforts were made to normalize the outputs of the model for general use. To do so, the embedment length was divided by the column depth, and the rotational stiffness was multiplied by $\lambda^{2.85}$, the coefficient relating the stiffness properties of the column and the concrete mentioned previously, and divided by the flange width or the depth for strong and weak axis oriented columns, respectively. The value of λ may be calculated by using Equation 3.7. To further ease calculations, the modulus of subgrade reaction k_0 was maintained at a conservative 500 kips/in^3, assuming normal strength concrete. Though the rotational stiffness calculated using the continuum model varies with exposed column length, this variation is small. As such, the normalized curves were generated assuming an exposed column length of 90 inches, which represents half of a typical story height. Each family of wide flange columns can therefore be represented by two plots, with one for strong axis orientation and the other for weak axis orientation. Only unlabeled plots for W8 shapes, shown in Figures 4.16 and 4.17, are presented in this section. All of these plots may be viewed in Appendix B, where they are labeled and divided into subfamilies for readability.

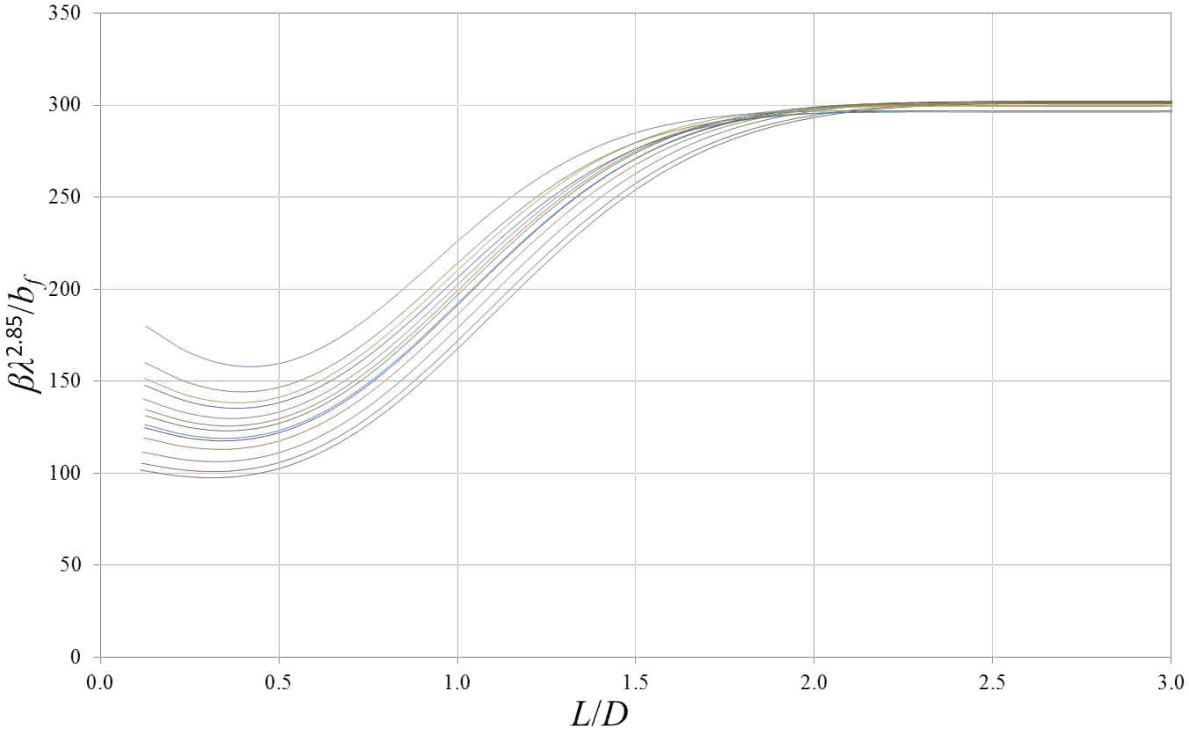

Figure 4.16: Normalized W8 Strong Axis Shapes

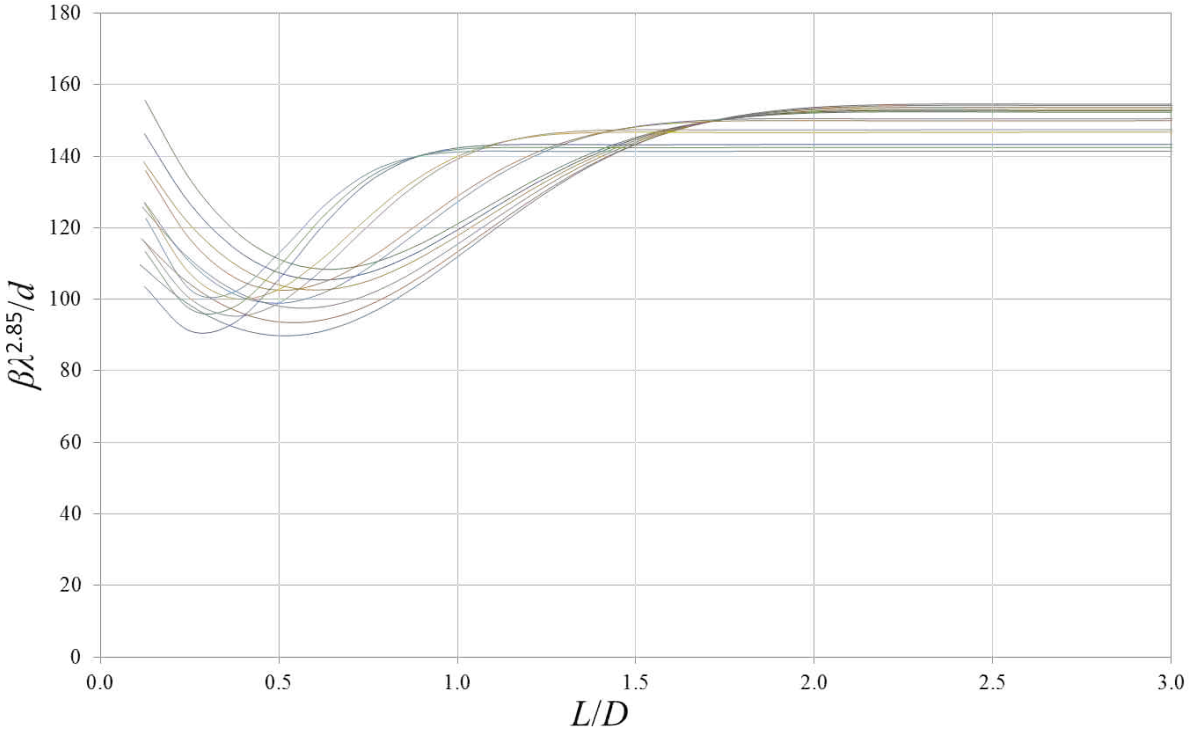

Figure 4.17: Normalized W8 Weak Axis Shapes

According to these plots, additional rotational stiffness is unlikely to be attained for embedment lengths greater than about twice the depth of a given column shape. It may also be observed that each of the plots roughly converge to a single value when maximum fixity is attained. These plots may be used to swiftly calculate the rotational stiffness of a specified column shape and embedment length embedded in normal strength concrete. To do this, the embedment length must first be divided by the column depth. Then, a vertical line may be drawn from that ratio for the appropriate axis orientation plot up to the corresponding shape curve. A line can then be drawn horizontally from the curve to the vertical axis, and the corresponding value of $\beta\lambda^{2.85}/(b_f \text{ or } d)$ can be read. With this information, the value of β can be calculated.

It is understood that reading values from these curves may be tedious, especially in cases where the precise shape or embedment length is unknown. Furthermore, as these curves represent a significant amount of literature that may be unavailable on site, they may be inconvenient for quick decisions. Cases may also exist where only an approximate rotational stiffness value is required for a connection. For cases such as these, sets of piecewise functions were developed that may be used to more swiftly calculate the rotational stiffness of any shape at the cost of some precision. Two sets of these equations are provided. The first is to be used for W10, W12, or W14 shapes, which are the most column common shapes used in design, and the second may be used for any wide flange shape. Equations for columns in both strong and weak axis orientation are provided. These piecewise functions are given in Equations 4.1 through 4.4. They are followed by plots of those functions superimposed on their respective data from the continuum model in Figures 4.18 through 4.21. It should be noted that these equations represent averages of rotational stiffness for the selected shapes and are not intended to be conservative. As such, these equations should only be used to obtain a rough estimate of the rotational stiffness of the connection. For more precise information, the family shape curves mentioned previously should be used.

For common shapes in strong axis orientation:

$$\frac{\beta\lambda^{2.85}}{b_f} = \begin{cases} 135 & \frac{L}{D} < 0.5 \\ 110\frac{L}{D} + 80 & 0.5 \leq \frac{L}{D} < 2.0 \\ 300 & 2.0 \leq \frac{L}{D} \end{cases} \tag{4.1}$$

For common shapes in weak axis orientation:

$$\frac{\beta\lambda^{2.85}}{d} = \begin{cases} 105 & \frac{L}{D} < 0.5 \\ 30\frac{L}{D} + 90 & 0.5 \leq \frac{L}{D} < 2.0 \\ 150 & 2.0 \leq \frac{L}{D} \end{cases} \tag{4.2}$$

For any shape in strong axis orientation:

$$\frac{\beta\lambda^{2.85}}{b_f} = \begin{cases} 174 & \frac{L}{D} < 0.5 \\ 84\frac{L}{D} + 132 & 0.5 \leq \frac{L}{D} < 2.0 \\ 300 & 2.0 \leq \frac{L}{D} \end{cases} \tag{4.3}$$

For any shape in weak axis orientation:

$$\frac{\beta\lambda^{2.85}}{d} = \begin{cases} 129 & \frac{L}{D} < 0.5 \\ 14\frac{L}{D} + 122 & 0.5 \leq \frac{L}{D} < 2.0 \\ 150 & 2.0 \leq \frac{L}{D} \end{cases} \tag{4.4}$$

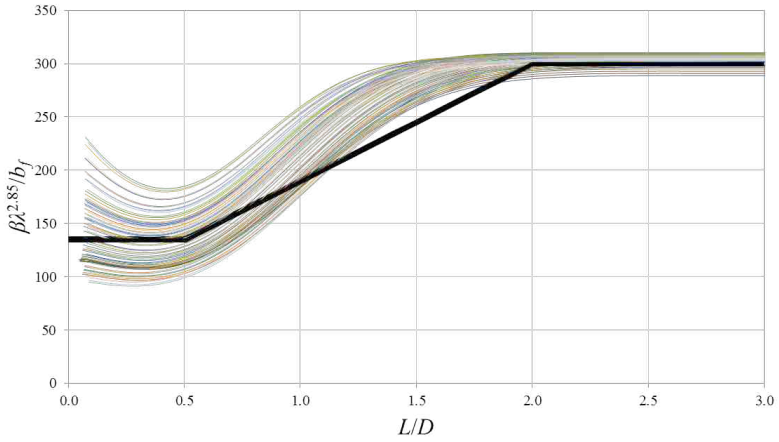

Figure 4.18: Common Normalized Strong Axis Curves with Simplified Equation

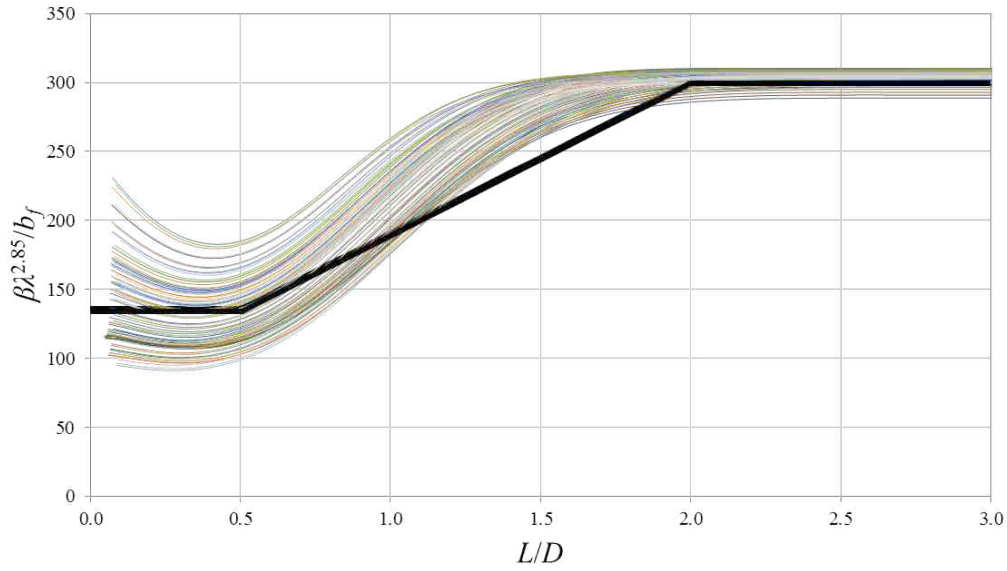

Figure 4.19: Common Normalized Weak Axis Curves with Simplified Equation

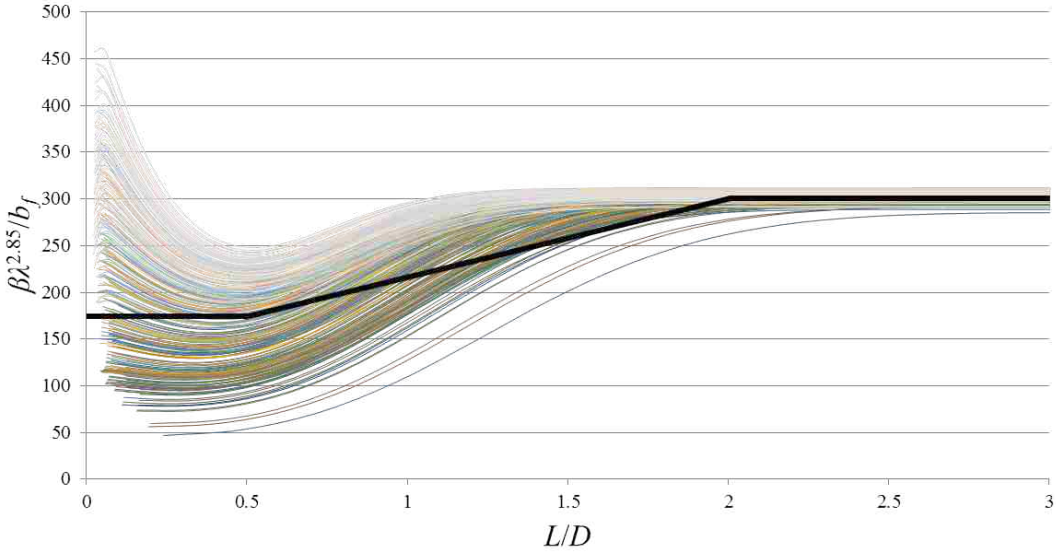

Figure 4.20: All Normalized Strong Axis Curves with Simplified Equation

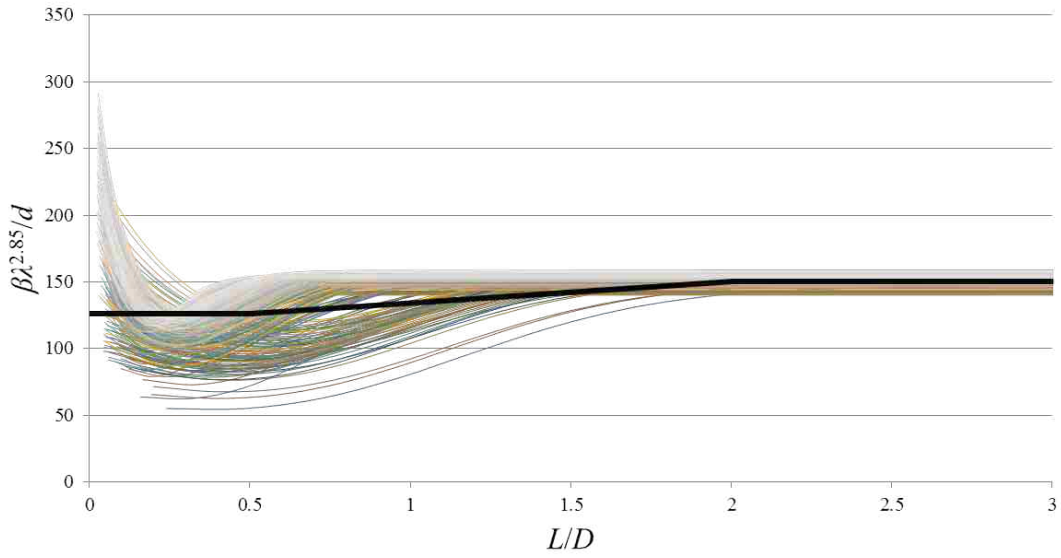

Figure 4.21: All Normalized Weak Axis Curves with Simplified Equation

These equations are intended to be simple to use. To demonstrate this simplicity, suppose the rotational stiffness of a W12X96 column in strong axis orientation embedded 16 inches into normal strength concrete is to be determined. Since this is a W12 shape, Equation 4.1 may be used.

$$\frac{L}{D} = \frac{16\text{in}}{12.7\text{in}} = 1.26 \leftarrow \text{The middle condition applies.}$$

$$\frac{\beta\lambda^{2.85}}{b_f} = 110\frac{L}{D} + 80 = 218.6$$

$$\lambda = \sqrt[4]{\frac{k_0(2b_f - t_w)}{4EI}} = \sqrt[4]{\frac{500\ \text{k/in}^3(2(12.2\ \text{in}) - 0.55\ \text{in})}{4(29000\ \text{ksi})(833\ \text{in}^4)}} = 0.1054\ \text{in}^{-1}$$

$$\beta = 218.6\frac{b_f}{\lambda^{2.85}} = 218.6\frac{12.2\ \text{in}}{0.1054^{2.85}} = 1.625 \times 10^6\ \text{kip-in/rad}$$

The continuum model yields a value of $\beta = 2.292 \times 10^6$ kip-in/rad. Though not precise, the equation produces a reasonable estimate for the rotational stiffness of the connection.

CHAPTER 5. CONCLUSION

This thesis has presented a method named the continuum model by which the rotational stiffness of embedded column connections may be calculated. Though a focus has been placed on shallow embedded connections, the model may be extended in application to all embedded connections. By comparing with experimental data provided by Barnwell [3] and Grilli, et al [5], the continuum model has been shown to reasonably predict the elastic stiffness of such connections for a calibrated range of moduli of subgrade reaction of concrete. Through the use of normalized rotational stiffness vs. embedment length plots, the rotational stiffness of any embedded wide flange column connection may be calculated. Similar values may be calculated with greater ease through the use of simplified piecewise equations at the cost of some accuracy and perhaps some conservatism.

By plotting rotational stiffness against embedment length, the model has been shown to agree with findings by Castilla, et al, in that little additional rotational stiffness can be attained at embedment lengths greater than twice the column depth [25]. Furthermore, by plotting elastic stiffness slopes produced through the continuum model on experimental hysteretic plots, the model has shown that no connection is devoid of flexibility, even when maximum fixity has been attained. This is in agreement with conclusions made by Grilli, et al [5]. Most importantly, through the use of this model, not only are shallow embedded connections shown to exhibit significant rotational stiffness in agreement with Barnwell [3], but this rotational stiffness can be quantified for use in design.

This research represents a number of significant contributions. First, the continuum model provides a new context for Hetenyi's derivations on the theory of beams on elastic foundation [4]. Though this theory is typically used exclusively to model beams lying flat on an elastic foundation, this work has extended it to a vertical column supported by elastic material on all sides. Second, this research has provided an innovative approach to modeling a base plate. Through represen-

tation of the base plate as a rotational spring, the stiffness contribution of the base plate to the connection as a whole may be quantified. In addition, a range of possible values for the modulus of subgrade reaction of concrete are proposed. This quantity has received very little attention, if any, in research. Through calibration, it is proposed that the modulus of subgrade reaction of concrete is in the range of 300 to 600 kips/in^3, with a value of 500 kips/in^3 being conservative for normal strength concrete.

The methods presented are catered to embedded wide flange steel shapes. As such, these models are not recommended for use with any other type of steel shape, and they have not been verified with the use of any other materials. This research may be furthered especially through the execution of experimental testing on concrete to determine more accurately its modulus of subgrade reaction. Doing so could validate the proposed values mentioned above. Comparison with finite element modeling of steel-column-to-concrete-footing connections may provide additional insight regarding the mechanisms governing their behavior.

REFERENCES

[1] Eastman, R. S., 2011. "Experimental investigation of steel pipe pile to concrete cap connections." Master's thesis, Brigham Young University, June. 3, 31

[2] Richards, P. W., Rollins, K. M., and Stenlund, T. E., 2011. "Experimental testing of pile-to-cap connections for embedded pipe piles." *Journal of Bridge Engineering,* **16**(2), pp. 286–294. 3, 29, 30

[3] Barnwell, N. V., 2015. "Experimental testing of shallow embedded connections between steel columns and concrete footings." Master's thesis, Brigham Young University, March. 3, 21, 23, 40, 56, 60, 78

[4] Hetenyi, M., 1971. *Beams on Elastic Foundation: Theory with Applications in the Fields of Civil and Mechanical Engineering*. University of Michigan. 3, 40, 41, 44, 78

[5] Grilli, D. A., and Kanvinde, A. M., 2015. "Embedded column base connections subjected to flexure and axial load: Tests and strength models.". 3, 16, 40, 58, 60, 68, 71, 78

[6] DeWolf, J. T., and Sarisley, E. F., 1980. "Column base plates with axial loads and moments." *Journal of the Structural Division,* **106**(11), pp. 2167–2184. 5

[7] Thambiratnam, D. P., and Paramasivam, P., 1986. "Base plates under axial loads and moments." *Journal of Structural Engineering,* **112**(5), pp. 1166–1181. 7, 51, 92

[8] Kanvinde, A., and Deirlein, G. G., 2011. "Recent research on column base connections." *Modern Steel Construction*, April. 8

[9] Gomez, I. R., 2010. *Behavior and Design of Column Base Connections*. University of California, Davis. 8, 10, 12, 23

[10] Fisher, J. M., and Kloiber, L., 2006. *Base plate and anchor rod design*. American Institute of Steel Construction. 8, 9, 12, 21, 26

[11] AISC, 2010. *Seismic provisions for structural steel buildings*. American Institute of Steel Construction. 8, 38

[12] Kanvinde, A., Grilli, D., and Zareian, F., 2011. "Rotational stiffness of exposed column base connections: experiments and analytical models." *Journal of Structural Engineering*. 9

[13] Picard, A., and Beaulieu, D., 1985. "Behaviour of a simple column base connection." *Canadian Journal of Civil Engineering,* **12**(1), pp. 126–136. 10

[14] Kanvinde, A., Jordan, S., and Cooke, R., 2013. "Exposed column base plate connections in moment framessimulations and behavioral insights." *Journal of Constructional Steel Research,* **84**, pp. 82–93. 11

[15] Pertold, J., Xiao, R. Y., and Wald, F., 2000. "Embedded steel column bases i. experiments and numerical simulation." *Journal of Constructional Steel Research,* **56**(3), pp. 253–270. 13, 19

[16] Pertold, J., Xiao, R. Y., and Wald, F., 2000. "Embedded steel column bases ii. design model proposal." *Journal of Constructional Steel Research,* **56**(3), pp. 271–286. 14

[17] Grauvilardell, J. E., Lee, D., Hajjar, J. F., and Dexter, R. J., 2005. *Synthesis of Design, Testing, and Analysis Research on Steel Column Base Plate Connections in High-seismic Zones*. Department of Civil Engineering, University of Minnesota. 19

[18] Cui, Y., Nagae, T., and Nakashima, M., 2009. "Hysteretic behavior and strength capacity of shallow embedded steel column bases." *Journal of Structural Engineering,* **135**(10), pp. 1231–1238. 20

[19] Marcakis, K., and Mitchell, D., 1980. "Precast concrete connections with embedded steel members." *Precast/Prestressed Concrete Institute Journal,* **56**(4), pp. 88–116. 26, 27, 30

[20] Committee, P. I. H., et al., 2004. Pci design handbook: Precast and prestressed concrete. 26

[21] Harries, K., and Petrou, M., 2001. "Behavior of precast, prestressed concrete pile to cast-in-place pile cap connections." *PCI journal,* **46**(4). 27

[22] Harries, K. A., Mitchell, D., Cook, W. D., and Redwood, R. G., 1993. "Seismic response of steel beams coupling concrete walls." *Journal of Structural Engineering,* **119**(12), pp. 3611–3629. 28

[23] Baltay, P., and Gjelsvik, A., 1990. "Coefficient of friction for steel on concrete at high normal stress." *Journal of Materials in Civil Engineering,* **2**(1), pp. 46–49. 30

[24] Xiao, Y., Wu, H., Yaprak, T. T., Martin, G. R., and Mander, J. B., 2006. "Experimental studies on seismic behavior of steel pile-to-pile cap connections." *Journal of Bridge Engineering,* **11**(2), pp. 151–159. 31

[25] Castilla, F., Martin, P., and Link, J., 1984. Fixity of members embedded in concrete Tech. rep., DTIC Document. 32, 68, 78

[26] Sheikh, T. M., Deierlein, G. G., Yura, J. A., and Jirsa, J. O., 1989. "Beam-column moment connections for composite frames: Part 1." *Journal of Structural Engineering,* **115**(11), pp. 2858–2876. 34

[27] Deierlein, G. G., Sheikh, T. M., Yura, J. A., and Jirsa, J. O., 1989. "Beam-column moment connections for composite frames: Part 2." *Journal of Structural Engineering,* **115**(11), pp. 2877–2896. 34

[28] Shahrooz, B. M., Remmetter, M. E., and Qin, F., 1993. "Seismic design and performance of composite coupled walls." *Journal of Structural Engineering,* **119**(11), pp. 3291–3309. 36

[29] Motter, C., Fields, D., Hooper, J., Klemencic, R., and Wallace, J., 2014. "Large-scale testing of steel reinforced concrete (src) coupling beams embedded into reinforced concrete shear walls.". 37

[30] Roeder, C. W., and Lehman, D. E., 2008. "An economical and efficient foundation connection for concrete filled steel tube piers and columns." In *International conference on composite construction in steel and concrete*. 39

[31] AISC, 2012. *Steel Construction Manual*., 14 ed. American Institute of Steel Construction, Chicago, IL. 56

[32] McCormac, J. C., and Brown, R. H., 2014. *Design of Reinforced Concrete*., 9 ed., Vol. 1 John Wiley & Sons, Inc., 111 River Street, Hoboken, NJ. 51, 91

[33] Sall, O. A., Fall, M., Berthaud, Y., and Ba, M., 2013. "Influence of the elastic modulus of the soil and concrete foundation on the displacements of a mat foundation." *Open Journal of Civil Engineering,* **3**(04), p. 228. 56

APPENDIX A. ALTERNATE APPROACH: STIFFNESS METHOD MODEL

A.1 Stiffness Method Model

The stiffness method model is a secondary approach to approximating the rotational stiffness of steel column-to-footing connections, and is derived using principles of the stiffness method of structural analysis. It should be noted that the continuum model was used to produce the majority of the results for two main reasons. First, the continuum model is believed to be more accurate since it is extended from closed-form solutions. The stiffness method model is viewed as a discretized, and therefore approximate, companion to the continuum model, though the two models produce similar results. Second, due to the computational effort required by a computer to invert very large stiffness matrices, the continuum model produces results far more efficiently.

A.1.1 Overview

Figure A.1 depicts a typical shallow embedded connection loaded with a lateral force P. The connection is embedded a length L into the block-out concrete, and the exposed portion extends a length S out of the concrete.

To model the connection behavior of such a specimen, the embedded portion is approximated as a vertical beam periodically supported by linear springs evenly spaced at a length s along the embedded region, as shown in Figure A.2. Though the number of springs, n_{spr}, is equal to 7 in Figure A.2, the value of n_{spr} may vary from specimen to specimen depending on the spacing s and the embedment length L. It is only required that n_{spr} be an integer for construction of the stiffness matrix to be possible. Equation A.1 shows the relationship between L, s, and n_{spr}.

$$L = s(n_{spr} - 1) \tag{A.1}$$

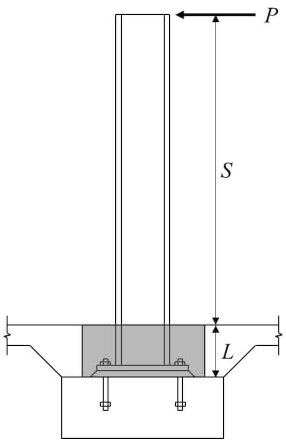

Figure A.1: Typical Shallow Embedded Connection

Each spring represents a portion of block-out material supporting the beam. The intermediate springs have a stiffness k, whereas the top and bottom springs have a stiffness $k/2$ since they represent half as much block-out material. At the bottom, a rotational spring with stiffness k_s is located, representing the stiffness contribution of the base plate. A shear force V and bending moment M are located at the concrete interface, representing the loads transferred to the connection by the exposed column. The magnitude of the bending moment M is equal to V times the length of the exposed column, S.

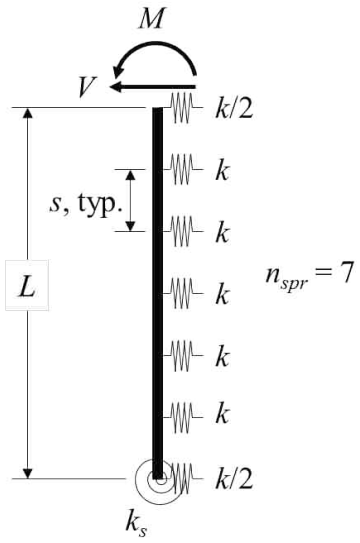

Figure A.2: Stiffness Method Model

A.1.2 Width Adjustment Factor

In Figure A.2, the value k represents the total stiffness of block-out concrete in contact with the steel column at all surfaces opposing the load. However, as discussed previously in Section 3.1.5, the amount of concrete in contact with the column varies depending on the orientation and shape of the column. Along the same vein as the previous discussion, the stiffness k of one spring is the product of the modulus of subgrade reaction k_0, the length of the corresponding side, a width adjustment factor accounting for potential flange duality ϕ_w, and the spring spacing s. For the top and bottom springs, the stiffness $k/2$ is used, which already accounts for the fact that it represents an amount of material equal to half the spring spacing. As such, accounting for it again here would be redundant and inaccurate. Again, the corresponding length is the flange width b_f for columns in strong axis orientation, and is d in weak axis orientation. For reference, Figure A.3 shows a slice of a column loaded along its strong axis. Block-out concrete in contact with both flanges is assumed to assist in resisting the load, as indicated by arrows. For a similar shape loaded along its weak axis, such as the slice shown in Figure A.4, the block-out concrete assumed to resist the load is located entirely along its depth.

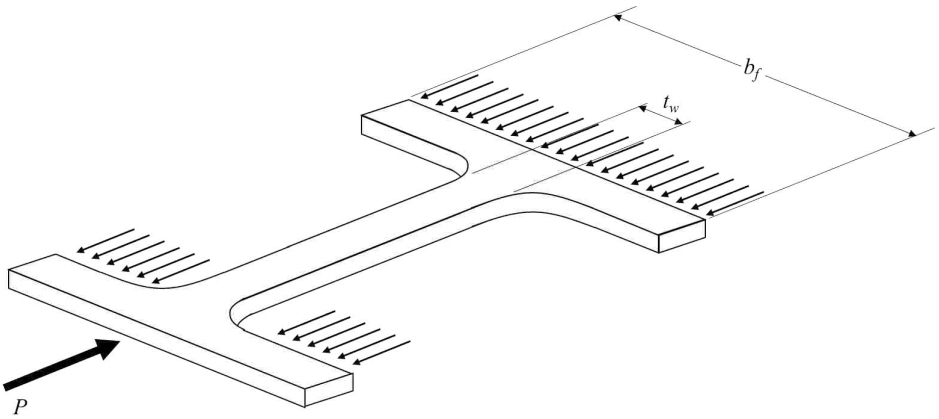

Figure A.3: Strong Axis Resisting Surfaces

The width adjustment factor has a magnitude equal to the ratio of the total bearing width for one slice of the column divided by what the total bearing width would be if the shape were rectangular. As discussed in Section 3.1.5, the width adjustment factor is the ratio of the total bearing width divided by the what the bearing width would be if the shape were rectangular. For a strong axis slice, the total bearing width is equal to twice the flange width minus the web thickness. If the shape were rectangular, its bearing width would equal the flange width. The width adjustment factor for columns in strong axis orientation is reiterated in Equation A.2, and the corresponding stiffness follows it in Equation A.3.

$$\phi_w = \frac{2b_f - t_w}{b_f} \tag{A.2}$$

$$k = \phi_w k_0 s b_f = k_0 s b_f \frac{2b_f - t_w}{b_f} = k_0 s(2b_f - t_w) \tag{A.3}$$

From Figure A.4, it may again be observed that the width of the resisting surface in the weak axis direction is equal to the column depth d. If the column were rectangular, then the resisting width would also equal d. Thus, the width adjustment factor for a weak axis I-shaped beam is 1, which is reiterated in Equation A.4. The corresponding stiffness k is given in the following equation.

$$\phi_w = \frac{d}{d} = 1 \tag{A.4}$$

$$k = \phi_w k_0 s d = k_0 s d \tag{A.5}$$

A.1.3 Base Plate Stiffness Calculation

Of particular importance is the manner by which the value k_s is calculated, which is the rotational stiffness contributed by the material anchoring the base plate. It is assumed that this stiffness is directly related to the linear stiffness of the material embedding the column. To assist in this calculation, the base plate is represented as a rigid beam supported as shown in Figure A.5, by parallel springs separated by the same spacing s as in rest of the model. However, no rotational spring is present, and only a moment is applied to the beam. This moment causes the beam to

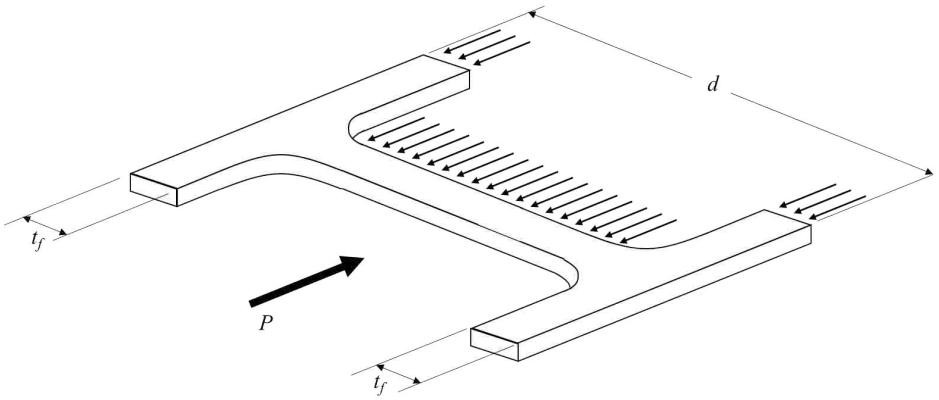

Figure A.4: Weak Axis Resisting Surfaces

rotate and the springs to stretch or compress proportional to their distance away from the center of the beam. In Figure A.5, the undisturbed beam is shown on the left, while the rotated beam is shown on the right.

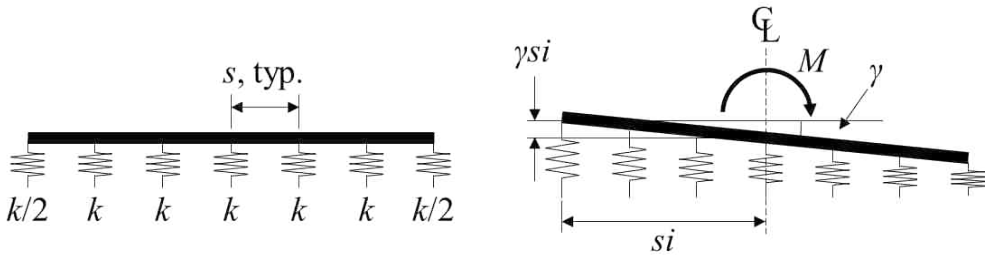

Figure A.5: Discrete Base Plate Model

It should be noted that the springs on either end of the base plate provide half as much stiffness as intermediate springs since they represent half as much material. Furthermore, the rotation γ is assumed to be very small, allowing the use of small angle approximations throughout the calculation. The distance of any one spring from the centerline is equal to the spring spacing s times i, an integer counting the number of springs away from the centerline. Thus, the vertical displacement at the ith spring away from the centerline can be found using Equation A.6.

$$\delta_i = \gamma si \tag{A.6}$$

From symmetry, the total vertical force acting on the beam sums to 0. However, the springs collectively apply a moment to the base plate equal and opposite to the applied moment. The magnitude of the moment applied to the beam by one spring can be found by multiplying the vertical displacement, δ_i, by its stiffness (k for intermediate springs and $k/2$ for end springs) and its distance from the centerline, si. These calculations are represented in Equations A.7 and A.8.

$$M_{i,int} = k\delta_i si^2 = ks^2 i^2 \gamma \tag{A.7}$$

$$M_{i,end} = \frac{k}{2}\delta_i si^2 = \frac{ks^2 i^2}{2}\gamma \tag{A.8}$$

The value of i for Equation A.8 will always be equal to half of one less than the number of springs, as expressed in Equation A.9. As such, $M_{i,end}$ can always be expressed as shown in Equation A.10.

$$i_{end} = \frac{n_{spr} - 1}{2} \tag{A.9}$$

$$M_{i,end} = \frac{ks^2}{2}\left(\frac{n_{spr} - 1}{2}\right)^2 \gamma \tag{A.10}$$

An equal amount of moment is applied on both sides of the centerline. Thus, the total moment applied to the base plate by one couple is equal to twice the moment applied by one spring. As such, the moment applied to the beam by one couple of intermediate springs can be expressed as shown in Equation A.11, and the couple moment applied by the end springs is shown in Equation A.12.

$$M_{c,int} = 2ks^2 i^2 \gamma \tag{A.11}$$

$$M_{c,end} = ks^2 \left(\frac{n_{spr} - 1}{2}\right)^2 \gamma \tag{A.12}$$

Since the springs are in parallel, the total moment applied to the base plate by the springs can be found by summing the couple moments. This summation is presented in Equation A.13.

$$M_T = \sum M_c = ks^2\left(\frac{n_{spr}-1}{2}\right)^2\gamma + \sum_{i=1}^{\frac{n_{spr}-1}{2}-1} 2ks^2i^2\gamma \tag{A.13}$$

The rotational stiffness k_s can then be found by dividing the total moment through by γ, as expressed in Equation A.14.

$$k_s = ks^2\left(\frac{n_{spr}-1}{2}\right)^2 + \sum_{i=1}^{\frac{n_{spr}-1}{2}-1} 2ks^2i^2 \tag{A.14}$$

Though Equation A.14 is theoretically accurate in calculating the rotational stiffness provided by the concrete surrounding the base plate, its use is unwieldy for the purpose of spreadsheet calculations. Thus, a simplified, equivalent polynomial form of it is given in Equation A.25. Inputting equal values of k, s, and n_{spr} into both equations will yield the same rotational stiffness k_s. The two equations can be proven to be equal through mathematical induction. This method is particularly helpful in the case of proving the equality of two equations where one equation is a summation and the other is a polynomial. Such a case is present in Equations A.14 and A.25. For reference, these equations are rewritten below in Equations A.15 and A.16.

$$\beta = ks^2\left(\frac{n_{spr}-1}{2}\right)^2 + \sum_{i=1}^{\frac{n_{spr}-1}{2}-1} 2ks^2i^2 \tag{A.15}$$

$$\beta = \frac{ks^2}{12}(n_{spr}^3 - 3n_{spr}^2 + 5n_{spr} - 3) \tag{A.16}$$

For ease in calculations, the expression $\frac{n_{spr}-1}{2}-1$ is replaced with u, as expressed in Equations A.17 and A.18. The updated and simplified versions of the original equations are included in Equations A.19 and A.20.

$$u = \frac{n_{spr}-1}{2} - 1 \tag{A.17}$$

$$n_{spr} = 2u + 3 \tag{A.18}$$

$$\beta(u) = ks^2(u+1)^2 + \sum_{i=1}^{u} 2ks^2i^2 \tag{A.19}$$

$$\beta(u) = \frac{ks^2}{12}[(2u+3)^3 - 3(2u+3)^2 + 5(2u+3) - 3] = \frac{ks^2}{12}(8u^3 + 24u^2 + 28u + 12) \tag{A.20}$$

To prove that these equations are equal by induction, it must first be shown that the relationship is true in the base case. In other words, $\beta(1)$ must be shown to be the same for both equations. The calculations for the summation are included in Equation A.21, and those for the polynomial are given in Equation A.22.

$$\beta(1) = ks^2(1+1)^2 + \sum_{i=1}^{1} 2ks^2i^2 = 4ks^2 + 2ks^2 = 6ks^2 \tag{A.21}$$

$$\beta(1) = \frac{ks^2}{12}(8(1)^3 + 24(1)^2 + 28(1) + 12) = \frac{ks^2}{12}(72) = 6ks^2 \tag{A.22}$$

By observation of these two equations, both produce the same result, $6ks^2$, for $\beta(1)$. Thus, the base case is true.

The second and final step, or the inductive step, is to prove that for any arbitrary integer v, if $\beta(v)$ is true, then $\beta(v+1)$ is also true. Expressions for $\beta(v)$ and $\beta(v+1)$ are included in Equations A.23 and A.24. Following the equations is the inductive proof.

$$\beta(v) = ks^2(v+1)^2 + \sum_{i=1}^{v} 2ks^2i^2 = \frac{ks^2}{12}(8v^3 + 24v^2 + 28v + 12) \tag{A.23}$$

$$\beta(v+1) = ks^2(v+2)^2 + \sum_{i=1}^{v+1} 2ks^2i^2 = \frac{ks^2}{12}(8v^3 + 48v^2 + 100v + 72) \tag{A.24}$$

$$\beta(v) = ks^2(v+1)^2 + \sum_{i=1}^{v} 2ks^2i^2 = \frac{ks^2}{12}(8v^3+24v^2+28v+12)$$

$$\begin{aligned}
\beta(v+1) = \beta(v+1) &= ks^2(v+2)^2 + 2ks^2(v+1)^2 + \sum_{i=1}^{v} 2ks^2i^2 \\
&= \frac{ks^2}{12}(8v^3+24v^2+28v+12) + 2ks^2(v+1)^2 - ks^2(v+1)^2 + ks^2(v+2)^2 \\
&= \frac{ks^2}{12}(8v^3+24v^2+28v+12) + ks^2(v+1)^2 + ks^2(v+2) \\
&= \frac{ks^2}{12}[8v^3+24v^2+28v+12+12((v+1)^2+(v+2)^2)] \\
&= \frac{ks^2}{12}[8v^3+24v^2+28v+12+12((v^2+2v+1)+(v^2+4v+4))] \\
&= \frac{ks^2}{12}[8v^3+24v^2+28v+12+(24v^2+72v+60)] \\
&= \frac{ks^2}{12}(8v^3+48v^2+100v+72)
\end{aligned}$$

$$\beta(v+1) = ks^2(v+2)^2 + \sum_{i=1}^{v+1} 2ks^2i^2 = \frac{ks^2}{12}(8v^3+48v^2+100v+72)$$

By induction, Equations A.14 and A.25 are equal to one another.

$$k_s = \frac{ks^2}{12}(n_{spr}^3 - 3n_{spr}^2 + 5n_{spr} - 3) \tag{A.25}$$

In its present form, the equation assumes that the properties of the base plate are the same as those of the column. Included in these properties are the moment of inertia, the concrete modulus of elasticity, and the resisting length of concrete. However, the base plate and the column have very different properties. As such, several adjustment factors must be included to transfer the base plate properties into the equation.

Most of the specimens tested by Barnwell used lower strength concrete for the block-out than for the slab. According to current conventions, the modulus of elasticity of concrete is an empirical function of its compressive strength. This equation is reiterated in Equation A.26 [32].

$$E = 57000\sqrt{f'_c} \tag{A.26}$$

In Equation A.26, f_c' is the concrete compressive strength in psi. As discussed previously in Section 3.1.6, when the base plate rotates, half of it pushes down into the underlying footing while the other half pushes up into the block-out concrete. As such, the modulus of elasticity that should be used for the base plate is the average of that of the column and that of the base plate. In contrast, the column pushes only into block-out concrete. To properly adjust for this discrepancy, the rotational stiffness k_s should be multiplied by the ratio of the average of the moduli of elasticity of the differing types of concrete to the modulus of elasticity of the block-out concrete. This ratio is expressed and simplified in Equation A.27. It should be noted that inputting equal moduli of elasticity into Equation A.27, indicating the block-out and slab concretes have equal strength, will result in a value of 1.

$$\frac{\left(\frac{E_{blockout}+E_{footing}}{2}\right)}{E_{blockout}} = \frac{1}{2}\left(\frac{E_{footing}}{E_{blockout}}+1\right) \tag{A.27}$$

Another property that differs from the column to the base plate is moment of inertia. Figure A.6 outlines the cross sections of the column and the base plate. By observation, the moment of inertia of the column is significantly larger than that of the base plate in both the strong and weak axis orientations. However, the base plate is significantly stiffened at locations where it is attached to the column. For this reason, it is suggested that the stiffness contribution of the base plate outside the dashed rectangular region at the base of the column outlined in Figure A.6 be neglected. This idea was introduced in Section 2.1.1 by Thambiratnam and Paramasivam [7]. As such, the depth and flange width of the column should be used in determining the number of base plate springs rather than the dimensions of the base plate itself. Though this does not require the introduction of an adjustment factor into Equation A.25, it does affect the values input into it.

Yet another property that varies from the column to the base plate is the width of resisting surfaces. To appropriately transfer the stiffness of the column to the base plate, the rotational stiffness must simply be divided by the same width adjustment factor applied to the stiffness originally. Doing so removes the effects of potential flange duality for a column oriented about its strong axis. These length adjustment factors may be recalled from Equations A.2 and A.4. As previously discussed, the stiffness contribution of the base plate material extending outside the

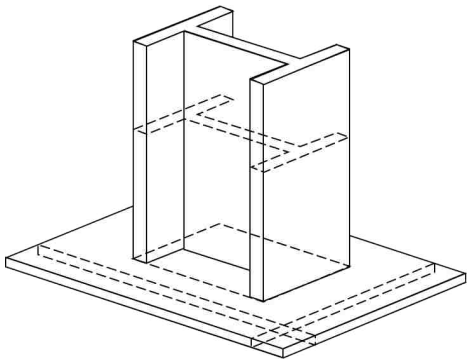

Figure A.6: Base Plate and Column Cross Sections

column is assumed to be negligible. Thus, the widths of resisting concrete that should be used for the base plate are equal to b_f and d for strong and weak axis orientations, respectively, as illustrated in Figure A.6. It follows that ϕ_w be equal to the ratio of these surface widths. With these adjustment factors, Equation A.25 can be appropriately adjusted to represent the stiffness of the base plate. These modifications are accounted for in Equation A.28.

$$k_s = \frac{ks^2}{24\phi_w}(n_{spr}^3 - 3n_{spr}^2 + 5n_{spr} - 3)\left(\frac{E_{slab}}{E_{blockout}} + 1\right) \tag{A.28}$$

A.1.4 Stiffness Matrix Assembly

Using the stiffness method, the embedded column can be represented by a number of beam elements bounded by the linear springs. For example, the column shown in Figure A.2 would be represented by six beam elements, as shown in Figure A.7. When broken into beam elements, the intermediate springs are also effectively split into two, providing half of their stiffness to each element.

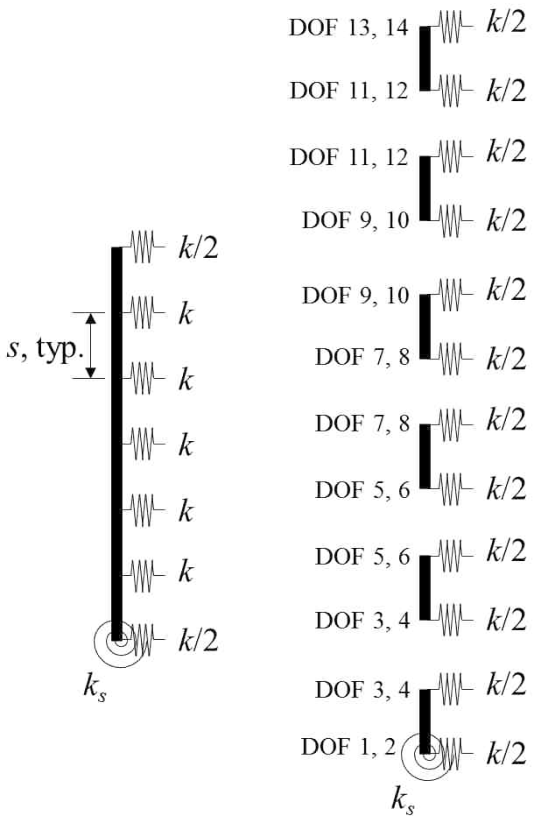

Figure A.7: Stiffness Method Model, Divided into Beam Elements

Each beam element is assumed to be fixed at each end. Thus, two degrees of freedom (DOF's) are located at each end of each beam element: one for horizontal translation, and another for rotation. As such, the number of DOF's, or n_{DOF}, for the embedded structure is twice the number of springs, as expressed in Equation A.29. Thus, in Figure A.7, n_{DOF} is equal to 14.

$$n_{DOF} = 2n_{spr} \tag{A.29}$$

The stiffness matrix for each beam element is comprised of the forces per unit displacement caused by a unit displacement at each DOF. Figures A.8 and A.9 below show free body diagrams of a beam element undergoing unit translations and rotations at each DOF with the forces per unit displacement associated with such displacements. It should be noted that Figure A.9(a) and Figure A.9(b) are only different in the inclusion of k_s in the bottommost rotational DOF. When a unit rotation is applied to the bottom of the bottommost beam element in Figure A.7, the rotational spring contributes its stiffness to the rotational force per unit displacement. Since no rotational springs are present throughout the rest of the structure, k_s is not included in any other DOFs.

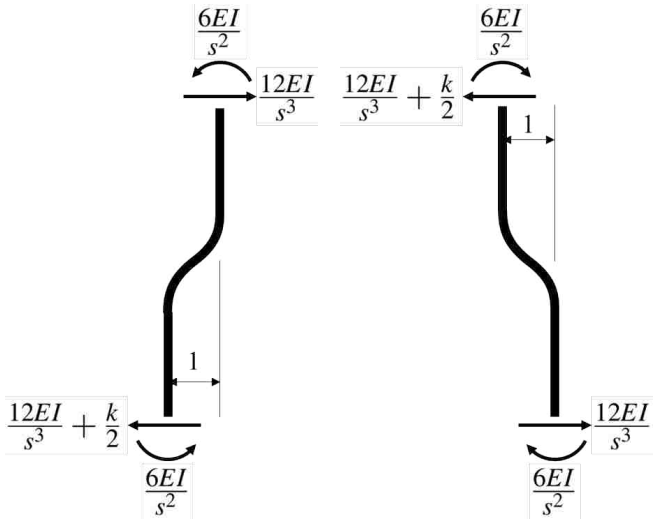

(a) Bottom (b) Top

Figure A.8: Free Body Diagrams of Unit Horizontal Translations at DOF's

The forces per unit displacement on the free body diagrams presented in Figures A.8 and A.9 can then be used to construct the element stiffness matrices. As noted in Figure A.7, the first DOF of each element is horizontal translation at the bottom, the second is rotation at the bottom, the third is horizontal translation at the top, and the last is rotation at the top. Thus, the first column of the stiffness matrix refers to the forces per unit displacement occurring at each DOF due to a unit displacement at the first DOF, and so on. The stiffness matrix for the bottommost beam element is

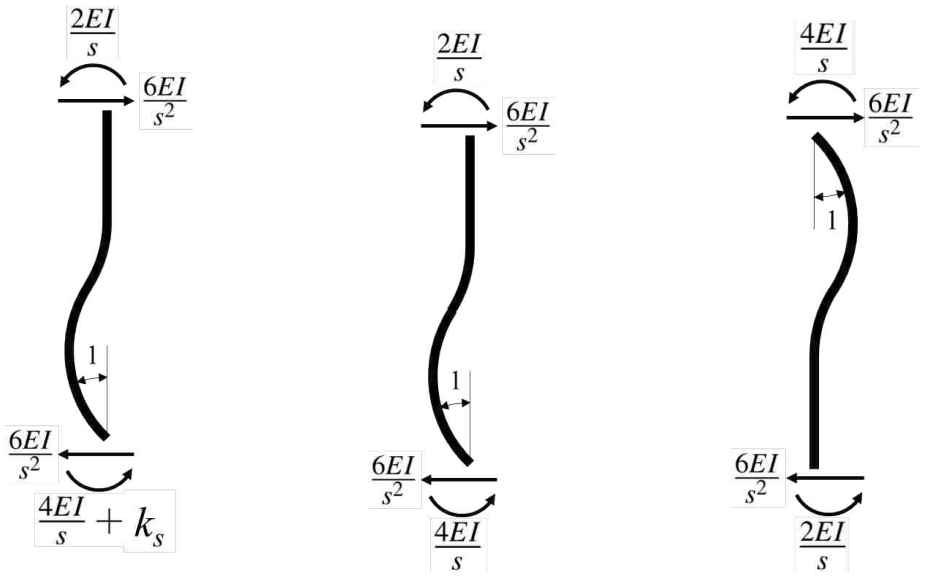

(a) Bottom, First Element

(b) Bottom, Other Elements

(c) Top

Figure A.9: Free Body Diagrams of Unit Rotations at DOF's

shown in Equation A.30, and the stiffness matrix of each of the other beam elements is shown in Equation A.31. It may be observed that the only difference between the two stiffness matrices is the inclusion of k_s in the second column and second row of the first matrix.

$$\begin{bmatrix} \frac{12EI}{s^3} + \frac{k}{2} & \frac{6EI}{s^2} & -\frac{12EI}{s^3} & \frac{6EI}{s^2} \\ \frac{6EI}{s^2} & \frac{4EI}{s} + k_s & -\frac{6EI}{s^2} & \frac{2EI}{s} \\ -\frac{12EI}{s^3} & -\frac{6EI}{s^2} & \frac{12EI}{s^3} + \frac{k}{2} & -\frac{6EI}{s^2} \\ \frac{6EI}{s^2} & \frac{2EI}{s} & -\frac{6EI}{s^2} & \frac{4EI}{s} \end{bmatrix} \tag{A.30}$$

$$\begin{bmatrix} \frac{12EI}{s^3} + \frac{k}{2} & \frac{6EI}{s^2} & -\frac{12EI}{s^3} & \frac{6EI}{s^2} \\ \frac{6EI}{s^2} & \frac{4EI}{s} & -\frac{6EI}{s^2} & \frac{2EI}{s} \\ -\frac{12EI}{s^3} & -\frac{6EI}{s^2} & \frac{12EI}{s^3} + \frac{k}{2} & -\frac{6EI}{s^2} \\ \frac{6EI}{s^2} & \frac{2EI}{s} & -\frac{6EI}{s^2} & \frac{4EI}{s} \end{bmatrix} \tag{A.31}$$

The stiffness matrix for each beam element is a piece, or member, of the stiffness matrix representing the stiffness of the embedded connection. In this structure stiffness matrix, there are n_{DOF} rows and columns, with each row and column representing its corresponding DOF. The el-

ements from the member stiffness matrices can be transferred into their corresponding locations in the structure stiffness matrix. For elements that are doubly represented, such as those representing the intermediate springs, the values of the elements may simply be added together. For example, the force per unit displacement at DOF 3 due to a unit translation at DOF 3 is present in two separate member stiffness matrices. The corresponding element in the structure stiffness matrix is the third row, third column element, and its value is the sum of those two forces per unit displacement. This value is calculated in Equation A.32. The structure stiffness matrix for any embedded connection representable by this model is presented in Equation A.33.

$$\left(\frac{12EI}{s^3}+\frac{k}{2}\right)+\left(\frac{12EI}{s^3}+\frac{k}{2}\right)=\frac{24EI}{s^3}+k \tag{A.32}$$

A structure force vector accompanies the structure stiffness matrix, representing external loads at each DOF. The structure force vector has n_{DOF} elements and is shown in Equation A.34. Since the only external loads in the model are at the concrete interface, all elements in the force vector are zero except for the bottom two. These two elements are the shear force V and the bending moment M from Figure A.2.

$$\begin{bmatrix} 0 \\ \vdots \\ 0 \\ V \\ M \end{bmatrix} \tag{A.34}$$

As is typical when using the stiffness method, the displacement vector can be obtained by inverting the stiffness matrix and multiplying it by the force vector. The second to last element in the displacement vector is the horizontal displacement of the DOF at the interface, and the last element is the rotation of the DOF at the same location.

The rotation at the top of the column, θ, may be calculated by dividing the horizontal translation of the DOF at the concrete interface, u_{nDOF-1}, by the exposed column length, S, and then adding the rotation at the interface, u_{nDOF}. This calculation is given in Equation A.35. Figure

$$
\begin{bmatrix}
\frac{12EI}{s^3}+\frac{k}{2} & \frac{6EI}{s^2} & -\frac{12EI}{s^3} & \frac{6EI}{s^2} & 0 & \cdots & \cdots & \cdots & \cdots & 0 & 0 & 0 & 0 \\
\frac{6EI}{s^2} & \frac{4EI}{s}+k_s & -\frac{6EI}{s^2} & \frac{2EI}{s} & 0 & \cdots & \cdots & \cdots & \cdots & 0 & 0 & 0 & 0 \\
-\frac{12EI}{s^3} & -\frac{6EI}{s^2} & \frac{24EI}{s^3}+k & 0 & -\frac{12EI}{s^3} & \frac{6EI}{s^2} & 0 & \cdots & \cdots & 0 & 0 & 0 & 0 \\
\frac{6EI}{s^2} & \frac{2EI}{s} & 0 & \frac{8EI}{s} & -\frac{6EI}{s^2} & \frac{2EI}{s} & 0 & \cdots & \cdots & 0 & 0 & 0 & 0 \\
0 & 0 & -\frac{12EI}{s^3} & -\frac{6EI}{s^2} & \frac{24EI}{s^3}+k & 0 & \ddots & & & \vdots & \vdots & \vdots & \vdots \\
\vdots & \vdots & \frac{6EI}{s^3} & \frac{2EI}{s} & 0 & \frac{8EI}{s} & & \ddots & & \vdots & \vdots & \vdots & \vdots \\
\vdots & \vdots & 0 & 0 & \ddots & & \ddots & & \ddots & 0 & 0 & \vdots & \vdots \\
\vdots & \vdots & \vdots & \vdots & & \ddots & & \ddots & & -\frac{12EI}{s^3} & \frac{6EI}{s^2} & \vdots & \vdots \\
\vdots & \vdots & \vdots & \vdots & & & \ddots & & \ddots & -\frac{6EI}{s^2} & \frac{2EI}{s} & 0 & 0 \\
0 & 0 & 0 & 0 & \cdots & \cdots & 0 & -\frac{12EI}{s^3} & -\frac{6EI}{s^2} & \frac{24EI}{s^2}+k & 0 & -\frac{12EI}{s^3} & \frac{6EI}{s^2} \\
0 & 0 & 0 & 0 & \cdots & \cdots & 0 & \frac{6EI}{s^2} & \frac{2EI}{s} & 0 & \frac{8EI}{s} & -\frac{6EI}{s^2} & \frac{2EI}{s} \\
0 & 0 & 0 & 0 & \cdots & \cdots & \cdots & \cdots & 0 & -\frac{12EI}{s^3} & -\frac{6EI}{s^2} & \frac{12EI}{s^3}+\frac{k}{2} & -\frac{6EI}{s^2} \\
0 & 0 & 0 & 0 & \cdots & \cdots & \cdots & \cdots & 0 & \frac{6EI}{s^2} & \frac{2EI}{s} & -\frac{6EI}{s^2} & \frac{4EI}{s}
\end{bmatrix}
\tag{A.33}
$$

A.10 depicts the same calculation. The rotational stiffness β can then be calculated by dividing the applied moment M by the rotation, as expressed in Equation A.36.

$$\theta = \frac{u_{nDOF-1}}{S} + u_{nDOF} \tag{A.35}$$

$$\beta = \frac{M}{\theta} \tag{A.36}$$

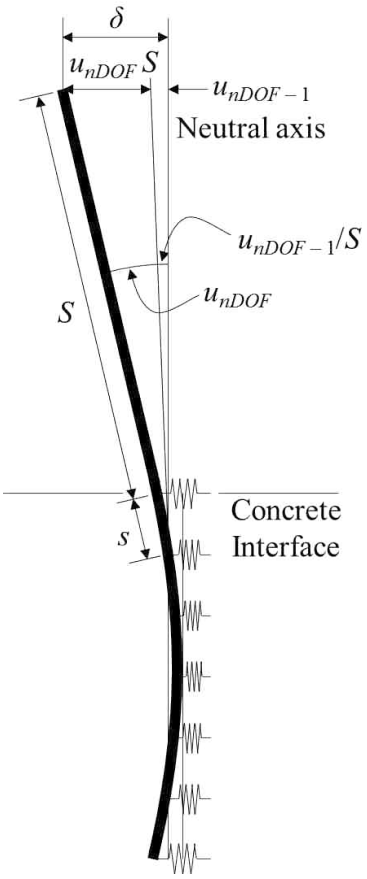

Figure A.10: Detail of Column Displacement and Rotation

It should be noted that this calculation neglects any flexural deformation in the exposed portion of the column. So doing allows the calculation of only the deflection associated with the block-out deformation.

A.2 Calibrated Values for Modulus of Subgrade Reaction (Barnwell)

By comparing the values calibrated for the modulus of subgrade reaction of concrete, k_0, from Barnwell's experimental data from both the continuum and stiffness method models, perspective on the computational similarities can be obtained. These values are documented in Table A.1.

Table A.1: Modulus of Subgrade Reaction Values Calibrated Using Continuous and Stiffness Method Models to Barnwell's Data

Specimen	Embedment Length	Modulus of Subgrade Reaction [kip/in^3]	
		Continuous Model	Stiffness Method Model
A1	6	364	462
A2	6	375	520
CA2	6	325	454
B1	14	353	341
B2	14	525	508
B3	14	445	432
CB2	14	534	517

A few observations are worth noting. It should be observed that though the two models do not produce identical values of k_0, the values attained are very close to each other. With the exception of specimen A3, all k_0 values fell within the range of 300 to 600 kips/in^3. As such, a k_0 value of 300 kips/in^3 can be conservatively used to estimate the stiffness of these specimens. Furthermore, the continuum model calibrated k_0 values lower than the stiffness method model for shallower embedment lengths, but comparatively higher k_0 values for deeper embedment lengths. The reason for this discrepancy is unknown. Finally, the k_0 values calibrated to specimen A3 are extremely high compared to those of the other specimens. This is due to an actuator control error at the beginning of the test that caused the column to be displaced much further than was intended at that point. As such, there were very few usable data points for calculating the stiffness, and both the continuum and stiffness method models vastly overestimate the subgrade modulus required to produce the specified displacement.

APPENDIX B. NORMALIZED ROTATIONAL-STIFFNESS VS. EMBEDMENT CURVES FOR WIDE-FLANGE COLUMN FAMILIES

B.1 Strong Axis Curves

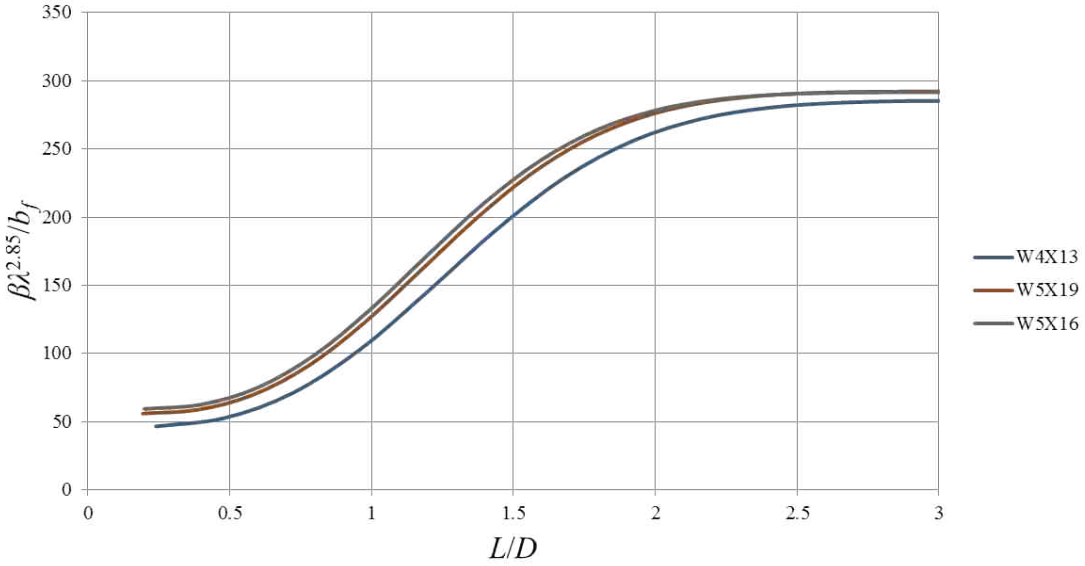

Figure B.1: W4 and W5 Strong Axis

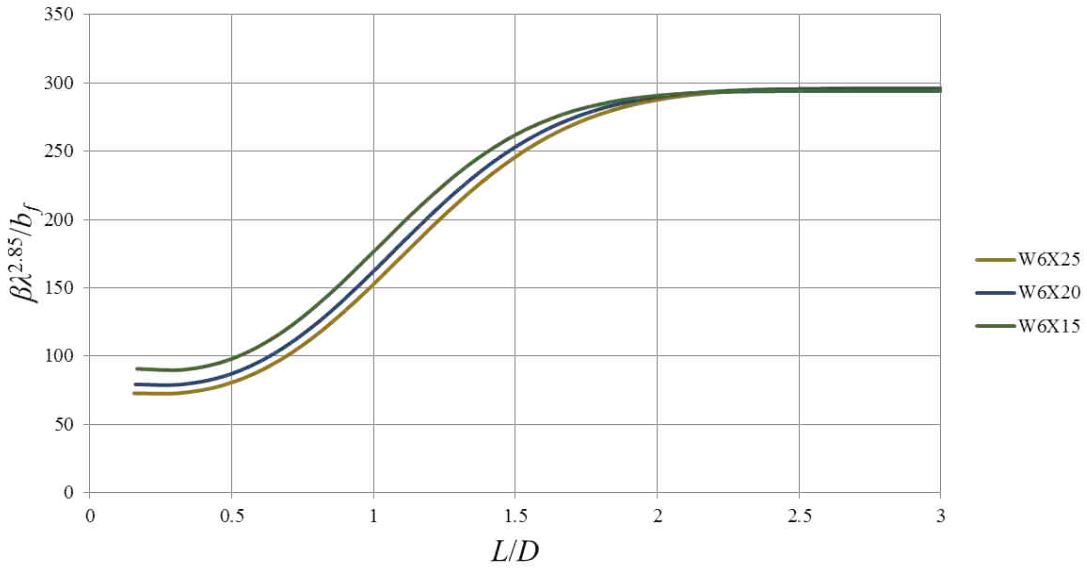

Figure B.2: W6 Strong Axis - Family 1

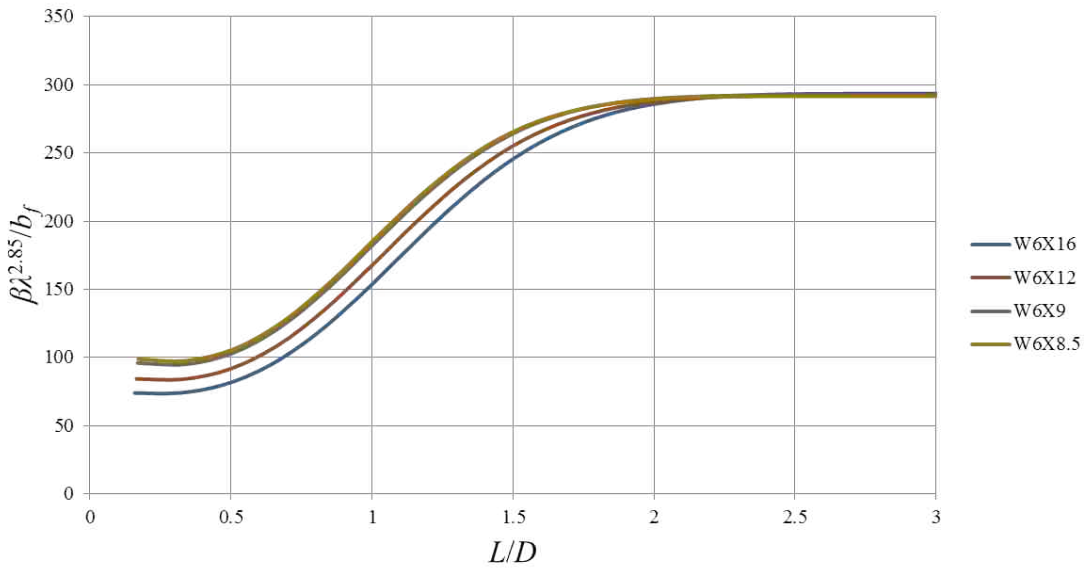

Figure B.3: W6 Strong Axis - Family 2

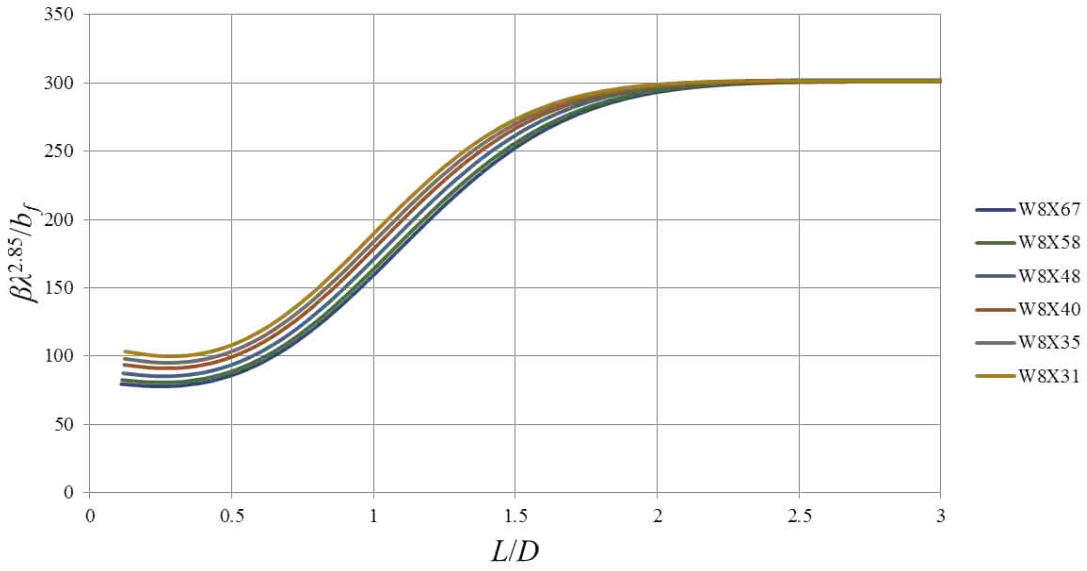

Figure B.4: W8 Strong Axis - Family 1

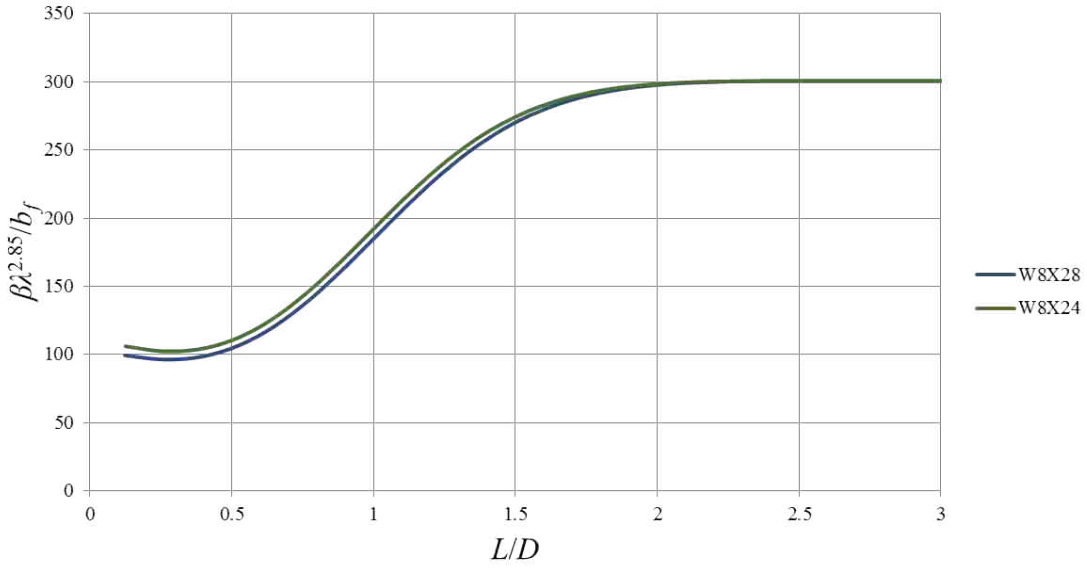

Figure B.5: W8 Strong Axis - Family 2

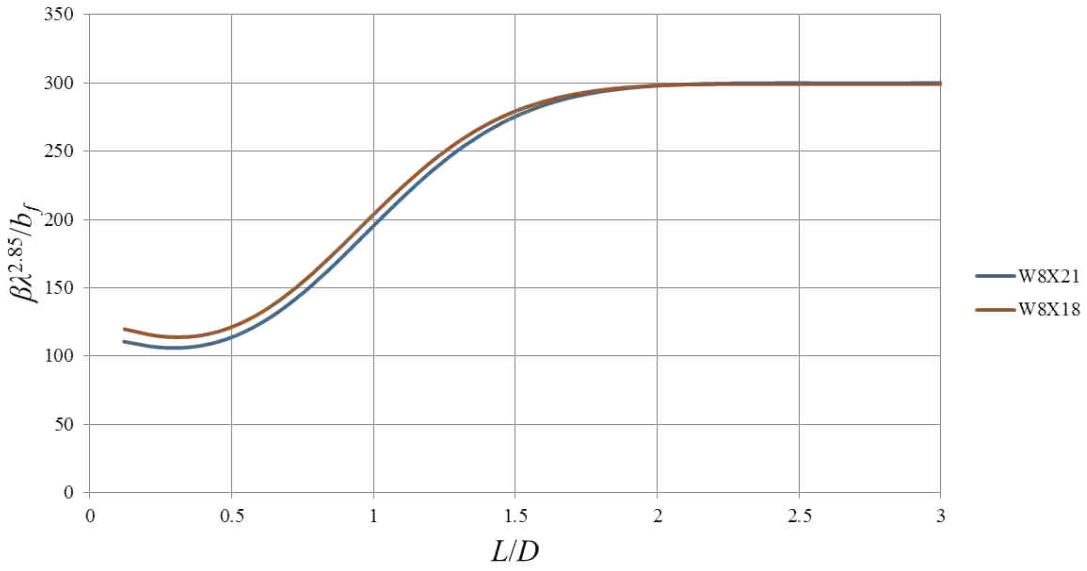

Figure B.6: W8 Strong Axis - Family 3

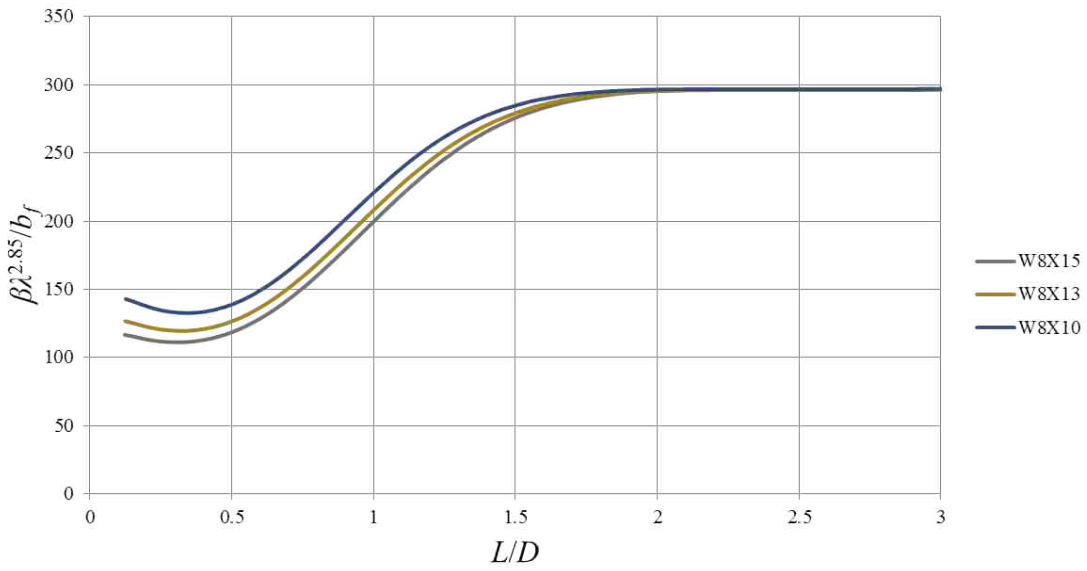

Figure B.7: W8 Strong Axis - Family 4

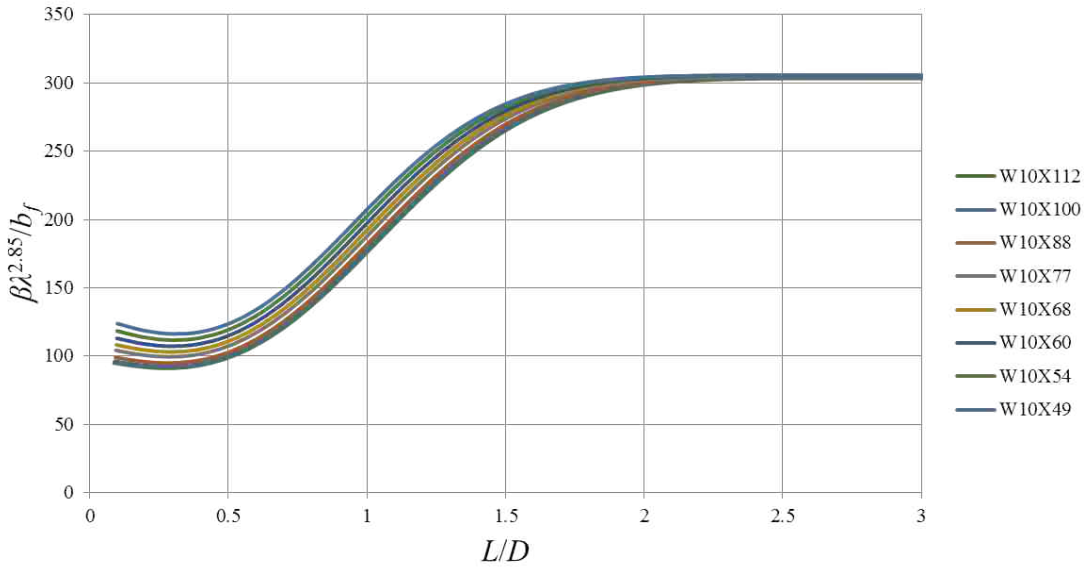

Figure B.8: W10 Strong Axis - Family 1

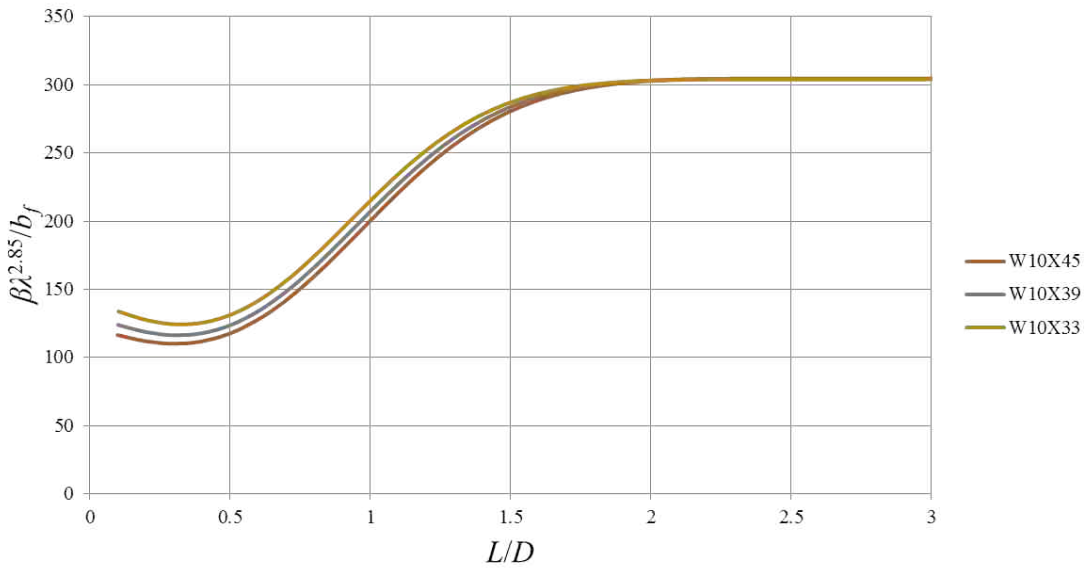

Figure B.9: W10 Strong Axis - Family 2

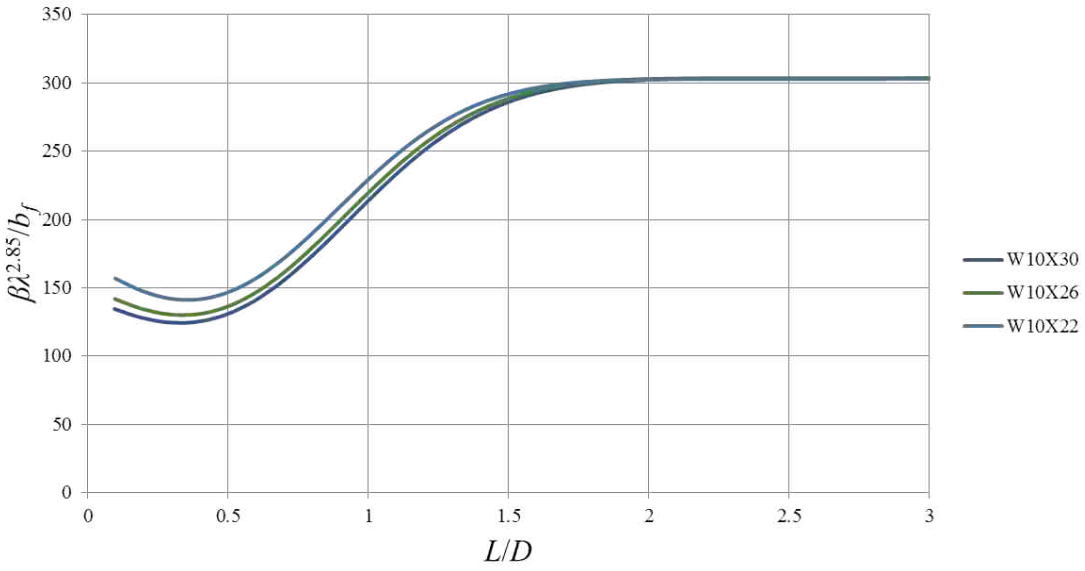

Figure B.10: W10 Strong Axis - Family 3

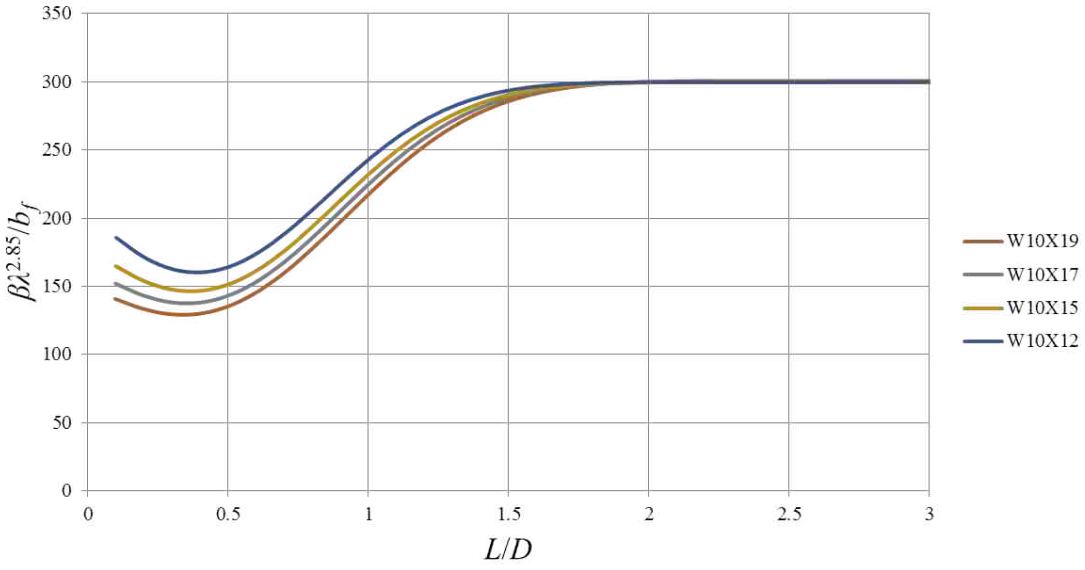

Figure B.11: W10 Strong Axis - Family 4

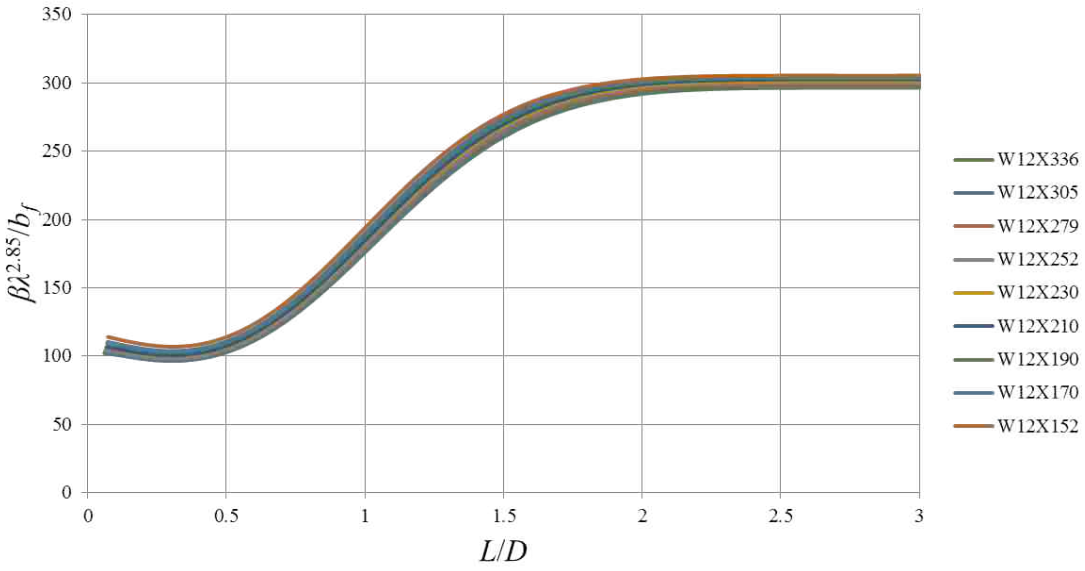

Figure B.12: W12 Strong Axis - Family 1

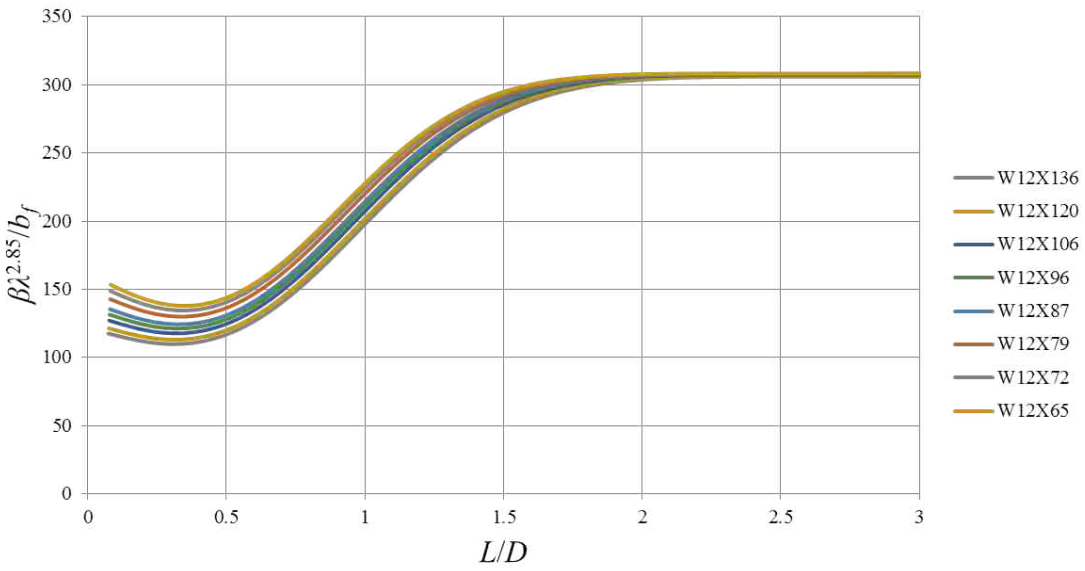

Figure B.13: W12 Strong Axis - Family 2

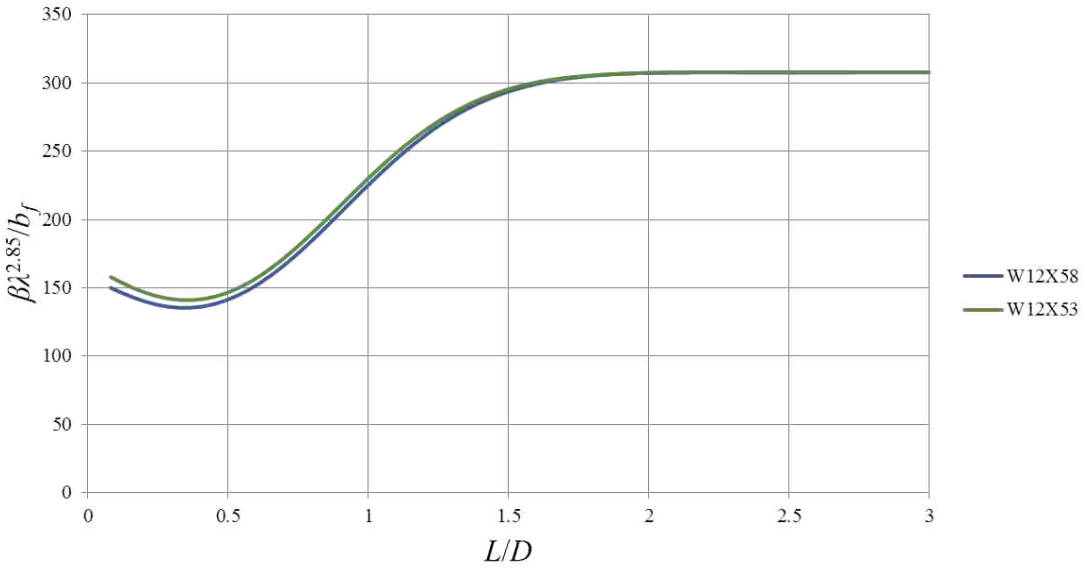

Figure B.14: W12 Strong Axis - Family 3

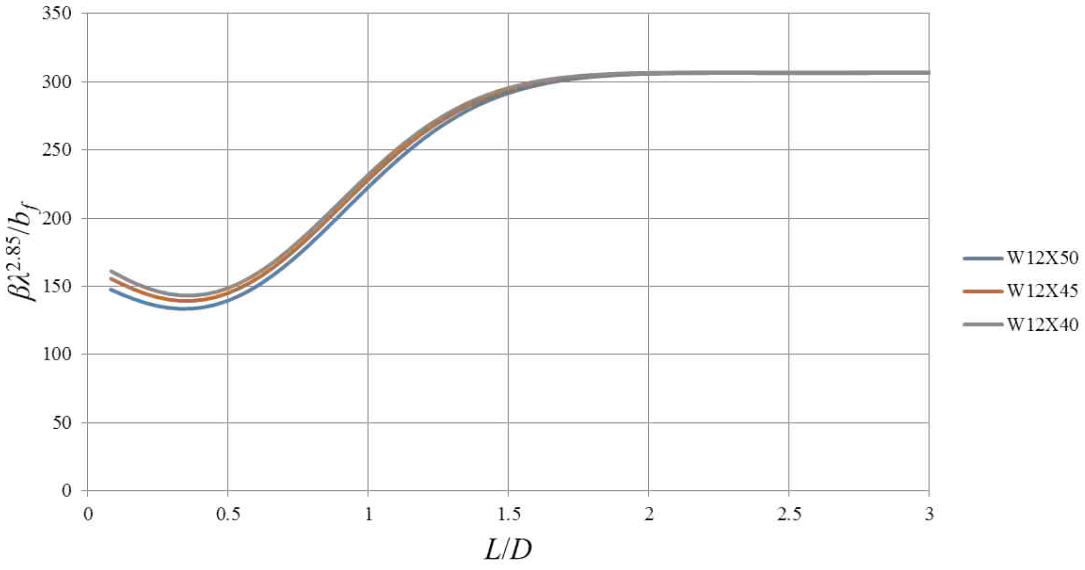

Figure B.15: W12 Strong Axis - Family 4

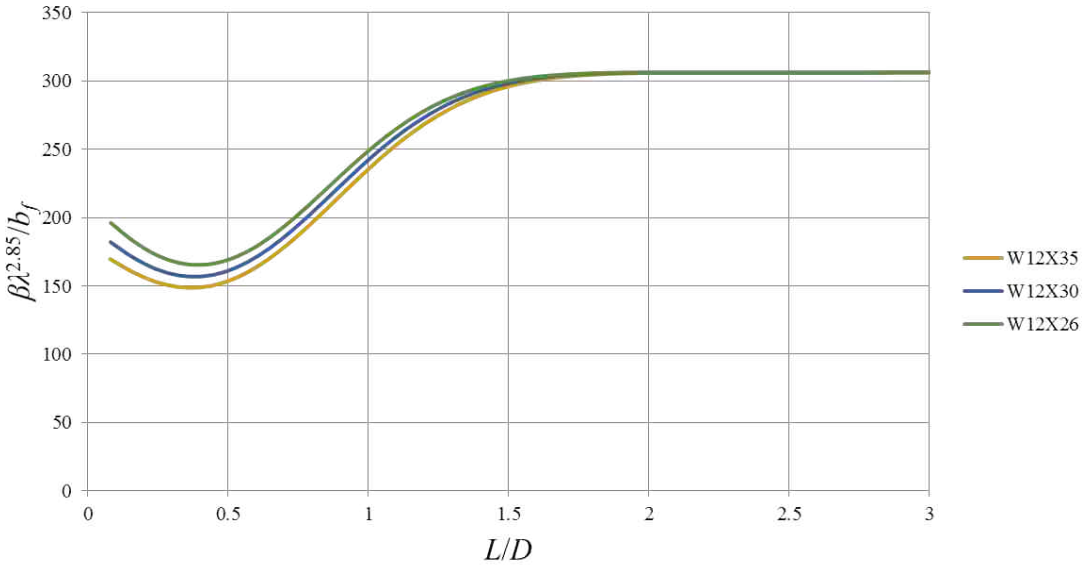

Figure B.16: W12 Strong Axis - Family 5

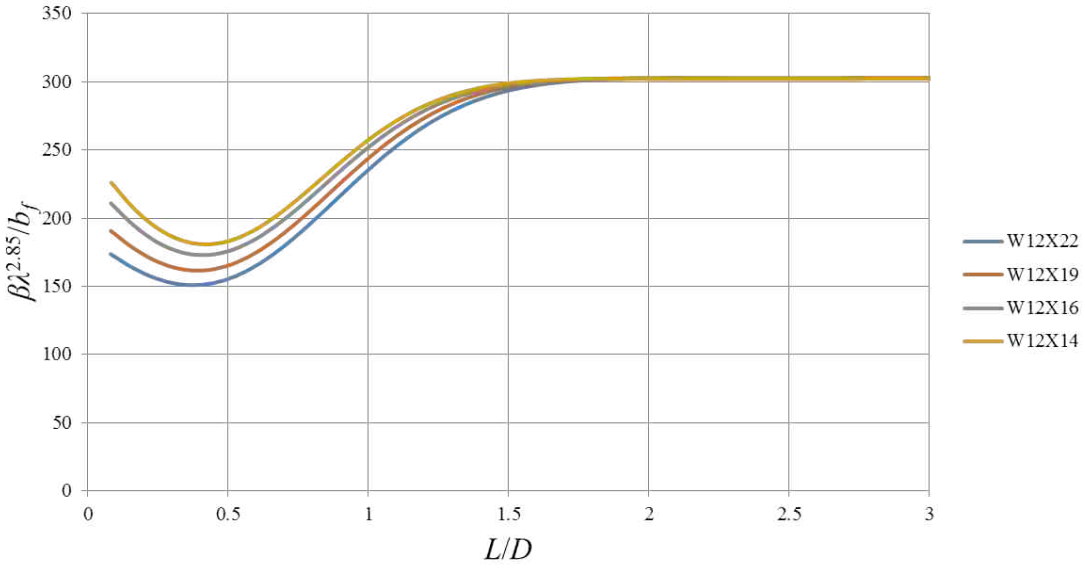

Figure B.17: W12 Strong Axis - Family 6

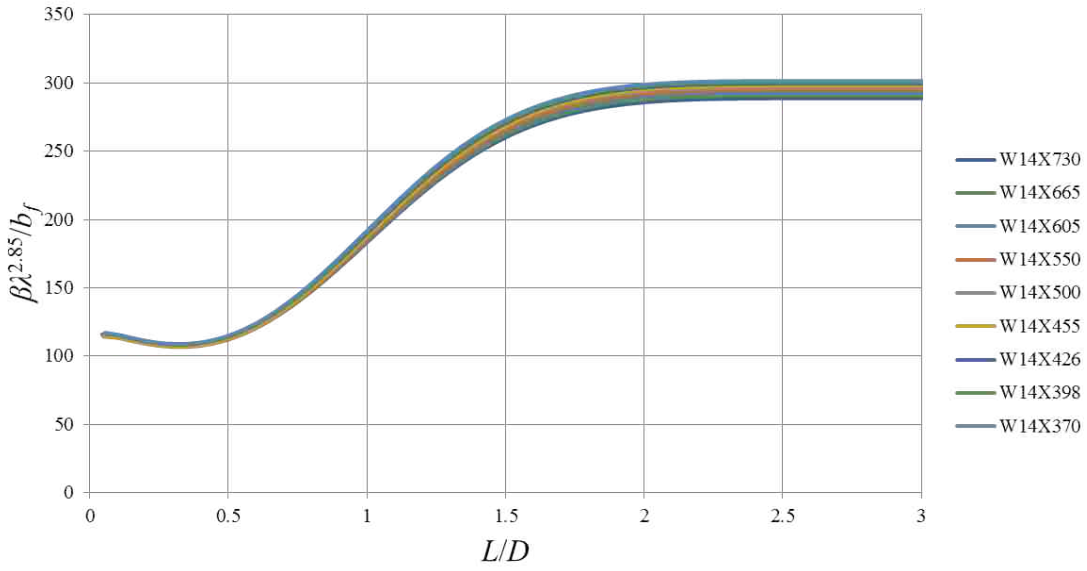

Figure B.18: W14 Strong Axis - Family 1

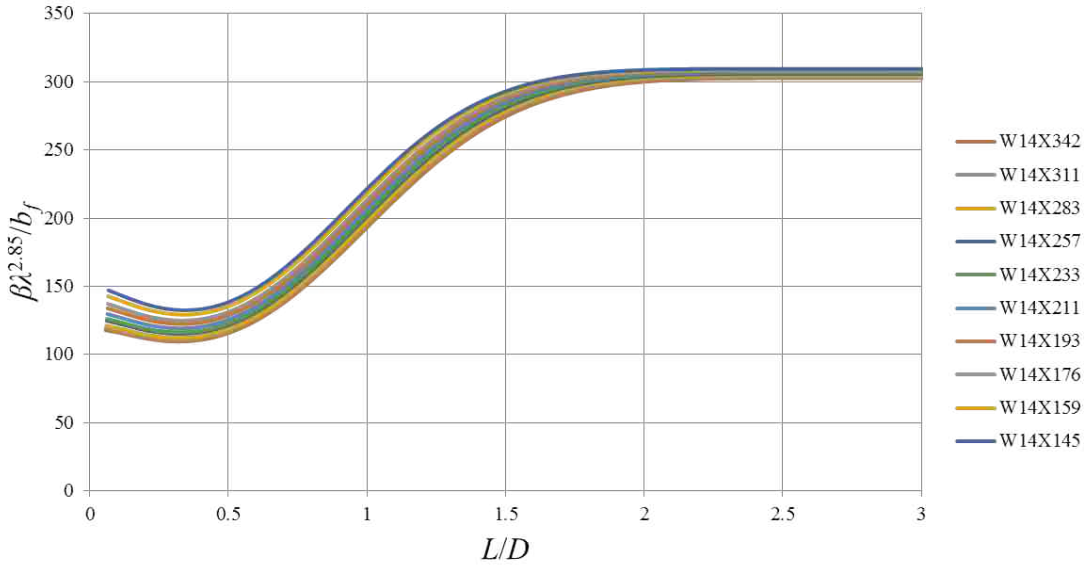

Figure B.19: W14 Strong Axis - Family 2

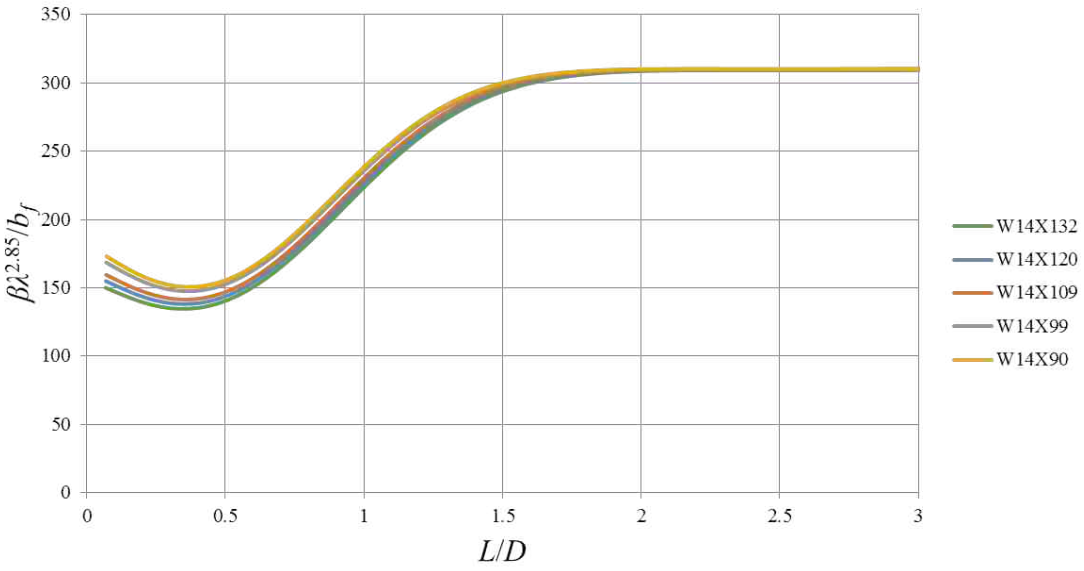

Figure B.20: W14 Strong Axis - Family 3

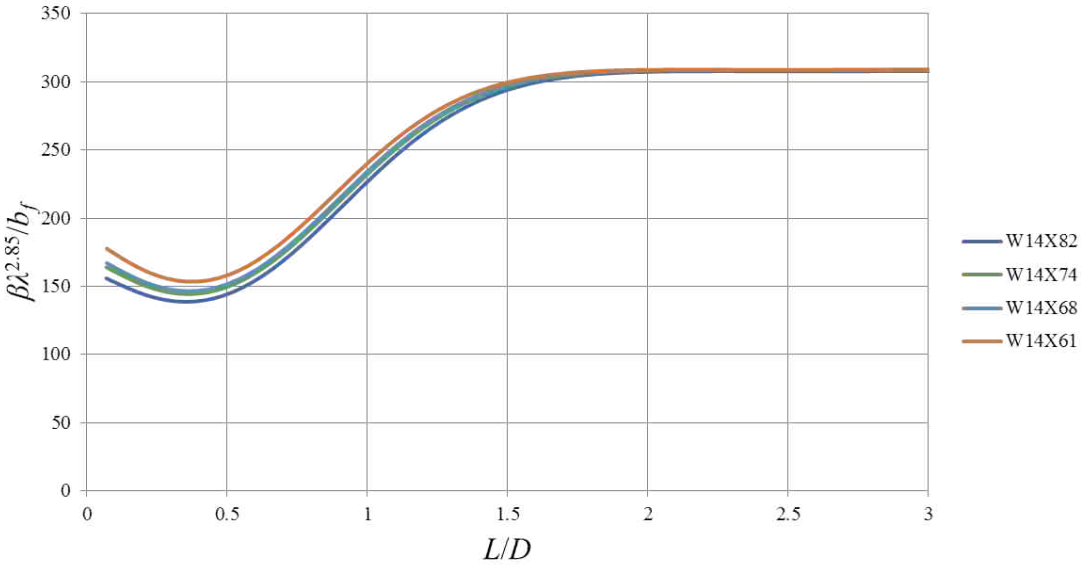

Figure B.21: W14 Strong Axis - Family 4

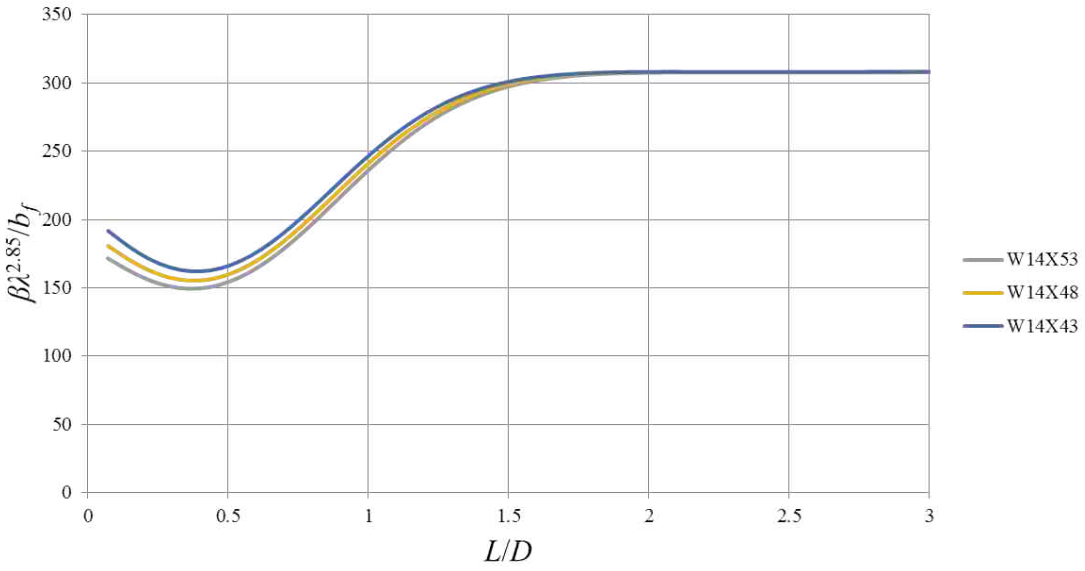

Figure B.22: W14 Strong Axis - Family 5

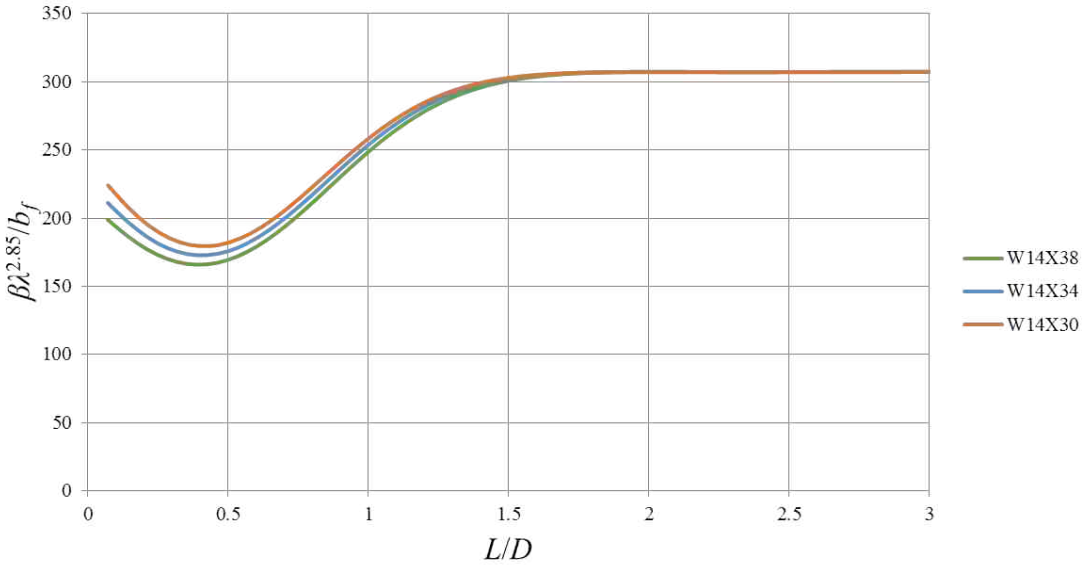

Figure B.23: W14 Strong Axis - Family 6

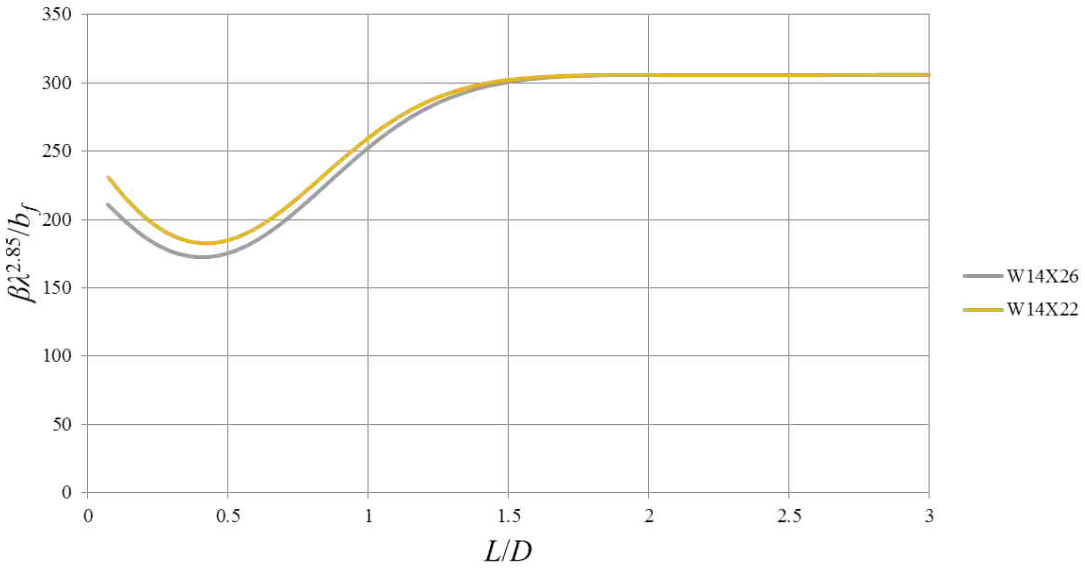

Figure B.24: W14 Strong Axis - Family 7

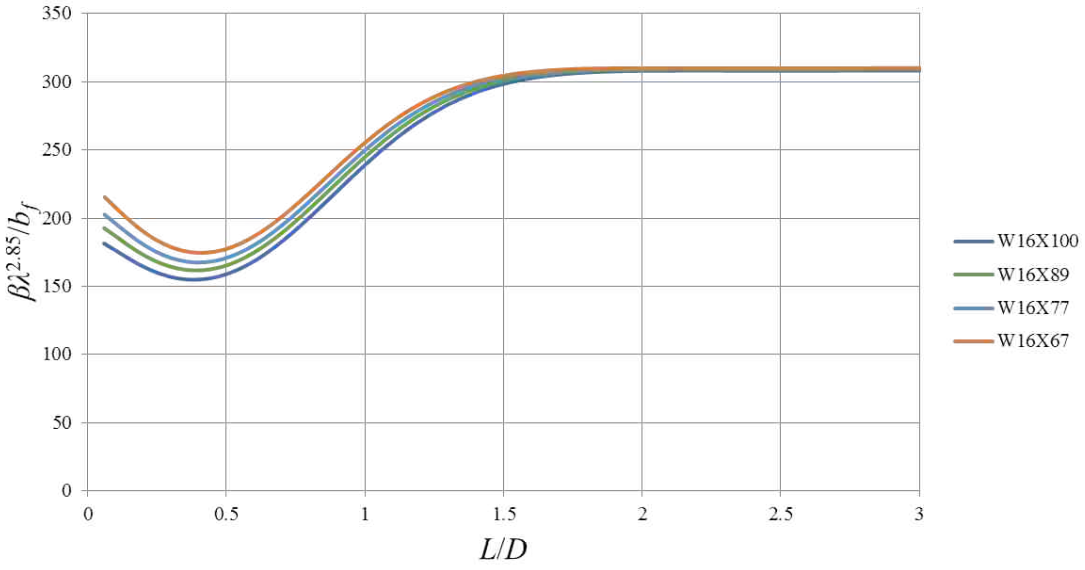

Figure B.25: W16 Strong Axis - Family 1

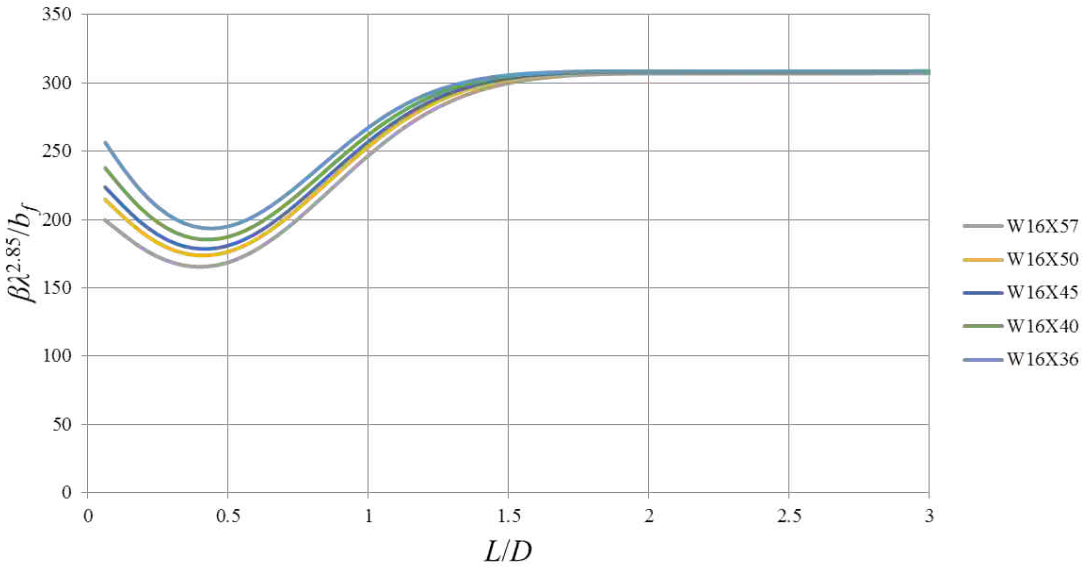

Figure B.26: W16 Strong Axis - Family 2

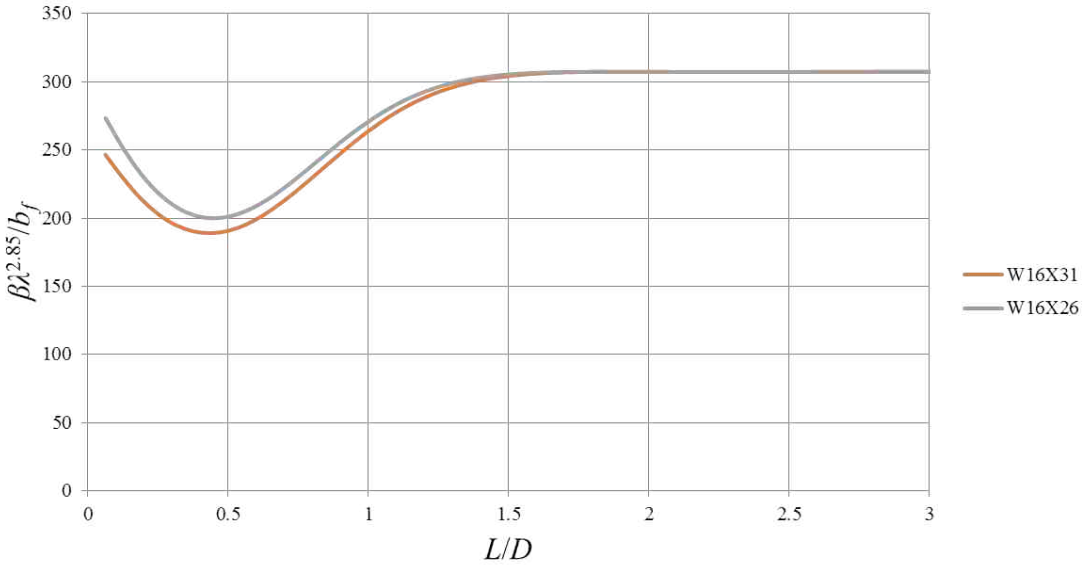

Figure B.27: W16 Strong Axis - Family 3

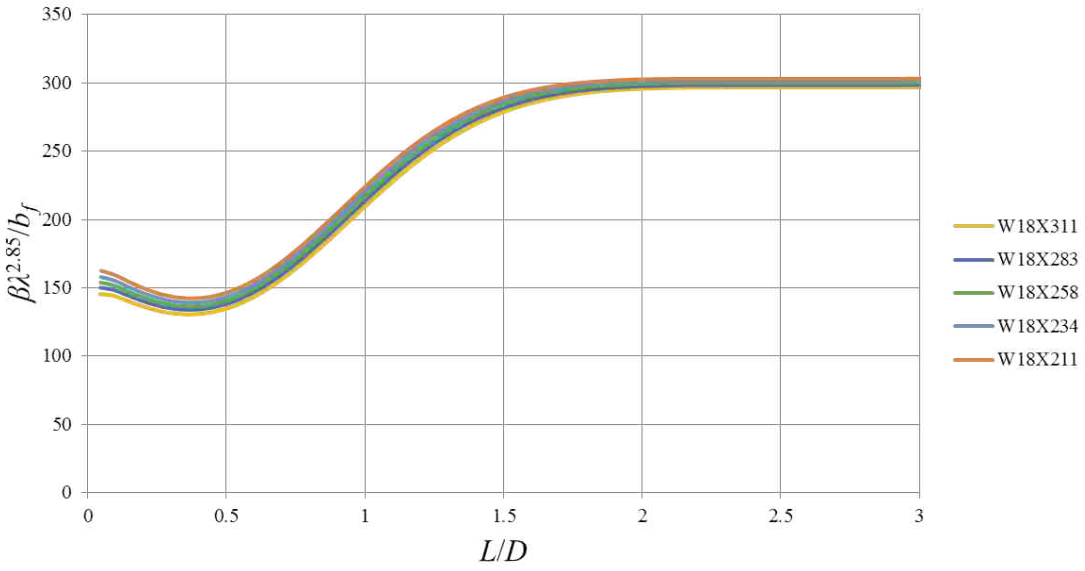

Figure B.28: W18 Strong Axis - Family 1

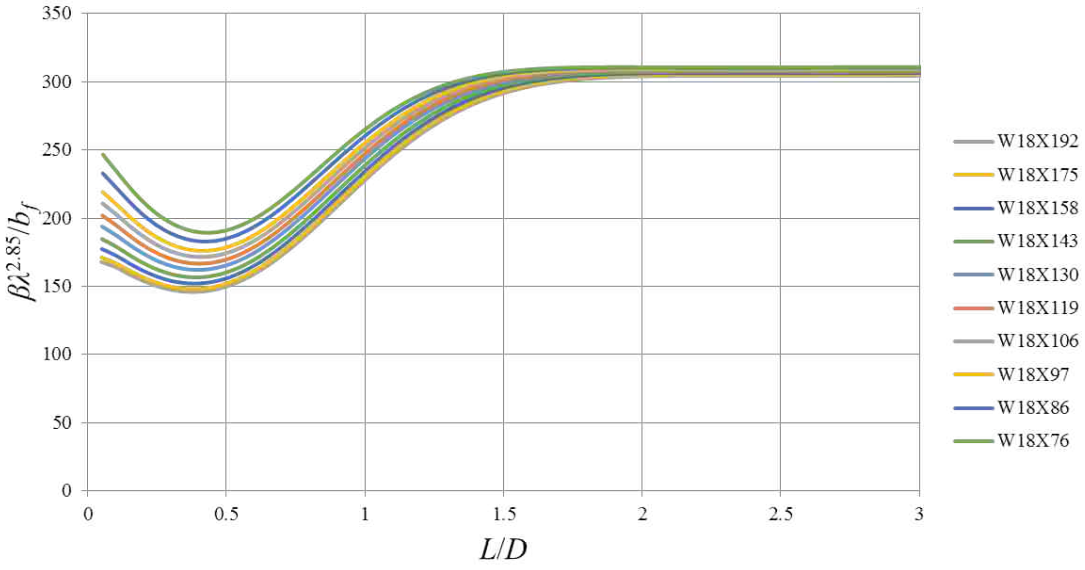

Figure B.29: W18 Strong Axis - Family 2

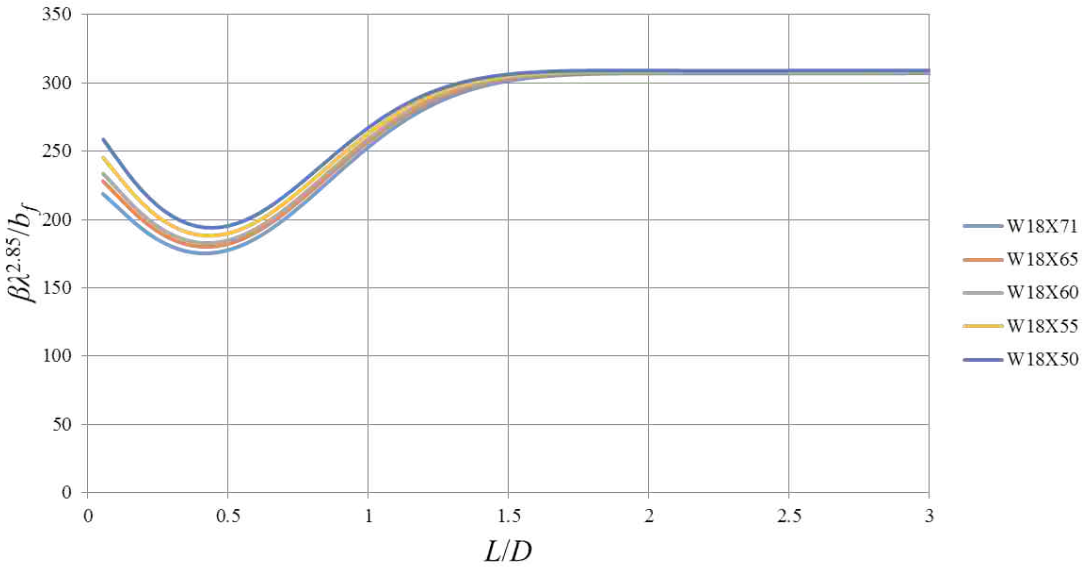

Figure B.30: W18 Strong Axis - Family 3

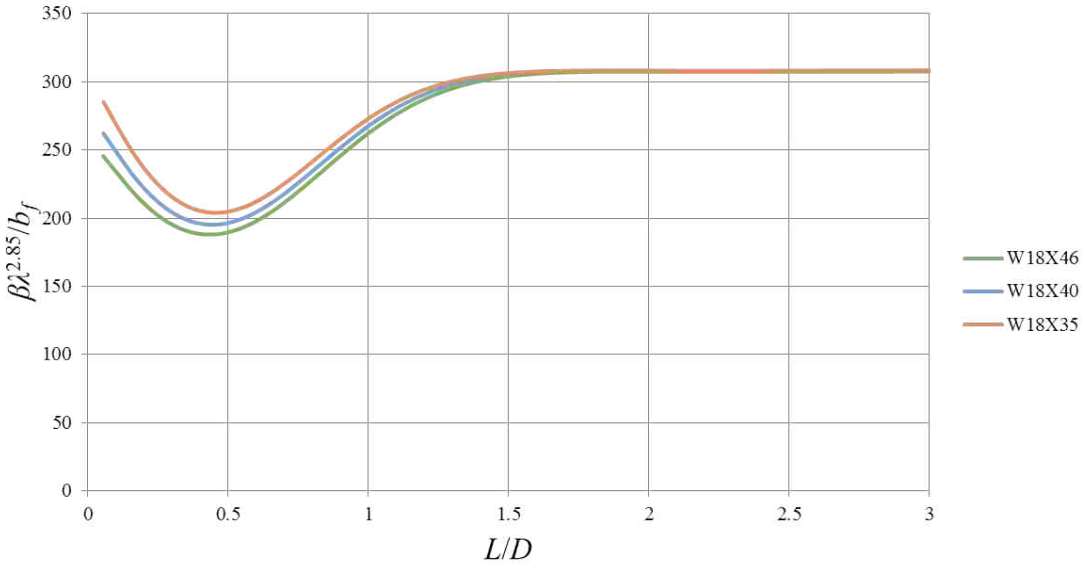

Figure B.31: W18 Strong Axis - Family 4

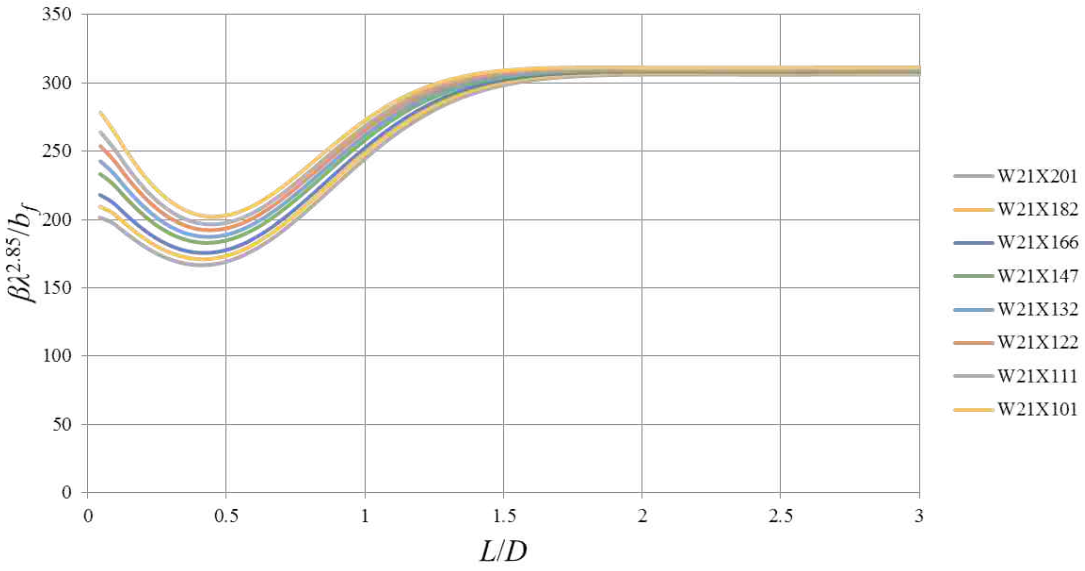

Figure B.32: W21 Strong Axis - Family 1

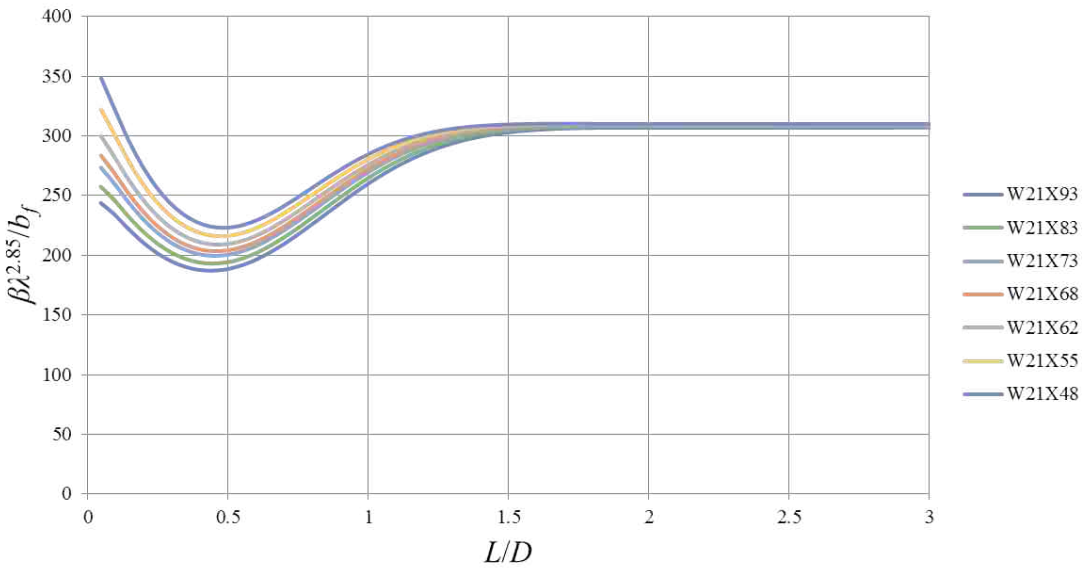

Figure B.33: W21 Strong Axis - Family 2

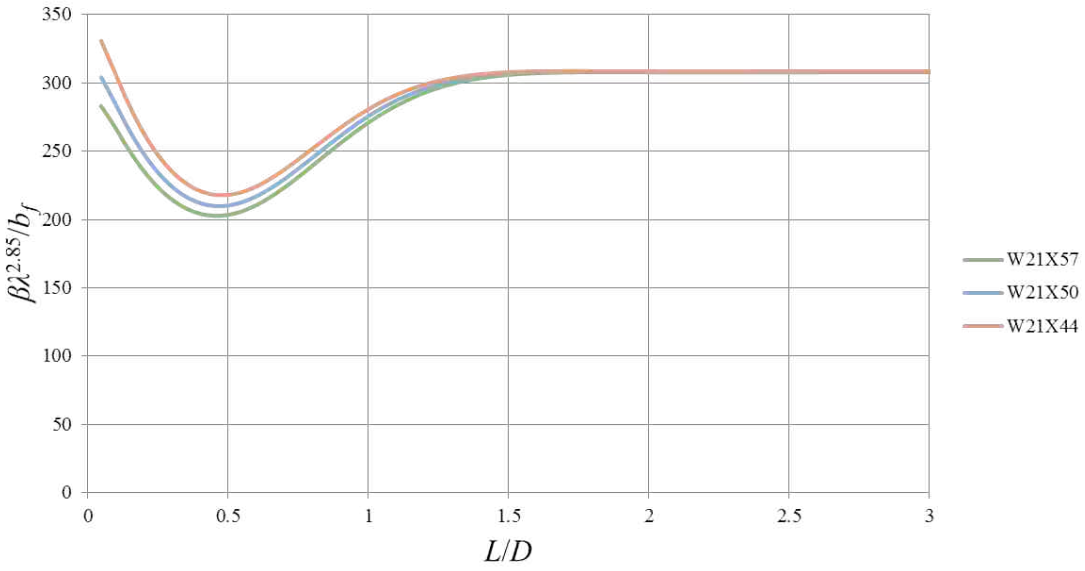

Figure B.34: W21 Strong Axis - Family 3

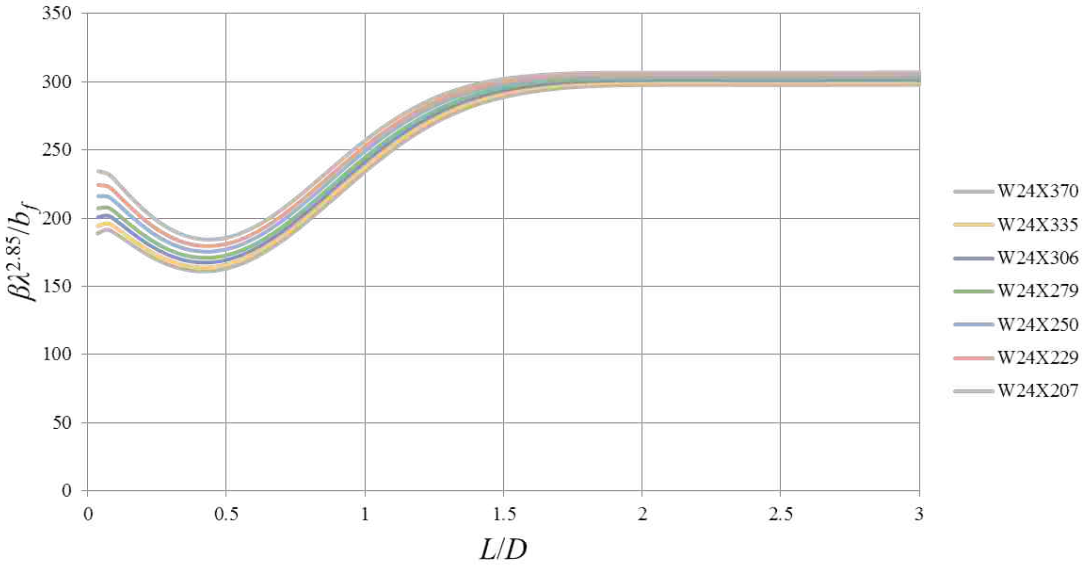

Figure B.35: W24 Strong Axis - Family 1

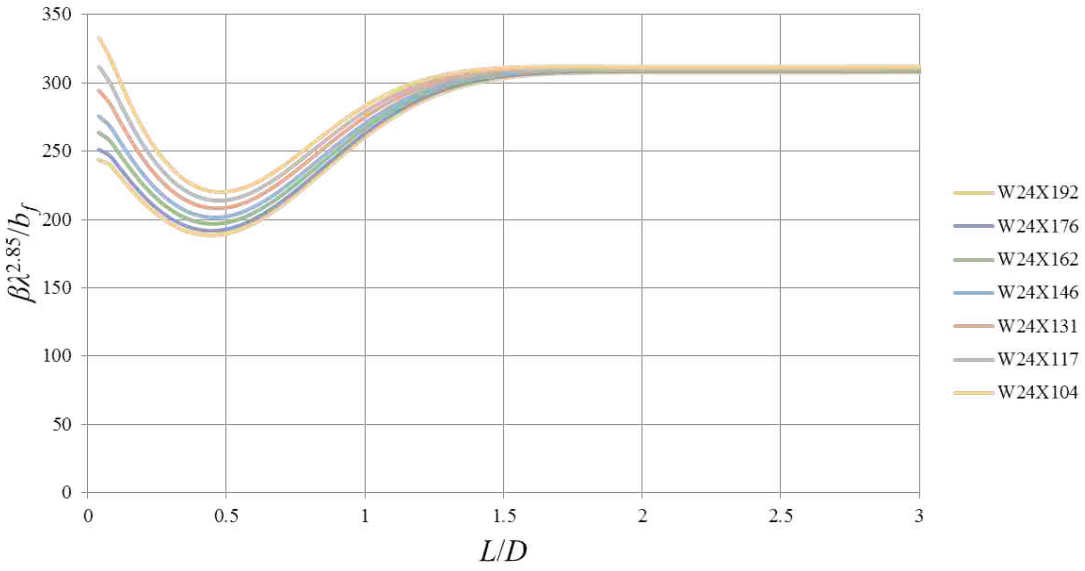

Figure B.36: W24 Strong Axis - Family 2

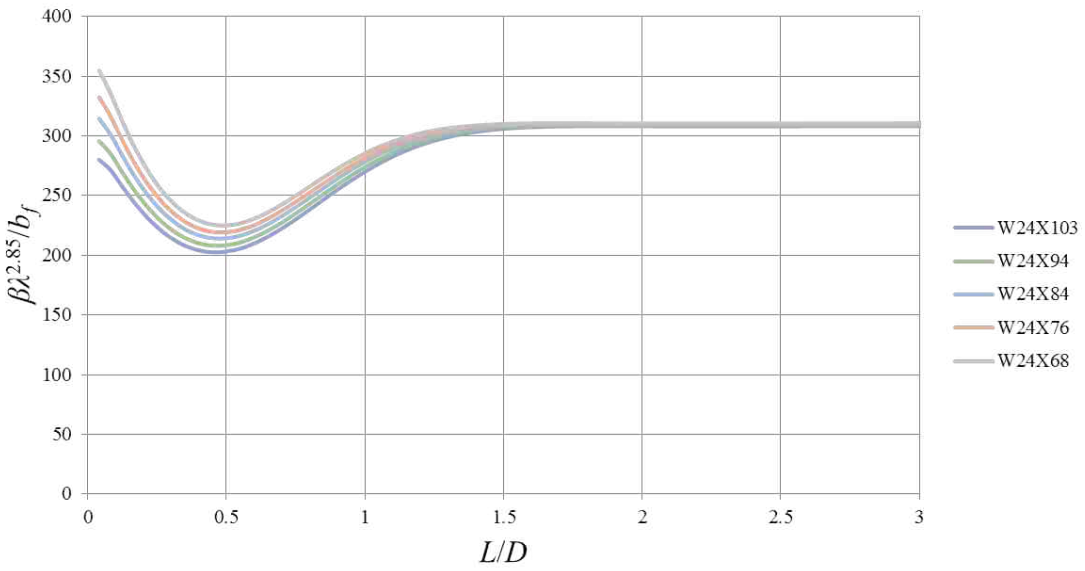

Figure B.37: W24 Strong Axis - Family 3

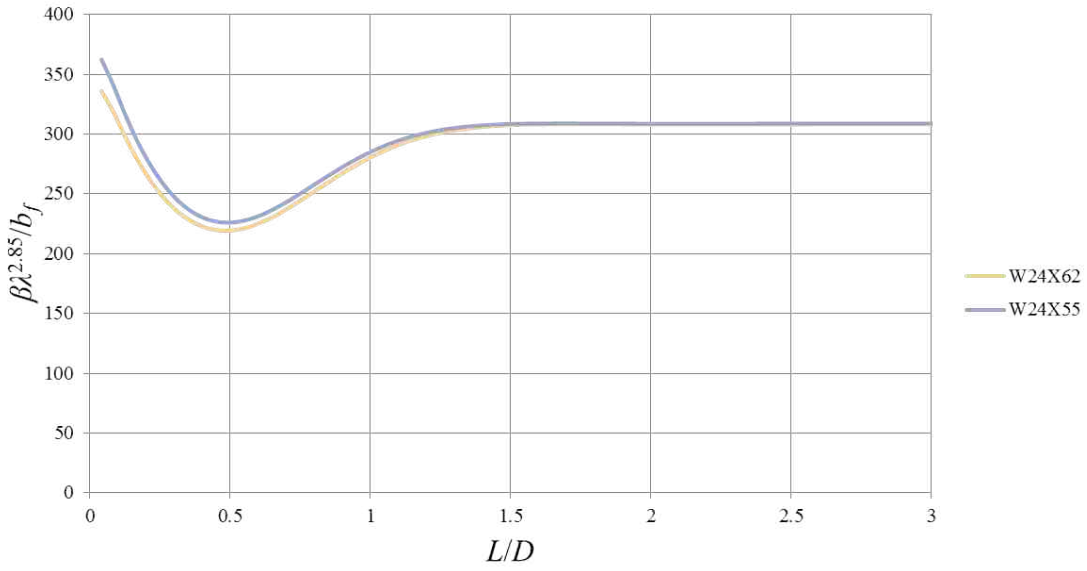

Figure B.38: W24 Strong Axis - Family 4

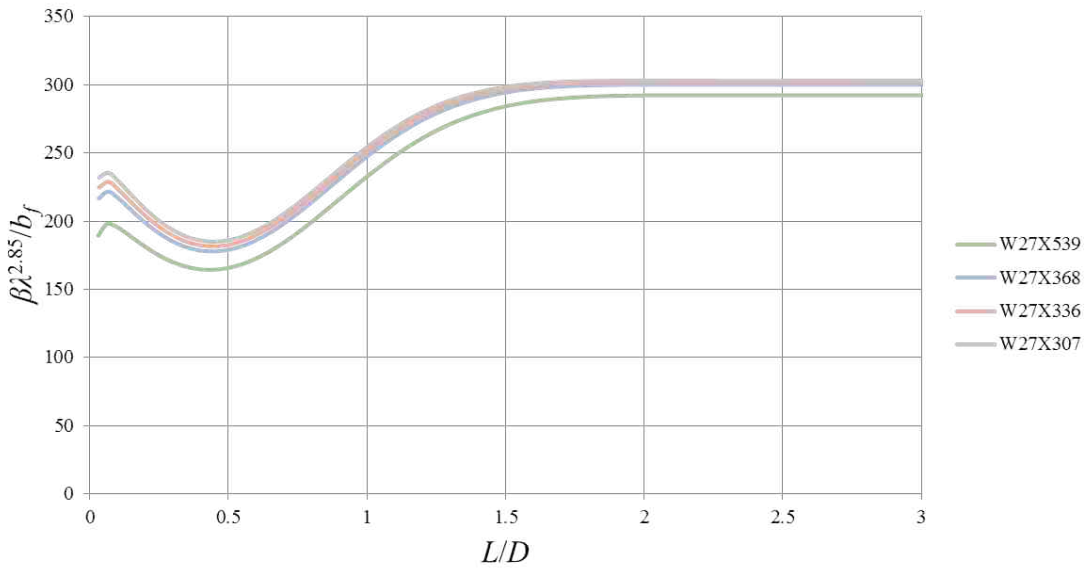

Figure B.39: W27 Strong Axis - Family 1

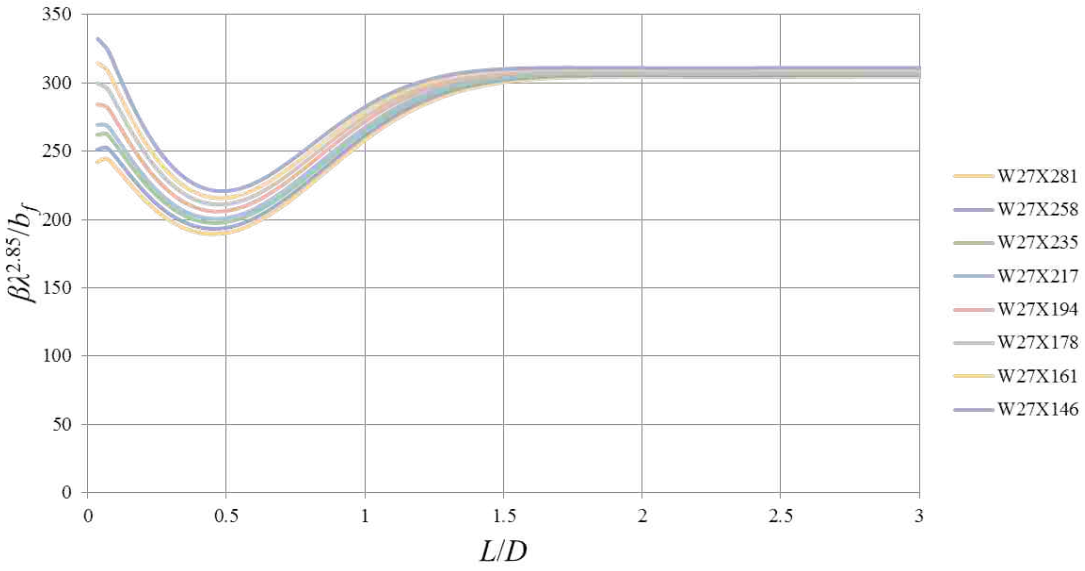

Figure B.40: W27 Strong Axis - Family 2

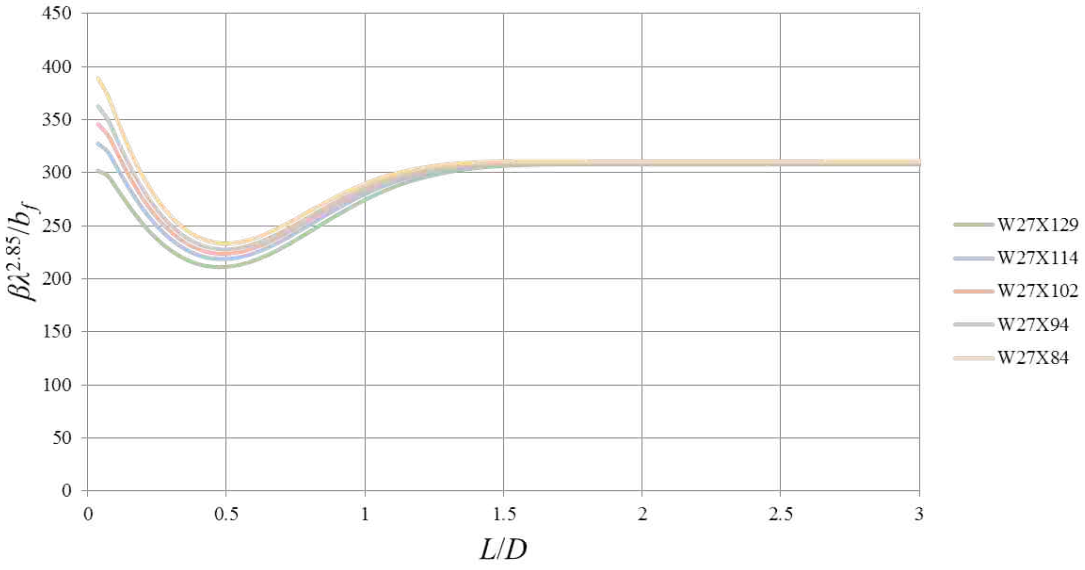

Figure B.41: W27 Strong Axis - Family 3

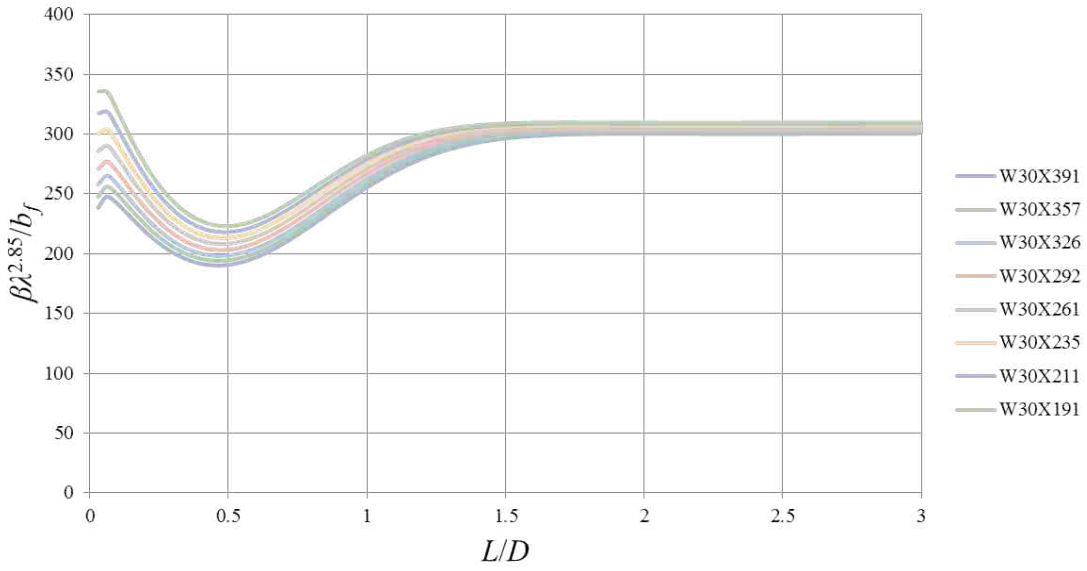

Figure B.42: W30 Strong Axis - Family 1

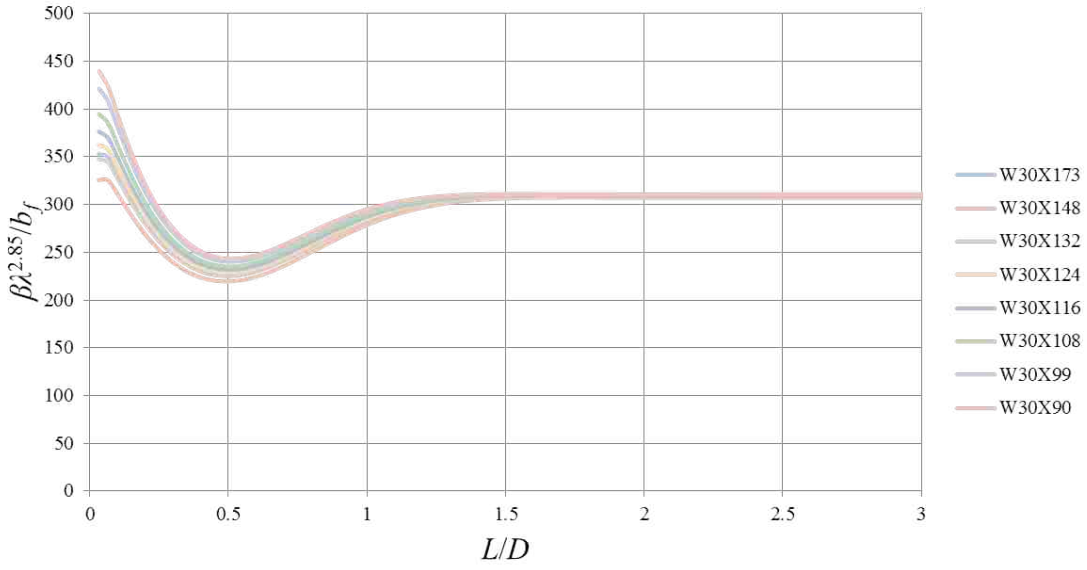

Figure B.43: W30 Strong Axis - Family 2

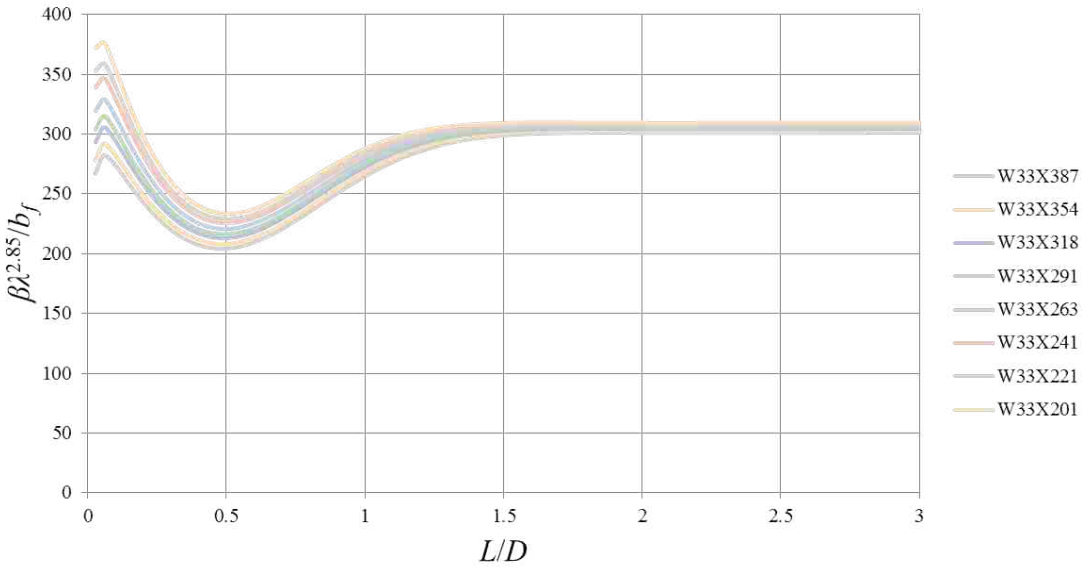

Figure B.44: W33 Strong Axis - Family 1

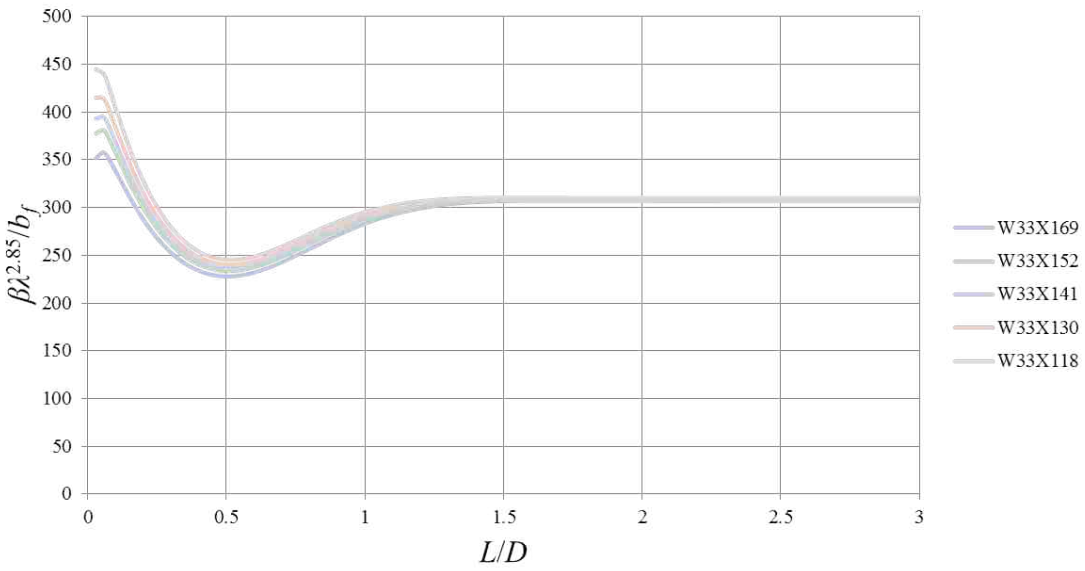

Figure B.45: W33 Strong Axis - Family 2

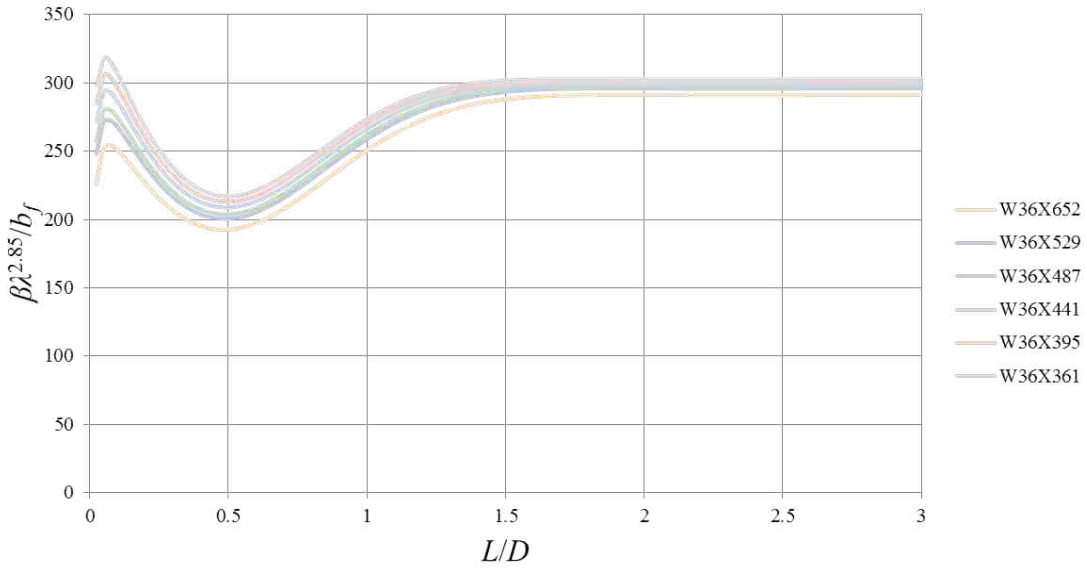

Figure B.46: W36 Strong Axis - Family 1

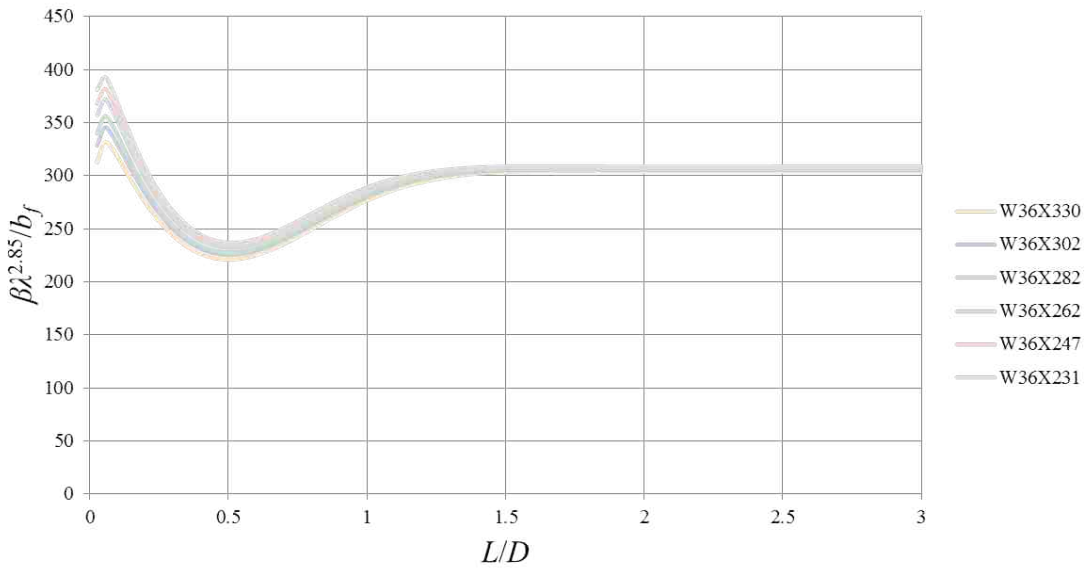

Figure B.47: W36 Strong Axis - Family 2

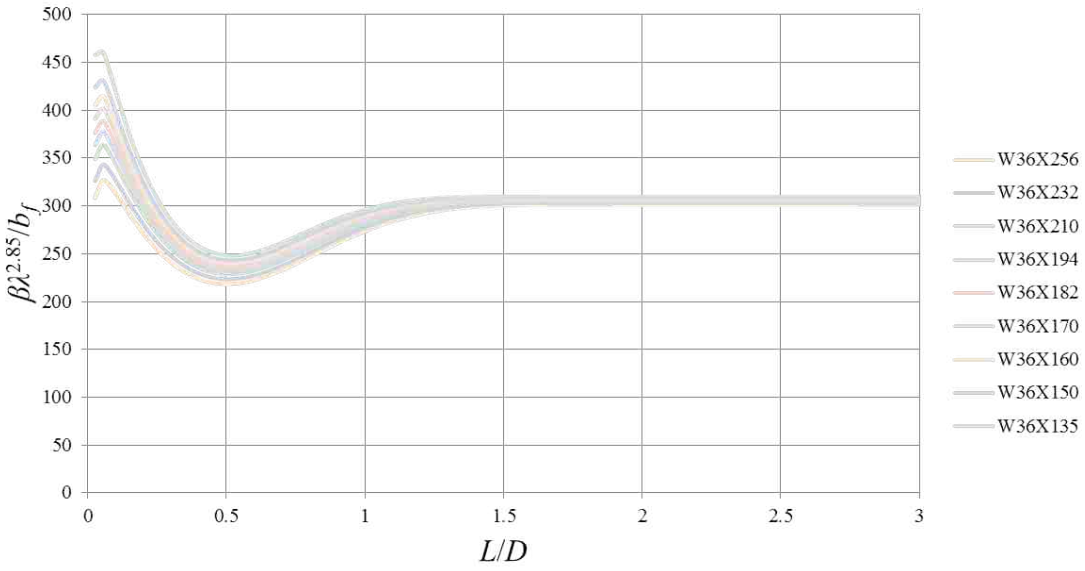

Figure B.48: W36 Strong Axis - Family 3

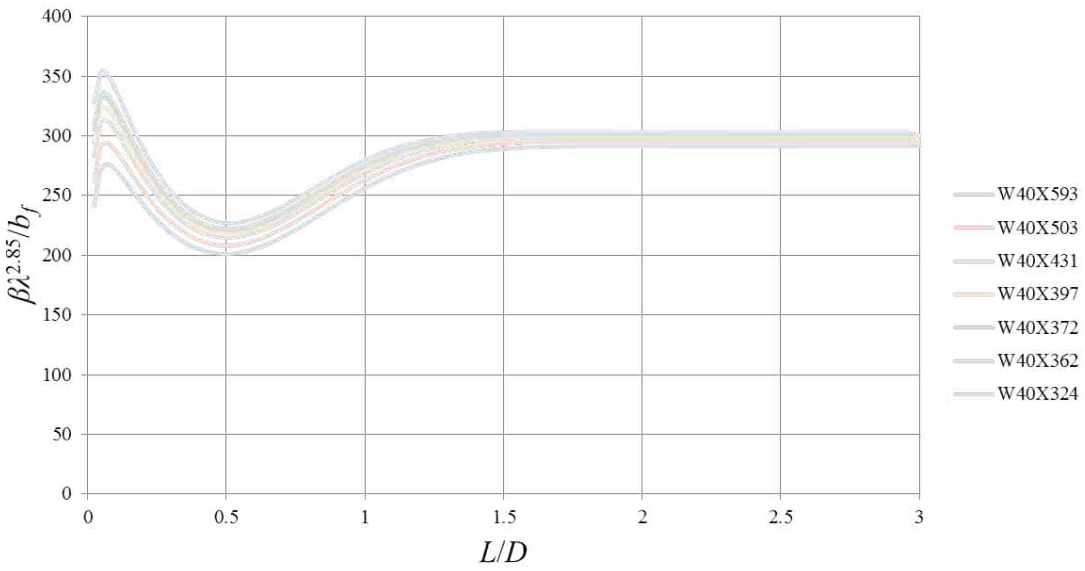

Figure B.49: W40 Strong Axis - Family 1

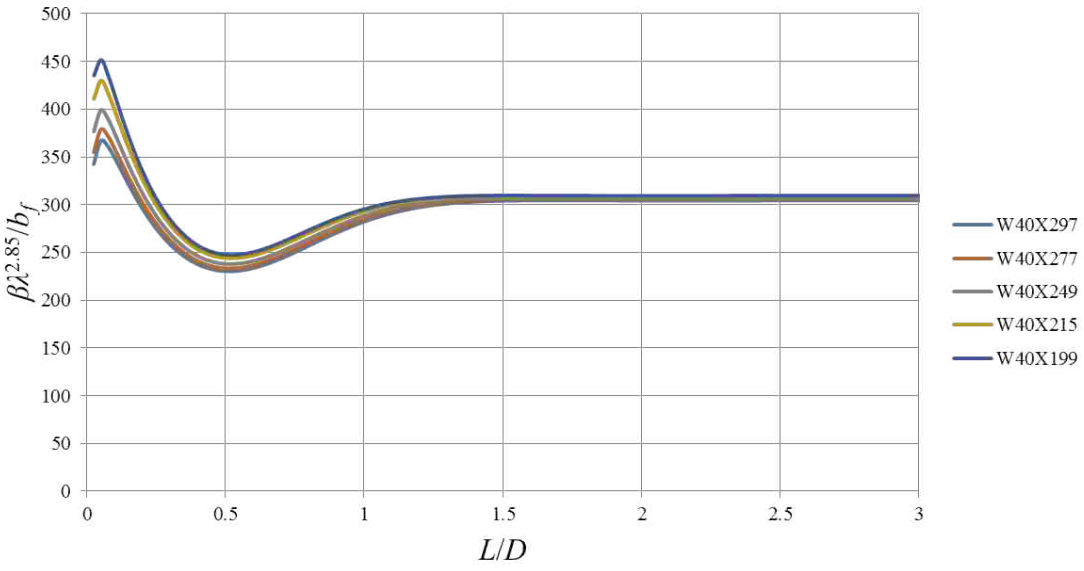

Figure B.50: W40 Strong Axis - Family 2

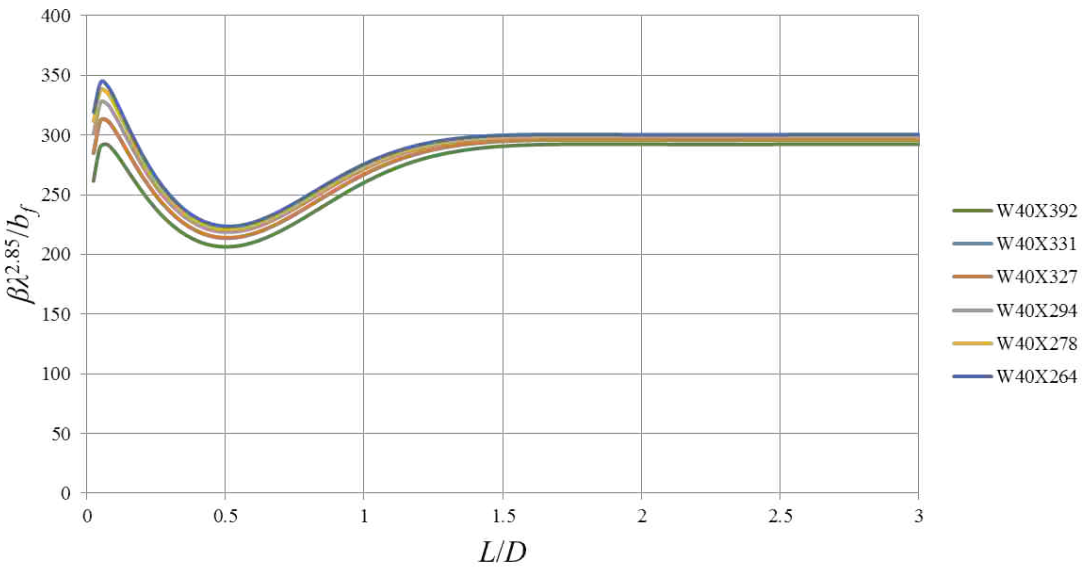

Figure B.51: W40 Strong Axis - Family 3

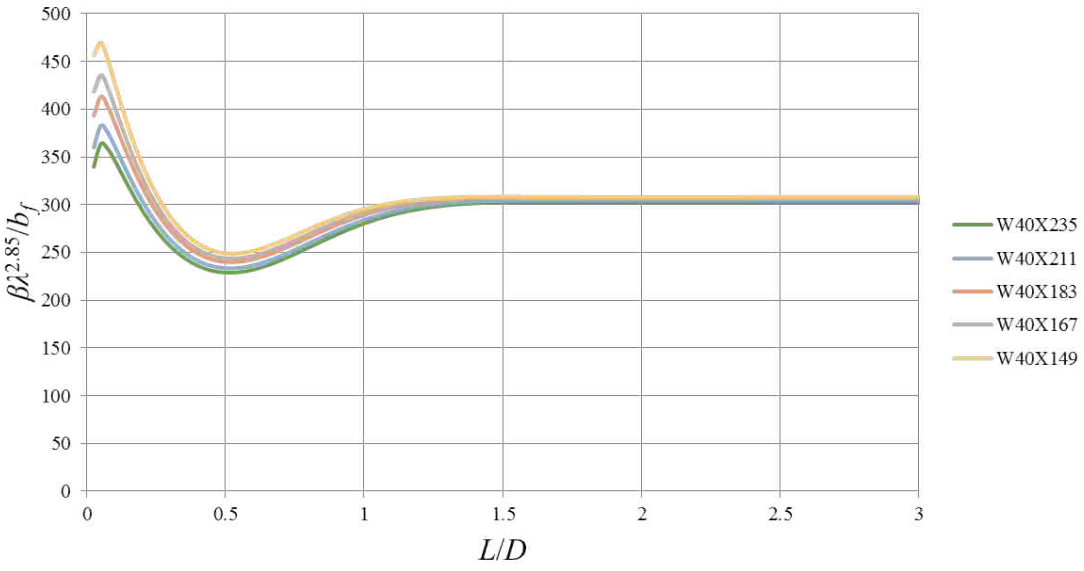

Figure B.52: W40 Strong Axis - Family 4

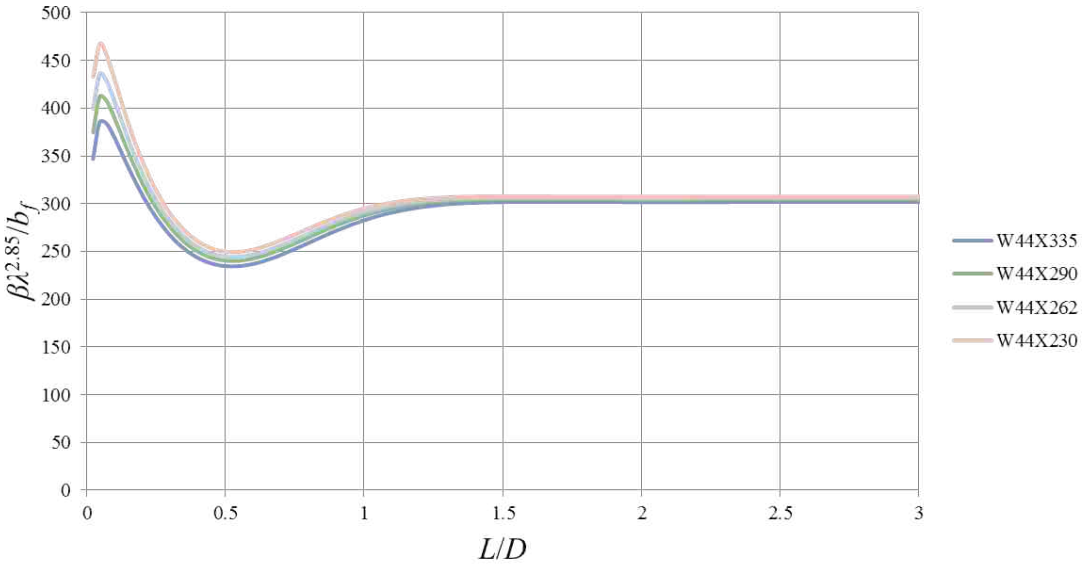

Figure B.53: W44 Strong Axis

B.2 Weak Axis Curves

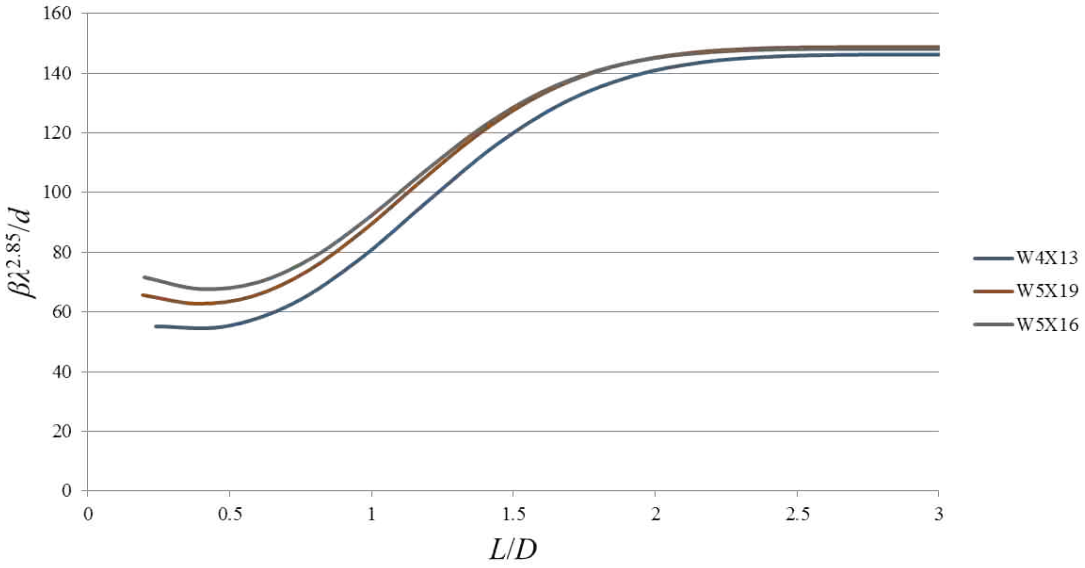

Figure B.54: W4 and W5 Weak Axis

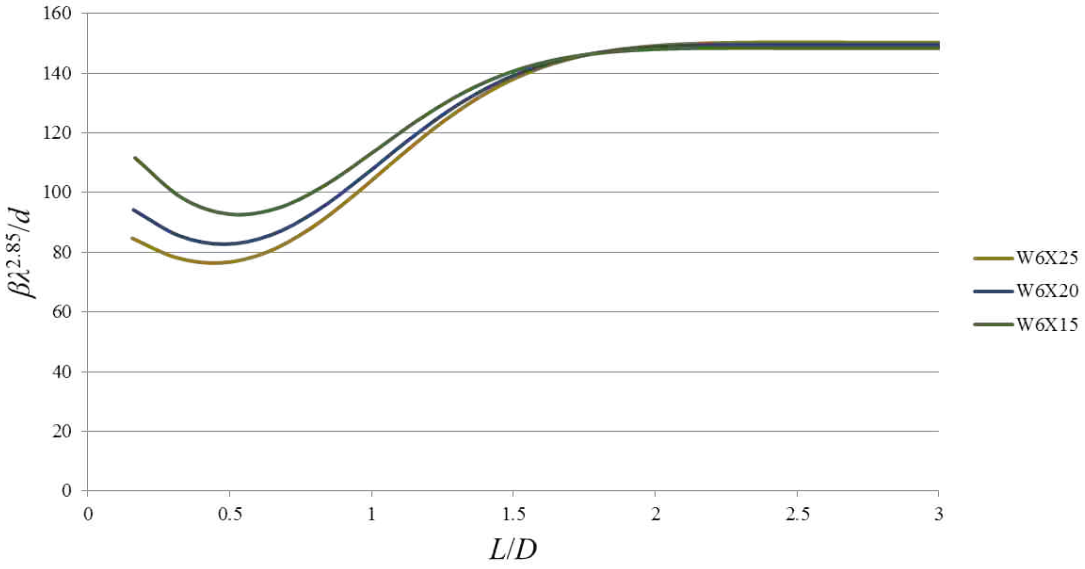

Figure B.55: W6 Weak Axis - Family 1

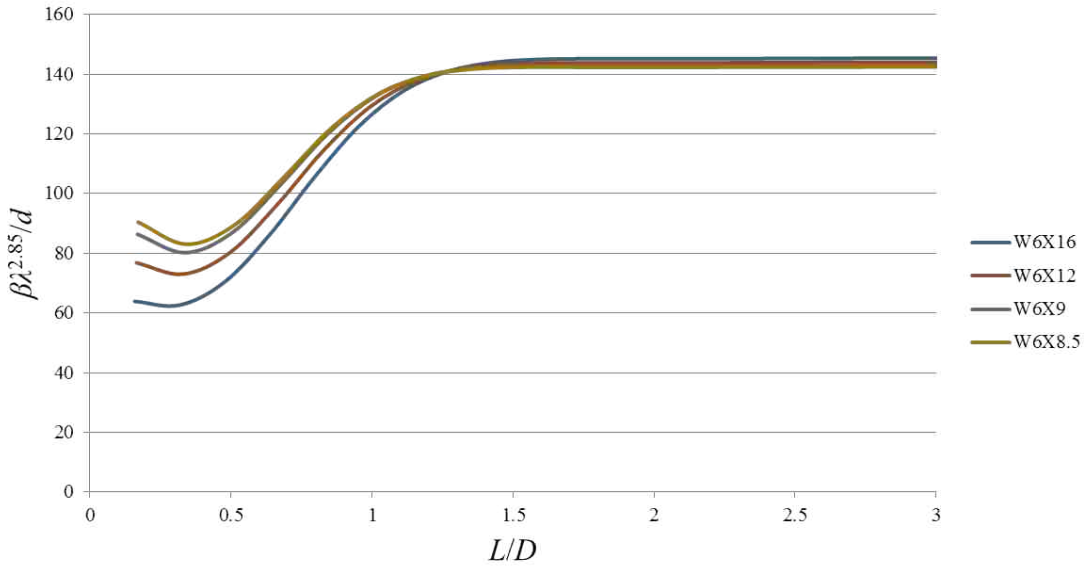

Figure B.56: W6 Weak Axis - Family 2

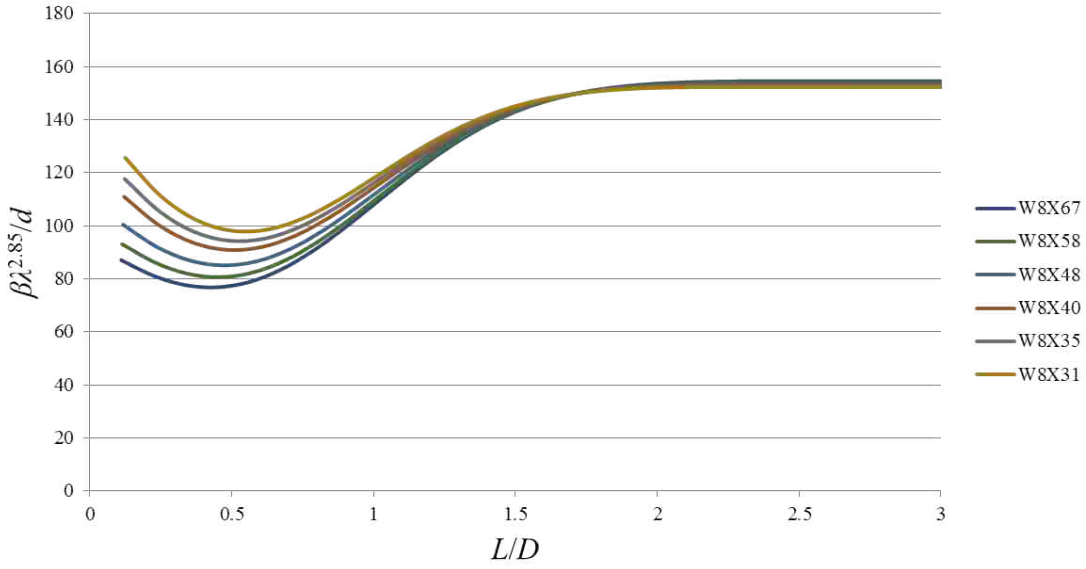

Figure B.57: W8 Weak Axis - Family 1

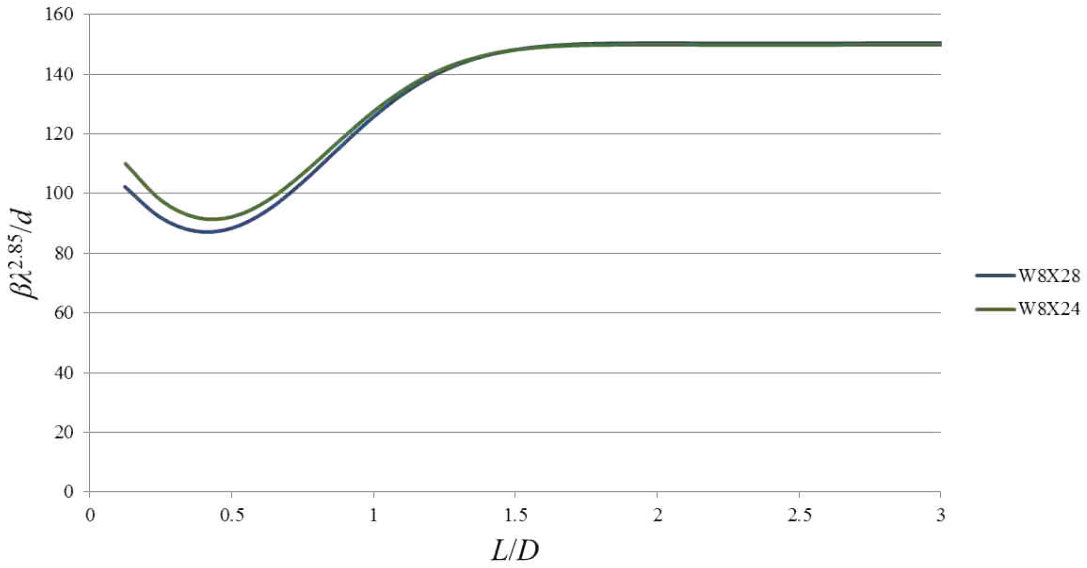

Figure B.58: W8 Weak Axis - Family 2

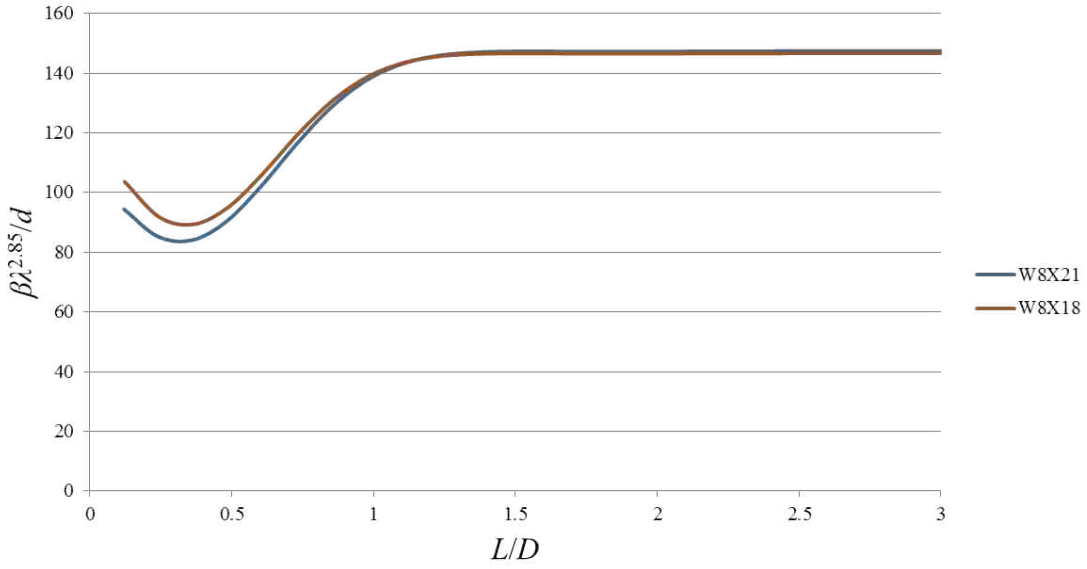

Figure B.59: W8 Weak Axis - Family 3

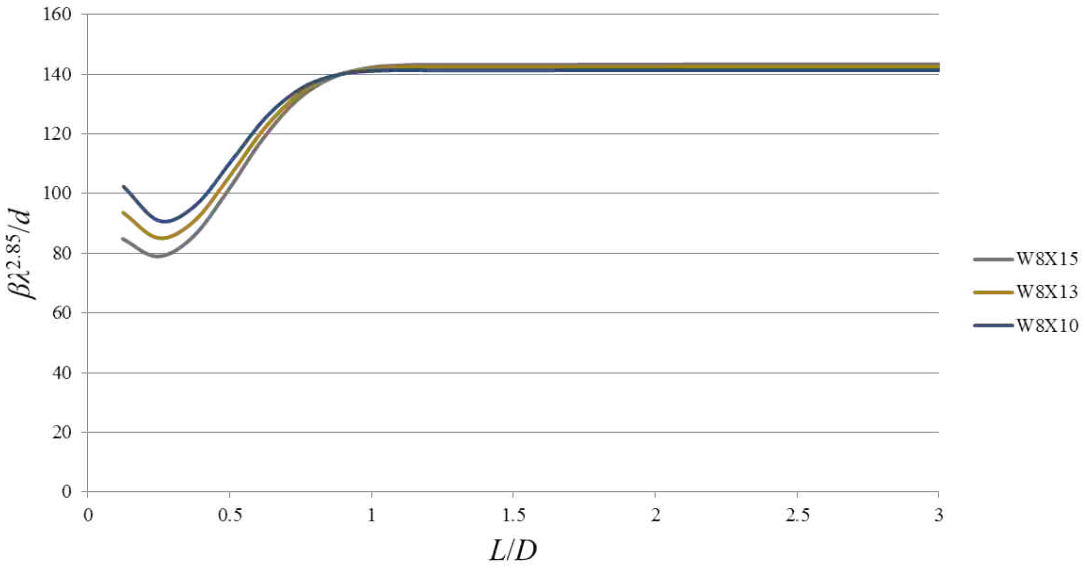

Figure B.60: W8 Weak Axis - Family 4

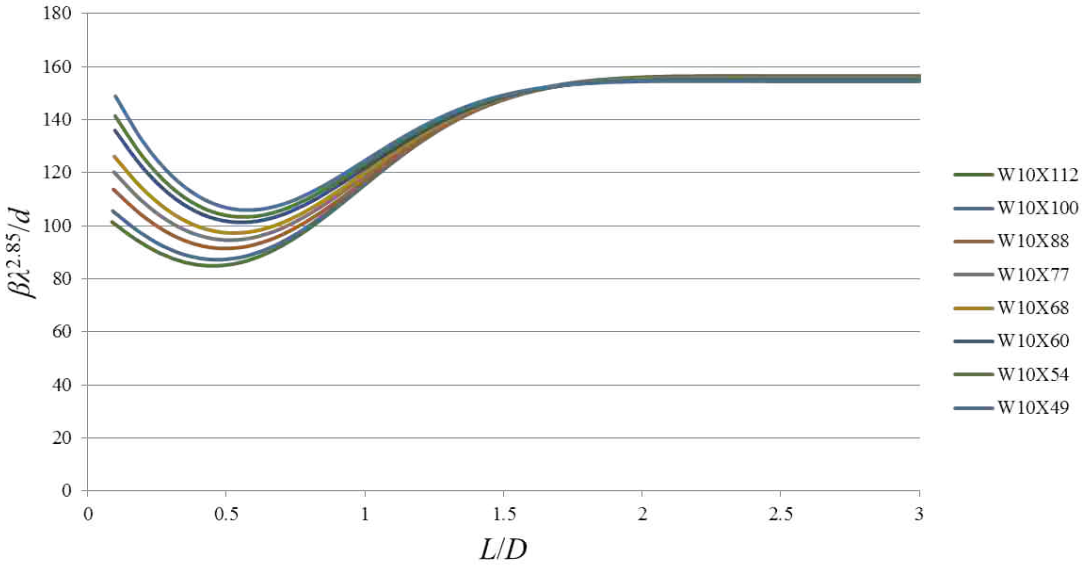

Figure B.61: W10 Weak Axis - Family 1

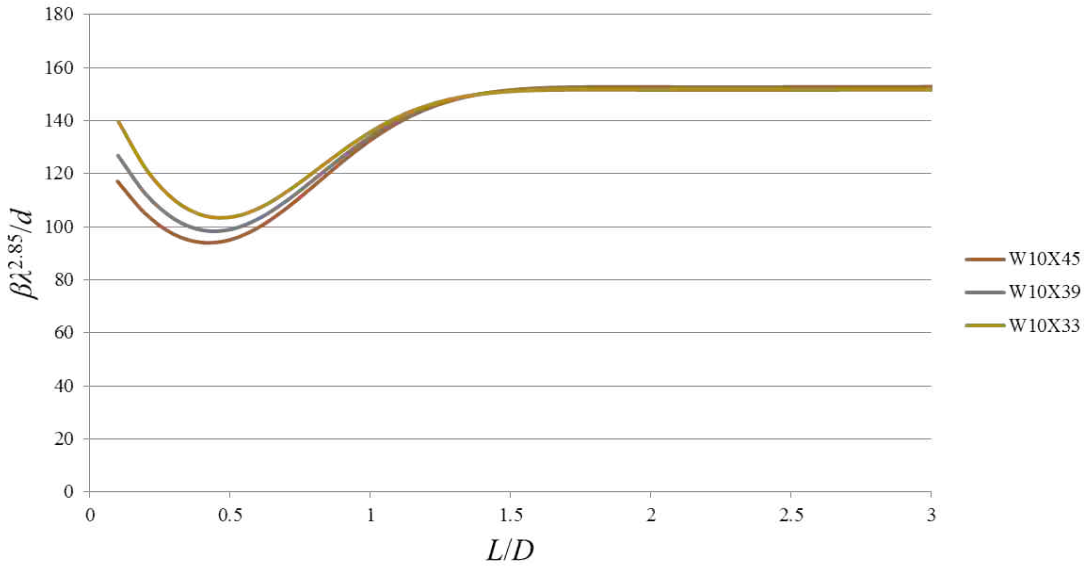

Figure B.62: W10 Weak Axis - Family 2

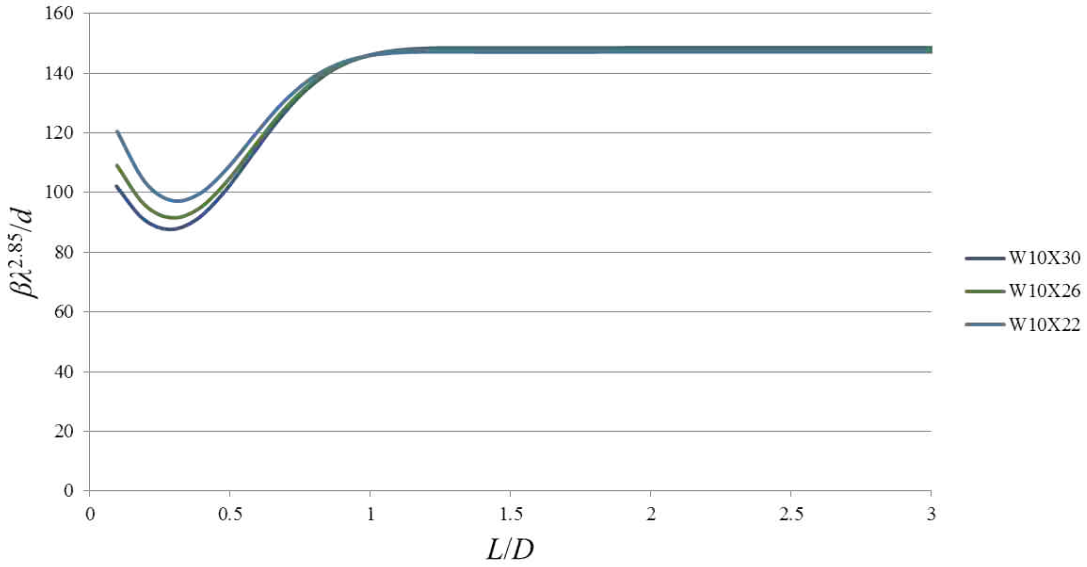

Figure B.63: W10 Weak Axis - Family 3

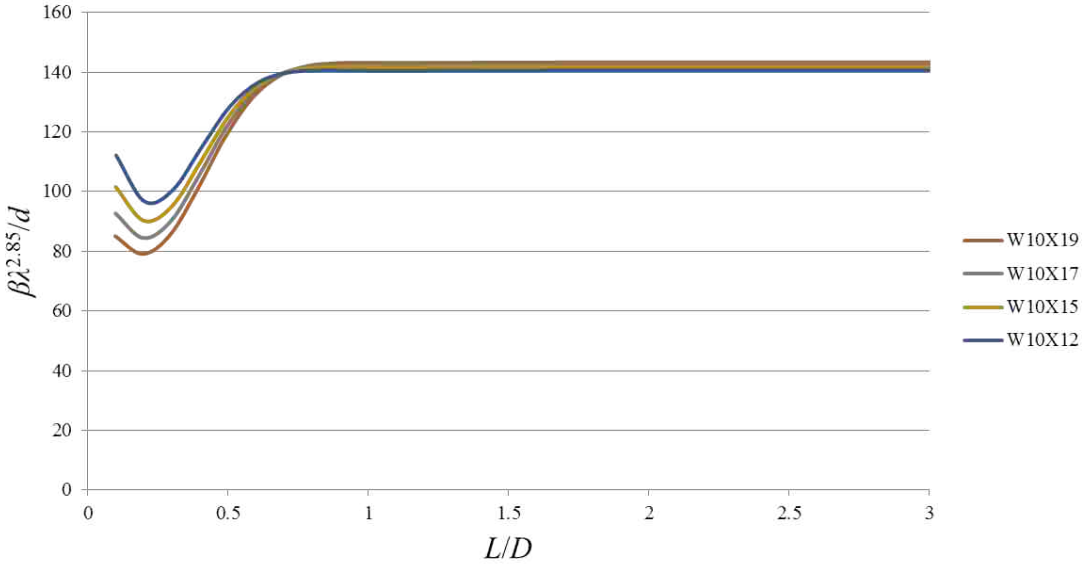

Figure B.64: W10 Weak Axis - Family 4

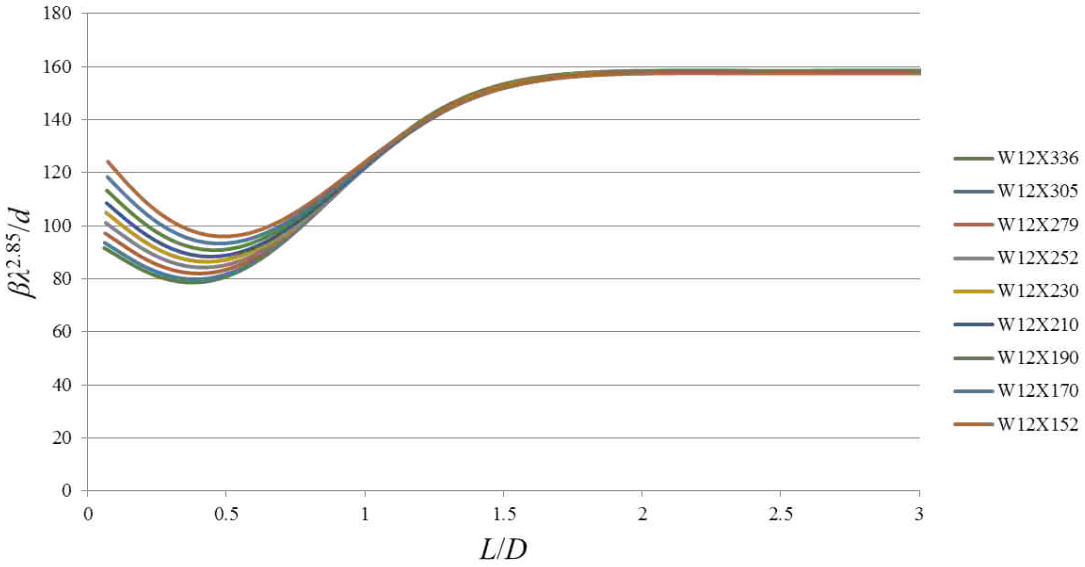

Figure B.65: W12 Weak Axis - Family 1

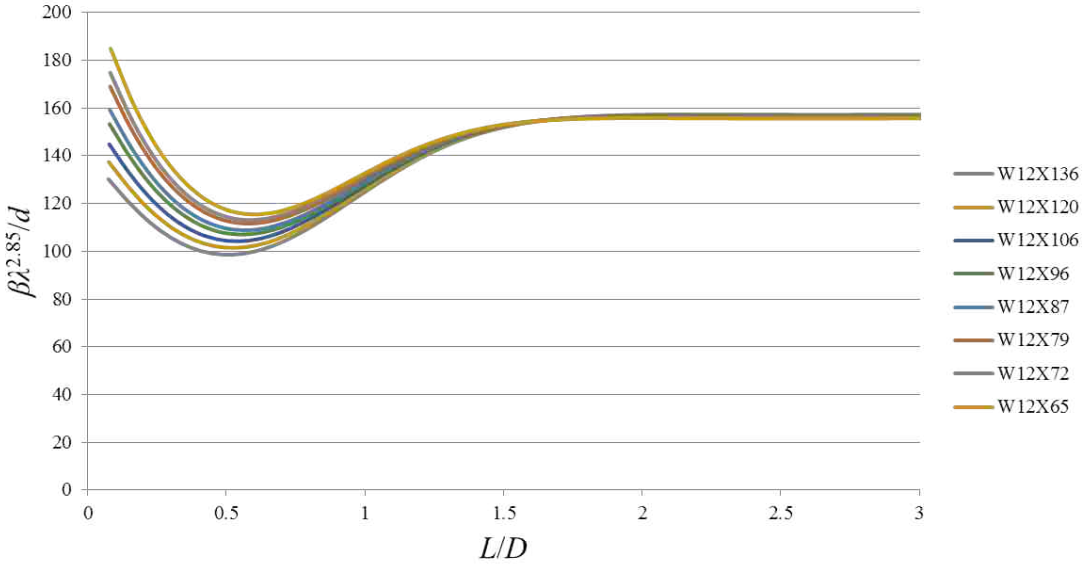

Figure B.66: W12 Weak Axis - Family 2

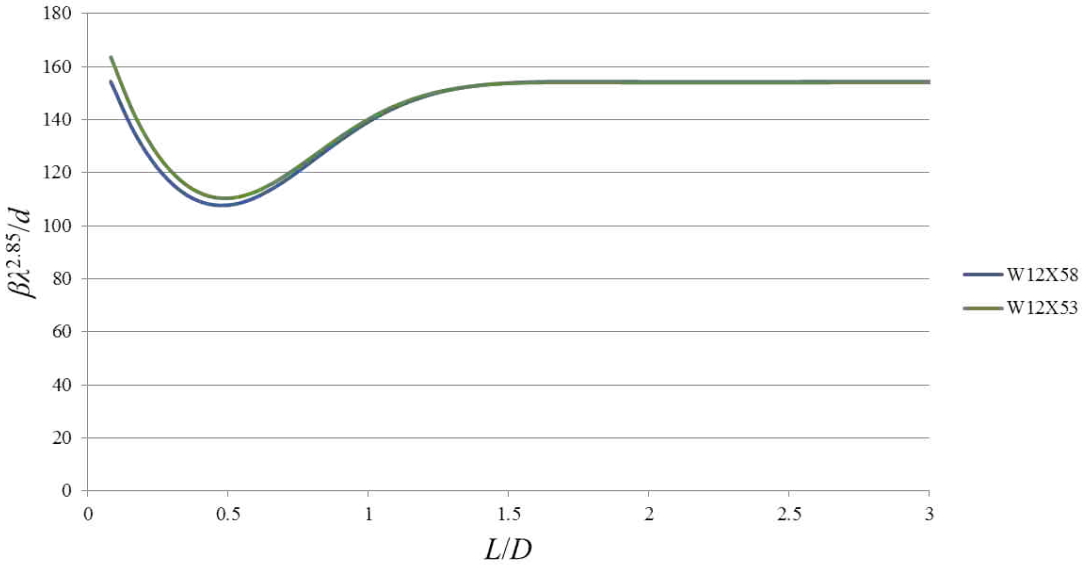

Figure B.67: W12 Weak Axis - Family 3

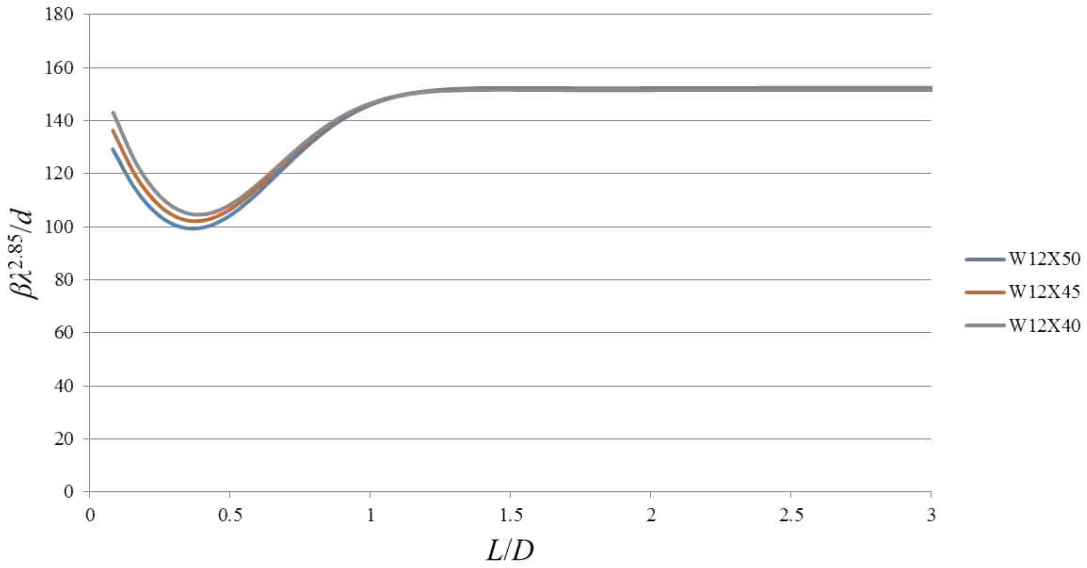

Figure B.68: W12 Weak Axis - Family 4

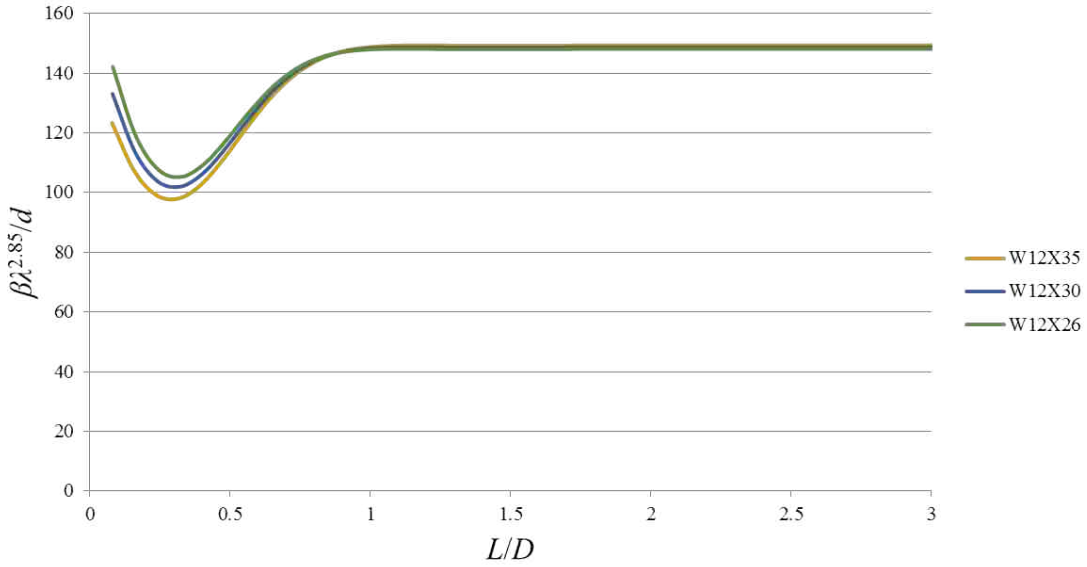

Figure B.69: W12 Weak Axis - Family 5

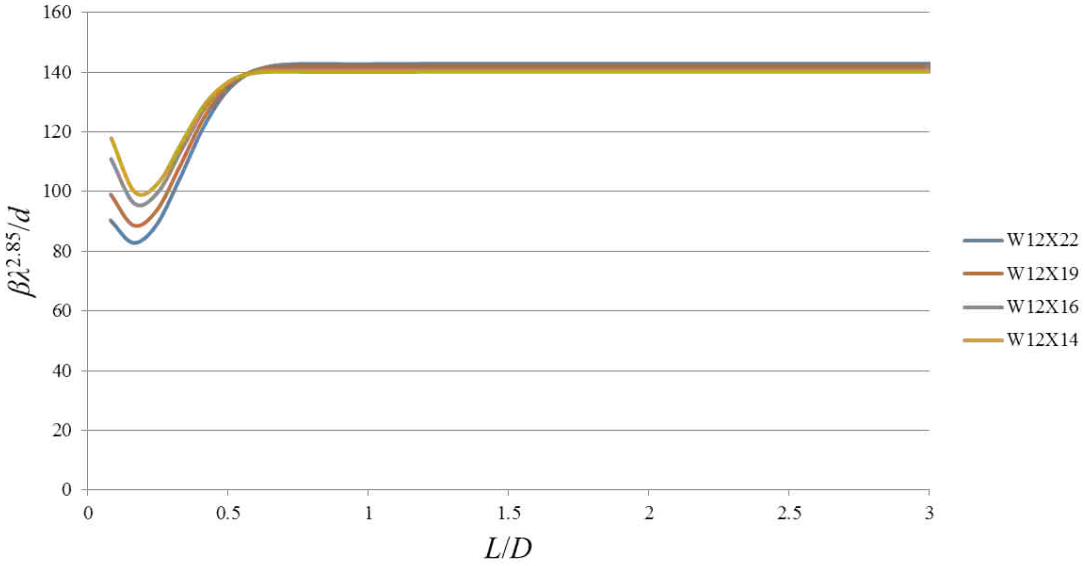

Figure B.70: W12 Weak Axis - Family 6

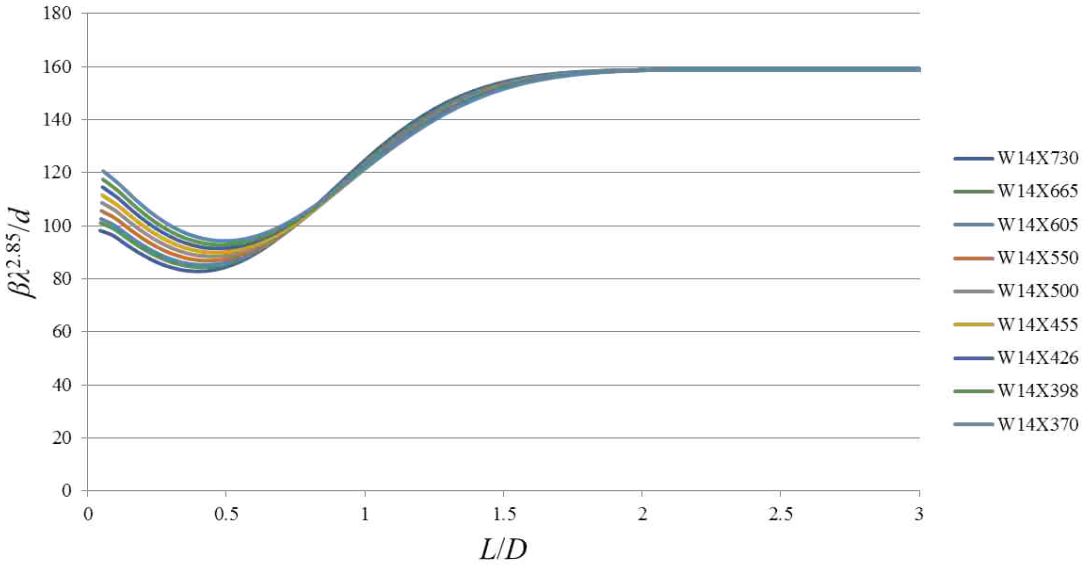

Figure B.71: W14 Weak Axis - Family 1

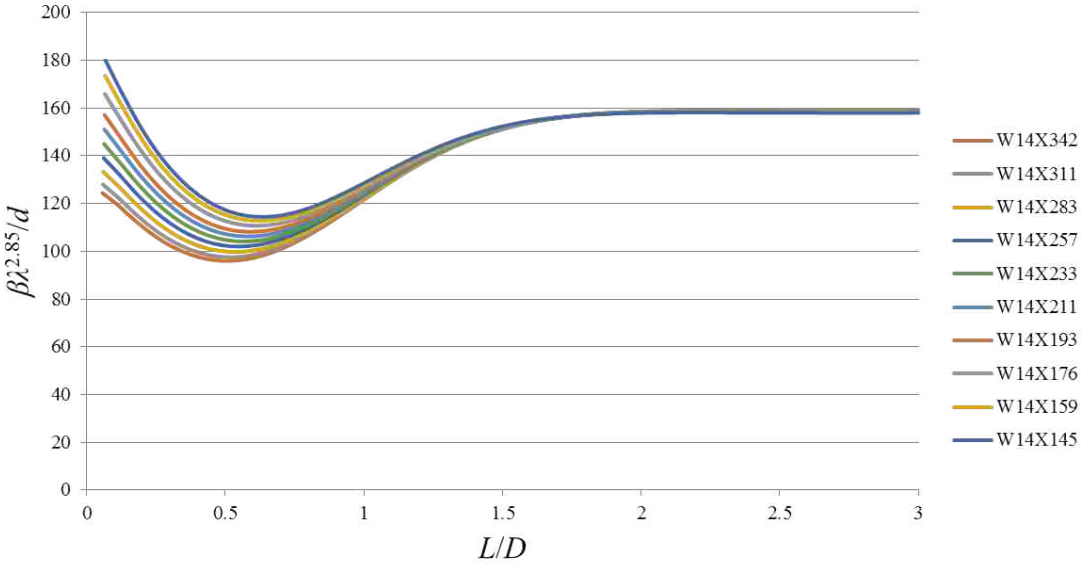

Figure B.72: W14 Weak Axis - Family 2

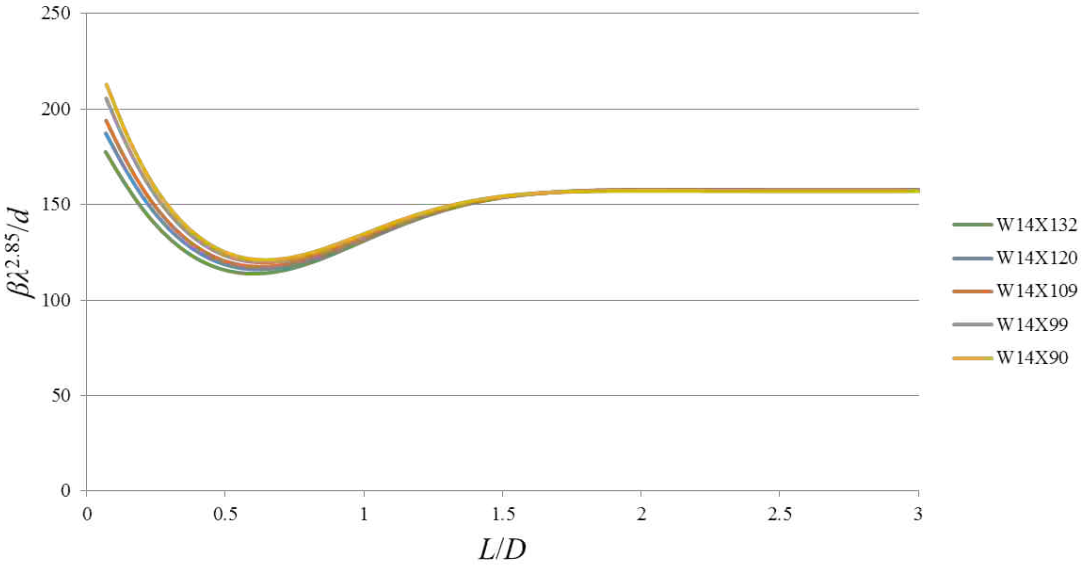

Figure B.73: W14 Weak Axis - Family 3

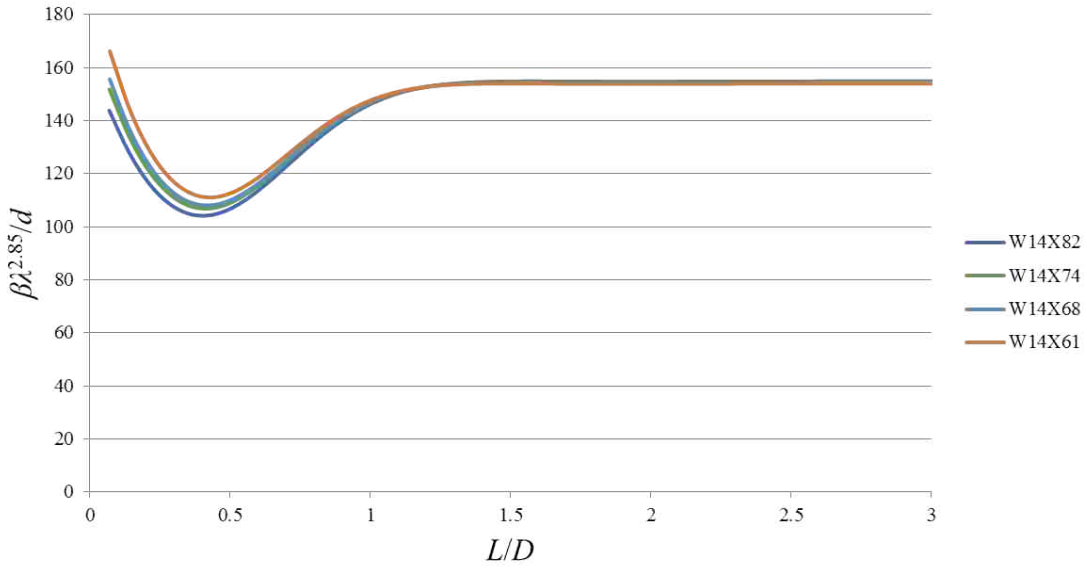

Figure B.74: W14 Weak Axis - Family 4

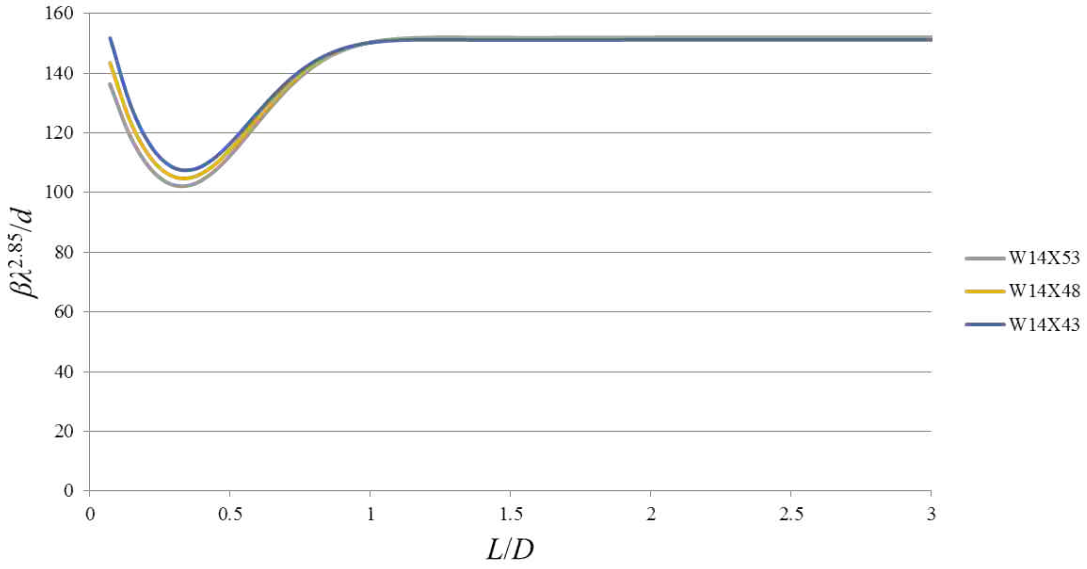

Figure B.75: W14 Weak Axis - Family 5

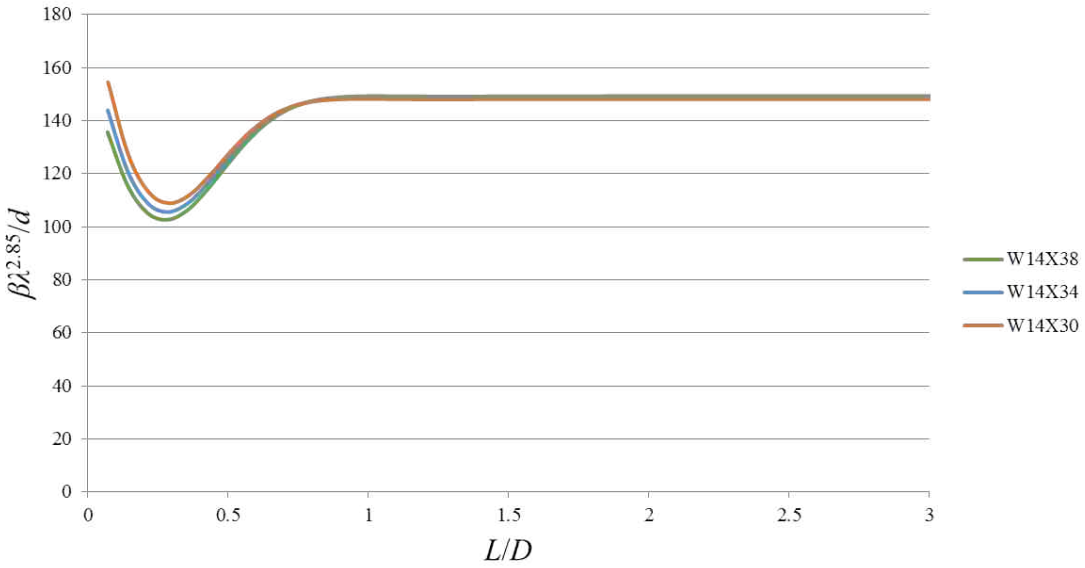

Figure B.76: W14 Weak Axis - Family 6

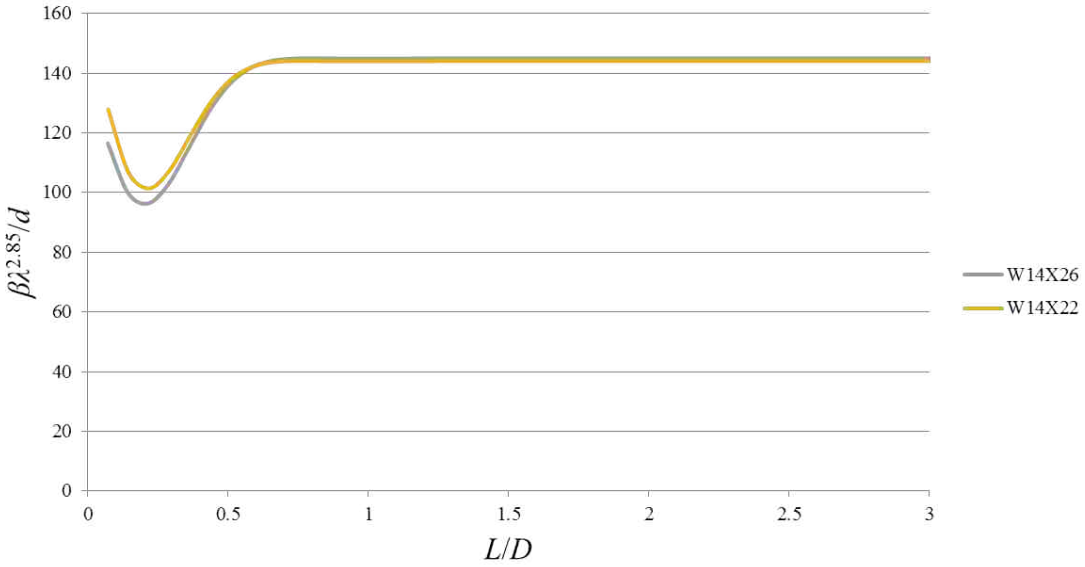

Figure B.77: W14 Weak Axis - Family 7

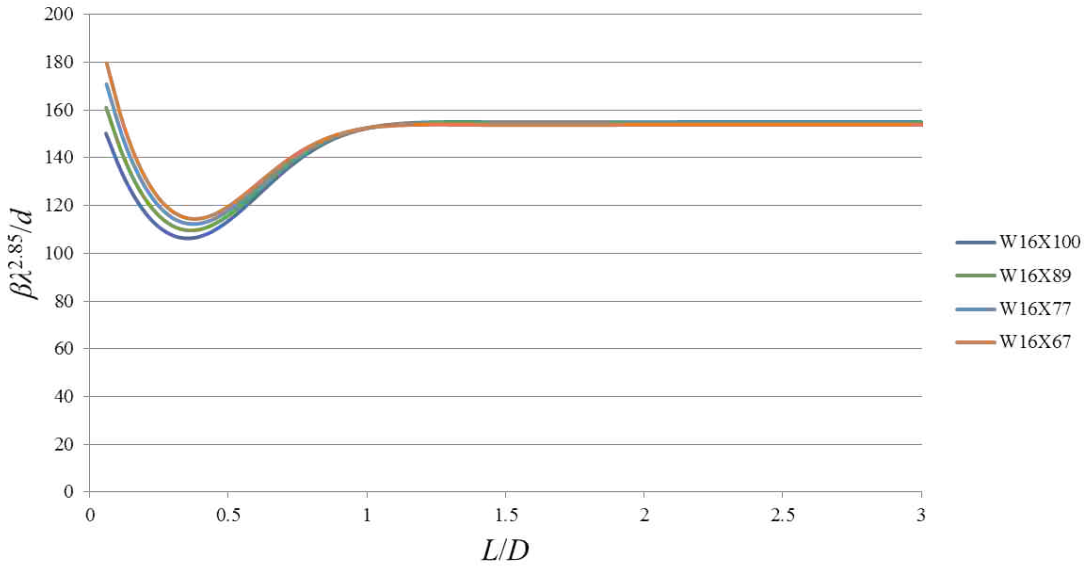

Figure B.78: W16 Weak Axis - Family 1

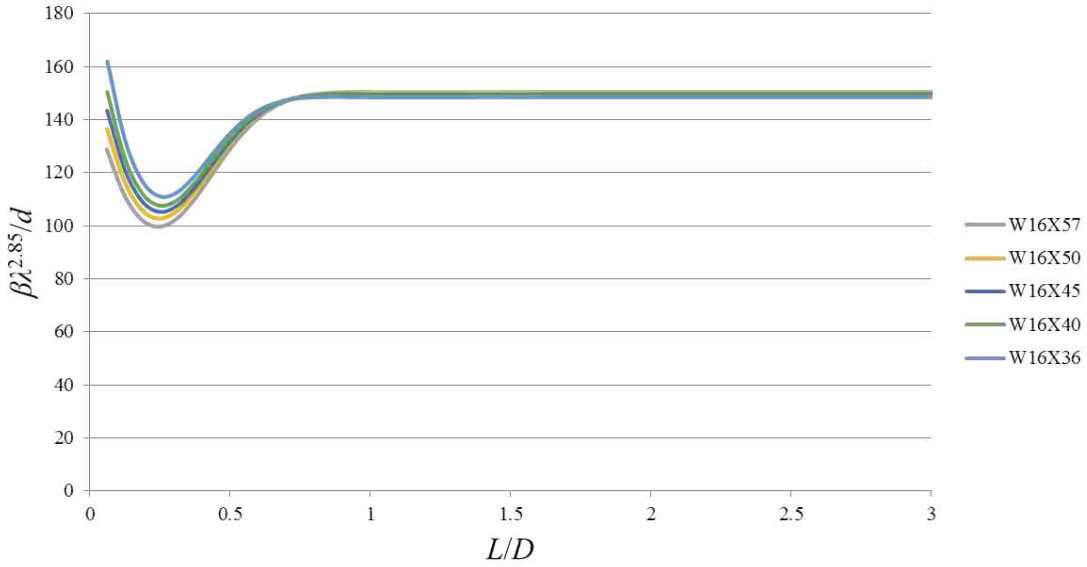

Figure B.79: W16 Weak Axis - Family 2

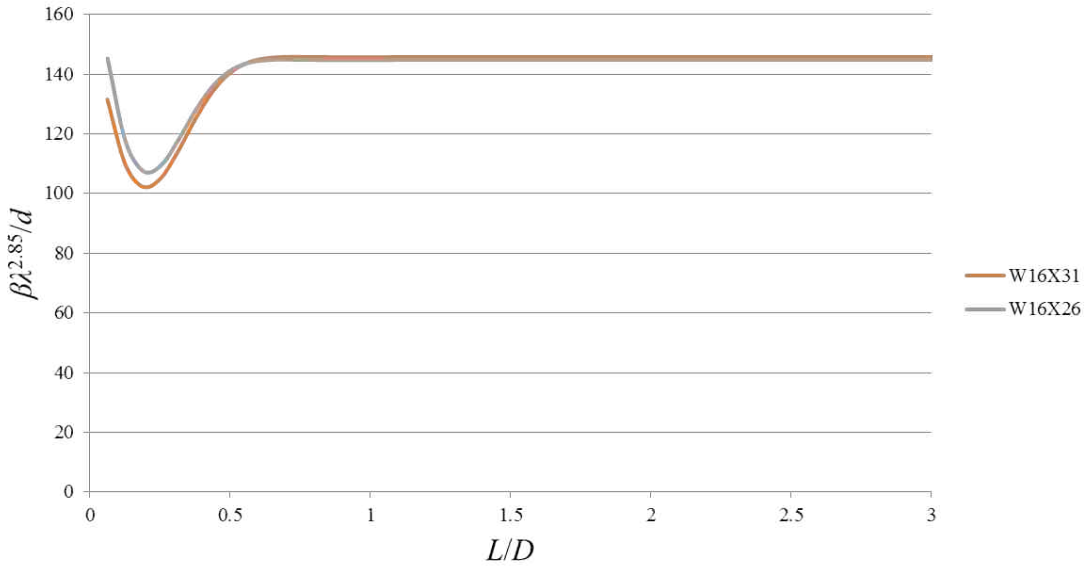

Figure B.80: W16 Weak Axis - Family 3

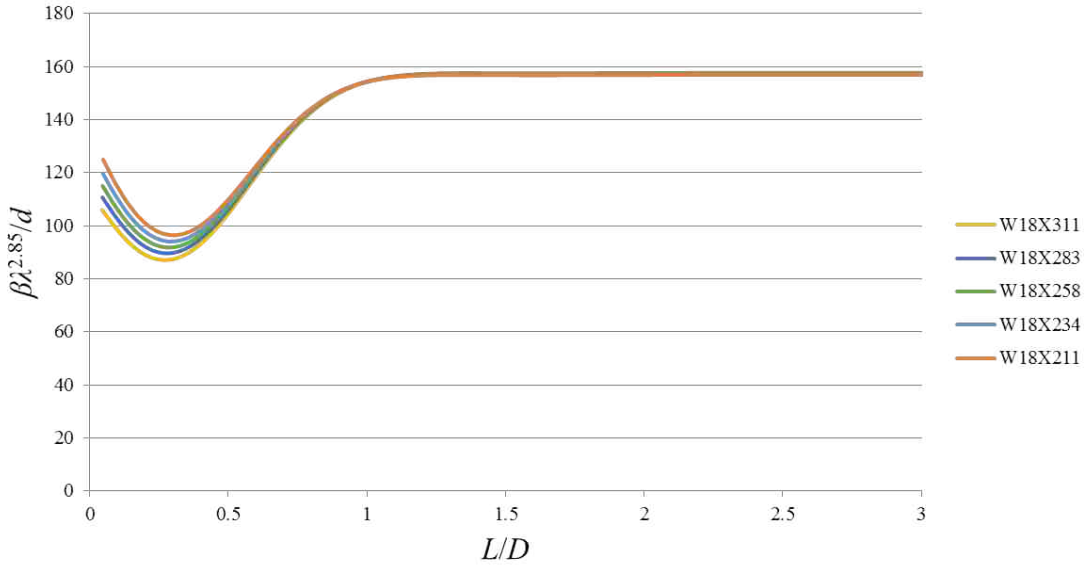

Figure B.81: W18 Weak Axis - Family 1

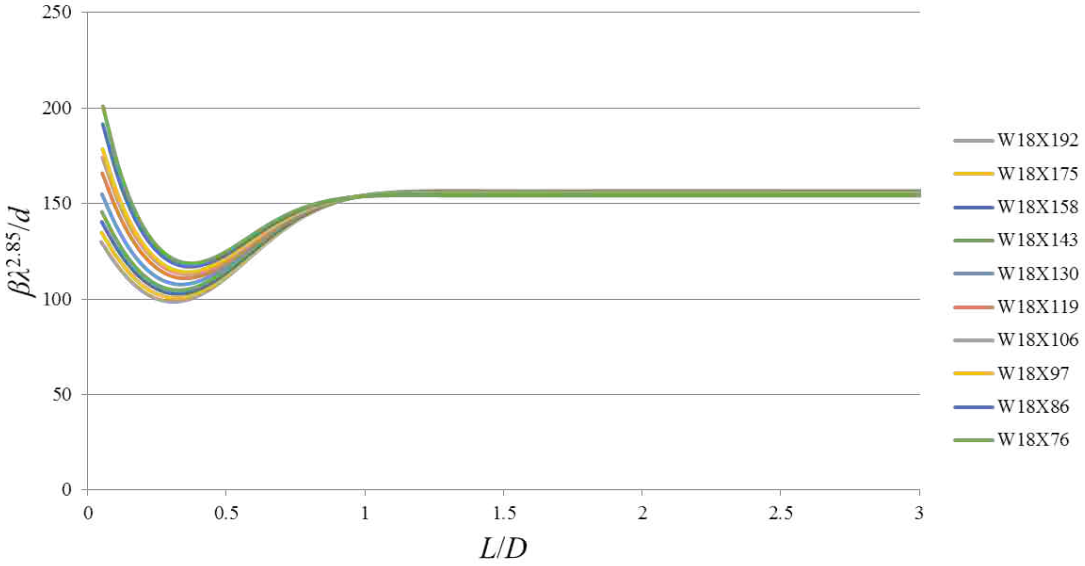

Figure B.82: W18 Weak Axis - Family 2

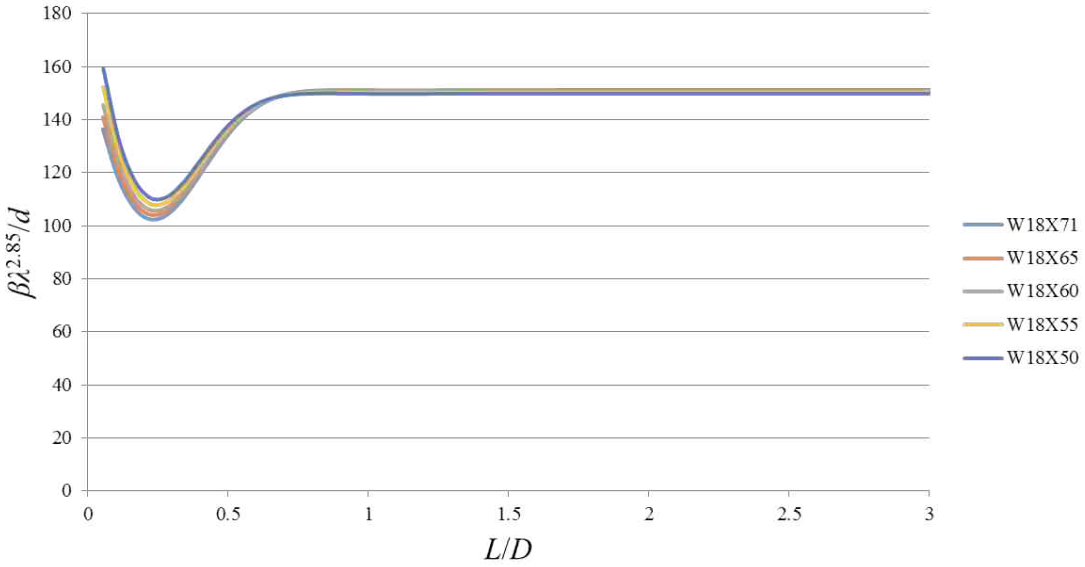

Figure B.83: W18 Weak Axis - Family 3

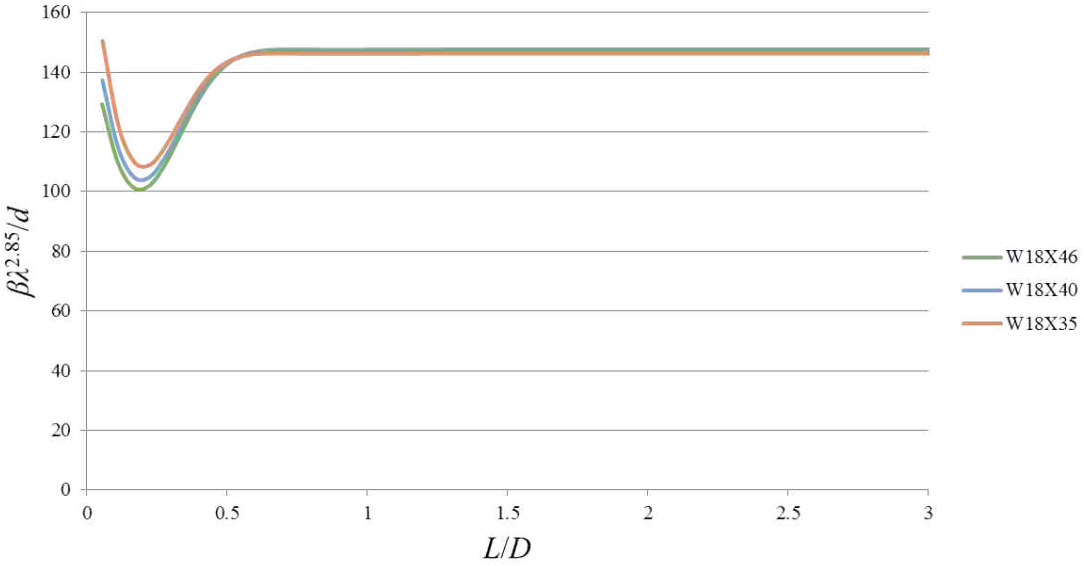

Figure B.84: W18 Weak Axis - Family 4

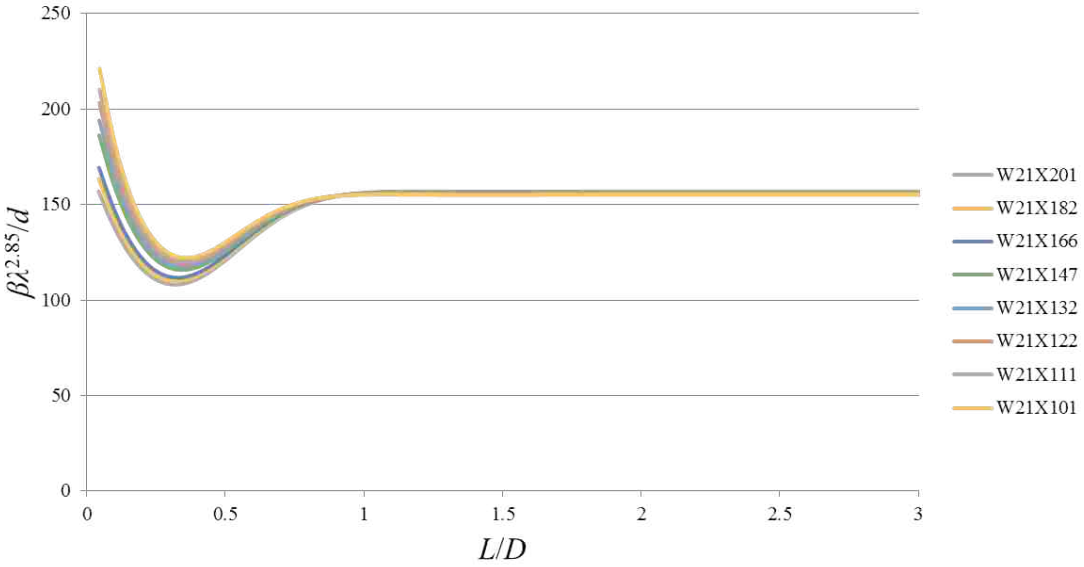

Figure B.85: W21 Weak Axis - Family 1

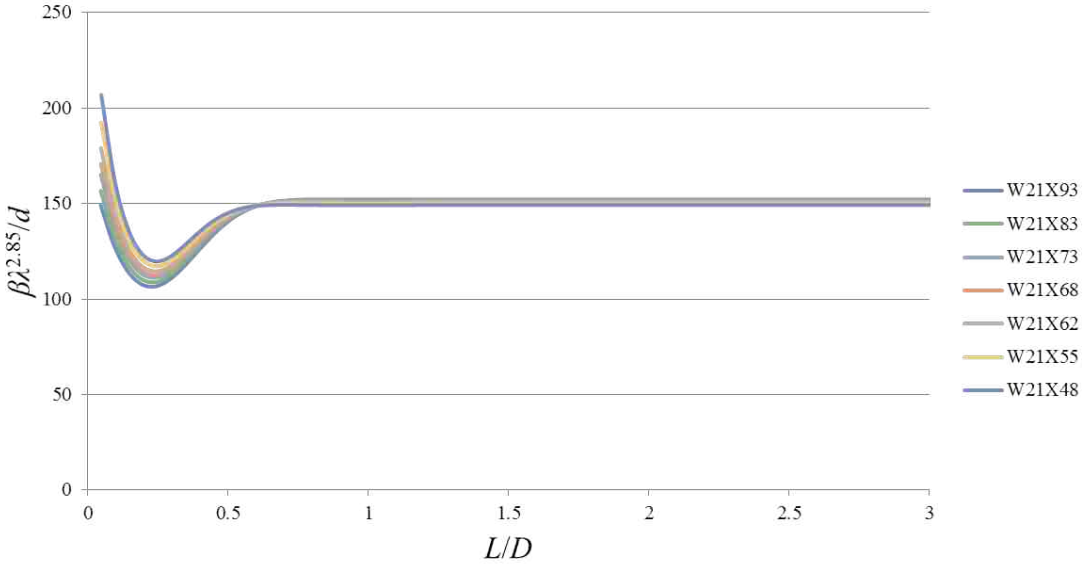

Figure B.86: W21 Weak Axis - Family 2

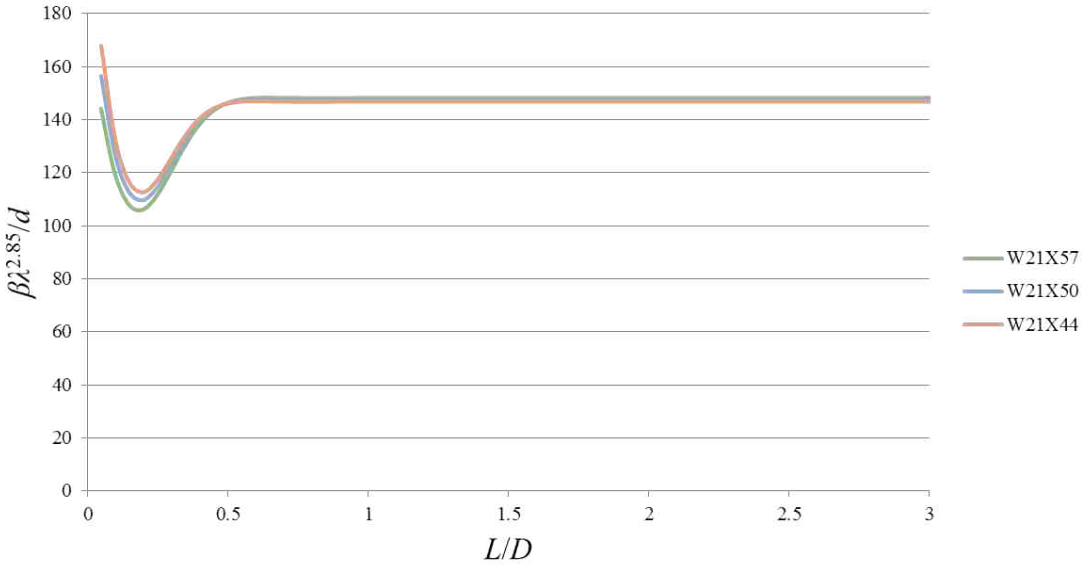

Figure B.87: W21 Weak Axis - Family 3

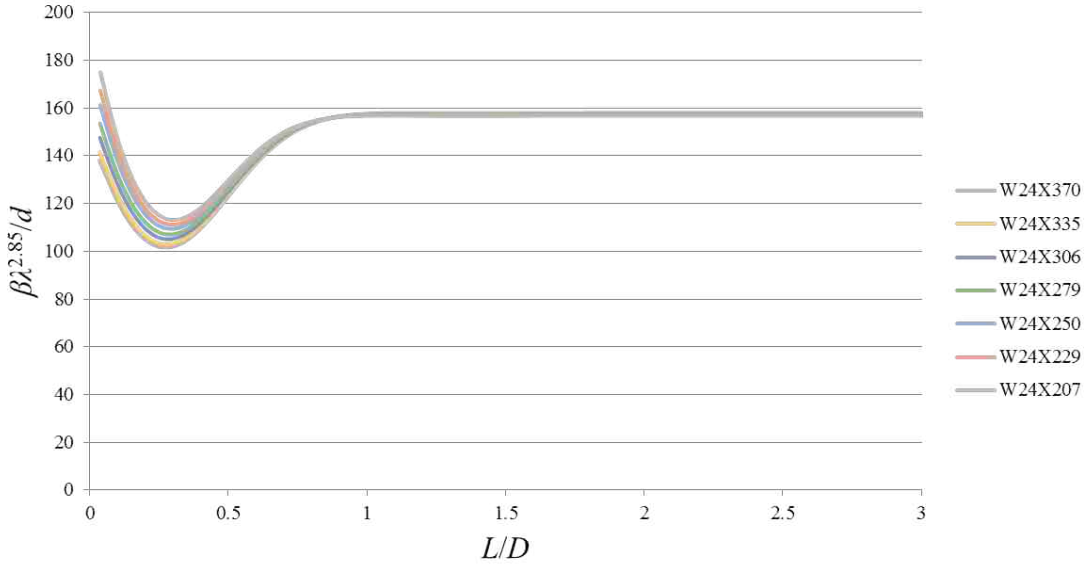

Figure B.88: W24 Weak Axis - Family 1

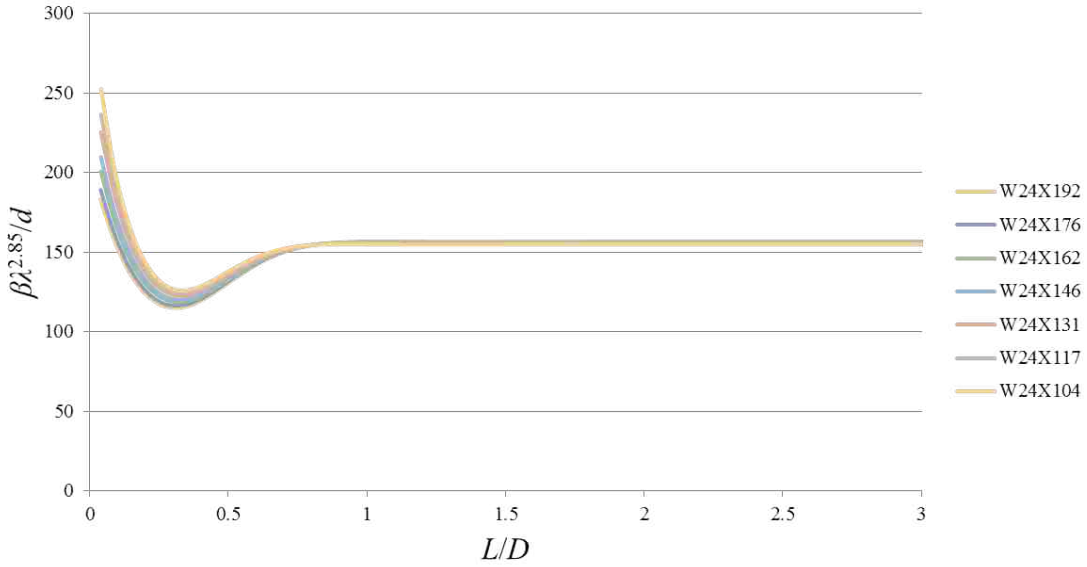

Figure B.89: W24 Weak Axis - Family 2

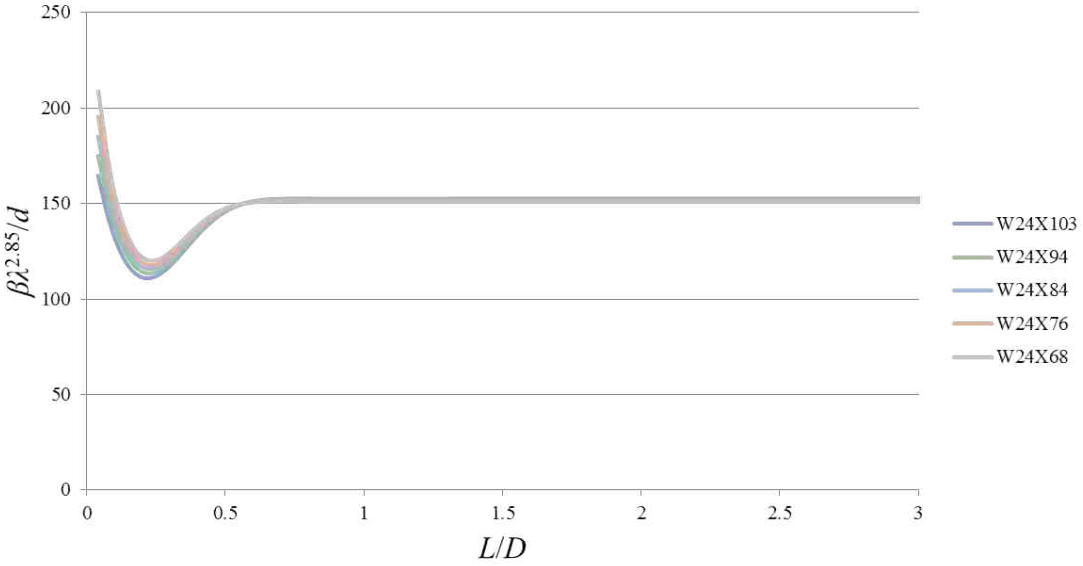

Figure B.90: W24 Weak Axis - Family 3

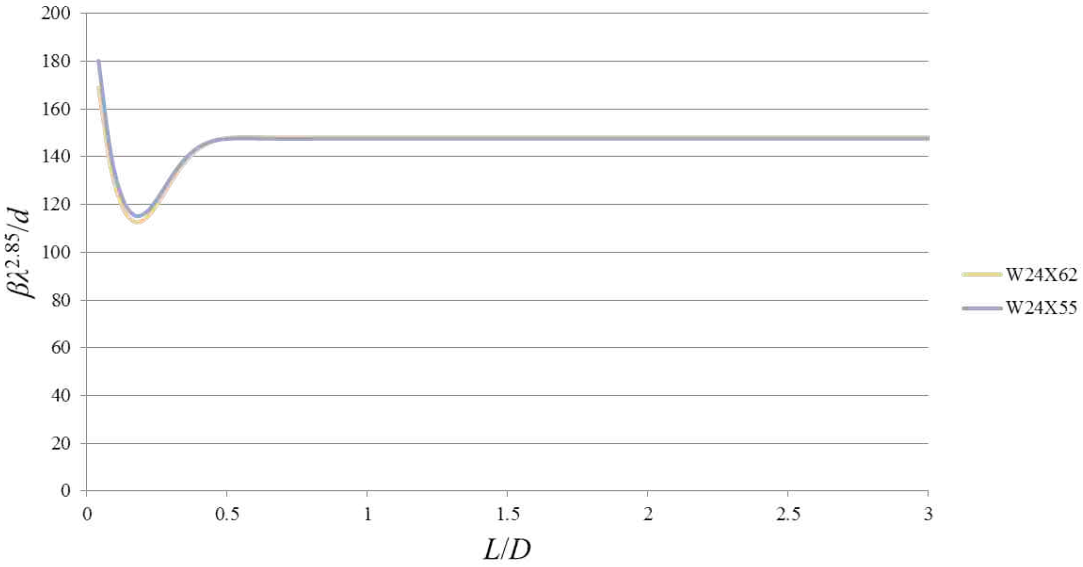

Figure B.91: W24 Weak Axis - Family 4

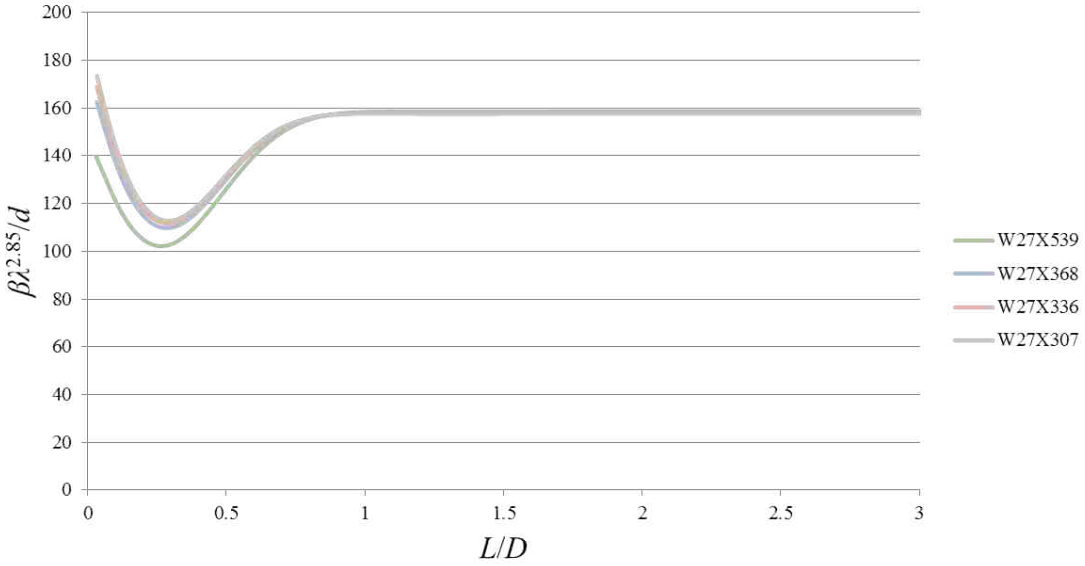

Figure B.92: W27 Weak Axis - Family 1

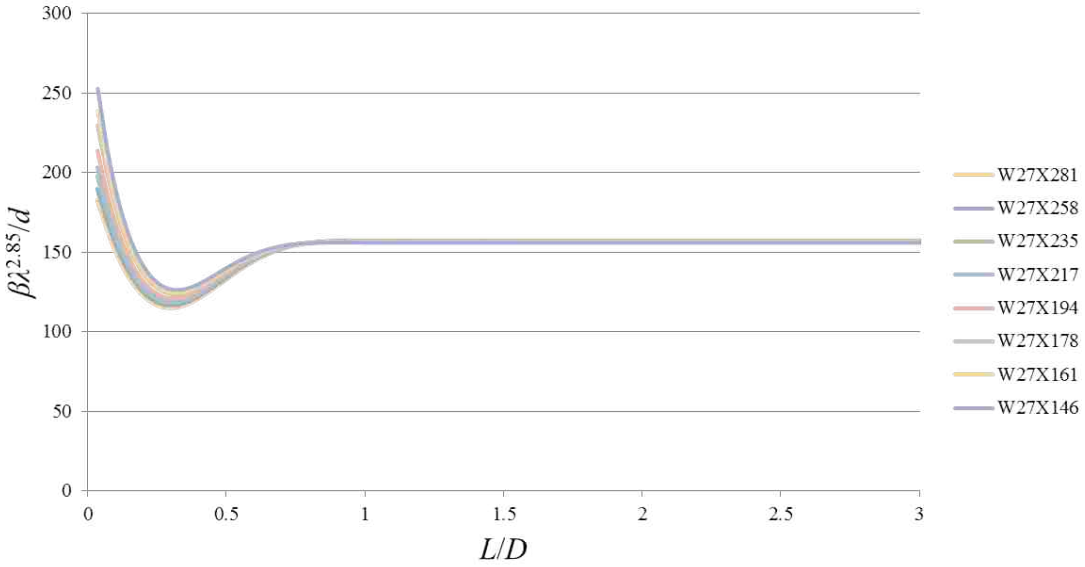

Figure B.93: W27 Weak Axis - Family 2

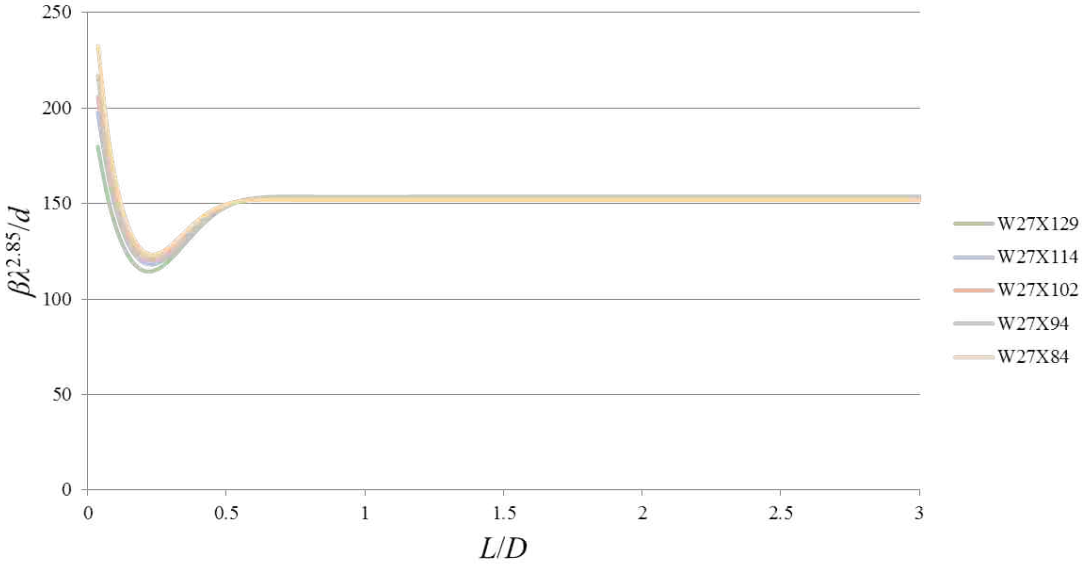

Figure B.94: W27 Weak Axis - Family 3

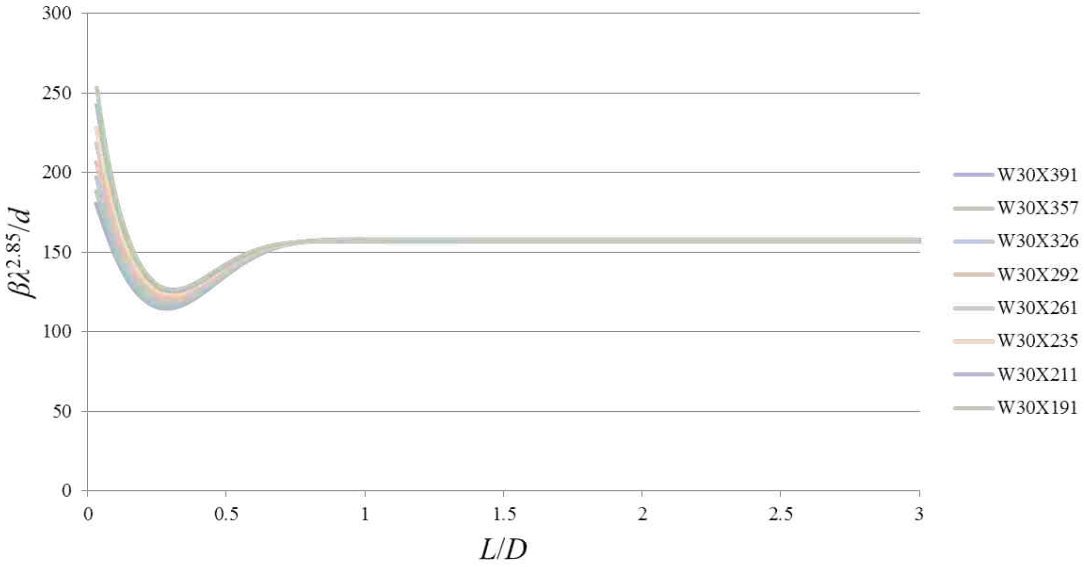

Figure B.95: W30 Weak Axis - Family 1

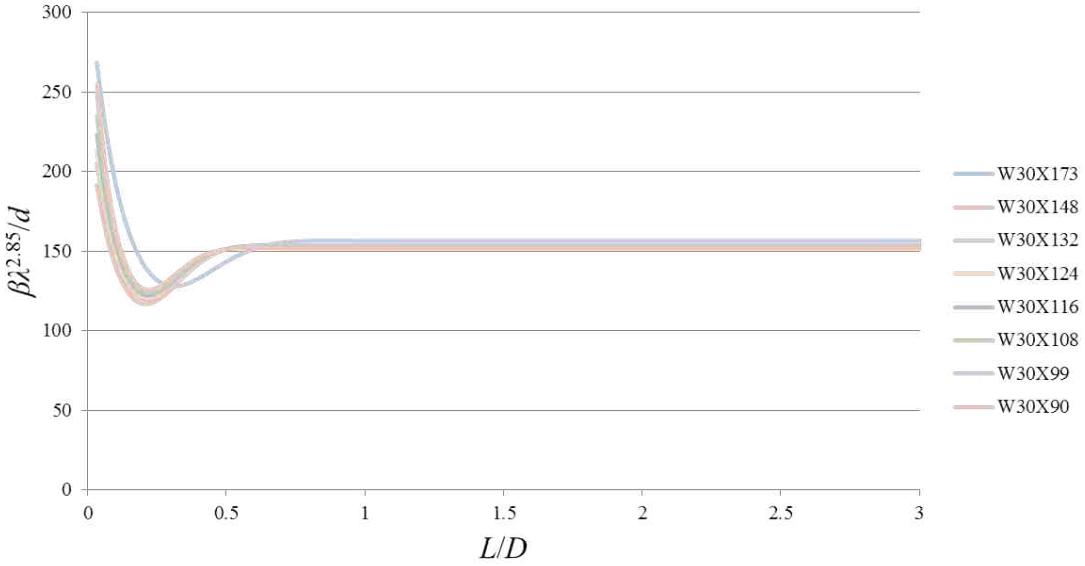

Figure B.96: W30 Weak Axis - Family 2

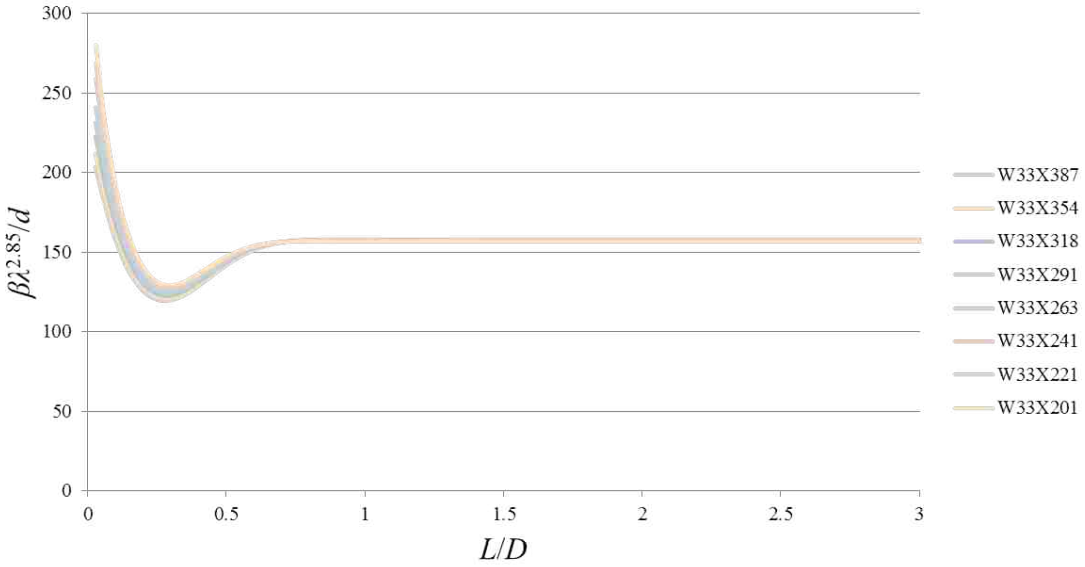

Figure B.97: W33 Weak Axis - Family 1

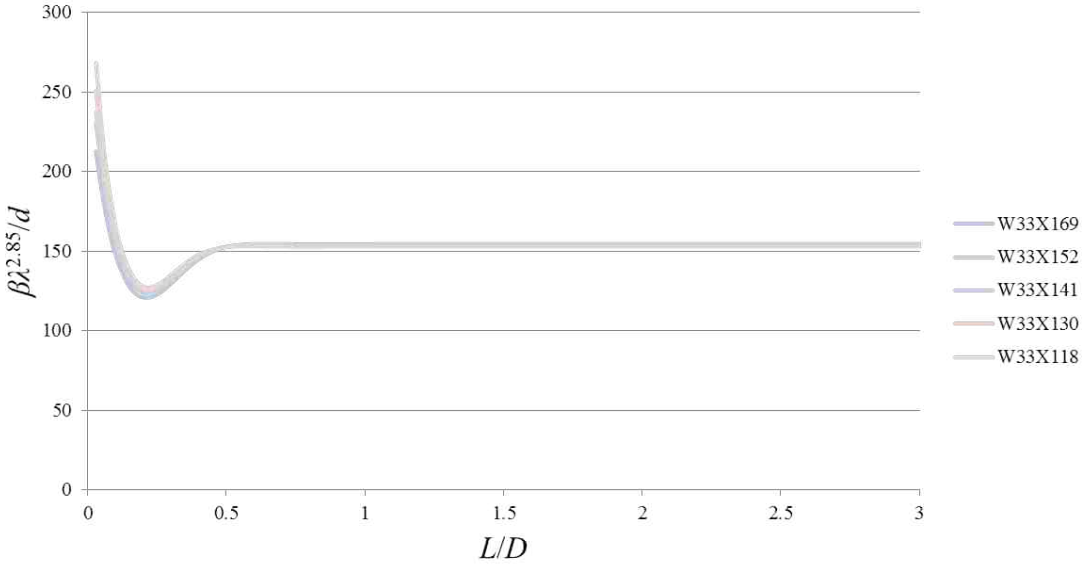

Figure B.98: W33 Weak Axis - Family 2

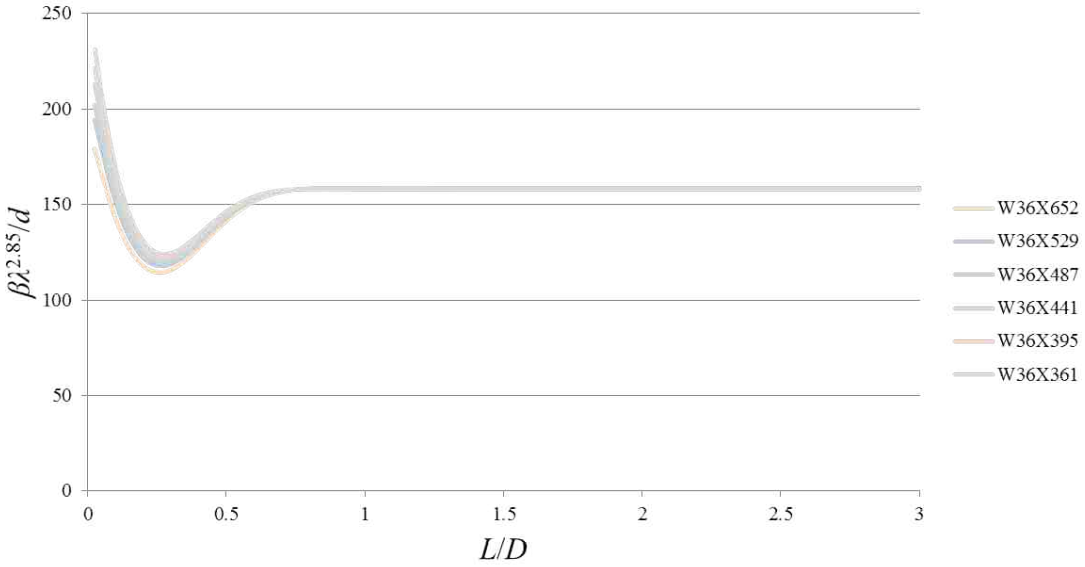

Figure B.99: W36 Weak Axis - Family 1

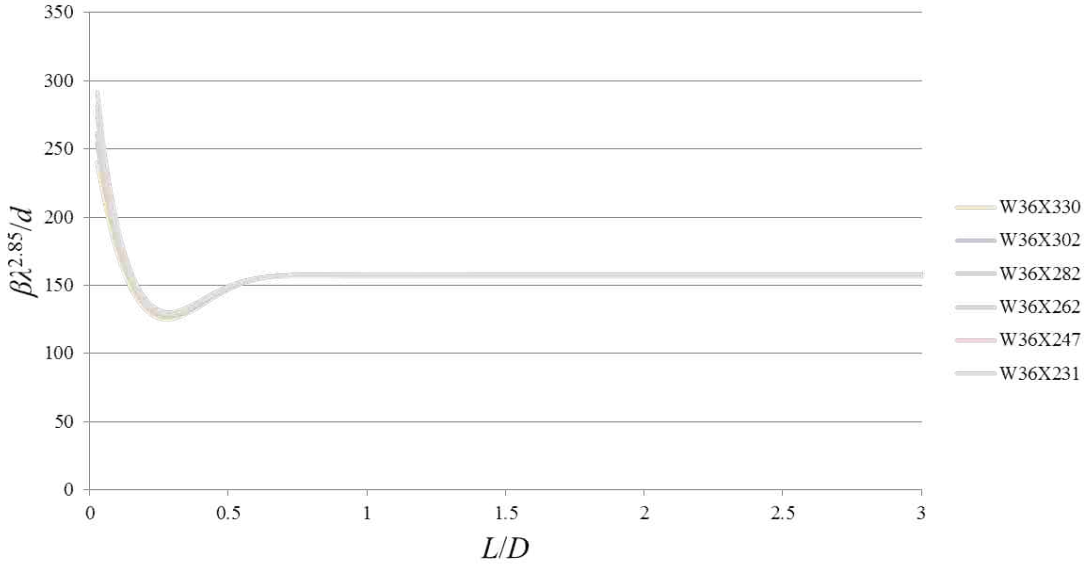

Figure B.100: W36 Weak Axis - Family 2

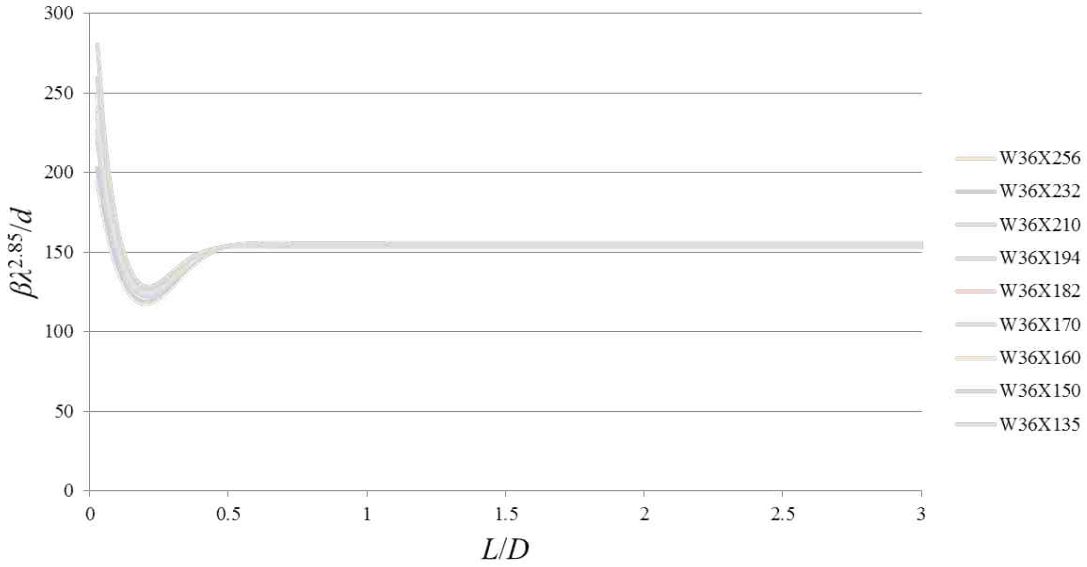

Figure B.101: W36 Weak Axis - Family 3

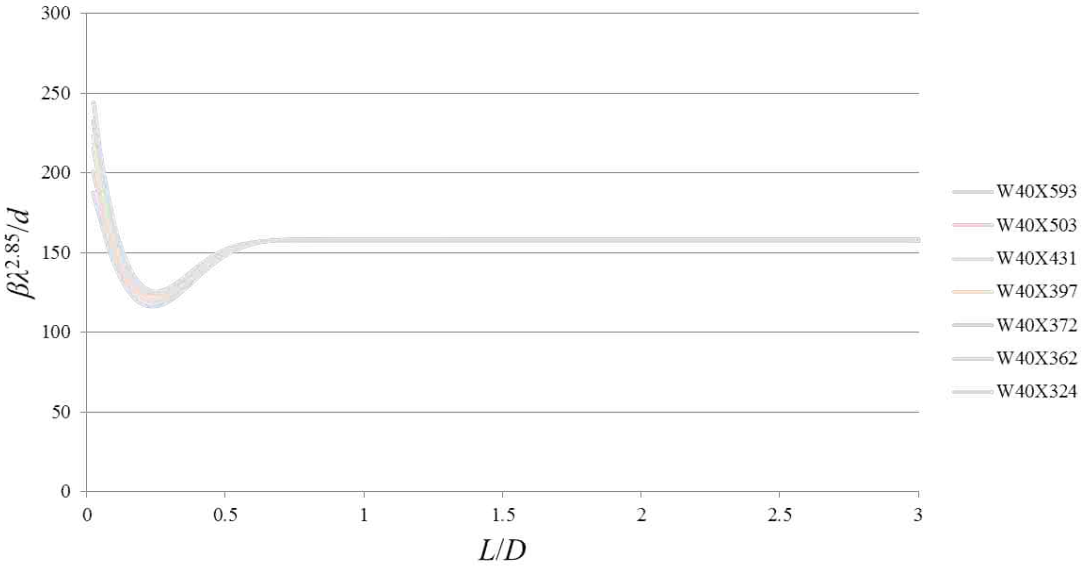

Figure B.102: W40 Weak Axis - Family 1

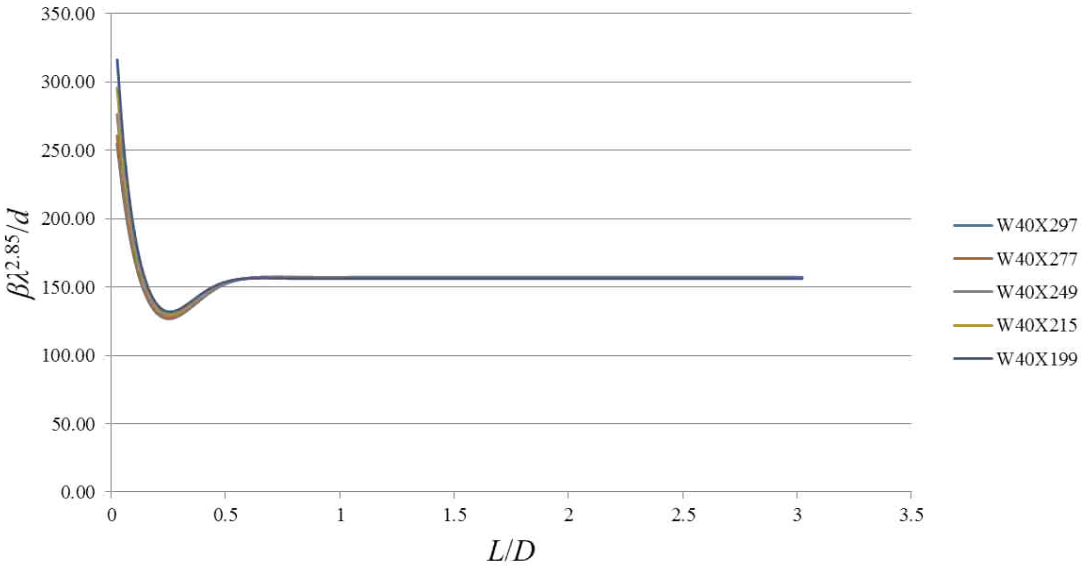

Figure B.103: W40 Weak Axis - Family 2

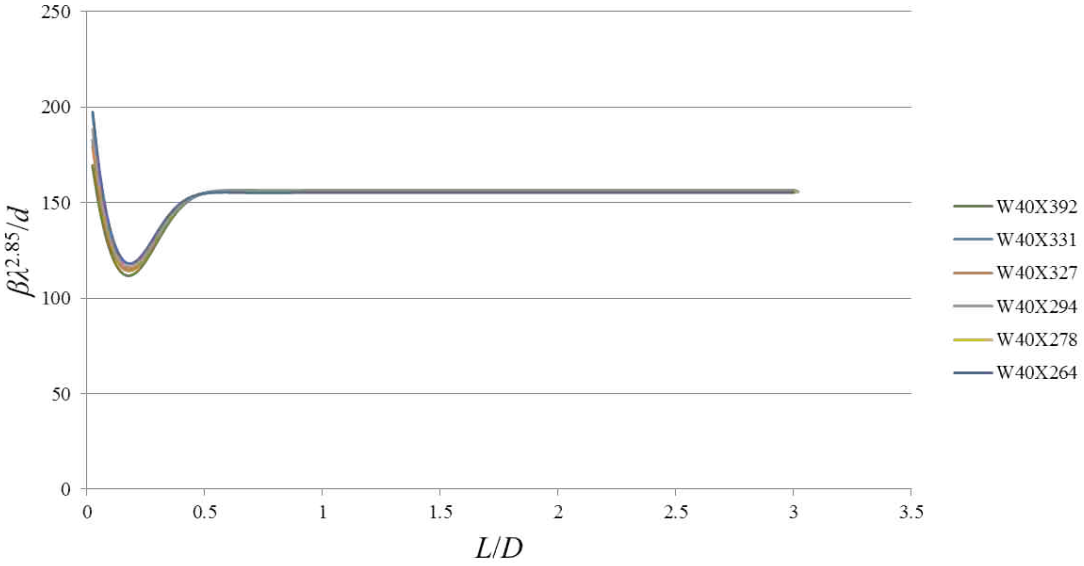

Figure B.104: W40 Weak Axis - Family 3

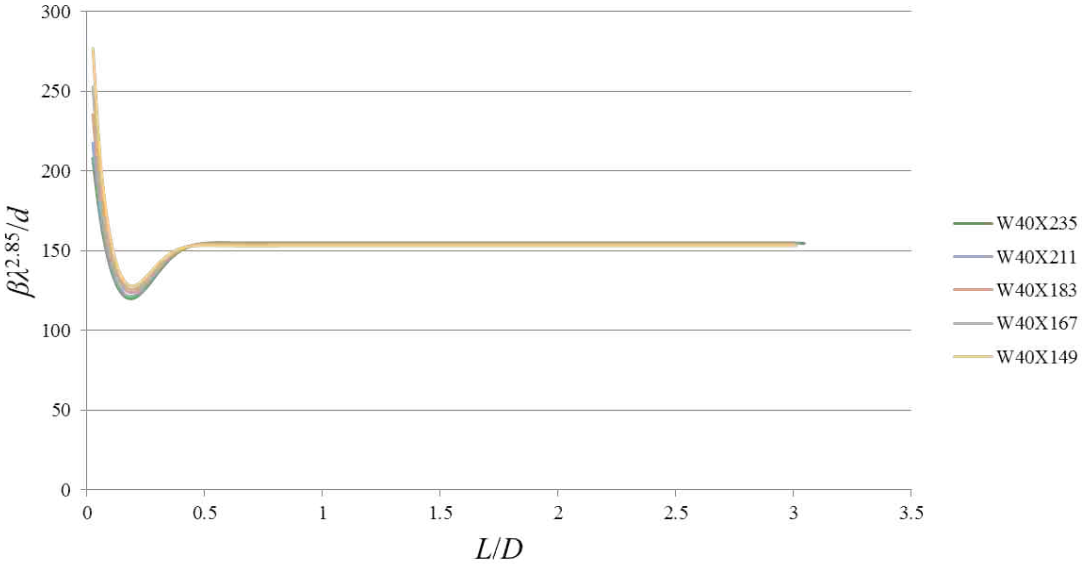

Figure B.105: W40 Weak Axis - Family 4

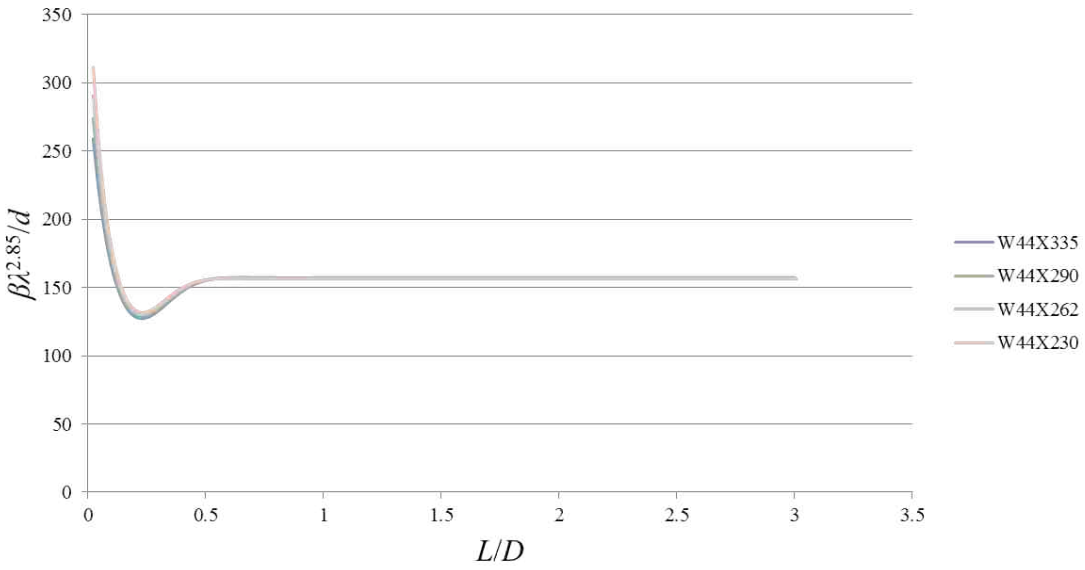

Figure B.106: W44 Weak Axis